Experimental Investigation of Thermal and Kinetic Impacts of Surface Acoustic Waves on Water Droplet

Mubbashar Mehmood

A thesis submitted for the degree of Doctor of Philosophy

Institute of Mechanical, Process and Energy Engineering

School of Engineering & Physical Sciences

Heriot-Watt University

July 2020

ABSTRACT

An analysis model for investigation of the coupling of kinetic and thermal impacts of surface acoustic wave (*SAW*) on a microscale droplet is proposed. The model is based on mass, momentum, and energy conservation principles with assistance from experimental observations. The investigation is carried out on a 25 µl water droplet placed on the *SAW* device fabricated on an aluminium (*Al*) plate substrate with deposition of 5 µm thick zinc oxide (*ZnO*) as a top layer. The devices have a thickness of 200 µm and 600 µm with the wavelength (λ) of 100 µm and 200 µm using Rayleigh, Sezawa, and a Lamb and Rayleigh hybridized mode. The SAW input power values are from 0.30 W to 4.0 W with a temperature range of 5-30 °C in this study.

A charged-coupled device (*CCD*) camera has been employed to monitor streaming inside the droplet. To visualise the streaming, 10 µm red polystyrene particles have been used whereas the velocity of particles estimated using particle image velocimetry (*PIV*). An infrared (*IR*) thermal camera has been used to detect the droplet surface temperature. However, temperature distributions of fluid layers of the droplet are estimated by developing a MATLAB code. The data has been used in the implementation of the analysis model to interpret the coupling mechanism inside the droplet. The thermal impact includes energy absorbed by the droplet, heat transfer from the substrate to the droplet, from the droplet to the air and the waves penetrated to the droplet (radiation). Whereas kinetic impact involves energy transferred by the streaming and friction inside the droplet.

Since this study is based on temperatures much lower than the boiling temperature, no phase change or evaporation observed, therefore, no significant mass transfer has been observed either with Rayleigh or Sezawa. However, at input power (P_{in}) of 4.0 W using Rayleigh wave (R-wave) where the droplet slightly moves away on the surface in the direction of the waves. Since Sezawa waves (S-waves) travel in the interlayers, they have less *SAW* force because of which droplet sticks to the surface and does not move away even at higher input power.

It has been observed that the thermal impacts of the *SAW* are more dominant than the kinetic when considering both Rayleigh and Sezawa wave modes. However, the streaming plays a key role in enhancing the heat transfer inside the droplet by internal convection. The major source of thermal impact is the radiation of *SAW* power (~ 0.05 W to 0.20 W) penetrated to the droplet at input power (P_{in}) ranging from 0.96 W to 3.2 W, while, at the power of 0.38 W or lower, is from both the *SAW* radiation (~0.025 W) and hot substrate (~0.01 W) using Rayleigh waves.

Inverse heat flux from droplet to the substrate is observed after 'reverse time' at $P_{in} >$ 0.50 W and $P_{in} >$ 1.0 W for Rayleigh and Sezawa, respectively. Heat always transfers from droplet to the air since this is the heat leaving the system.

The thermal impacts of both Rayleigh and Sezawa modes on the droplet showed an exactly similar trend when compared to each other based on the results from the analysis model and experimental data. However, the thermal impacts of *SAW* on the droplet with a Sezawa wave is slightly less as compared to the Rayleigh. The thermal energy absorbed by the droplet using Rayleigh waves is 4% more as compared to the Sezawa at an input power of 0.96 W. However, this dropped to 1.5% at a higher input power of 3.2 W after the same time frame.

It has been found that using the same wave mode, temperature rise inside the droplet is directly proportional to the resonant frequency of the device. Furthermore, Lamb and Rayleigh hybridized waves generate intense thermal impacts, showed 3.5 times and 2.5 times higher temperature as compared to the pure Rayleigh mode at P_{in} of 2.2 W and 3.2 W, respectively. The same trend and difference have been observed when the hybridized mode is compared with pure Sezawa mode.

DEDICATION

This thesis is dedicated to

To my wonderful parents

Tariq Mehmood, Samina Khanum

My wife

Sanya Zareen

And Children

Muhammad Hashir, Muhammad Hanzala &

Bareerah Mubbashar

ACKNOWLEDGEMENTS

First, I thank Allah (SWT) who has supported me to do this work and helped me in every phase of my PhD. I have been very fortunate to get support from my three supervisors: Dr Baixin Chen, Dr Yeaw Chu Lee, and Prof. Richard Fu. Special thanks to my primary supervisor, Dr Baixin Chen, for his guidance and full support during the entire project that enables me to reach to this stage. Thanks to Prof. Richard Fu and his team for allowing me to use their lab facilities and their guidance at the University of Northumbria, Newcastle upon Tyne.

I acknowledge the financial support from EPS through my supervisor (Dr Chen) to cover the tuition fee of the entire course. Financial support from the Higher Education Commission (HEC) of Pakistan for providing me with funds in my last year of studies is also much appreciated. I acknowledge travel grant from UK fluids network (UKFN) in 2018 and 2019 for a short research visit to Northumbria University to collect data for this study.

Thanks to all my friends and family members who always encouraged me to achieve this target. Special thanks to my parents and my wife who allowed me to study abroad and they lived back home in my absence. Their prayers helped me a lot to achieve this goal.

Finally, I would like to thanks to my friends, Dr Umar Khan, Dr Mohsin Raza, Dr Atif Rasheed, Dr Waqas Tanveer, Dr Afaq Ahmed, Dr Muhammad Iqbal, Dr Syed Ali Hasnain, Dr Tariq Nawaz Chaudhry and Dr Muhammad Farooq for their suggestions and motivation.

HERIOT
WATT
UNIVERSITY

Research Thesis Submission

Please note this form should be bound into the submitted thesis.

Name:	**Mubbashar Mehmood**		
School:	Engineering & Physical Sciences		
Version: *(i.e. First, Resubmission, Final)*	Final	Degree Sought:	PhD in Mechanical Engineering

Declaration

In accordance with the appropriate regulations, I hereby submit my thesis and I declare that:

1. The thesis embodies the results of my own work and has been composed by myself
2. Where appropriate, I have made acknowledgement of the work of others
3. The thesis is the correct version for submission and is the same version as any electronic versions submitted*.
4. My thesis for the award referred to, deposited in the Heriot-Watt University Library, should be made available for loan or photocopying and be available via the Institutional Repository, subject to such conditions as the Librarian may require
5. I understand that as a student of the University I am required to abide by the Regulations of the University and to conform to its discipline.
6. I confirm that the thesis has been verified against plagiarism via an approved plagiarism detection application e.g. Turnitin.

ONLY for submissions including published works

Please note you are only required to complete the Inclusion of Published Works Form (page 2) if your thesis contains published works)

7. Where the thesis contains published outputs under Regulation 6 (9.1.2) or Regulation 43 (9) these are accompanied by a critical review which accurately describes my contribution to the research and, for multi-author outputs, a signed declaration indicating the contribution of each author (complete)
8. Inclusion of published outputs under Regulation 6 (9.1.2) or Regulation 43 (9) shall not constitute plagiarism.

* *Please note that it is the responsibility of the candidate to ensure that the correct version of the thesis is submitted.*

Signature of Candidate:		Date:	13-07-2020

Submission

Submitted By *(name in capitals)*:	Mubbashar Mehmood
Signature of Individual Submitting:	
Date Submitted:	13-07-2020

For Completion in the Student Service Centre (SSC)

Limited Access	Requested	Yes		[✓ No]		Approved	Yes		No	
E-thesis Submitted ***(mandatory for final theses)***										
Received in the SSC by *(name in capitals)*:						Date:				

Inclusion of Published Works

Please note you are only required to complete the Inclusion of Published Works Form if your thesis contains published works under Regulation 6 (9.1.2).

Declaration **N/A**

This thesis contains one or more multi-author published works. In accordance with Regulation 6 (9.1.2) I hereby declare that the contributions of each author to these publications is as follows:

Citation details	e. g. Author 1 and Author 2, Title of paper, Title of Journal, X, XX-XX (20XX)
Author 1	Contribution….
Author 2	Contribution….
Signature:	
Date:	

Citation details	e. g. Author 1 and Author 2, Title of paper, Title of Journal, X, XX-XX (20XX)
Author 1	Contribution….
Author 2	Contribution….
Signature:	
Date:	

Citation details	e. g. Author 1 and Author 2, Title of paper, Title of Journal, X, XX-XX (20XX)
Author 1	Contribution….
Author 2	Contribution….
Signature:	
Date:	

TABLE OF CONTENTS

Contents

ABSTRACT i

DEDICATION iii

ACKNOWLEDGEMENTS iv

Research Thesis Submission v

*E-thesis Submitted (**mandatory for final theses)*** v

Inclusion of Published Works vi

TABLE OF CONTENTS vii

LIST OF TABLES xiii

LIST OF FIGURES xiv

Lists of Publications by The Candidate xxvii

Nomenclature and Abbreviations xxviii

Chapter 1 : INTRODUCTION 1

1.1 Research background 1

1.2 Research aim and objectives 2

1.3 Thesis outline 2

Chapter 2 : Literature Review 5

2.1 Introduction 5

2.2 Devices to generate SAW and applications 5

2.2.1 Straight IDT 5

2.2.2 Focussed IDT 7
2.2.3 Slanted or tapered IDT 7
2.2.4 Circular IDT 8
2.2.5 Bending IDT 8
2.2.6 Other applications of SAW 9
2.2.7 Types of piezoelectric material, parameters 10
2.2.8 Parameters to find out the behaviour of the devices 10
2.3 Type of waves, properties and applications 11
2.3.1 Rayleigh waves (R-waves) 13
2.3.2 Sezawa waves (S-waves) 13
2.3.3 Lamb waves 14
2.3.4 Effect of substrate thickness and wavelength on the wave mode 15
2.3.5 Standing surface acoustic waves (SSAW) 16
2.4 Different mechanisms and applications related to R-SAW and Sezawa 18
2.4.1 Microfluidics by R-SAWs 18
2.4.2 Sezawa waves for microfluidics and sensitivity 23
2.4.3 Hybrid modes: a mixture of Rayleigh and Lamb waves 24
2.5 Kinetic and thermal impacts caused by the SAW 27
2.5.1 Internal streaming inside the droplet 27
2.5.2 Thermal impact of the SAW on the droplet 29
2.6 Applications of SAW-based heating system 34
2.6.1 Acoustothermal heating of the channel-based microfluidic system 35
2.6.2 Polymerase chain reaction (PCR) 35
2.6.3 R-SAW compatibility with PCR 35
2.6.4 Controlling temperature of the droplet 36

2.6.5 With an applied input voltage/power and duty factor 36

2.6.6 Applications other than PCR 39

2.6.7 Acoustic tweezers 41

2.6.8 Temperature distribution inside the droplet 41

2.7 Numerical work related to this study 42

2.7.1 Streaming inside the droplet 42

2.7.2 Numerical study of acoustothermal heating of the fluid 43

2.8 Summary and research gap 44

Chapter 3 : An Analysis Model of Kinetic and Thermal Coupling Impacts of SAW on The Droplet. 46

3.1 The analysing model 46

3.1.1 The conservation of mass 46

3.1.2 The conservation of momentum 48

3.1.3 The conservation of energy 50

3.2 Summary 51

Chapter 4 : Methodology and Experimental Setup 53

4.1 Experimental Details 53

4.1.1 ZnO as a thin-film piezoelectric material 53

4.1.2 Thin-film deposition for IDT 55

4.2 The design of the system to detecting the data for model analysis 56

4.2.1 The data for mass and momentum models 56

4.2.2 The data for the energy model 57

4.3 The experimental setup 57

4.3.1 Equipment required to generate SAW 58

4.3.2 Identification of resonant frequency of the device 59

4.3.3 Surface treatment of the device 60

4.3.4 Detail of SAW devices for this study..61

4.4 Method to measure the mass transfer of the droplet.......................................63

4.5 Method to measure the velocity and temperature distribution 64

4.5.1 Measurement of velocity of particles using PIV 64

4.5.2 Analysis of the thermal impacts 66

4.5.3 Temperature data treatments 68

4.5.4 Coupling of thermal and kinetic impacts 71

4.5.5 Calculation of the average temperature of the whole droplet 72

4.5.6 Implementing energy conservation to our model 74

4.5.7 Challenges during data treatment..77

4.6 Summary 77

Chapter 5 : Analysis of The Impact Mechanisms of Rayleigh SAW on Microdroplet ..78

5.1 Introduction 78

5.2 Analysing of the mass impact of SAW on droplet using mass conservation principle. 79

5.3 Analysis of the mechanical impact mechanism of *SAW* on droplet by momentum conservation. 82

5.4 The diagnostics of the thermal and kinetic coupling mechanism of *SAW* on droplet using the energy conservation principle. 86

5.4.1 The mechanical power due to the changes in the volume of the droplet ..86

5.4.2 The thermal impacts of SAW on the droplet 87

5.4.3 The kinetic impacts of SAW on the droplet: streaming inside the droplet92

    - 5.4.4 Diagnosis of heat transfers inside the droplet 93
    - 5.4.5 Diagnostics of kinetics inside the droplet 99
    - 5.4.6 Estimation of heat radiated inside the droplet 101
- 5.5 Repeatability of experiments 103
- 5.6 Summary 105

Chapter 6 : Analysis of The Impact Mechanisms of Sezawa SAW on Microdroplet.. 107

- 6.1 Introduction 107
- 6.2 Analysing of the mass impact of SAW on droplet by mass conservation principle 107
- 6.3 Analysis of the mechanical impact mechanism of SAW on droplet using momentum conservation 110
- 6.4 The diagnostics of the thermal and kinetic coupling mechanism of SAW on the droplet using the energy conservation principle. 111
    - 6.4.1 The mechanical power due to the changes in the volume of the droplet 112
    - 6.4.2 The thermal impacts of SAW on the droplet 112
    - 6.4.3 The kinetic impacts of SAW on the droplet 118
    - 6.4.4 Diagnostics of heat transfers inside the droplet 120
    - 6.4.5 Diagnostics of kinetics inside the droplet using Sezawa 123
    - 6.4.6 Estimation of heat radiated inside the droplet 125
- 6.5 Repeatability of experiments 126
- 6.6 Summary 128

Chapter 7 : Comparison of The Impacts of SAW Modes and Other Parameters on The Droplet 130

7.1 The comparison of impacts of Rayleigh and Sezawa waves on droplet 130

7.1.1 The mass impacts of R-wave Vs S-wave 130

7.1.2 The momentum impacts of R-wave Vs S-wave 131

7.1.3 The thermal impacts of R-wave Vs S-wave on droplet 132

7.2 The thermal impacts of hybridized waves on the droplet 132

7.2.1 Comparison of thermal impact of hybridized wave versus pure Rayleigh 134

7.2.2 Comparison of thermal impact of hybridized wave versus pure Sezawa 135

7.3 Thermal impacts of Sezawa at two different frequencies 137

7.4 Summary 139

Chapter 8 : Conclusions and Future Recommendations 140

8.1 Conclusions 140

8.2 Answer to the questions from literature 143

8.3 Limitations of this work 144

8.4 Future work 144

References 145

Appendices 170

Appendix A: MATLAB code to get temperature distribution inside the droplet 170

Appendix B: Code for the rise in T_d and generating multiple lines on graphs 180

LIST OF TABLES

Table 2.1: Summary of common device structure and their applications [2], [12], [42]–[45], [32], [34]–[37], [39]–[41][46][47]. 9

Table 2.2: Different waves and their applications [36], [66], [86], [92]–[95], [107], [108], [110]–[112], [67]–[71], [80], [81], [85] 26

Table 4.1: Electromechanical coupling co-efficient, *TCF* and acoustic velocity of $LiNbO_3$, *PZT*, *AlN* and *ZnO* [75], [161], [162] 54

Table 4.2: Summaries of devices with the detail of wavelength of the waves, thickness of the substrate, resonant frequencies and wave mode of the waves. 62

Table 5.1: Mass change of droplet versus time at P_{in} 2.0 W using Rayleigh waves. 80

Table 5.2: Mass change of the droplet versus time at P_{in} 3.2 W using Rayleigh waves. 81

Table 5.3: Specific heat capacity and the density of the water within temperature range 0 to 50.0 °C [199], [200]. 95

Table 5.4: Dynamics viscosity of the droplet (water) at temperature values 20 °C to 50 °C. 100

Table 6.1: Mass change of the droplet versus time at P_{in} 2.07 W using Sezawa waves. 108

Table 6.2: Mass change of the droplet versus time at P_{in} 3.34 W using Sezawa waves. 109

LIST OF FIGURES

Figure 2.1: Working principle of a *SAW* device (a) Comb-like interdigital transducer showing wave propagation direction [2] (b) A pair of *IDT*s fabricated on a piezoelectric substrate, one acts as an input transducer and other as an output [32]............................6

Figure 2.2: A focused *IDT* with a droplet [34]. 7

Figure 2.3: Basic structure of slanted *IDT* [35]. 7

Figure 2.4: Basic structure of circular *IDT* design [38]. 8

Figure 2.5: Flexible/bendable devices (a) *ZnO*/PET SAW device in bending (2 µm thick *ZnO* film deposited onto 120 micron PET foil) [39] (b) *ZnO* of 5 µm thickness on Al foil of thickness 50 µm in a bendable position [45]..9

Figure 2.6: Classification of acoustic wave modes: bulk acoustic wave (*BAW*) and surface generated acoustic wave (*SGAW*) [36]. 12

Figure 2.7: Propagation of Rayleigh surface acoustic waves [73]................................13

Figure 2.8: Effect of film thickness (in the range 1.5 µm to 6.6 µm) on the resonant frequency of Rayleigh and Sezawa waves. Reflection signal of the device is shown versus resonant frequency [75]. 14

Figure 2.9: Frequency response (S_{11}) spectra of the *ZnO*/*Al* foil *SAW* devices with different wavelengths (200 & 400 µm) [45]. 16

Figure 2.10: Schematic of *SSAW* device, showing a working mechanism [85]. 16

Figure 2.11: Schematic of the separation mechanism showing particles beginning to translate from the sidewall to the centre of the channel due to axial acoustic forces applied to the particles when they enter the working region of the *SSAW* [87].............17

Figure 2.12: Platelet separation from the whole blood using the acoustic device (a) Polydimethylsiloxane (*PDMS*) channel with *IDT* pairs using *LN* as substrate (b) the whole blood sample is injected and focused hydrodynamically by two layers of sheath flow (c) Blood particles in the working region of SSAWs are separated in a size-gradient manner (d) platelets are mainly sorted and collected in the centre outlet (e) Platelets in the middle of the channel [92]. 17

Figure 2.13: Pumping of a 2 µl droplet at an input power of 4.0W (a) 0.0s; (b) 0.08 s; and (c) 0.16 s after applying *SAW* [93]. 18

Figure 2.14: Liquid droplet on *ZnO*/diamond surface driven by *SAW*. Waves propagate from right to left) (a) Original 10 µl droplet (b) Droplet deformation on *SAW* power of 21.0 W [93]. 19

Figure 2.15: Summary of different phenomena (streaming, pumping and jetting) inside the liquid droplet at different power levels and variable droplet sizes [93]. 19

Figure 2.16: Side (left) and top (right) views of the nebulization behaviour of a 0.5 µl water droplet with a *SAW* frequency of 11.8 MHz at a power of 7.2W. (a) Original droplet (b) mist generation and satellite droplets at 0.003s; (c) significant nebulization at 0.0006 s [98]. 21

Figure 2.17: Nebulization speed (µL/s) as a function of frequency (11.8 MHz, 23.1 MHz, and 37.20 MHz) and *SAW* power [98]. 22

Figure 2.18: Effect of input power and droplet size on nebulization time with a fixed resonant frequency of 23.3 MHz [100]. 22

Figure 2.19: The principle of interfacial droplet jetting using *F-SAW* device (b) photographs of interfacial droplet jetting angle under a single *IDT* experimental case after 0 ms, 2.5 ms, 4.5 ms, and 9.5 ms [105]. 23

Figure 2.20: 1 µl droplet on ZnO SAW device before (a) and after (b) driven by *RF* signal with frequency 178.7 MHz [110]. 24

Figure 2.21: (a) *HYDRA* device with bulk mode sensing area, hatched in red and *SAW* mode runway hatched in blue, (b) Schematic depiction of the experimental setup used for concurrent nebulization of insulin and detection of its residual mass on the device (c) Schematic illustration of the underlying mechanism governing the *HYDRA* device. [112]. 25

Figure 2.22: SAW propagation from *IDT* to the droplet on $LiNbO_3$ piezoelectric substrate showing Rayleigh angle with internal streaming inside the droplet [113]. 28

Figure 2.23: Schematic drawings of acoustic streaming within droplet using top (left) and side (right) view [114]. 28

Figure 2.24: Flow velocity induced by the acoustic wave as a function of *RF* signal voltage. All *SAW* devices have 60 finger pairs [114] 29

Figure 2.25: Dependence of streaming velocity on the signal voltage with droplet size as a parameter, all devices have λ 32 µm [114]. 29

Figure 2.26: Thermal measurement results for the *F-SAW* device in air and water (a) Temperature increases and resonance frequency shift of *F-SAW* device with input power (b) temperature variation of *F-SAW* device with time in air and water [105] 30

Figure 2.27: Experimental setup for monitoring of streaming and temperature change [118]. 31

Figure 2.28: Peclet number for heat transfer mechanism as a function of P_{IDT} for water-glycerin mixture [119]....32

Figure 2.29: Effect of power input on the streaming velocity of particles for various viscosities (Pure water-glycerin mixture) [119]....32

Figure 2.30: Evolution of droplet temperature in function of acoustic power for four different viscosities (0.89, 13.1, 509 and 934 mPa.s) at 25℃ [122]....34

Figure 2.31: *PCR* reaction yield of a common industrial thermocycler as a function of dynamic viscosity of liquid [18]....36

Figure 2.32: Comparison of temperature with and without droplet [13]....36

Figure 2.33: Experimental results for 10 µl water droplet (a) Temperature rise Vs time with an applied input voltage as a parameter (b) Temperature obtained one minute after the voltage is applied [13]....37

Figure 2.34: Droplet heating can be controlled by varying the a) input power to the device or the b) duty cycle at constant input power (23 dBm here). In each case, the steady-state reached after 3.0 s [132]....38

Figure 2.35: Experimental setup to control the temperature of the liquid on the path of *SAW* [134]....39

Figure 2.36: Temperature obtained after one minute of power applied. The power applied was fixed at 1.0 W [135]....40

Figure 2.37: Time responses during coagulation reaction (a) and (b) with and without temperature control by *SAW* [135]....40

Figure 2.38: (a) Water-in-oil droplet are focused at the centre of microchannel by two oil sheath flows travelling downstream. (b) On applying acoustothermal heating from

the left, the droplet pushed to the right (c) On applying power from the right, the droplet pushed to the left [138]. 41

Figure 2.39: Liquid streaming in 80 wt% glycerol/water droplet which is placed at the centre of the *SAW* propagation path [14]. 42

Figure 2.40: T_d at point 1 and point 2, *SAW* is generated from left side [14]. 42

Figure 2.41: Streaming velocity at the top of a 30 µl droplet positioned symmetrically within the SAW propagation direction. Solid lines represent numerical results whereas markers denote experimentally measured data at different *RF* powers [139]. 43

Figure 2.42: Schematic diagram of the device with the *PDMS* channel [140]. 44

Figure 2.43: Temperature of the fluid at different aspect ratios (δ) at different power inputs [122]. 44

Figure 3.1: A *SAW*-based solid-liquid interaction analysis model of mass conservation. The heated droplet by *SAW* can change the phase of the liquid and droplet can transfer mass to the surrounding air. 47

Figure 3.2: The momentum conservation showing buoyancy, drag, friction forces with the droplet velocity...48

Figure 3.3: A thermodynamic energy conservation model of *SAW*-droplet interaction showing heat transfers and kinetic change inside the droplet. 51

Figure 4.1: Device specifications with *Al* electrodes as *IDT*s, *ZnO* thin film of thickness 5 µm and *Al* plate substrate. 56

Figure 4.2: Schematic diagram of the experimental setup with the IR thermal camera, *CCD* camera, a lighting source, water droplet placed on the *IDT*. 58

Figure 4.3: Equipment to generate and amplify signals (a) Signal generator to generate electrical signals (b) Power amplifier to amplify the signals (c) Power meter to measure input in watts. 59

Figure 4.4: Flow chart for working of the experimental setup. Signal generator, power amplifier, power meter, a *SAW* device. A side view image is captured by *CCD* and *IR* thermal camera. 59

Figure 4.5 The network analyser to identify the resonant frequencies of the device...... 60

Figure 4.6: Droplet on the solid surface with (a) hydrophilic when the contact angle less than 70° and (b) hydrophobic surface after the treatment when the contact angle more than 90°. 61

Figure 4.7: Aluminum plate with different thicknesses (a) h=600 μm, λ= 100 μm, (b) h= 200 μm, λ= 200 μm (c) h= 200 μm, λ= 100 μm. 62

Figure 4.8: Measurement of length and height of the droplet (a) using *IR* camera (b) using the *CCD* camera. 63

Figure 4.9 (a) *CCD* video camera (b) Configuration to capture videos with the camera. 64

Figure 4.10: Image from the tracker showing three different positions inside the droplet: Position 1 close to the substrate, position 2 on the top of the droplet and position 3 is where vortices generate. 66

Figure 4.11: FLIR thermal camera (T-620) with a side view of the device fixed on a printed circuit board (*PCB*). 67

Figure 4.12: Side View image from the thermal camera (a) Whole frame 480*640 matrix (b) Zoomed and cut image of the droplet with dimension 28*40 with the help of MATLAB. 67

Figure 4.13: Four layers of droplet showing 16 elements, MATLAB treated with temperature distribution at 2.0 W Rayleigh waves (a) 0.0 s (b) 5.0 s (c) 10.0 s (d) 15.0 s. The number of elements is showing in (a) from 1 to 16. 69

Figure 4.14: Rise in temperature of each element of the droplet using Rayleigh waves at 26.300 MHz for Rayleigh with power of 2.0 W (a) Elements 1-4 (b) Elements 5-8 (c) Elements 9-12 (d) Elements 13-16. 71

Figure 4.15: Coupling of streaming and thermal part (a) thermal part showing 16 elements with ovals to represent the element's temperature for Qs and Qa (b) streaming image from the tracker, tracking of particles at three different positions. 72

Figure 5.1: (a) Numerical simulation of vibration modes for ZnO (5 µm)/Al (600 µm) based SAW devices. The wavelength of SAW devices is varied from 100 µm to 400 µm. (b) The simulated and measured resonant frequencies of different types of wave modes depend on the wavelength of the SAW devices [197]. 79

Figure 5.2: Volume of the droplet versus time at an input power of 2.0 W and 3.2 W using Rayleigh waves. 80

Figure 5.3: Droplet movement/pumping (a) Before providing SAW (b) After 1.0 s of input power (c) After 2.0 s of input power at 3.2 W using R-waves. 83

Figure 5.4: Droplet movement/pumping (a) Before providing SAW (b) After 0.66 s of input power (c) After 1.0 s of input power (d) After 3.0 s of input power at 4.0 W using R-waves. 84

Figure 5.5: Pumping velocity of the droplet versus time at different input power levels 3.2 W and 4.0 W with Rayleigh waves. 85

Figure 5.6: Momentum of the droplet versus time at an input power of 3.2 W and 4.0 W with Rayleigh waves. 85

Figure 5.7: Thermal images of droplet by Rayleigh at (a) 0.38 W, (b) 0.96 W, (c) 2.0 W, (d) 3.2 W (Time 0.0, 5.0, 11.50, 23.53 and 43.0 s from left to right) observed by FLIR (T-620). 88

Figure 5.8: T_d using Rayleigh waves from 0.0 to 43.0 s at different power levels (0.38 W, 0.96 W, 2.0 W & 3.2 W). T_d is the rise in temperature of the droplet and time is measured in seconds. 89

Figure 5.9: Maximum average temperature of the droplet after 43.0 s of *SAW* acting time for input power values from 0.38 W to 3.2 W. 89

Figure 5.10: Droplet temperature gradient vs time at variable power levels (0.38 W, 0.96 W, 2.0 W and 3.2 W) by Rayleigh *SAW*. 90

Figure 5.11: Max. dT/dt vs input power values of 0.38 W, 0.96 W, 2.0 W and 3.2 W using Rayleigh waves. 91

Figure 5.12: Temperature difference of droplet and substrate at different P_{in} values (0.38 W, 0.96 W, 2.0 W and 3.2 W) by Rayleigh. $T_{(s-d)}$ is in °C and time is measured in seconds. 92

Figure 5.13: Velocity of particles at three different positions with Rayleigh waves for an input power of (a) 0.38 W (b) 0.96 W, (c) 2.0 W and (d) 3.2 W. U_1 is the velocity at a position close to the substrate inside the droplet, U_2 is on the top and U_3 is the vortex velocity. 93

Figure 5.14: Rates of energy absorbed, heat transfers inside and outside of the droplet at power levels of 0.38 W, 0.96 W, 2.0 W and 3.2 W (a) Ed (rate of energy absorbed by the droplet), (b) Qs rate of heat transfer from substrate to the droplet, (c) Qa rate of heat transfer from air to the droplet. Rates of heat transfers are measured in watts and time is measured in seconds. 94

Figure 5.15: Effective heat transfer coefficient (αs) for power values 0.38 W, 0.96 W, 2.0 W and 3.2 W against time 0.0 to 43.0 for R-waves, where α is in W/m^2K and time is in seconds. 96

Figure 5.16: Temperature of the bottom layer of the droplet (T_{db}) directly contacts with the substrate at P_{in} values of 0.38 W to 3.2 W using R-waves. 97

Figure 5.17: Effective heat transfer coefficient (αa) for power values 0.38 W, 0.96 W, 2.0 W and 3.2 W against time 0.0 to 43.0 for R-waves, where α is in W/m^2K and time is in seconds. 98

Figure 5.18: Temperature of the outer layer of the droplet (T_{ds}) directly contact with air at P_{in} values of 0.38 W to 3.2 W using R-waves. 99

Figure 5.19: Rate of kinetic energy, Kst(W), Kinetic streaming power inside the droplet for P_{in} (0.38 W, 0.96 W, 2.0 W and 3.2 W), kinetic power is measured in watts and time is measured in seconds. 100

Figure 5.20: Rate of kinetic energy, Kf(W), Kinetic power due to friction near the bottom of the droplet for P_{in} (0.38 W, 0.96 W, 2.0 W and 3.2 W), kinetic power is measured in watts and time is measured in seconds. 101

Figure 5.21: Qr rate of heat radiated from left edge of the droplet. Qr is measured in watts whereas SAW is applied for 43.0 seconds. 102

Figure 5.22: Summary of kinetic energies (K_{st} & K_f) and heat transfers (Q_r, Q_s & Q_a) inside the droplet using Rayleigh waves. Heat transfer from substrate to the droplet (Q_s) takes place when $P_{in} < 0.50$ W and inverse will be the case when $P_{in} > 0.50$ W..........102

Figure 5.23: (a) Rate of energy absorbed (Ed), (b) Heat transfer from substrate to the droplet (Qs) (c) Heat radiated from the edge of the droplet (Qr) at input power of 0.38 W, 0.96 W, 2.0 W, 3.2 W using Rayleigh waves..104

Figure 6.1: Volume of the droplet versus time at an input power of 2.07 W and 3.34 W using Sezawa waves...108

Figure 6.2: Droplet movement/pumping (a) Before providing SAW (b) After 1.0 s (c) After 2.50 s (d) After 9.0 s of the SAW acting time at 3.34 W with Sezawa waves.....110

Figure 6.3: Droplet movement/pumping (a) Before providing SAW (b) After 1.0 s (c) After 2.50 s (d) After 9.0 s of the SAW acting time at 4.18 W with Sezawa waves.....111

Figure 6.4: Thermal images of droplet by Sezawa waves at (a) 0.30 W, (b) 0.99 W, (c) 2.07 W, (d) 3.34 W (Time 0.0, 5.0, 11.50, 23.53 and 43.0 s from left to right) observed by FLIR (T-620). Temperature is measured in °C and time in seconds.......................113

Figure 6.5: Average temperature increase inside the droplet using Sezawa waves at a power input of 0.30 W, 0.99 W, 2.07 W and 3.34 W. Temperature is measured in °C and time in seconds...115

Figure 6.6: Maximum average temperature of the droplet after 43.0 s of SAW acting time for the input power values from 0.30 W to 3.34 W using Sezawa waves. 115

Figure 6.7: Temperature gradient dT/dt using Sezawa waves at 52.220 MHz with a power input values of 0.30 W, 0.99 W, 2.07 W and 3.34 W using S-waves...............116

Figure 6.8: Max *dT/dt* at input power values of 0.30 W, 0.99 W, 2.07 W and 3.34 W using S-waves. 117

Figure 6.9: Temperature difference $T_{(s-d)}$ at different power levels using Sezawa waves at 0.30 W, 0.99 W, 2.07 W and 3.34 W from zero to 43.0 s. The negative difference means the temperature of the droplet is more as compared to the substrate. 118

Figure 6.10: Temperature of the bottom boundary layer of the droplet T_{db} at power input values of 0.30 W, 0.99 W, 2.07 W and 3.34 W required to calculate Qs. T_{db} is measured in °C and time is measured in seconds. 118

Figure 6.11: Average velocities of particles at three different positions inside the droplet at an input power of (a) 0.30 W (b) 0.99 W (c) 2.07 W (d) 3.34 W from zero to 43.0 s. U_1 belongs to the velocity close to the substrate, U_2 on the top of the droplet and U_3 is the vortex velocity. 119

Figure 6.12: Rates of energy absorbed, heat transfers inside and outside of the droplet (a) Ed (rate of energy absorbed by the droplet), (b) Qs rate of heat transfer from substrate to the droplet, (c) Qa rate of heat transfer from air to the droplet using Sezawa waves at power input values of 0.30 W, 0.99 W, 2.07 W and 3.34 W. 121

Figure 6.13: Effective heat transfer coefficient (αs) for power values 0.30 W, 0.99 W, 20.7 W and 3.34 W against time 0.0 to 43.0 s for Sezawa. αs is in W/m^2K and time is in seconds. 122

Figure 6.14: Effective heat transfer coefficient (αa) for power values 0.30 W, 0.99 W, 20.7 W and 3.34 W against time 0.0 to 43.0 s for Sezawa. αa is in W/m^2K and time is in seconds. 123

Figure 6.15: Temperature of the outer layer of the droplet (T_{ds}) directly in contact with air at power input values of 0.30 W, 0.99 W, 2.07 W and 3.34 W using Sezawa waves. 123

Figure 6.16: Rate of kinetic energies Kst (W), frictional power near the at power input values of 0.30 W, 0.99 W, 2.07 W and 3.34 W using S-waves. The rate of kinetic energies is measured in watts and time is measured in seconds. 124

Figure 6.17: Rate of kinetic energies, Kf (W), Kinetic streaming power inside the droplet at power input values of 0.30 W, 0.99 W, 2.07 W and 3.34 W using S-waves. The rate of kinetic energies is measured in watts and time is measured in seconds..... 124

Figure 6.18: Qr rate of heat radiated using Sezawa waves at power input values of 0.30 W, 0.99 W, 2.07 W, 3.34 W... 125

Figure 6.19: Summary of kinetic energies (K_{st} & K_f) and heat transfers (Q_r, Q_s & Q_a) inside the droplet using Sezawa waves. 126

Figure 6.20: Rate of energy absorbed (Ed), heat transfer from substrate to the droplet (Qs), heat radiated inside the droplet (Qr) at input power values of 0.30 W, 0.99 W, 2.07 W and 3.34 W using Sezawa waves.. 127

Figure 7.1: Comparison of relative change in mass of the droplet versus time for Rayleigh and Sezawa at 2.0 W... 131

Figure 7.2: Comparison of relative change in mass of the droplet versus time for Rayleigh and Sezawa at 3.2 W... 131

Figure 7.3: Numerical simulation of vibration modes for *ZnO* (5 µm)/Al(200 µm) based *SAW* devices. The wavelength of the *SAW* device varies from 100 µm to 400 µm. (b) The measured S_{11} of the devices with different wavelengths (c) the simulated and

measured resonant frequencies of different types of wave modes depend on the wavelength of the *SAW* devices fabricated on *Al* plates with thickness of 200 µm [197]. 133

Figure 7.4: Comparison of temperature rise of the droplet by Rayleigh and hybridized mode using the same thickness of the substrate at the power input of 2.2 W. The average temperature is measured in °C whereas time is measured in seconds............134

Figure 7.5: Comparison of Rayleigh and hybridized mode using the same thickness of the substrate at P_{in} of 3.2 W. The average temperature is measured in °C whereas time is measured in seconds...135

Figure 7.6: Comparison of temperature rise of the droplet by hybridized mode and Sezawa using the same device at the input power of 2.2 W. The average temperature is measured in °C whereas time is measured in seconds. 136

Figure 7.7: Comparison of temperature rise of the droplet by hybridized mode and Sezawa using the same device at the input power of 3.2 W. The average temperature is measured in °C whereas time is measured in seconds. 136

Figure 7.8: Temperature rise of the droplet using Sezawa waves at two different frequencies (26.450 MHz and 52.220 MHz) at an input power of 2.0 W. The average temperature is measured in °C whereas time is measured in seconds. 138

Figure 7.9: Temperature rise of the droplet using Sezawa waves at two different frequencies at P_{in} 3.20 W. The average temperature is measured in °C whereas time is measured in seconds...138

Lists of Publications by The Candidate

Journal papers

1. Experimental investigation of kinetic and thermal impacts of Rayleigh surface acoustic waves on the microdroplet using a thin-film piezoelectric device. (Ready to submit)

2. Comparison of kinetic and thermal impacts of surface acoustic waves by using Rayleigh and Sezawa waves. (Ready to submit)

Conference presentations

1. "Experimental study of the coupling mechanism of kinetic and thermal impacts of SAW on micro-droplet" is presented in special interest group (SIG) "*fluid mechanics of cleaning and decontamination*" meeting at the **University of Oxford,** UK dated 08th & 09th July 2019.

2. A poster titled "Kinetics and thermal impacts of Rayleigh-SAW on water micro-droplet" in special interest group (SIG) meeting arranged by UK Fluid Network (UKFN) in **Heriot-Watt University** Edinburgh, UK on 07th December 2018.

3. "Experimental study of thermal impacts of Rayleigh SAW on microdroplets" is presented in UKFN-SIG mini-symposium – Structural Surfaces and Liquid Surfaces Interactions, **Heriot-Watt University**, Edinburgh, UK on 20th April 2018.

4. A presentation titled "Preliminary observations on thermal impacts of SAW on droplet" in an International acoustofluidics forum and Olympics, **Northumbria University**, Newcastle upon Tyne, UK on 26th, 27th April 2018.

Nomenclature and Abbreviations

Al	Aluminium
AlN	Aluminium Nitride
AlScN	Scandium Aluminium Nitride
Ar	Argon
BAW	Bulk Acoustic Waves
CVD	Chemical Vapor Deposition
CYTOP	Cyclic Transparent Optical Polymer
DC	Direct Current
DNA	Deoxyribonucleic Acid
FPW	Flexural Plate Waves
F-SAW	Focussed Surface Acoustic Waves
F_d	Drag Force
F_r	Friction Force
F_b	Buoyancy Force
f_0	Fundamental Resonant Frequency
fps	Frames Per Second
Gr	Grashof Number
h	Thickness of Substrate
HYDRA	Hybrid Resonant Acoustics
IDT	Interdigital Transducer

IR	Infrared
IRT	Infrared Thermography
LDV	Laser Doppler Vibrometer
$LiNbO_3$	Lithium Niobate
LN	Lithium Niobate ($LiNbO_3$)
LOC	Lab-on-a-Chip
μ-TAS	Micro Total Analysis System
MBE	Molecular Beam Epitaxy
MEMS	Microelectromechanical Systems
MPECVD	Microwave Plasma Enhanced Chemical Vapor Deposition
M_{ev}	Mass Transfer Due to Evaporation
M_{ph}	Mass Transfer Due to Phase Change
mPa.s	Milli Pascal Second
NSB	Non-Specifically Bound
NDT	Non-Destructive Testing
OTS	Octadecyl-Trichloro-Silane
ODS	Octa-Decyle-Silane
ODT	Octadecyl thiol
Pa	Pascal
PCR	Polymerase Chain Reaction
Pe	Peclet Number

PDMS	Polydimethylsiloxane
PET	Polyethylene Terephthalate
PLD	Pulsed Laser Deposition
PVD	Physical Vapor Deposition
PZT	Lead Zirconate Titanate
RBC	Red Blood Cells
Re	Reynold Number
RF	Radio Frequency
R_0	Rayleigh
R-wave	Rayleigh wave
s	second (s)
S-wave	Sezawa wave
ST X	Cut Direction of The Substrate
SCCM	Standard Cubic Centimetre per Minute
SAW	Surface Acoustic Waves
SSAW	Standing Surface Acoustic Waves
SGAW	Surface Generated Acoustic Waves
SRBW	Surface Reflected Bulk Wave
Sh	Schmidt Number
Si	Silicon
T_d	Average Temperature of The Droplet

T_{db}	Temperature of The Droplet Bottom Layer
T_{ds}	Temperature of The Droplet Outer Layer/Surface
U_d	Velocity of The Whole Droplet (Pumping)
WBC	White Blood Cells
ZnO	Zinc Oxide
λ	Wavelength

Chapter 1: INTRODUCTION

1.1 Research background

The propagation of surface acoustic waves (*SAWs*) on the substrate was first demonstrated by Lord Rayleigh in 1885 [1]. White and Voltmer in 1965 [2] introduced fabrication of an interdigital transducer (*IDT*) on the substrate for the generation of *SAWs*. The generation of *SAW* from tens to hundreds of MHz was not possible without using the *IDT*.

Recently, the increasing research efforts have been devoted to understanding the physical, chemical, and biological impact mechanisms of *SAWs* on fluids, especially in microfluidics [3]–[5]. When an alternating current (*AC*) is applied to an *IDT* fabricated on the piezoelectric substrate, the electrical energy converts to mechanical waves because of the piezoelectric effect. These waves travel on the surface, that is why they are called *SAW* [6]. When a microdroplet of water is placed on the path where the *SAW* propagates, as the sound velocities for solid and liquid are different, *SAW* penetrates inside the droplet along the Rayleigh angle (θ). This solid-liquid interaction is defined by Snell's law [7]; $\theta = sin^{-1}(\frac{V_s}{V_f})$, where V_s is the sound velocity in solid and V_f is the sound velocity in the fluid [8]. The liquid will be driven to flow inside the droplet along this Rayleigh angle. When the liquid inside the droplet flows to the droplet boundary, the interaction at the solid-liquid bottom boundary generates reverse flow. When this flow approaches the substrate, *SAW* driven flow causes this flow to move to the top of the droplet which generates vortex pattern and leads to internal streaming inside the droplet [9]–[11].

In microfluidics, this streaming or convection inside the droplet enhances fluid mixing and the chemical/biological reactions [12]. On the other hand, the *SAW* energy transferred to both the droplet and solid is partially converted to thermal energy to heat the droplet and the solid which is referred to as thermal impact [13]–[16]. The rise in temperature leads to either positive aspects, such as being used as a heater [17] in processes such as Polymerase Chain Reaction (*PCR)* [18], or negative aspects, such as cell damage in biological devices [19], [20]. Streaming and heating effect caused by the Rayleigh waves has been well investigated and discussed in the literature. It has been realised from the literature review that little research has been conducted to address the coupling mechanism of kinetic and thermal impacts but it is not yet fully explored to understand its mass, momentum, and energy conservation principles. To control the temperature of the droplet efficiently and to select a device suitable for a temperature-sensitive process, a model needs to be designed to interpret the thermal and kinetic impacts of the *SAW* on the droplet.

Since resonant frequency changes with the rise in temperature [21], [22] therefore, this work is limited to low power/low temperature before any deformation, breakup, pumping or evaporation.

Since *SAW* nebulizers work at low power (≈ 2-3 W), degradation of bioactive agents such as proteins and *DNA* does not occur [23]–[25]. Compared to the standard ultrasonic nebulizer, large molecules such as plasmid DNA (pDNA) work as cavitation bubble [26] which destroys molecules whereas damage caused by *SAW* nebulizer is minimum [23]. Therefore, an input power of 2-3 W does not damage biological samples [20].

1.2 Research aim and objectives

The main aim of this research is to develop an analytical model to investigate mass, momentum and energy conservation principle of *SAW* energy transferred into the water droplet. The key objectives include, (1) coupling mechanism of streaming and thermal energy of the input power caused by the *SAW* on the microdroplet; (2) validation of the proposed model using both Rayleigh and Sezawa waves; (3) the effect of change in wavelength of the waves and impact of a mixture of waves on the temperature rise of the droplet.

1.3 Thesis outline

This thesis has been divided into the following chapters.

Chapter 1: Introduction: This chapter gives a background of the present work including motivation, research objectives of the work.

Chapter 2: Literature Review: This chapter starts with the introduction of the devices based on their structures and materials to generate *SAW*s followed by the type of waves, properties and their applications. The literature further includes physics of *SAW* generation, propagation, solid-liquid interaction with some engineering background and applications. The literature also explains the streaming mechanism, deformation of the droplet, jetting, atomization, nebulization etc. caused by the waves. Experimental and theoretical work done so far related to the kinetic and thermal impact of *SAW* is summarized, with more focus on thermal impact issue. Furthermore, physical principles related to the temperature rise of the droplet caused by the *SAW* are also discussed. Finally, current challenges and research/knowledge gap that need to be addressed are summarized.

Chapter 3: An Analysis Model of Kinetic and Thermal Coupling Impacts of *SAW* on The Droplet: This chapter provides an analysing model with assumptions to present conservation of mass, momentum and energy. This has been done with relevant equations and figures to provide evidence on how the proposed model works in this study.

Chapter 4: Methodology and Experimental setup: This chapter gives details about the experimental setup that includes a selection of piezoelectric material, fabrication of device and equipment required to generate *SAW*. This chapter also comprises details of different devices used in this study about how to make them efficient (hydrophobic). Furthermore, the methodology and calculations to find the coupling mechanism between streaming and thermal impact are also included in this chapter.

Chapter 5: Analysis of The Impact Mechanisms of Rayleigh *SAW* on Microdroplet: This chapter presents the implementation of the proposed model by using Rayleigh surface acoustic waves (*R-SAW*). Mass, momentum and energy conservation principles have been implemented to find the coupling mechanism and to evaluate different heat transfers and kinetic mechanisms inside the droplet.

Chapter 6: Analysis of The Impact Mechanisms of Sezawa *SAW* on Microdroplet: The mass, momentum and energy conservation principles have been implemented and validated to find the coupling mechanism using Sezawa waves. Different heat transfers and kinetic energies have been discussed in detail.

Chapter 7: Comparison of The Impacts of *SAW* Modes and Other Parameters on the Droplet: This chapter discusses the comparison of Rayleigh and Sezawa waves in terms of their kinetic and thermal impacts. Moreover, the impact of a mixture of Rayleigh and Lamb wave (hybridized wave) and a comparison of the hybridized wave with other waves have also been discussed in this chapter. Furthermore, for the same wave mode, the influence of the frequency of the device on the temperature rise of the droplet is also considered.

Chapter 8: Conclusions and future work: Overall concluding remarks and proposed future work is discussed in this chapter.

Chapter 2: Literature Review

This chapter gives a detailed overview of previous work including physics of *SAW* generation, propagation, and interaction with the droplet. This focuses on droplet-based microfluidics which includes streaming, pumping, jetting, atomization/nebulization and heating. This chapter is divided into experimental studies, theoretical analysis and modelling work that also reports different engineering applications in industry. Finally, the current challenges are discussed that needs to be addressed.

2.1 Introduction

Research into life sciences in parallel with microfluidic technology had been broadly carried out since 1973 to develop microdevices, which are at the scale of micrometres for using in different chemical analysis systems [27]**.** One of the new fields of research in micro total analysis system (μ-*TAS*), in which the whole laboratory functions can be integrated on a single chip named as Lab-on-a-chip (*LOC*) [28], [29]**.** These devices can be used for different biological, biochemical and bio-fluidics applications. For example, in the diagnosis of the human immunodeficiency virus (*HIV*), rapid purification system (to purify the protein from sample blood) [30] and handheld medical diagnostic devices are needed for detection of single molecules associated with heart diseases [31]**.**

2.2 Devices to generate SAW and applications

Before the invention of *IDT*, people used bulk substrates to generate acoustic waves but with the help of *IDT*, a few hundred MHz can be easily generated [2]. There can be different structures of *IDT*s depending upon the required application. Following are a few of them discussed here.

2.2.1 Straight IDT

IDT varies in shape and design, but the basic working principle of these devices remains the same. When the *IDT* is fabricated on a piezoelectric substrate, it is also called as a *SAW* device as shown in Figure 2.1, where a comb-like structure is called *IDT* fingers [2]. The length of each finger is called an aperture. *IDT* fingers are connected with a bus bar and electrode pads at the end where the electrical signal is given to these fingers. Furthermore, the width of one finger is λ/4, so one wavelength (λ) of the wave is equal to four times the width of one finger [2]. The wave travels perpendicularly to these fingers as shown in Figure 2.1-a.

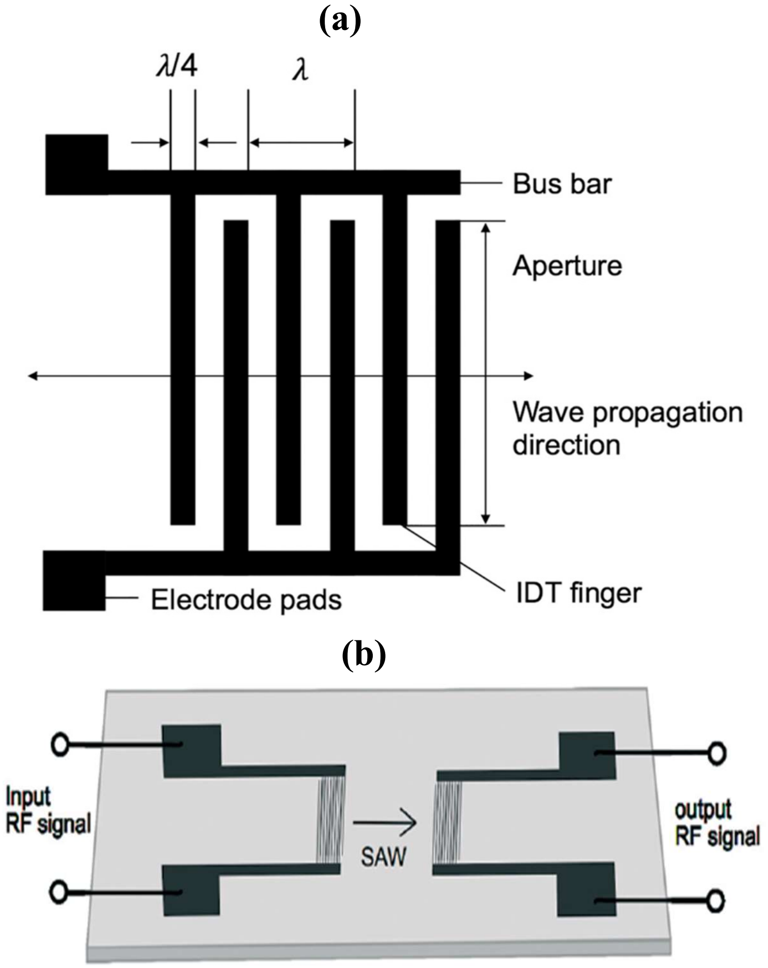

Figure 2.1: Working principle of a *SAW* device (a) Comb-like interdigital transducer showing wave propagation direction [2] (b) A pair of *IDT*s fabricated on a piezoelectric substrate, one acts as an input transducer and other as an output [32].

A pair of *IDT*s with an input and output transducers are shown in Figure 2.1-b [32]. When an electrical signal is applied to the input transducer, these signals are converted to the mechanical waves due to the inverse piezoelectric effect [33], where 90% of the signal is transmitted in the mechanical form and 10% is transmitted in the electrical form to the output transducer [12]. The resulting travelling waves can be observed using laser doppler vibrometer (*LDV*). The periodicity of the finger pairs defines the wavelength of the resulting *SAW* [12]. With the help of *LDV*, acoustic waves can be visualised to travel on their path. The amplitude of the wave can be visualised against frequency on *LDV*, the frequency at which the signal has maximum amplitude is the resonant frequency of the device. Furthermore, Love, *BAW*, *SAW* waves have different shapes which can also be visualised on the screen of *LDV*, therefore, type of the wave can be identified.[12].

2.2.2 Focussed IDT

The device in which *IDT*s from both sides are focussed at one point is called focussed *IDT* (*FIDT*) and *SAW* generated by these *IDT*s are called focussed *SAW* (*F-SAW*). These devices are used when specifically required jetting or deformation of the droplet is required [34]. A *FIDT* with a droplet is presented in Figure 2.2.

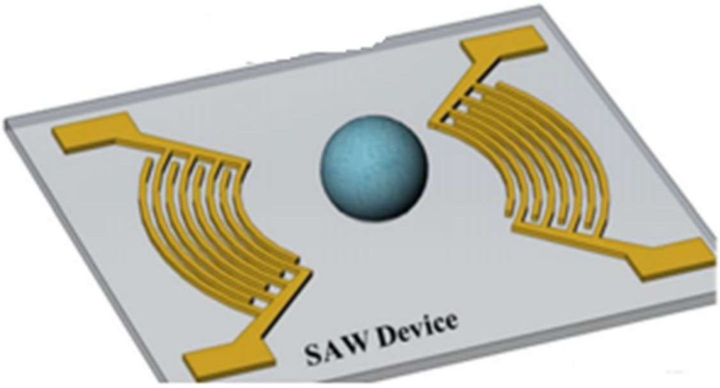

Figure 2.2: A focused *IDT* with a droplet [34].

2.2.3 Slanted or tapered IDT

Slanted *IDT*s are also called as tapered *IDT*s in which the electrodes are tapered from one side to other as given in Figure 2.3 [35]. In this type of design, the direction of movement of particles or droplets can be changed by changing the operating frequency continuously. One can change the position of pairs of *IDT*, patterns of electrodes, and the alignment direction of microchannels [36].

Figure 2.3: Basic structure of slanted *IDT* [35].

2.2.4 Circular IDT

This is also a type of *FIDT*s in which the *IDT* is in a circle shape and droplet can be placed in the centre as given in Figure 2.4. As the design predicts, more acoustic pressure and energy generated by circular *IDT*s cause improved pumping and mixing inside the droplet and other sensing applications. Highest droplet velocity and concentration effects are observed using the circular *IDT*s [37].

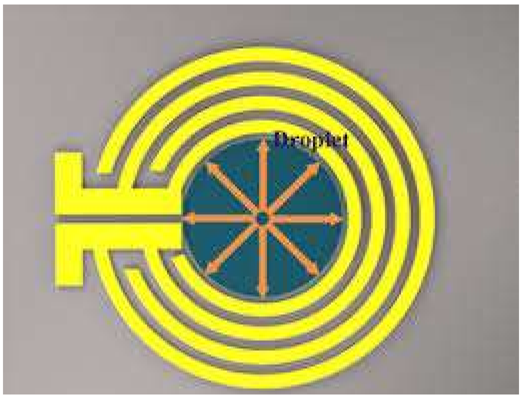

Figure 2.4: Basic structure of circular *IDT* design [38].

2.2.5 Bending IDT

Straight *IDT* with the thin piezoelectric film on a flexible substrate material can be used as deformable or bendable *IDT*s. These devices can be used in several medical sensing applications, wearable diagnostics, drug delivery and surgical treatments [39]–[44]. Flexible/bendable devices can be fabricated with *ZnO* film as a top layer and flexible substrate as presented in Figure 2.5. *ZnO* of 2 µm is deposited on Polyethylene Terephthalate (*PET*) foil with thickness 120 µm as shown in Figure 2.5-a whereas *ZnO* of 5 µm is deposited on *Al* foil (50 µm) for bendable *IDT* as shown in Figure 2.5-b [39], [45].

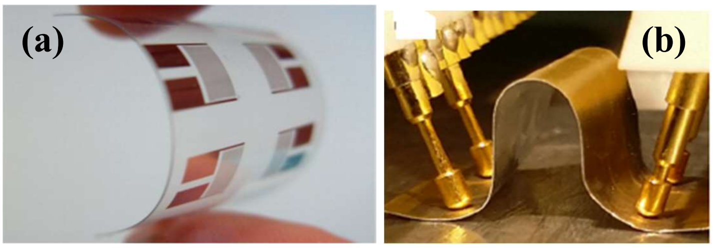

Figure 2.5: Flexible/bendable devices (a) *ZnO*/PET SAW device in bending (2 µm thick *ZnO* film deposited onto 120 micron PET foil) [39] (b) *ZnO* of 5 µm thickness on Al foil of thickness 50 µm in a bendable position [45].

Table 2.1: Summary of common device structure and their applications [2], [12], [42]–[45], [32], [34]–[37], [39]–[41][46][47].

Device structure	**Applications**
Circular *IDT*	Pumping of the droplet, mixing inside, sensing applications.
Slanted *IDT*	Detection of the position of particles.
Focused *IDT*	Jetting, deformation of the droplet
Bendable *IDT* s	Medical sensing, wearable diagnostics, surgical instruments
Straight *IDT*	General usage, different sensings like chemical sensing, biosensing, humidity sensing, *MEMS*, Nondestructive testing (*NDT*) and other microfluidics applications.

2.2.6 Other applications of SAW

Since 1950, *SAW*s with frequencies range from 10 MHz to several GHz have been widely used in the telecommunication industry for signal processing and filtering [48]. Different *SAW* filters have also been used in mobile phones [2]. Different types of *SAW* devices have also been used in a variety of sensing applications such as gas sensors, biochemical sensors, liquid and density sensors [49]. *SAW* can also be used for sorting of cells or particles in microchannels [50]. It has been widely used for particle/cell manipulation with very small liquid volumes [51], [52]. Moreover, *SAW* has tremendous applications in wearable diagnostics in sensing and actuating applications with less cost of the material and improved functionality [36]. Each application depends on the type of wave mode used and fabrication of the device which is discussed in the following sections.

2.2.7 Types of piezoelectric material, parameters

The most common piezoelectric materials that can generate *SAW* include quartz, lithium niobate (*LN*, $LiNbO_3$), lithium tantalate (*LT*, $LiTaO_3$) [12]. Others include gallium arsenide (*GaAs*), cadmium sulfide (*CdS*), lithium tetraborate ($Li_2B_4O_7$) and langasite ($La_3Ga_5SiO_{12}$) [53]. Moreover, thin-film materials include zinc oxide (*ZnO*), Aluminium Nitride (*AlN*) and Lead Zirconate Titanate (*PZT*) [36].

LN and *LT* have a substantially greater electromechanical coupling coefficient than quartz [54]. Because of the remarkably high coupling coefficient as compared to other crystalline materials, *LN* has become famous for SAW-based applications. As *LN* is anisotropic, therefore, its properties can be improved by changing the cut direction of their crystal [12]. Y-cut, Z-propagating orientation of *LN* (YZ LN) has been used widely in the past as SAW filters with Rayleigh waves but the problem was observed later on in the propagation alignment with their principal axis [55]. In 1970, this problem was resolved using 131° Y-rotated cut of *LN* that has a high electromechanical coupling coefficient and becomes widespread [56], [57]. This cut-direction has some spurious parasitic waves, therefore 127.86° Y-rotated cut introduced in 1976 that overcome parasitic waves problem and have the highest coupling co-efficient and less insertion loss [58]. Some other cuts have more electromechanical coupling coefficient but they have some challenges which impede them to produce "true" *SAW* that is why 128° Y-cut X propagating *LN* becomes more popular and widely recognized for the Rayleigh based applications [12].

2.2.8 Parameters to find out the behaviour of the devices

Piezoelectric substrates vary in their characteristics which depend on a few parameters. It is quite important to select a suitable substrate desired for a study with the specific requirements. The key parameters that help to select suitable substrate/device are discussed as follows.

2.2.8.1 Temperature coefficient of frequency (TCF)

The thermal stability of the resonator is defined by *TCF*. It can also be defined as a graduate change of resonant frequency by the change in temperature. $TCF = \frac{1}{f0} \times \frac{df}{dT}$ where f_0 is the resonant frequency, $\frac{df}{dT}$ is the change in frequency with the temperature [36].

High *TCF* means that part of the acoustic energy is wasted out in thermal energy. High *TCF* is desired for the development of high-temperature sensors but not suitable for microfluidic applications. *TCF* less means the resonant frequency does not change much by the rise in temperature [36].

2.2.8.2 Electro-mechanical coupling coefficient

It is a numerical measure of conversion efficiency between electrical and acoustic energy in piezoelectric materials and is given by equation (2.1) [36];

$$k^2 = \frac{e_{31}^2}{C_{11}\varepsilon_{33}} \tag{2.1}$$

where e_{31}^2 is the electric field, ε_{33} is the permittivity at a constant strain and C_{11} is the elastic constant of the material [36].

2.3 Type of waves, properties and applications

Different types of bulk acoustic waves (*BAW*)s and *SAW*s are shown in Figure 2.6 [59]–[61]. The classification of the surface generated acoustic wave (*SGAW*) includes Lamb waves and *SAW*s. *SAW*s have further four modes depending upon the type of substrate used and resonant frequency named as Rayleigh-*SAW* (*R-SAW*), Sezawa, Shear-horizontal *SAW* (*SH-SAW*) and Love wave [62]. Other types of *SGAW* are pseudo-*SAW* (*PSAW*) and leaky *SAW*s (*LSAW*) [62].

Rayleigh *SAW*s can be generated on specifically oriented bulk piezoelectric substrates such as *ST* cut and *Y*-cut quartz, 128° Y-X-cut $LiNbO_3$ and X-112° *Y*-cut $LiTaO_3$

substrates, as well as vertically aligned or (0002) oriented films (often called c-plane or z-plane orientated) of *ZnO*, *AlN*, *PZT* or $LiNbO_3$. *SH-SAW*s can be generated with a few to hundreds of MHz, have low power consumption, low cost and wireless control. These waves show better performance in sensitivity/detection especially in liquids and humid conditions as compared to the Rayleigh [63], [64]. The devices and materials that can be used to generate these waves include Quartz, 36° *YX*-cut $LiNbO_3$ and 64° *YX*-cut $LiNbO_3$ [36].

Love mode *SAW* can be generated with the same device as for *SH-SAW* whose surface is covered with a thin-wave guide layer (such as SiO_2, *ZnO* and polymers). The acoustic waves are mostly enclosed in this wave-guide layer which leads to a high sensitivity [65]. Therefore, these waves are suitable for accurate biosensing in the liquid environment [66]–[68]. Because of their high sensitivity, both *SH-SAW* and Love waves are inefficient for microfluidic applications [69], [70]. Love mode wave has the highest sensitivity among *SAW*-based sensors and can be generated with a few to hundreds of MHz. The material and devices used for these waves include 36° *YX*-cut $LiTaO_3$, Quartz, 64° *YX*-cut $LiNbO_3$ [36].

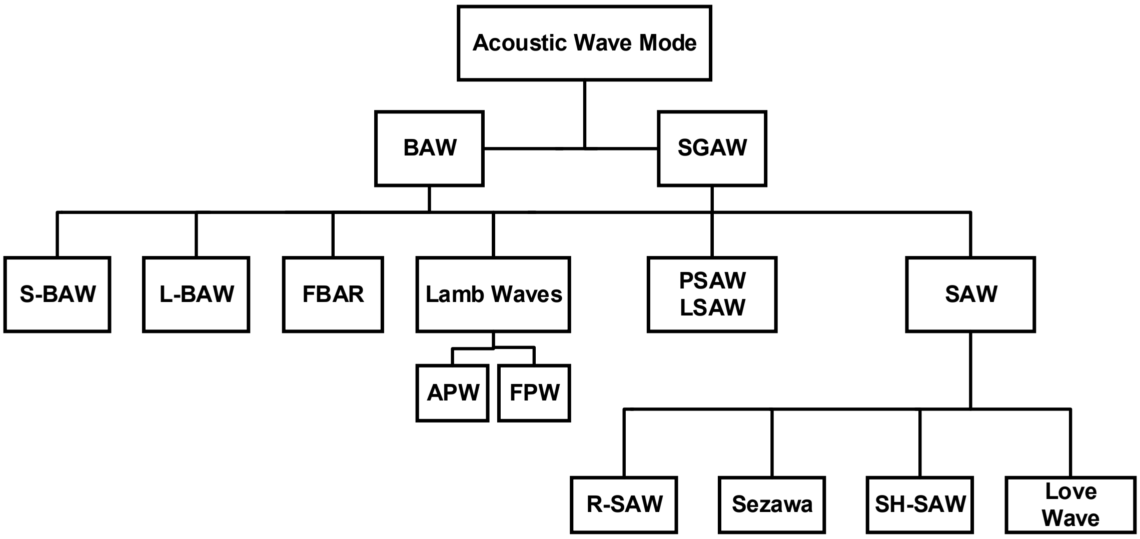

Figure 2.6: Classification of acoustic wave modes: bulk acoustic wave (*BAW*) and surface generated acoustic wave (*SGAW*) [36].

*BAW*s include shear *BAW* (*S-BAW*), longitudinal *BAW* (*L-BAW*), film bulk acoustic wave resonator (*FBAR*) and Lamb waves. Lamb waves have further two modes: acoustic plate wave (*APW*) and flexural plate wave (*FPW*) [62]. Every mode of the wave has its advantages and disadvantages. A few of these important waves with their relevant applications are discussed in the following paragraph.

The most widely used material for the *BAW* is quartz crystal microbalance (*QCM*). Other types of *BAW* resonator include *FBAR* whose operating frequency ranges from a few GHz to tens of GHz. *FBAR* has high sensitivity, small size and low power consumption [71]. However, they have high fabrication cost, large noise/signal ratio, and not good for microfluidic applications [36]. *SBAW*s are also called 'surface skimming bulk waves' (*SSBW*s) and shear horizontal *BAW*s travels beneath the surface [36].

2.3.1 Rayleigh waves (R-waves)

Rayleigh waves travel along the surface of a piezoelectric substrate where its acoustic energy decays exponentially with depth into the material until it becomes negligible after penetration by more than a few wavelengths [72]. The Rayleigh wave has both longitudinal and vertical shear (transverse) components that travel on the surface of the substrate. The pattern that these waves travel on the surface is shown in Figure 2.7 [73].

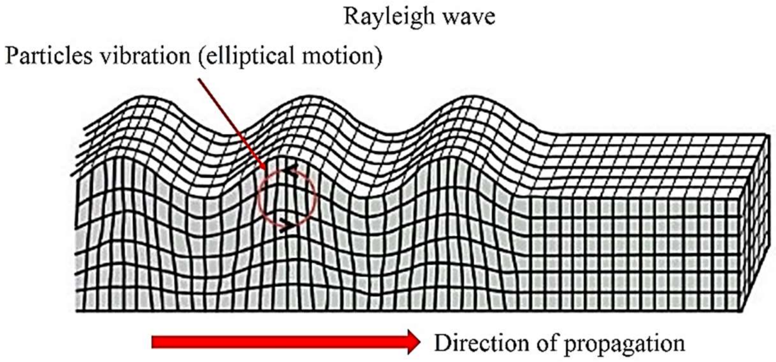

Figure 2.7: Propagation of Rayleigh surface acoustic waves [73].

The key materials that can generate Rayleigh include lithium niobate (*$LiNbO_3$*), ST-cut quartz, *ZnO*, aluminium nitride (*AlN*) and lead zirconate titanate (*PZT*) thin-film devices [36].

2.3.2 Sezawa waves (S-waves)

Sezawa waves are the waves propagating along with the film/substrate interface when the acoustic wave velocities of the thin film are much smaller than those of the substrate [74]. This mode can be generated along with the Rayleigh waves by depositing a film onto the same substrate. Rayleigh and Sezawa can be obtained at different resonant frequencies by the change in the piezoelectric film thickness [75]. No wave mode is observed when the thickness of the piezoelectric layer is less than 1 µm (due to the wavelength is 64 microns), and the Rayleigh wave is observed at the film thickness of 1.5 µm as given in Figure 2.8. However, the Sezawa wave appeared at the layer thickness of 4 µm [36]. Depending on the film thickness, the Sezawa wave has a stronger transmission peak as compared to that of the Rayleigh wave, which is why it has much higher acoustic velocity and larger signal amplitude than Rayleigh wave [75].

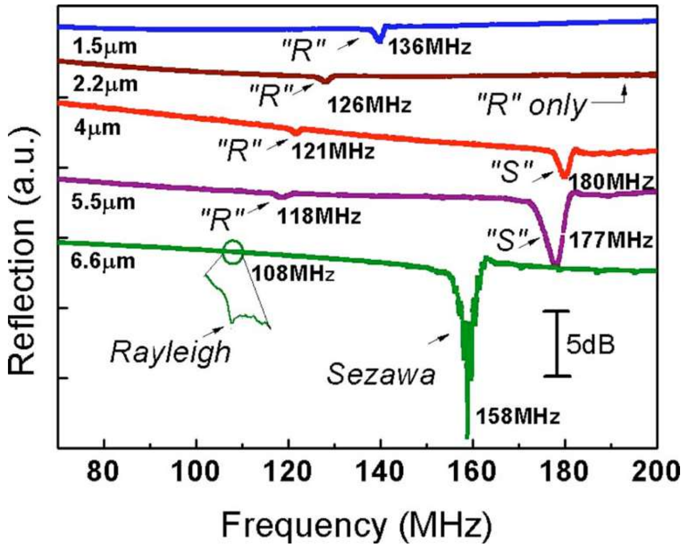

Figure 2.8: Effect of film thickness (in the range 1.5 µm to 6.6 µm) on the resonant frequency of Rayleigh and Sezawa waves. Reflection signal of the device is shown versus resonant frequency [75].

2.3.3 *Lamb waves*

Lamb waves can be generated by aluminium nitride (*AlN*), *ZnO* or lead zirconate (*PZT*) that are available in thin-film forms [36]. They can be sputtered on other substrates to make a different type of devices. If the substrate is flexible, these devices are called as flexible devices. The reason why these are called flexible is that a very thin substrate (50 µm in case of *Al* foil) can be easily bent. Normally, the Lamb waves are generated when the substrate thickness is smaller than the wavelength of the wave [36]. There are two types of Lamb waves; firstly, passive Lamb waves, which can be generated by a remote source, and secondly, positive Lamb waves, which are generated by the piezoelectric material. Resonant frequency varies from kHz to MHz and in case of thin-film based higher Lamb waves, it can go up to 1 GHz [76]. Based on thin plates or membranes, it has two propagation modes i.e. zero-order anti-symmetric mode (A_0) and zero-order symmetrical Lamb wave mode (S_0) [36], [77]. A_0 mode of the Lamb wave is also called flexural plate waves (*FPW*) [78], [79]. The *FPW* has been extensively used in mixing and pumping applications [80]. However, the wave energy caused by S_0 mode into the liquid is generally small, therefore, this mode is often used for sensing applications in the liquid [36], [81]. Moreover, a better microfluidic performance was observed when these devices are made on Al foils as compared to the polymers [36].

The performance of the Lamb wave depends on the type of material and its thickness [82]. Lamb wave using *FPWs* generated by $Si/SiO_2/Si_3N_4/Cr/Au/ZnO$ device has been used to detect the concentration of immunoglobulin E (IgE) in the human blood [83].

2.3.4 Effect of substrate thickness and wavelength on the wave mode

For piezoelectric thin film devices, acoustic velocity, electromechanical coupling coefficient, and other quality factors change significantly with the change in substrate thickness and wavelength of acoustic waves [45], [75], [84]. The generation of waves depends on the ratio of acoustic wavelength (λ) and substrate thickness (h).

If the thickness of *Al* foil and *ZnO* are fixed, an increase or decrease in wavelength (λ) of the wave will change the mode of the wave [45]. Figure 2.9 shows frequency responses for *Al* foil with two different wavelengths with the same thickness of the device. As we change λ, the resonant frequencies of A_0 and S_0 mode of the Lamb wave are shifted accordingly [45].

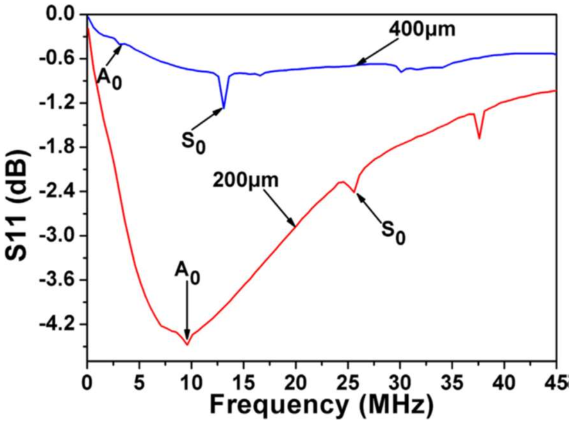

Figure 2.9: Frequency response (S_{11}) spectra of the *ZnO*/*Al* foil *SAW* devices with different wavelengths (200 & 400 µm) [45].

2.3.5 Standing surface acoustic waves (SSAW)

Standing surface acoustic waves are generated when a pair of *IDT*s are used with the same electrical signal is provided from both sides. Excited waves from both sides generate standing surface acoustic waves which help in cell sorting and focusing on different applications [85]. *SSAW* is good for focusing, jetting, particle manipulation, patterning and separation of particles [36], [86].

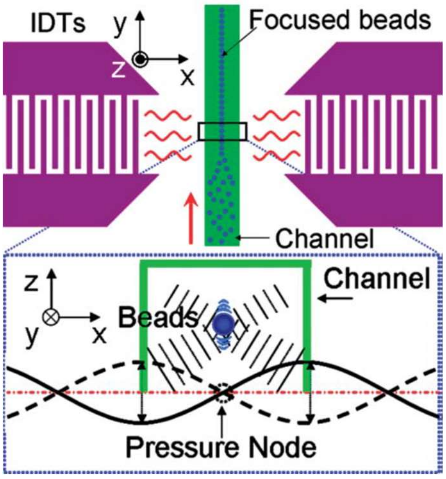

Figure 2.10: Schematic of *SSAW* device, showing a working mechanism [85].

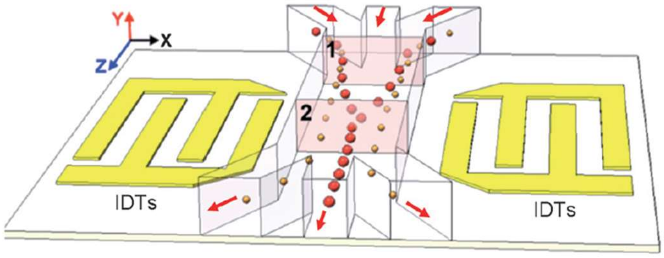

Figure 2.11: Schematic of the separation mechanism showing particles beginning to translate from the sidewall to the centre of the channel due to axial acoustic forces applied to the particles when they enter the working region of the *SSAW* [87].

When waves travel from both sides and meet each other, they form pressure nodes and anti-nodes as shown in Figure 2.10. When these waves enter inside the channel, leaky waves are generated which creates pressure instabilities inside the medium [88]. These variations in pressure generate an acoustic radiation force that acts in x-direction on the particles [89]–[91] as shown in Figure 2.10 [85].

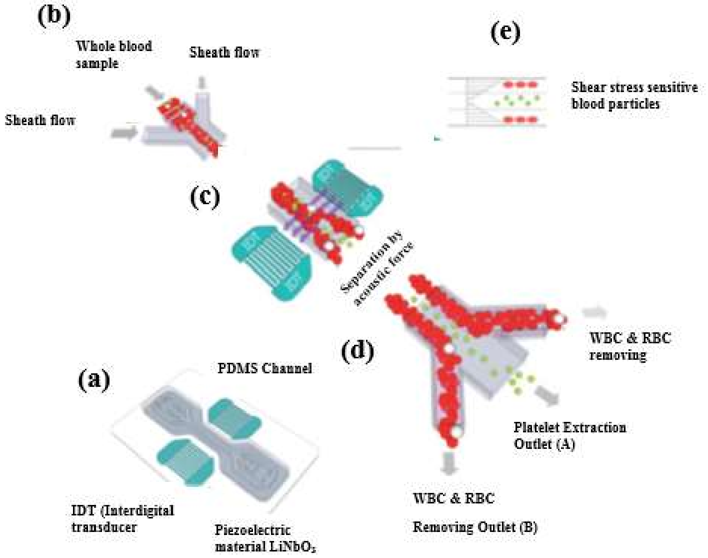

Figure 2.12: Platelet separation from the whole blood using the acoustic device (a) Polydimethylsiloxane (*PDMS*) channel with *IDT* pairs using *LN* as substrate (b) the whole blood sample is injected and focused hydrodynamically by two layers of sheath flow (c) Blood particles in the working region of SSAWs are separated in a size-gradient manner (d) platelets are mainly sorted and collected in the centre outlet (e) Platelets in the middle of the channel [92].

The particles inside the channel will be forced towards a pressure node or an anti-node depending upon concentration and compressibility of the particles and the medium. Acoustic force is proportional to the volume (r^3) of the particles. If the particles have a different size/volume, larger particles experience a much larger force, therefore move towards the pressure node quicker than the smaller ones as shown in Figure 2.11 [87]. Figure 2.12 shows an example of the size-based separation of platelets from whole blood using the *SSAW* [92].

2.4 Different mechanisms and applications related to R-SAW and Sezawa

Both *R-SAW* and Sezawa have been used in sensing and microfluidic applications. Since this study is based on microfluidics, thus the focus of the review will mainly include but not limited to the streaming, deformation, jetting, atomization, nebulization, and heating of the droplet.

2.4.1 Microfluidics by R-SAWs

2.4.1.1 Deformation and pumping

Streaming and mixing can be observed at low radio frequency (*RF)* powers, however, at higher powers, the droplet may be deformed or moved from one place to another [93].

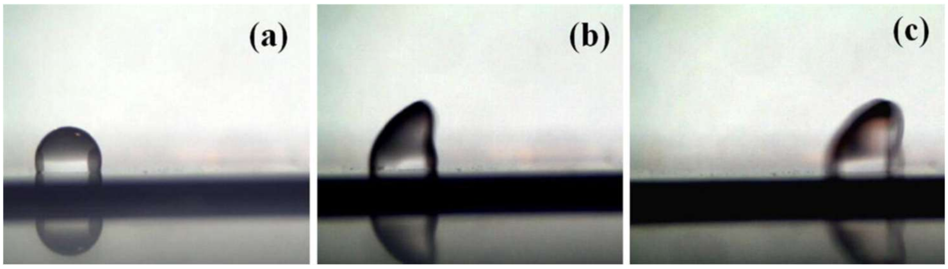

Figure 2.13: Pumping of a 2 µl droplet at an input power of 4.0W (a) 0.0s; (b) 0.08 s; and (c) 0.16 s after applying *SAW* [93].

The pumping of 2 µl droplet with *R-SAW* at P_{in} of 4.0 W by using *ZnO* on a diamond substrate at 65.4 MHz is shown in Figure 2.13. Diamond has higher mechanical strength and the highest sound speed of all the materials [93]. The streaming pattern was visualized at *SAW* powers of 50 to 100 mW without deformation. However, the droplet moves within 0.20 s of an input *SAW* power of 4.0 W as shown in Figure 2.13 [93].

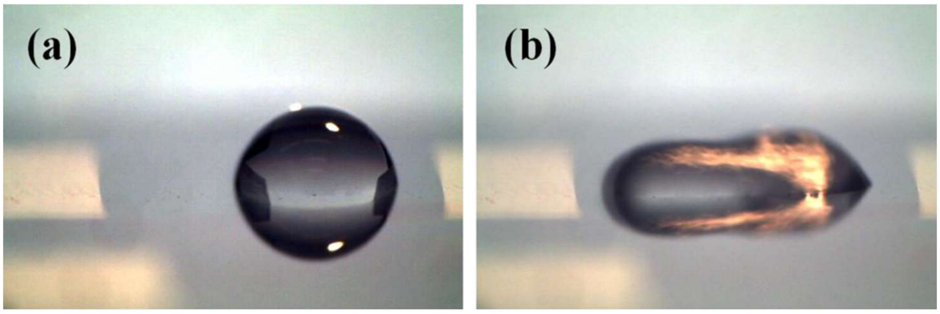

Figure 2.14: Liquid droplet on *ZnO*/diamond surface driven by *SAW*. Waves propagate from right to left) (a) Original 10 µl droplet (b) Droplet deformation on *SAW* power of 21.0 W [93].

A 10 µl droplet is placed on the *ZnO*/diamond surface with applied *SAW* power of 21.0 W as shown in Figure 2.14. The large *SAW* pressure agitates the droplet and causes internal streaming inside the droplet that can be observed from the figure. After a certain time, internal steaming is high enough that pushes the droplet on the opposite side of *SAW* propagation. Because of the hydrophilic surface, the droplet cannot be pumped away [93].

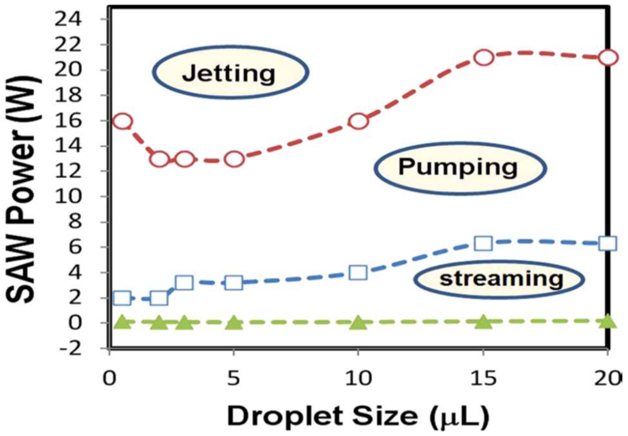

Figure 2.15: Summary of different phenomena (streaming, pumping and jetting) inside the liquid droplet at different power levels and variable droplet sizes [93].

Furthermore, it is interesting to understand several other phenomena that occur at different input power and droplet sizes. Figure 2.15 shows that at low power and the small droplet, no microfluidic phenomenon observed. If the droplet size is fixed, then at *SAW* power values from 2.0 to 6.0 W, excellent streaming is visualised but with the increase in P_{in}, a pumping phenomenon can be observed between 10-12 W. With a smaller droplet size of 0.5 µl, it is difficult to achieve jetting because of smaller size, less area to generate sufficient energy to the droplet. Similarly, with the droplet size higher than 10 µl, even at very high power, it's difficult to eject droplet probably because of higher mass and less acoustic energy per width [93].

2.4.1.2. Atomization of droplet using R-SAW

As the leaky wave propagates inside the liquid, capillary waves are generated at the liquid-air interface. If *SAW* power is high enough, the acoustic pressure dominates the capillary stress and destabilizes the interface which induces atomization [94].

Inkjet technology using ultrasonic waves has been used in the past to spread small quantities over a smaller region [95] and *SAW* can be a good tool for this application. Based on *SAW* streaming effects, liquid actuators and manipulators were developed. *SAW* streaming was also used for droplet positioning and localization system in the past. The angle and height of mist can be controlled by *SAW* input voltage and the direction of atomization can be controlled by the *DC* electrostatic field [96]. Moreover, change in the state of liquid (from the jet stream to atomization) depends on the amount of liquid present on the *SAW* device [96]. Furthermore, when the *SAW* power increases to 1.0 W, the acceleration of particles increases to 10^8 m/s^2 which causes it to destabilize and break up to form 1 μm small droplets [96].

SAW atomization has revolutionized the pulmonary drug delivery system intending to deliver drugs with droplet diameters 1-5 μm range to deep lung region. Compared to ordinary inhalers that require training to make coordination between breadth and hand, the *SAW*-based drug delivery system is user-friendly [97]. Moreover, ordinary inhalers have a poor agreement between infants and children but the dose in *SAW*-based devices can be adjusted with age, gender, size, and severity of diseases. *SAW*-based pulmonary delivery of asthmatic steroids has 10-30 % higher efficiency than commercially available inhalers and nebulizers [97].

The sequenced images of the nebulization of a droplet at different time after applying Rayleigh *SAW* are shown in Figure 2.16. The resonant frequency of 11.8 MHz was used with an *RF* power of 7.2W using a droplet of size 0.5 μl. When the leaky *SAW* propagates into the droplet, acoustic wave pressure drives the liquid droplet and results in significant capillary waves on the droplet surface as presented in Figure 2.16-b. However, the capillary wave quickly becomes unstable (in less than 0.002s) and few satellite droplets are ejected from the surface, followed by significant mist generation in the vicinity of the top of the droplet. Along with the formation and rising of the mist, many satellite droplets with estimated diameters of 25-35 microns are also generated from the peripheral droplet as shown in Figure 2.16. *ZnO* thin film *SAW* devices showed better thermal dissipation and less cracking susceptibility during fabrication and operation. Fine nebulization mist was observed at high frequency and high power. Moreover, efficient pumping and jetting of the droplet can be observed at higher power and frequency with *ZnO* thin film as shown in Figure 2.17 [98]. It is clear from in Figure 2.17 that an input *SAW* power has negligible impact on the nebulization speed for the low frequency of 11.8 MHz. However, at higher frequencies (23.10 MHz and 37.20 MHz), it increases with the increase in input power [98]. It is also clear from Figure 2.17 that lower SAW frequency has higher nebulization speed as compared to the higher frequency *SAW*. This is because lower *SAW* frequency has increased wavelength, higher vibration amplitude causes capillary waves to generate quickly and eject the droplet faster than higher frequency *SAW*s [99].

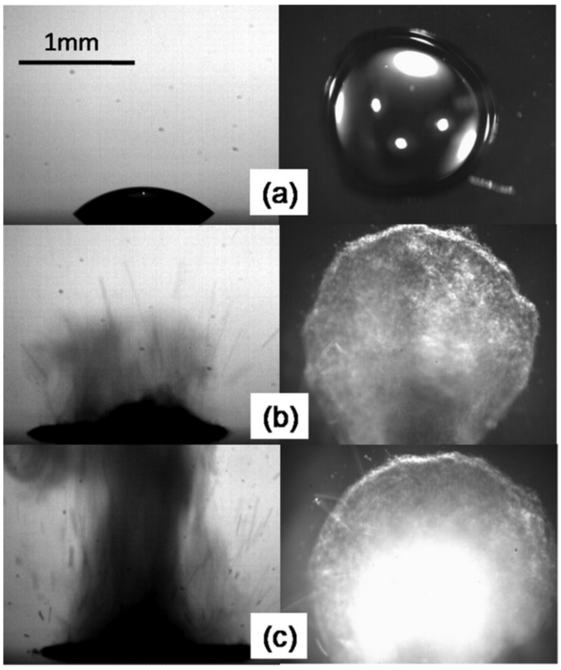

Figure 2.16: Side (left) and top (right) views of the nebulization behaviour of a 0.5 µl water droplet with a *SAW* frequency of 11.8 MHz at a power of 7.2W. (a) Original droplet (b) mist generation and satellite droplets at 0.003s; (c) significant nebulization at 0.0006 s [98].

Nebulization time can be decreased by increasing *RF* input power and decreasing droplet volume [100]. If the resonant frequency is fixed, then by changing the droplet size, nebulization time can be changed. It is understandable from Figure 2.18 that at low input power, the smaller droplets have less nebulization time. Furthermore, at higher power values (65-70 W), all droplets have almost the same nebulization time [98].

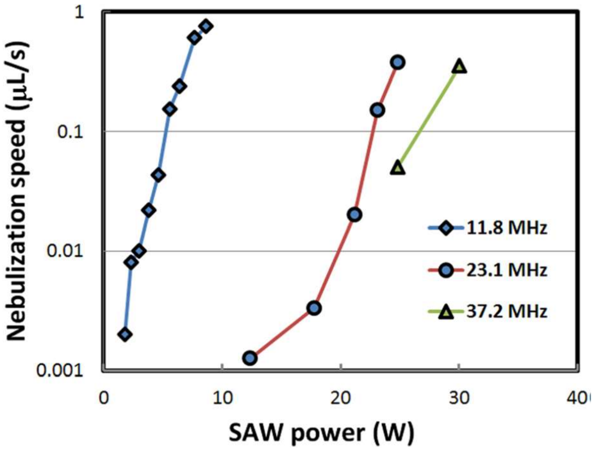

Figure 2.17: Nebulization speed (µL/s) as a function of frequency (11.8 MHz, 23.1 MHz, and 37.20 MHz) and *SAW* power [98].

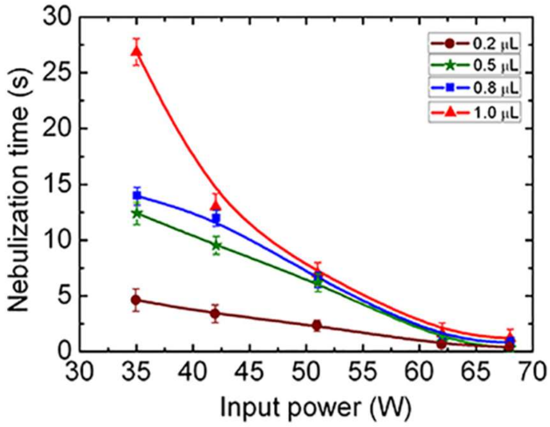

Figure 2.18: Effect of input power and droplet size on nebulization time with a fixed resonant frequency of 23.3 MHz [100].

Nebulizers play an important role in drug delivery as compared to the ordinary inhalers that can waste expensive medicines and the drug cannot reach the targeted point. Mist diameter of 1.1 µm was generated with the device having a frequency of 29.78 MHz and an input power of 2-3 W which should not damage biomolecules [25]. This method is very efficient for delivering antibodies with both local delivery and systematic delivery system especially diseases related to lung cancer. Furthermore, it can be used for the diagnosis of different respiratory-related diseases with a low cost and a portable setup [20].

As compared to conventional nebulizers, *SAW*-based nebulizers are low-cost, the small system can be powered by ordinary batteries [101], [102]. Moreover, degradation does not occur using *SAW* for nebulization of bioactive agents such as proteins and *DNA* [23]–[25]. *SAW* nebulizer can run at lower power of ≈2-3 W as compared to a conventional nebulizer which requires the power of 10 W [103].

2.4.1.3. Jetting using F-SAW device

Figure 2.2 shows *FIDT* for droplet jetting fabricated on 128° rotated *YX*-cut piezoelectric *LiNbO*$_3$. At high *RF* input power values, acoustic heating also occurs that increases the temperature of the droplet (T_d) [13], [34], [104].

Droplet jetting is also possible through single *IDT*. The principle of droplet jetting a single *SAW* device is shown in Figure 2.19. Rayleigh angle (the angle at which *SAW* enters inside the droplet) is seen from Figure 2.19-a while Figure 2.19-b shows how the jetting generates after a few milliseconds of input *SAW*. Acoustic radiation enters inside the droplet at the Rayleigh angle and is converted into a body force. When this body force overcomes the surface tension of the droplet, then the jetting will occur [105].

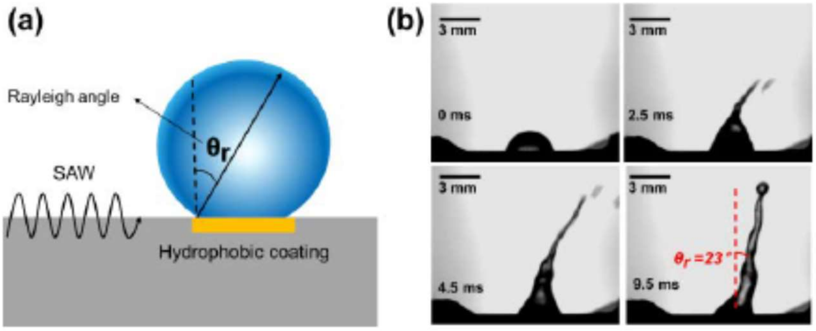

Figure 2.19: The principle of interfacial droplet jetting using *F-SAW* device (b) photographs of interfacial droplet jetting angle under a single *IDT* experimental case after 0 ms, 2.5 ms, 4.5 ms, and 9.5 ms [105].

2.4.2 Sezawa waves for microfluidics and sensitivity

As discussed above, Sezawa waves (S-waves) is the higher-order mode that can be generated and propagate along with the film/substrate interface when the piezoelectric film thickness is larger than 4.0 µm. The resonant frequency of Sezawa decreases with the increase in film thickness [75]. S-waves has potential applications both in microfluidics and sensing. A few of them are presented below.

2.4.2.1 *Sezawa waves for sensing*

The *SAW* devices with *AlN*/SiO_2/*Si* structure using Sezawa waves have been used for the sensing of volatile organic compounds (VOC). It was observed that the sensitivity of the Sezawa for these gases was double than Rayleigh wave mode [106]. Moreover, Sezawa wave with *SAW* device *ZnO*/Si_3N_4/*Si* have also been used to detect human immunoglobulin-E (lg-E) in the last decade [107]. Sezawa has higher electromechanical coupling co-efficient and higher phase velocity [108]. The temperature sensitivity and *TCF* of Sezawa are 1.6 and 1.8 times more than Rayleigh waves respectively [109].

2.4.2.2 *Sezawa wave for microfluidics*

A device with a *ZnO* thin film of 6.6 μm thickness deposited on a silicon substrate has been used to generate Sezawa waves. The investigation of pumping of a droplet at a resonant frequency of 178.7 MHz is shown in Figure 2.20 [93]. The droplet moved 4 mm after two seconds of applying *SAW*. It was also observed that smaller droplets have a higher velocity because of reduced adhesion [110]. The acoustic force of 100 μN was produced that pumped a liquid droplet of 10 μl with a pumping speed of 1 cm/s with a surface contact angle greater than 100°. This structure is very useful for different *LOC* applications [110].

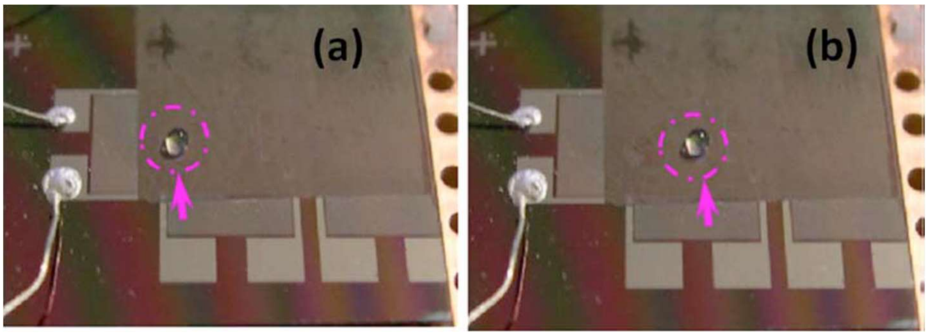

Figure 2.20: 1 μl droplet on ZnO SAW device before (a) and after (b) driven by *RF* signal with frequency 178.7 MHz [110].

2.4.3 *Hybrid modes: a mixture of Rayleigh and Lamb waves*

If h/λ >1, *R-SAW* will be generated, and if h/λ <1 then Lamb waves will be generated. In other words, when λ is significantly smaller than h, then the Rayleigh wave will produce and when λ is much larger than h then lamb wave will generate [45]. However when h/λ≈1, then surface reflected bulk wave (*SRBW*) will generate also called hybrid resonant acoustics (*HYDRA*) device, where h is the substrate thickness and λ is the wavelength of the wave [111]. Hybrid wave is the mixture of both Rayleigh and Lamb waves. It has been reported that the vibrational velocity for these hybrid waves is one time more than pure Rayleigh waves and two to three times more than pure Lamb wave which means these waves have more acoustic efficiency than pure waves [111].

Results of nebulization with pure *SAW* waves and with *HYDRA* device were experimentally compared by using a 128° *YX* double-sided polished *LN* substrate [111]. It is possible to achieve fast nebulization of up to 8 mL/min with the *HYDRA* device which is not possible with either pure Rayleigh or Lamb waves. This can help for new pulmonary drug delivery devices [111].

2.4.3.1 Nebulization using hybrid surface acoustic devices

Sensing and actuation both have opposite operating requirements. Devices that we need for sensing have a lower electromechanical coupling coefficient that is not ideal for actuation. It is important to know how we can perform both operations on the same device. Generally, Lamb waves are good for sensing than *R-SAWs*, however, *SAWs* are good for actuation [112].

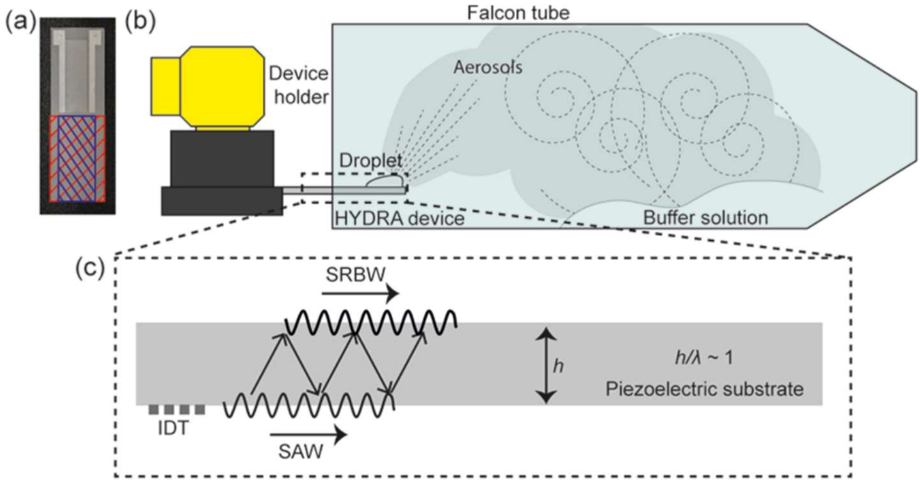

Figure 2.21: (a) *HYDRA* device with bulk mode sensing area, hatched in red and *SAW* mode runway hatched in blue, (b) Schematic depiction of the experimental setup used for concurrent

nebulization of insulin and detection of its residual mass on the device (c) Schematic illustration of the underlying mechanism governing the *HYDRA* device. [112].

HYDRA device is shown in Figure 2.21 in which the substrate thickness '*h*' matches the acoustic wavelength of the waves. These waves are transmitted through the thickness of the substrate and reveal on the opposite facet of the device as surface-reflected bulk wave (*SRBW*). This device can be used as feedback to inform the doctor and the data can be transmitted wirelessly for several applications [112].

Table 2.2: Different waves and their applications [36], [66], [86], [92]–[95], [107], [108], [110]–[112], [67]–[71], [80], [81], [85]

Type of waves	**Applications**	**Problems/Limitations**
SSAW	Particles separation, manipulation and patterning.	Only limited in microchamber or microchannel.
BAW-FBAR	High sensitivity, small size, low power consumption.	High fabrication cost, large noise/signal ratio, not good for microfluidic applications.
Lamb waves	S_0 mode good for sensing, A_0 mode good for mixing and pumping applications.	S_0 mode not good for microfluidic applications whereas A_0 mode is also not efficient as Rayleigh mode in microfluidics.
Love waves	Accurate biosensing in a liquid environment.	Not good for microfluidic applications.
Rayleigh	Streaming, deformation, Jetting, and nebulization.	Not useful for liquid sensing.

Sezawa	Gas sensing double than Rayleigh. Liquid pumping.	Only occur in thin-film (with its velocity lower than substrate).
Hybridized waves	High vibrational velocity leads to higher nebulization rate.	Vibration modes are varied with structures.

2.5 Kinetic and thermal impacts caused by the SAW

Streaming inside the droplet can be visualised by adding particles inside the droplet. Furthermore, since waves carry the energy that transfers inside the droplet that increases the temperature and in some cases, the droplet may evaporate. The following sections discuss the streaming and heating of the droplet because of the surface acoustic waves.

2.5.1 Internal streaming inside the droplet

SAW is responsible for the build-up of acoustic radiation pressure inside liquids along with the propagation of sound in the fluid [12]. Radiation pressure can be calculated by using equation (2.2) given below [12];

$$P = \rho_o V_s^2 \left(\frac{\Delta\rho}{\rho_o}\right)^2 \tag{2.2}$$

where P is the radiation pressure, ρ is the density of the fluid, V_s is the speed of sound in solid and $\Delta\rho$ is the change in densities. Figure 2.22 shows the interaction of SAW with a droplet on the $LiNbO_3$ piezoelectric substrate where the Rayleigh angle and the streaming can be visualised [113].

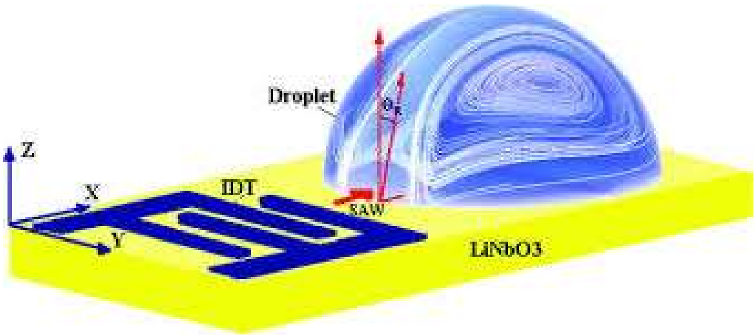

Figure 2.22: SAW propagation from *IDT* to the droplet on *LiNbO*$_3$ piezoelectric substrate showing Rayleigh angle with internal streaming inside the droplet [113].

When moving from fundamental harmonic signal to higher signals, propagation losses increase, however, streaming and hence mixing efficiency reduces [114]. When the *RF* signal voltage is increased, this increases streaming velocity and mixing efficiency inside the droplet. Pumping speed of 1.4 cm/s can be obtained with 5 µl droplets at an input signal voltage of 40 V [114]. Different types of micropumps based on *SAWs* help to actuate the droplet without moving parts on the surface which is also the potential application of *LOC* devices [115], [116].

Figure 2.23 shows side and top views of acoustic streaming inside the droplet whereas the effect of the applied input voltage on the streaming velocity with different *SAW* signals is shown in Figure 2.24 [114]. However, the effect of applied voltage on streaming velocity with the droplet size as a parameter is given in Figure 2.25 [114].

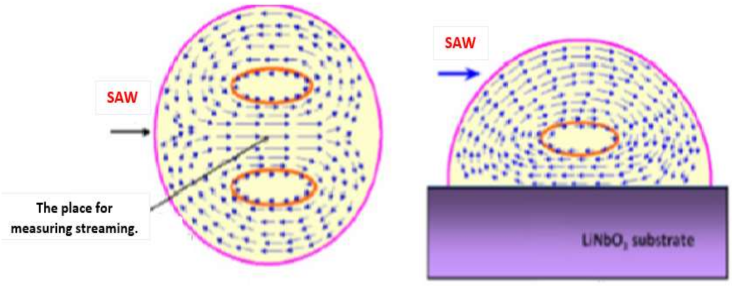

Figure 2.23: Schematic drawings of acoustic streaming within droplet using top (left) and side (right) view [114].

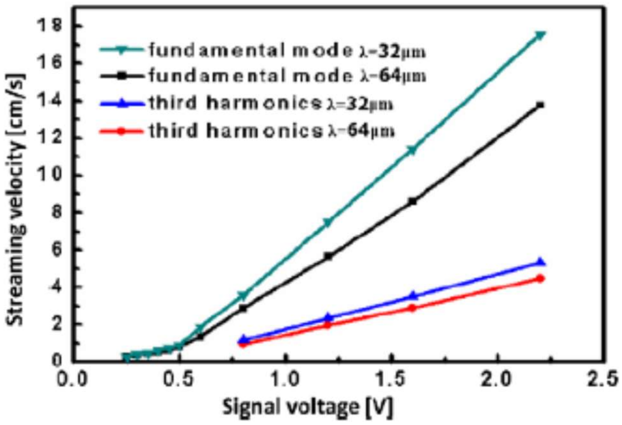

Figure 2.24: Flow velocity induced by the acoustic wave as a function of *RF* signal voltage. All *SAW* devices have 60 finger pairs [114].

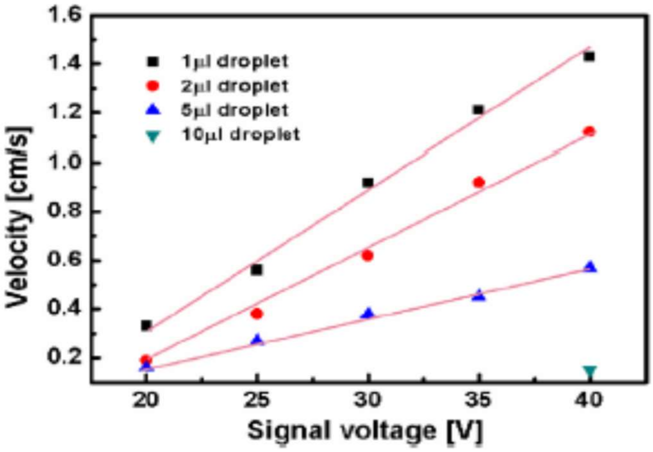

Figure 2.25: Dependence of streaming velocity on the signal voltage with droplet size as a parameter, all devices have λ 32 μm [114].

2.5.2 *Thermal impact of the SAW on the droplet*

It was also widely reported that other than internal streaming, *SAWs* cause heating of liquid droplets and substrate [13],[14] [15] especially at high *RF* input power [16].

2.5.2.1 *Effect of electric field on heating of the droplet*

The heating of the droplet is a combination of acoustic-thermal effect and Joule heat (Joule heat is heating caused by electric resistance) [117]. When an electric current passes through the conductor, it produces heat which is called a Joule-heat effect. Gold (Au) layer was used to provide a shield to alternating current (*AC*) which helps to analyse the heating effect. It was investigated that the droplet without the shield has a higher temperature (43.50 °C) as compared to the droplet with the shield (34.50 °C). Furthermore, the droplet with only having Joule-heat effect has a temperature of 26 °C.

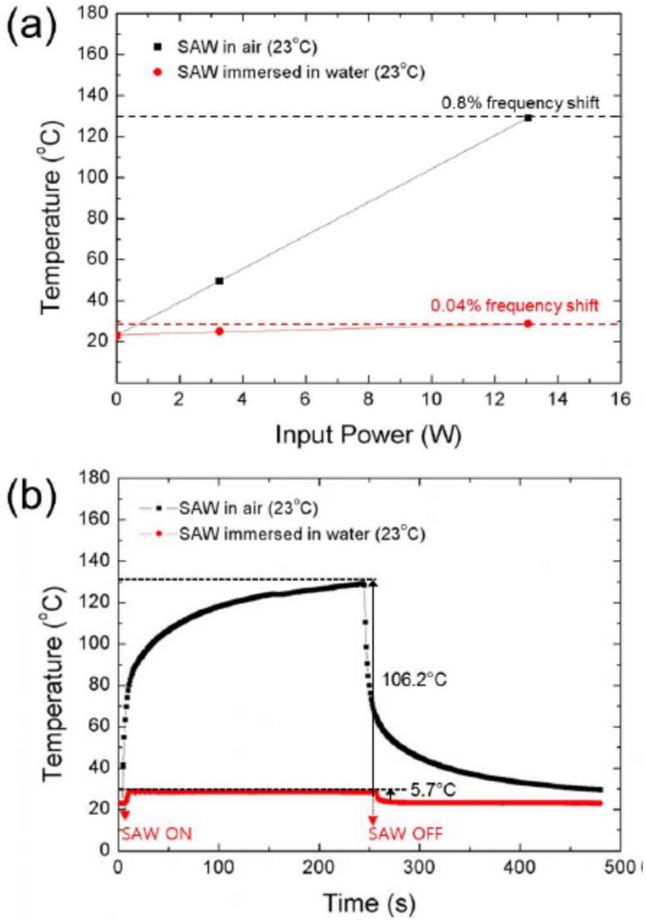

Figure 2.26: Thermal measurement results for the *F-SAW* device in air and water (a) Temperature increases and resonance frequency shift of *F-SAW* device with input power (b) temperature variation of *F-SAW* device with time in air and water [105].

When the temperature of *IDT* device changes, it can change the performance of the device. The maximum temperature of the device was measured as 28 °C and 129 °C in water and air, respectively at 13.0 W of input power after 250 s of input *SAW* [105]. Figure 2.26 shows the temperature measurement of the F-SAW device in air and water. It is clear from Figure 2.26-a that the resonant frequency is shifted for the device in water is 0.04% which is 1/20 lesser than that in the air (0.8%). A higher convective heat transfer coefficient in water prevents it to decrease its performance and increase its temperature [105]. Moreover, it takes more time to reach the room temperature with the device in the air as compared to the water because of the difference in heat transfer co-efficient as shown in Figure 2.26-b [105].

2.5.2.2 *Heating related to the streaming inside the droplet*

Peclet number ($Pe = \frac{\rho.c.v.L}{k}$) was used to determine the heat transfer mechanism inside the droplet, where ρ is the liquid density (kg.m^{-3}), c is the heat capacity (J.Kg^{-1}.K^{-1}), v is the streaming velocity (m. s^{-1}), L is the characteristic length (m) and k is the thermal heat conductivity (W.m^{-1}.K^{-1}) [118].

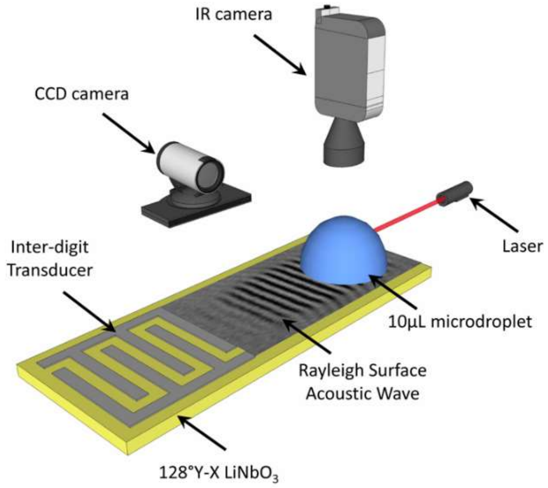

Figure 2.27: Experimental setup for monitoring of streaming and temperature change [118].

It was observed that when the streaming velocity inside the droplet is increased, the temperature is increased, and vice versa [118]. At a lower power (100 mW), streaming velocity inside the droplet is low (Pe <<1), so thermal conduction takes place, whereas, at higher power (1.6 W), streaming is more significant (Pe >>1), so convection takes place. When we increase the viscosity, because of friction, streaming is not as dominant as conduction, thus and it will take more time to reach a thermal equilibrium [118], [119]. The experimental setup used to monitor streaming and thermal impacts inside the droplet is shown in Figure 2.27 [118].

2.5.2.3 *R-SAW as an efficient heating system (uniformity of the droplet)*

It was found that with the help of Rayleigh *SAW*, we can develop an efficient heating system for biological reactions [118], [119]. There are three parameters on which temperature uniformity depends, namely the volume of droplet, frequency of *SAW* and *RF* power applied to the *SAW IDT*. Attenuation (reduction in the strength of signal or loss of signal of waves) has a major role to gain the uniformity of temperature T_d [119].

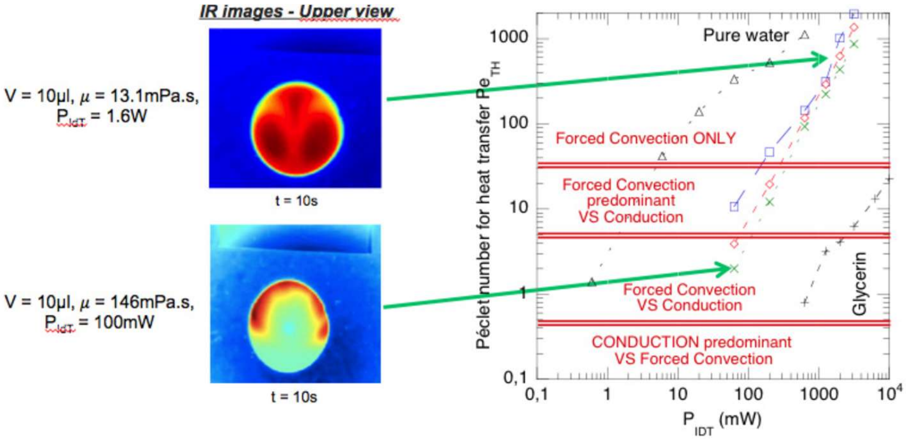

Figure 2.28: Peclet number for heat transfer mechanism as a function of P_{IDT} for water-glycerin mixture [119].

Figure 2.28 shows the relation between power input to the *IDT* (P_{IDT}) and *Pe* with a comparison of different viscosities of the droplet [119]. Figure 2.29 shows the effect of input power on streaming velocity for different viscous fluids. Water with a low viscosity has shown significant streaming inside the droplet, so convection will be dominant. On the other hand, glycerine is a viscous fluid in which streaming is less effective, which results in more time to reach a uniform stage [119].

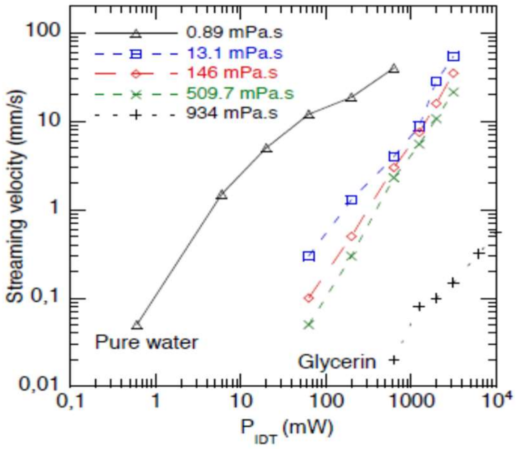

Figure 2.29: Effect of power input on the streaming velocity of particles for various viscosities (Pure water-glycerin mixture) [119].

The length along the surface of the piezoelectric substrate over which a Rayleigh wave decays by the leakage of *SAW* is called attenuation [12]. Attenuation of longitudinal waves is given by equation (2.3) [119];

$$\alpha = \frac{R}{2}\omega^2/C_L^3 \tag{2.3}$$

$$R = \frac{1}{\rho L}\left[(\frac{4}{3}\mu + \mu' + \frac{K}{C_p}(\gamma - 1)\right] \tag{2.4}$$

where R is the dissipation coefficient defined in equation (2.4), ω is the pulsation, C_L is the velocity of the wave in a liquid, ρ is the density of the liquid, μ is the dynamic viscosity, μ^- is the volume viscosity, K is the thermal conductivity of the liquid, C_p is the heat capacity at constant pressure and γ is the ratio of C_p/C_v with C_v heat capacity at constant volume [119].

With the increase in the frequency of *SAW*, attenuation increases which make it longer to achieve thermal equilibrium. Similarly, the volume of droplet and *RF* power has a direct relation with the attenuation of waves and hence uniformity of temperature [119]. Heating systems in microfluidics involve conduction only whereas the *SAW*-based heating system involves forced convection [119]. This is the reason latter one called as an efficient heating system [119].

It was reported that resonant frequency increases linearly with the increase in temperature of the device that can change the performance of the device [120], [121].

2.5.2.4 Mechanisms of heating-up of the droplet

Heating-up of the droplet can occur in two ways, one is the waves travel on a substrate that generates temperature and transfers to the droplet, the other is Rayleigh waves that transfer the energy directly to the droplet. The latter phenomenon dominates the heating process [122]. For instance, at an input power of 2.0 W, temperature rise by the substrate is only 20 °C whereas the temperature rise by the droplet is 30 °C that is much higher as compared to the substrate. Therefore, droplet heating is only because of longitudinal waves entered inside the droplet [122]. Furthermore, more viscous liquid has more energy dissipation by the longitudinal waves inside the droplet which increases the T_d [122].

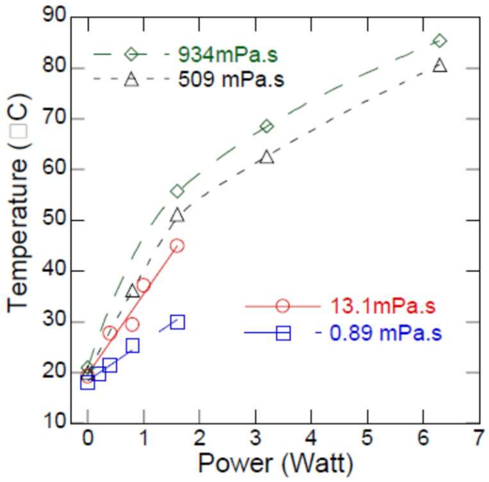

Figure 2.30: Evolution of droplet temperature in function of acoustic power for four different viscosities (0.89, 13.1, 509 and 934 mPa.s) at 25℃ [122].

The maximum temperature of 55 °C achieved with droplet having higher viscosity (934 mPa.s) whereas the droplet with low viscosity (13.1 mPa.s) reached only to 45 °C, at P_{in} of 2.0 W as shown in Figure 2.30 [122]. Therefore, high viscous fluids have more temperature rise than low viscous fluids.

Different substrates such as *LN* and *ST X* quartz were used to compare the temperature rise by the substrate [17]. *LN* showed less temperature rise without a droplet and greater temperature rise with a droplet as compared to *ST X* (cut direction) quartz substrate [17]. The heating of the droplet is majorly caused by viscous dissipation by streaming not by anelastic effect (conversion of acoustic waves to heat). It was found that *LN* is better in terms of heating of the droplet as compared to *ST X* quartz [17]. Therefore, the electric field has a significant role in the temperature rise of the droplet. Combination of both Joule heat and waves energy results in higher temperature as compared to the individual one.

2.6 Applications of SAW-based heating system

There are several ways to heat the droplet and they have countless applications. Since this study is limited mainly to the *SAW*-based heating system, in this section, only applications related to the *SAW*-based heating system are discussed.

2.6.1 Acoustothermal heating of the channel-based microfluidic system

The performance of *PCR* can be increased if there is a continuous flow of fluid to different temperature zones for denaturation, annealing, and extension. This is called a continuous flow polymerase chain reaction (*CFPCR*) [123]. Rapid heating of Polydimethylsiloxane (*PDMS*) channel-based microfluidic system using *LN* was achieved by gaining temperature of 68 °C in 1.0 s that is suitable for different temperature zones of *CFPCR* [121].

2.6.2 Polymerase chain reaction (PCR)

PCR is one of the most important tools for the amplification of *DNA* [124]. *PCR* amplification and analysis can be used for *DNA* genotyping, virus identification, and forensic applications [124], [125]. The *PCR* employs low-cost tests with an increased ramp rate and uniform thermal equilibrium. By using microfluidic thermal heat exchangers and Peltier junctions, an experiment was performed to get rapid heating (44 °C/s) and cooling (17 °C/s) [126]. This equipment was successfully tested to amplify *DNA*/*RNA* of H5N1 influenza, human immunodeficiency virus (*HIV*) [126]. However, by combining a thermocouple device with a Peltier junction [127], reported a *PCR* cycling system with rapid heating (100 °C/s) and cooling (90 °C/s).

Most widely Peltier elements are in use for rapid heating and cooling, however, recently *SAW* is also found as an efficient tool for *PCR* applications.

2.6.3 R-SAW compatibility with PCR

PCR requires continuous heating and cooling cycles [128]. Normally in high viscous liquids, species of *PCR* cannot be interacted with each other [18]. When the dynamic viscosity reaches 3.5 mPa.s, the efficiency of reaction reduces significantly as shown in Figure 2.31. However, with the help of *R-SAW*, efficiency can be increased [18]. The temperature of 95 °C was achieved with 10 µl droplet and viscosity of 10.8 mPa.s at an electrical power of 3.2 W. One reference sample was also used to validate *R-SAW* compatibility with the *PCR*. It was found that the wave's power and duration of irradiation do not affect the *PCR* mixture, so *R-SAW* has compatibility with microdroplet *PCR* [18].

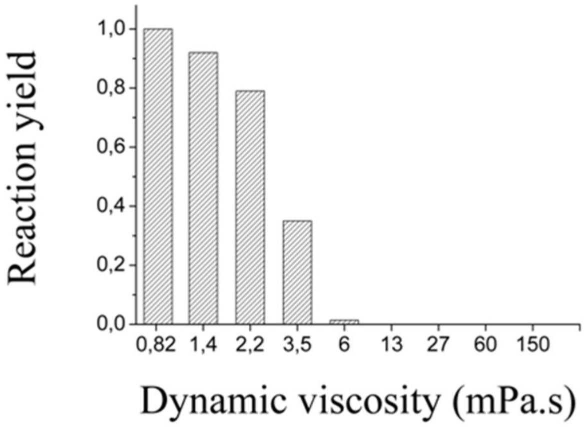

Figure 2.31: *PCR* reaction yield of a common industrial thermocycler as a function of dynamic viscosity of liquid [18].

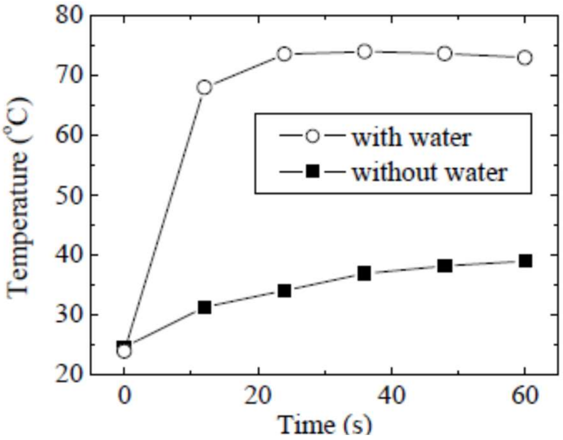

Figure 2.32: Comparison of temperature with and without droplet [13].

The temperature rise with and without a droplet against time is shown in Figure 2.32. It is clear from this figure that the temperature of the substrate is almost half of the T_d at the input voltage of 35 $V_{p\text{-}p}$ and a duty factor of 50% [13].

2.6.4 Controlling temperature of the droplet

There are different ways to control the temperature of the droplet. A few methods have been discussed in the following sections.

2.6.5 With an applied input voltage/power and duty factor

The temperature rise of the droplet is dependent on the applied input voltage as shown in Figure 2.33. The temperature rise of 10 µl droplet at applied voltages from 5 $V_{p\text{-}p}$ to 20

$V_{p\text{-}p}$ for two minutes is shown in Figure 2.33-a [13], where $V_{p\text{-}p}$ is peak to peak voltage. It is evident from the figure that by the increase in applied voltage, the T_d increases. *SAW* input was stopped after the 60 s [13]. The maximum temperature of around 50 °C was achieved with an applied input voltage of 20 $V_{p\text{-}p}$ after one minute of input *SAW*. Figure 2.33-b shows the relationship between the applied input voltage with temperature. It is clear from Figure 2.33-b that the temperature has a quadratic relation with the applied voltage. On the other hand, the *SAW* amplitude is proportional to applied voltage [129], [130], so the temperature is proportional to the square of the *SAW* amplitude. The amplitude is also proportional to the streaming force [131], therefore the temperature is proportional to the streaming force [13].

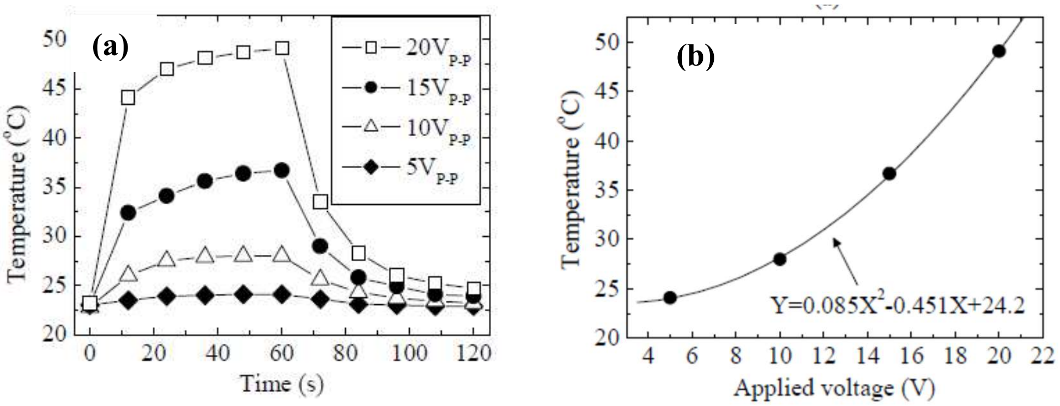

Figure 2.33: Experimental results for 10 µl water droplet (a) Temperature rise Vs time with an applied input voltage as a parameter (b) Temperature obtained one minute after the voltage is applied [13].

The temperature of the droplet can be controlled by two methods, one with applied *SAW* power and the other with a duty cycle as shown in Figure 2.34 [132]. Figure 2.34-a shows droplet heating is controlled by changing input power (dBm), whereas Figure 2.34-b shows that heating is controlled by varying duty cycle (percentage). These results can be used for different chemical and biological reactions [132].

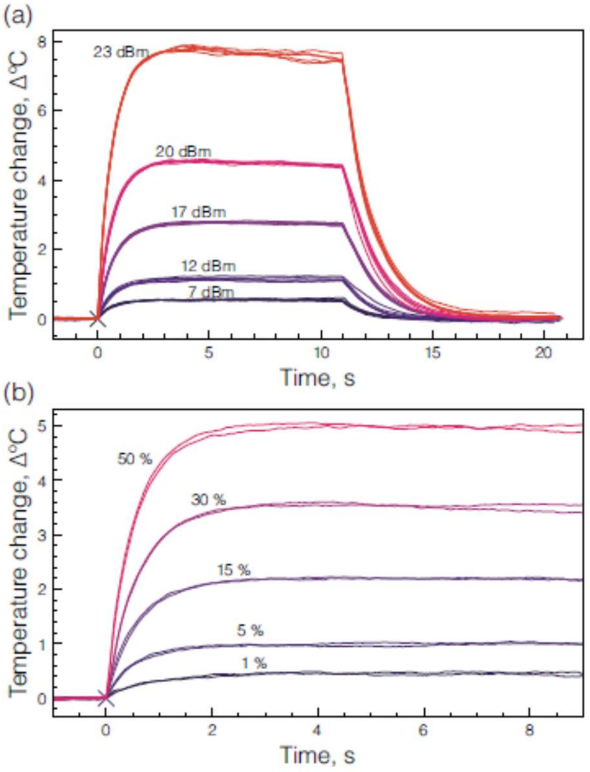

Figure 2.34: Droplet heating can be controlled by varying the a) input power to the device or the b) duty cycle at constant input power (23 dBm here). In each case, the steady-state reached after 3.0 s [132].

2.6.5.1 Development of SAW thermo-cycler

The controlled temperature of the droplet is required in a thermo-cycler. Thermo-cycler is also known as a *PCR* machine or *DNA* amplifier [133]. The temperature of the liquid can be changed by changing the applied voltage, duty factor and viscosity by using the *SAW* [134]. An experimental setup used to control the temperature of the liquid is shown in Figure 2.35. Thermocouple thermometer and a non-contact infrared thermometer were used to measure the temperature [134]. Water cannot be heated more than 50 °C but with 80% water/glycerol mixture it can be heated to 120 °C with a duty factor of 80%. With duty factor of 20%,40% and 60%, temperature can go up to 50°C, 72 °C and 98°C [134]. This means T_d is directly proportional to the duty factor.

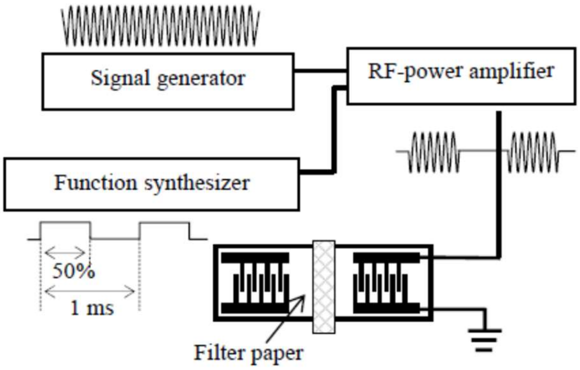

Figure 2.35: Experimental setup to control the temperature of the liquid on the path of *SAW* [134].

An industrial thermocycler can only work at a low viscosity. After a certain viscosity, the efficiency of reaction falls as shown in Figure 2.31 since conduction starts with high viscous fluids. The *SAW*-based system involves convection caused by internal mixing which enhances the efficiency of *PCR* [18].

2.6.6 *Applications other than PCR*

There are some biological processes and applications other than *PCR* where the controlled temperature of the droplet is also a requirement. Following are a few of them.

2.6.6.1 *SAW-based device to monitor blood coagulation*

T_d can be controlled by using a duty cycle that can help to monitor blood coagulation [135]. A fixed input power level of 1.0 W was used with the centre frequency of 50.6 MHz by using Lamb waves [135]. It is evident from Figure 2.36 that the T_d increases with the increase in the duty ratio. A constant temperature of 37 °C was used along with the electromechanical sensor to measure the impedance of the blood sample [135]. A solution of activated partial thromboplastin time (*APTT*), plasma and calcium chloride ($CaCl_2$) of 5 µl were used to test this. *APTT* helps to measure the coagulation time of the blood [135]. From the change in impedance, blood coagulation can be identified [136], [137]. The advantage of *SAW* is because of streaming, it has good mixing efficiency which causes a uniform mixture of solution. Figure 2.37 shows time responses for the sample with and without *SAW*. It is evident from Figure 2.37-a that when there is *SAW*, there is a sharp increase and decrease in the impedance with time (temperature kept 37 °C). However, results in Figure 2.37-b are at room temperature without *SAW* where there is no significant change in the impedance [135]. The coagulation will not occur if there is no proper mixing inside the droplet [136].

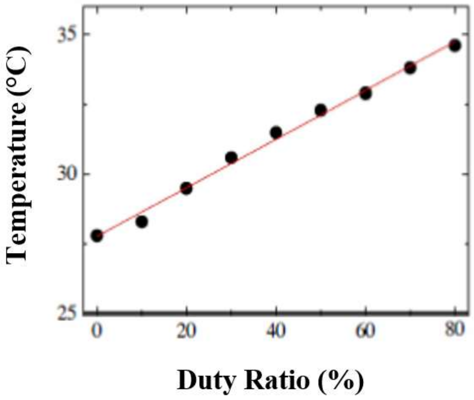

Figure 2.36: Temperature obtained after one minute of power applied. The power applied was fixed at 1.0 W [135].

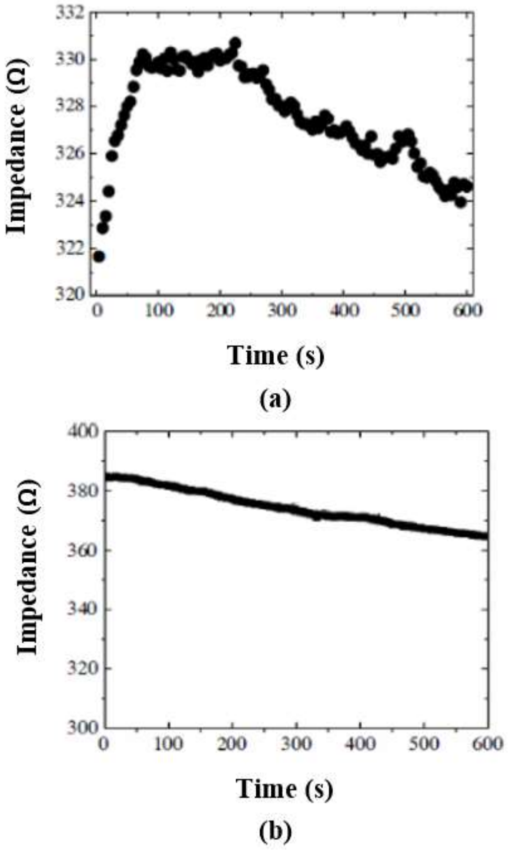

Figure 2.37: Time responses during coagulation reaction (a) and (b) with and without temperature control by *SAW* [135].

2.6.7 *Acoustic tweezers*

SAW can also be used as an acoustic tweezer or droplet sorting system. Slanted finger interdigital transducer (*SFIT*) has been used with $LiNbO_3$ as a substrate and *PDMS* microchannel [138]. Water-in-oil droplets have been used, aligned in the centre of the channel. The centre frequency for this device was 70-95 MHz. The input electrical power density varies with an applied frequency. Droplet sorted out with the help of temperature gradient and droplet moves from higher temperature area to the lower temperature area as shown in Figure 2.38 [138].

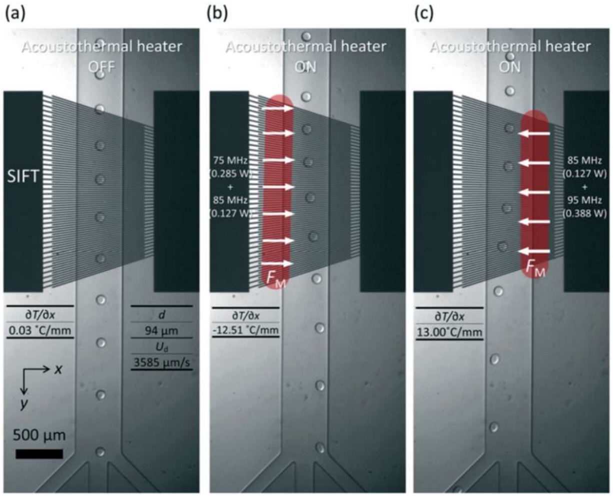

Figure 2.38: (a) Water-in-oil droplet are focused at the centre of microchannel by two oil sheath flows travelling downstream. (b) On applying acoustothermal heating from the left, the droplet pushed to the right (c) On applying power from the right, the droplet pushed to the left [138].

2.6.8 *Temperature distribution inside the droplet*

Relationship between attenuation of a longitudinal wave, temperature, and viscosity of the liquid was investigated using a thermocouple with 80% glycerol/water droplet [14]. The T_d was measured from two points of the droplet, one point where *SAW* enters the droplet and other on the opposite side. Figure 2.39 shows droplets with points 1 and 2 to measure the T_d [14].

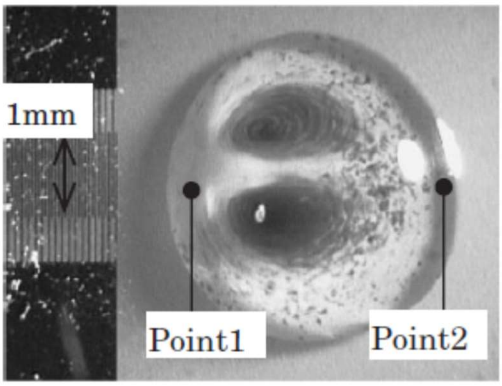

Figure 2.39: Liquid streaming in 80 wt% glycerol/water droplet which is placed at the centre of the *SAW* propagation path [14].

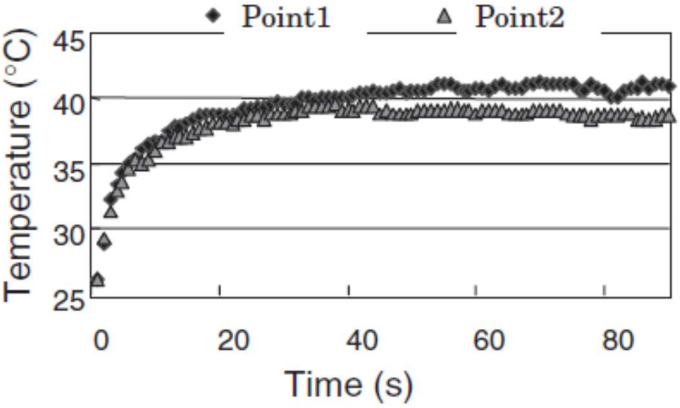

Figure 2.40: T_d at point 1 and point 2, *SAW* is generated from left side [14].

It was observed that the temperature at point 2 was smaller than the temperature at point 1 as shown in Figure 2.40. Probably attenuation of a radiated longitudinal wave in high viscosity droplet [14].

2.7 Numerical work related to this study

Although empirical work has already been discussed in the previous sections of this chapter, it is necessary to include numerical work done so far that motivated the author to find the knowledge gap.

2.7.1 Streaming inside the droplet

Both experimental and numerical investigations were carried out to visualize streaming velocity inside the droplet at different *RF* power levels [139].

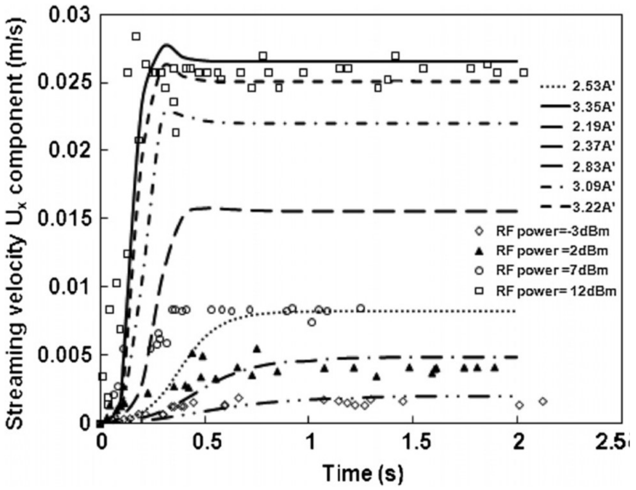

Figure 2.41: Streaming velocity at the top of a 30 µl droplet positioned symmetrically within the SAW propagation direction. Solid lines represent numerical results whereas markers denote experimentally measured data at different *RF* powers [139].

All experiments were performed at lower *RF* powers, so there was no deformation in the droplets. A good agreement was found between experimental and numerical data. It is clear from Figure 2.41 that streaming velocity becomes constant within one second of the input *SAW*. The temperature effect was not considered in this study [139].

2.7.2 Numerical study of acoustothermal heating of the fluid

A theoretical model was developed using *SSAW* in a *PDMS* microchannel with *$LiNbO_3$* as a substrate. *IDT* is used from both sides to generate *SSAW*. A device with the *PDMS* chamber, *IDT* and the substrate are shown in Figure 2.42 [140]. It was observed that with the increase in the length of the microchannel by keeping the same aspect ratio (δ=W/H), where '*W*' is the width and '*H*' is the height of the microchannel, the temperature of the liquid increases. Input power has a direct relation with the temperature rise of the droplet as shown in Figure 2.43. Moreover, with the increase in the frequency of the waves, the temperature of the fluid increases [140].

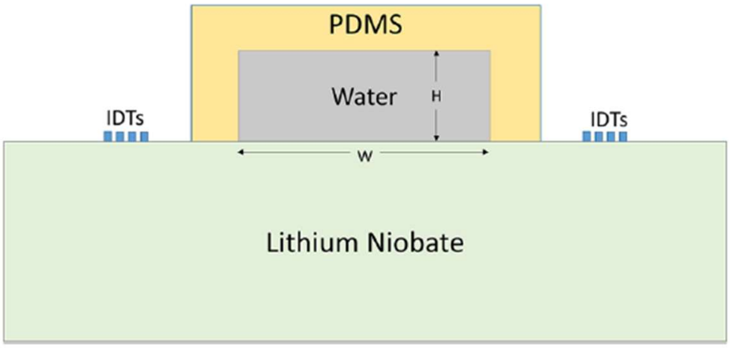

Figure 2.42: Schematic diagram of the device with the *PDMS* channel [140].

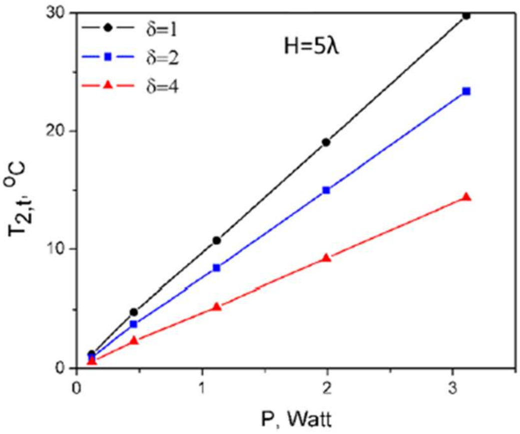

Figure 2.43: Temperature of the fluid at different aspect ratios (δ) at different power inputs [122].

2.8 Summary and research gap

The *SAW* devices have found tremendous applications both in microfluidics and sensing which are ranged from telecommunications to biological sciences. The physics of different type of structure of *IDT*, different form of waves and their related applications have been discussed in this chapter.

The conclusion of the above discussion is summarized below.

- The impact of input *SAW* on the droplet in terms of streaming and thermal have been discussed in the literature but a model needs to be designed that can interpret different heat transfer mechanisms inside the droplet in detail.

- It can be concluded that the temperatures on the substrate and the droplet are different, but the literature lacks the information if this behaviour remains the same.

- The literature shows that the portion of the droplet closed to the *SAW* has shown higher temperature readings as compared to those of the other side of the droplet. However, how much is the temperature in other portions of the droplet is still unknown.

- For some biological reactions such as *PCR*, regular heating and cooling cycles are required, however, some biological cells damage inside the droplet during heating. Therefore, this study only focused on droplet temperature of less than 55 °C with an input power of 2-3W that doesn't damage the cells.

- $LiNbO_3$ has been used extensively as a piezoelectric substrate to generate *SAW*. Information regarding streaming and thermal impact using thin-film piezoelectric material is also available but not in detail.

- Using the hybridized waves, only droplet nebulization has been discussed but no study has been done to see the thermal impact of these waves on the droplet.

Keeping in view the above research gaps, this research is focussed on developing a model to analyse how much *SAW* input given to the droplet coverts to the streaming and thermal energy inside the droplet. This leads to investigating the coupling mechanism between streaming and thermal impact. Furthermore, investigation of the effect of wave mode and frequency of the waves on the temperature rise of the droplet is also part of this study. This leads to the methodology and experimental setup required for this work which is part of the next chapter.

Chapter 3: An Analysis Model of Kinetic and Thermal Coupling Impacts of SAW on The Droplet.

Based on the discussions on the current research on *SAW*-droplet interactions, it has been concluded that thermal and kinetic impacts play an important role in digital microfluidics. In this chapter, an analysing model is proposed to demonstrate the mass, momentum and energy conversion principles. These principles are based on kinetic and thermal impacts of *SAW* on the droplet. The details of the model, with assumptions, are introduced in the following sections.

3.1 The analysing model

Taking an individual droplet on the surface of the *SAW* device as the analysing system, a model is constructed by the conservations of mass, momentum, and energy of the system. The *SAW* travels on the piezoelectric substrate, converts to leaky wave when entering inside the droplet and causes internal streaming [9], [10], [141], meanwhile radiating the thermal energy to the droplet [13],[14] [15].

3.1.1 The conservation of mass

The analysis system of the droplet for mass conservation is shown in Figure 3.1 where *SAW* propagates inside the droplet and changes to leaky wave to heat the droplet. If the temperature of droplet reaches the saturation temperature, bubbles (phase changes) can generate inside the droplet [142], as indicated by M_{ph} in Figure 3.1. Moreover, the mass transfer of liquid droplet occurs at the interface between droplet and surrounding air by either the molecular diffusion or convections, as indicated by M_{ev} in Figure 3.1. Then, by the mass conservation, the mass changes of the droplet can be expressed as equation (3.1) [143],

$$\frac{dm_d}{dt} = -\dot{s}_m \tag{3.1}$$

where 'm_d' is the mass of the droplet (kg), 't' the time (sec), '$\dot{s}_m$' is the source term of the droplet. The mass and phase changes of the droplet can be predicted by equation (3.2);

$$\dot{s}_m = -k_m A_t \rho_d B_m - m_d\, \dot{\chi} \tag{3.2}$$

where, the first term on the right-hand side is the rate of droplet evaporation with 'k_m' the effective mass transfer coefficient (m/s), 'A_t' the total area of the droplet, 'ρ_d' the density of droplet liquid (kg/m^3), and 'B_m' the Spalding mass transfer number, $B_m = \frac{X_s - x_0}{1 - x_0}$, defined by droplet surface mass fraction, 'x_s', and that far away, 'x_o', respectively. The effective mass transfer coefficient can be estimated by correlations of Sherwood number, $Sh = k_m D/D_f$, with flow parameter of Reynold's number, $Re = \frac{U_r D}{\nu}$, and physical properties of kinetic viscosity, ν (m^2/s) and diffusivity of air (m^2/s) by Schmidt number, $Sc = \frac{\nu}{D_f}$, as [144],

$$Sh = 1 + 0.276 Re^{0.5} Sc^{0.5} \tag{3.3}$$

where D is the diameter of the droplet (m). The second term on the right-hand side of equation (3.2) is the mass transfer rate due to the phase changes, which occurs when the temperature of droplet reaches the saturation temperature. The quality of vapour (mass fraction), χ, has to be determined by coupling with the energy equation.

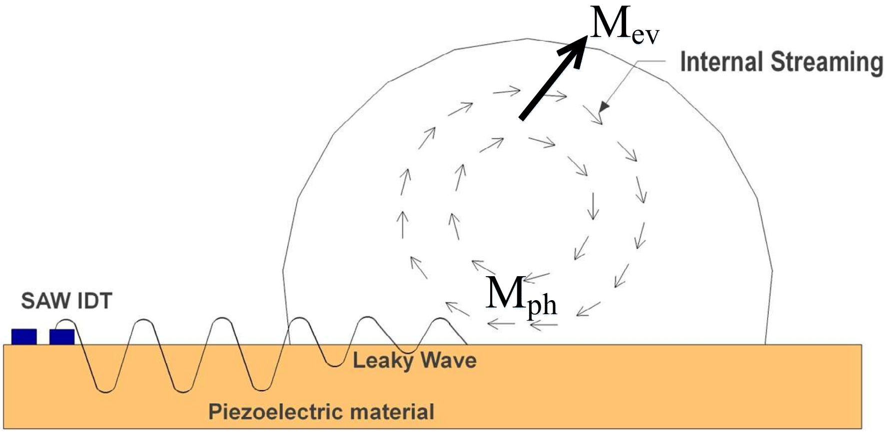

Figure 3.1: A *SAW*-based solid-liquid interaction analysis model of mass conservation. The heated droplet by *SAW* can change the phase of the liquid and droplet can transfer mass to the surrounding air.

The model is general, while in case if the temperature of the droplet is lower than the saturated temperature, there will be no phase change and only the mass transfer to the air should be considered.

The mass transfer because of evaporation can be detected by detecting the size (volume) of the droplet monitored from experimental observations. The phase change can be identified either by the direct observation (*CCD* camera) or by the temperature of droplet measured by an infrared camera.

3.1.2 The conservation of momentum

Consider the entire droplet placed on the *SAW* device surface, as shown in Figure 3.2, the following equation can be derived by Newton's second law;

$$\frac{dm_d U_d}{dt} = \sum F_i \tag{3.4}$$

where, the acceleration of the entire drop is driven by the forces acting to the droplet, which are inertial force, *SAW* force, the drag force (F_d), the friction force (F_r) between the drop and the device surface, and buoyancy force (F_b) [145] as shown in Figure 3.2. U_d is the droplet velocity that can be calculated by measuring the distance moved by the droplet with time.

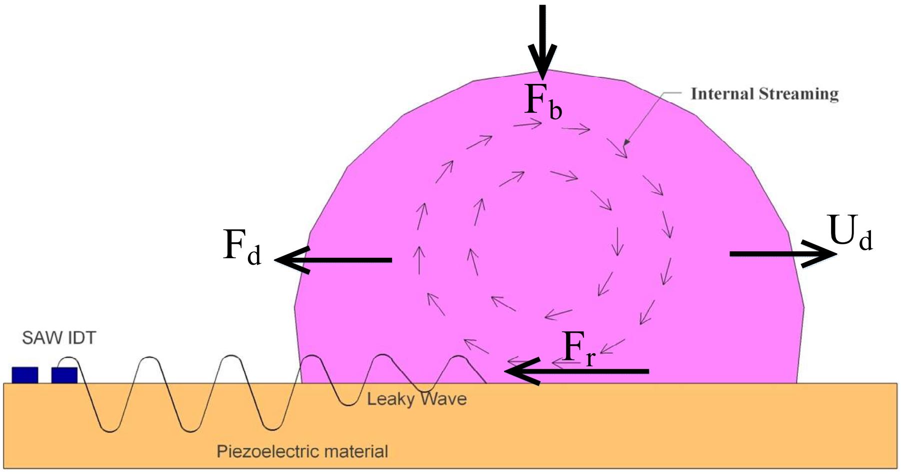

Figure 3.2: The momentum conservation showing buoyancy, drag, friction forces with the droplet velocity.

At higher power, the *SAW* force can develop to drive the droplet moving horizontally and vertically to form jets or atomize at the Rayleigh angle. Based on the study [145], the *SAW* force can be predicted as;

$$F_s = -\frac{\rho_f}{\delta_x \delta_y}(1+\alpha_1^2)^{3/2} A^2 \omega^2 k_i \int_0^{\delta_x} \int_0^{\delta_y} exp2(k_i x + \alpha_1 k_i y)\, dxdy \tag{3.5}$$

where 'A' is equivalent to the SAW wave amplitude at the edge of the liquid, $\omega = 2\pi f_0$ is the angular frequency, k_i the leaky SAW number (m^{-1}), 'α_1^2' is attenuation co-efficient [145]. The drag force if droplet moves on the device surface can be calculated by equation (3.6) [144],

$$F_d = -0.5\, C_d A_c \rho_d U_d^2 \tag{3.6}$$

where A_c is the cross-section area of the droplet (m^2), ρ_d is the density of the droplet, U_d is the droplet velocity in the direction of waves, and C_d is the drag coefficient can be calculated by equation (3.7) [144];

$$C_d = f(Re_d, \frac{\varepsilon}{d}, \frac{L}{d}) \tag{3.7}$$

where Re_d is Reynold's number for the droplet, ε is wall roughness height, which is important for turbulent flow, L/d is the cylinder's length to diameter ratio. Furthermore, the friction force between the droplet and the substrate (device) can be calculated by (3.8) [144];

$$F_f = -0.5\, C_f A_f \rho_d U_x^2 + F_{f0} + F_\sigma \tag{3.8}$$

where A_f is the interfacial area of the drop and device (m^2), U_x is the streaming velocity inside the droplet near the substrate, F_{f0} is the static friction force, and C_f, the friction coefficient to be calculated by equation (3.9) [144];

$$C_f = \frac{2\tau_w}{\rho U_x^2} \approx \left(\frac{\frac{8}{15}}{Re_x}\right)^{\frac{1}{2}} = 0.73 Re_x^{0.5} \tag{3.9}$$

where C_f is a dimensionless quantity, analogous to the friction factor. Re_x is Reynold's number related to the streaming velocity. The term on most right side of the equation (3.8), F_σ, is the interfacial tension force that can be calculated using equation (3.10);

$$F_\sigma = \pi \sigma d \tag{3.11}$$

Where σ is surface tension co-efficient with value 27.8 (mN/m) of water and ZnO for hydrophobic surface, '*d'* is the droplet diameter (m) [146]. Finally, the buoyancy force, if the droplet jump or breakup is given by equation (3.12) [144];

$$F_b = (\rho_d - \rho_a)gV_d \tag{3.12}$$

where 'V_d' is the displaced volume of the fluid (m^3), $(\rho_d - \rho_a)$ is the density difference of the droplet and the air, 'g' is the gravitational acceleration (m/s^2).

By detecting the droplet velocity, U_d, from experiments coupling with the data of mass of droplet, the interaction force terms on the right-hand side of equation (3.4) can be identified.

3.1.3 The conservation of energy

It is straightforward to apply the first law of thermodynamics to this system as in equation (3.13),

$$\frac{dE_d}{dt} = \sum \dot{Q}_i + \dot{W} \tag{3.13}$$

where E the total energy of the droplet (J), $\dot{Q}_i$ is the rate of the ith heat interaction with the system, and $\dot{W}$ is the rate of mechanical interaction of the droplet with surroundings. The heat interactions including the partial of *SAW* power transferred into a droplet that converts to thermal energy by radiation, given in equation (3.14) [147], [148];

$$\dot{Q}_t = \alpha_T \dot{E}_s = 2\pi^2 \alpha_T D \rho_d V_R^3 (a/\lambda)^2 = 2\pi^2 \alpha_T D \rho_d V_R V_f^2 (a/\lambda_f)^2 \tag{3.14}$$

where $0 < \alpha_T < 1$ is the part of the total SAW power penetrated to the droplet, $\dot{E}_s$ (W), the V_R and V_f are the velocities of *SAW* transportation in the solid device and the droplet, respectively. The amplitude of the wave using the normal component of particle displacement is represented by a, whereas λ_f is the wavelength of longitudinal waves in the fluid and λ the wavelength of the *SAW* [148].

Other heat interactions are the heat transfer from the device surface to the droplet, $\dot{Q}_s$, heat transfer from droplet to the air, $\dot{Q}_a$, and heat enter from the corner of the droplet, radiated heat, $\dot{Q}_r$. Furthermore, input *SAW* energy also causes the changes in kinetic energies inside the droplet either due to streaming, $\dot{K}_{st}$, or friction energy, $\dot{K}_f$. An analysing thermodynamic model describing energy conservation with all heat transfers and changes in kinetic energies inside the droplet is schematically shown in Figure 3.3.

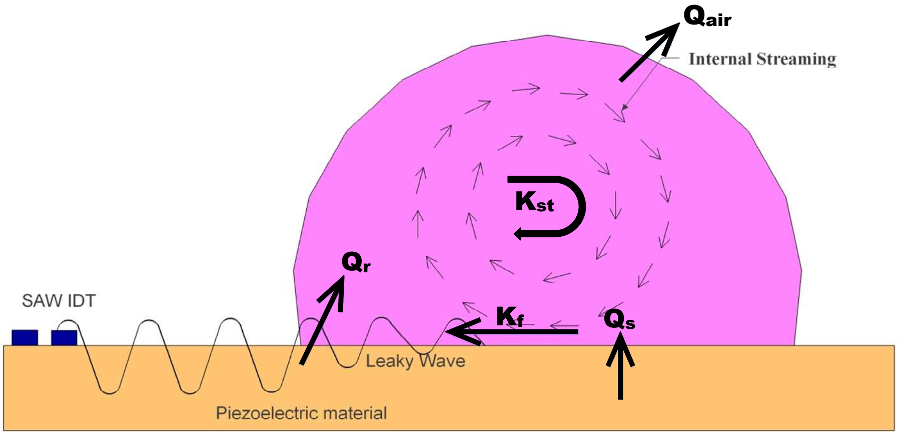

Figure 3.3: A thermodynamic energy conservation model of *SAW*-droplet interaction showing heat transfers and kinetic change inside the droplet.

The work done on the system by the surroundings must be considered when it occurs that the volume of droplet significantly changes, which can be predicted by equation (3.15),

$$\dot{W} = -p(V_d)\frac{dV_d}{dt} \tag{3.15}$$

where, $\dot{W}$ is the mechanical power due to droplet volume changes against the pressure. $p(V_d)$ is the pressure inside the droplet as a function of droplet volume, V_d, and t is time (s), more detail in section 5.4.1. The model can be applied to analyse the coupling mechanism of kinetic and thermal impacts of *SAW* on the droplet when the temperature distribution of the droplet can be detected. Meanwhile, the velocity and velocity distribution inside the droplet can be measured with assistance from mass and momentum models presented in the sections 3.1.1 and 3.1.2.

3.2 Summary

In this chapter, an analysing model is proposed for thermal and kinetic impacts of *SAW* on the droplet. This is a general model based on mass, momentum and energy conservation principles. The conservation of mass includes mass change either by change in phase or evaporation. The conservation of momentum is based on Newton's second law of motion whereas conservation of energy is based on the first law of thermodynamics. To implement these models, an experimental setup and a methodology are required to detect these changes in the droplet which is part of the next chapter.

Chapter 4: Methodology and Experimental Setup

Based on the discussion on the analysing model, experimental setup on the thermal and kinetic impacts of *SAW* on a droplet are designed and introduced in this chapter. Before the details of the experimental setup, the selection of piezoelectric material, fabrication of *IDT*, equipment required to generate and propagate *SAW* has been discussed. Then, the methods and the data treatments of visualisation of acoustic streaming and capture of temperature change of the droplet are followed for finding the coupling mechanism.

4.1 Experimental Details

This section starts with the selection of the piezoelectric material followed by the deposition of a thin film on the substrate and fabrication of the *IDT*. The necessary equipment and the procedure to generate and propagate *SAW*, identifying the resonant frequency of the device and detail of the necessary surface (device) treatment are also conferred here.

4.1.1 ZnO as a thin-film piezoelectric material

The bulk piezoelectric materials such as quartz and $LiNbO_3$ have good electromechanical coupling coefficient but are difficult to integrate with Si-based integrated circuits (IC) [3]. On the other hand, the thin films such as *ZnO*, *AlN*, and *PZT* have lower power consumption, lower cost, higher electromechanical coupling coefficient, and higher sensitivity and reliability [3], [75]. Higher electromechanical coupling coefficient means electrical signals will be converted to mechanical waves more efficiently than the device with a lower coupling coefficient. Thin-film acoustic wave devices have been used in the medical industry for the detection of viruses, bacteria and cells [149]. *ZnO* and *AlN* have higher acoustic velocity as compared to $LiNbO_3$ that helps in different sensing applications [150] hence why they are widely used as a thin-film material.

PZT has the largest electromechanical coupling co-efficient but has a low-quality factor, high energy loss and hard to fabricate [36]. Moreover, *PZT* is toxic because of excessive lead oxide that appears along the grain edges [151] and requires policies that reduce its use [152].

The mechanical properties of *AlN* are good and it can retain decent piezoelectric properties even at high temperatures between 700-1000 °C [153], [154]. The acoustic velocity for *AlN* is highest as compared to all other thin-film devices. Moreover, the dielectric properties of *AlN* are good and have higher thermal conductivity [155], [156]. However, the texture control and deposition of *AlN* films are more challenging than *ZnO* film [157]. The deposition conditions have a substantial effect on *AlN* film growth and structure. *AlN* films are good when high frequency (hundreds of MHz or GHz) *SAW* devices are required [158], [159]. Moreover, *ZnO* is suitable for devices running at a lower frequency range and for thick film SAW devices [160].

Few important parameters like electromechanical coupling co-efficient, *TCF* and the acoustic velocity of important piezoelectric materials are presented in Table 4.1.

Table 4.1: Electromechanical coupling co-efficient, *TCF* and acoustic velocity of $LiNbO_3$, *PZT*, *AlN* and *ZnO* [75], [161], [162]

SAW Device	Electromechanical coupling coefficient, k^2 (%)	*TCF* (ppm/°C)	The acoustic velocity of longitudinal waves (m/s)	Comparison
128° Cut $LiNbO_3$	5-11.3	75	3680-3980	Expensive
PZT	20-35		4500	Toxic because of excessive lead.
AlN	3.1-8	-19 to -25	10150-11050	Deposition challenging
ZnO	1.5-1.7	-40 to -60	6336	Biosafe, easy to integrate, low-frequency applications, v. high acoustic velocity

Based on the assessment parameters on the materials presented in section 2.2.7, and the comparison in Table 4.1, the following device has been selected for this study with possible reasons.

ZnO thin films can be possibly integrated with different substrates including silicon-based circuits for different *SAW*-based microfluidics applications that are promising for different LOC devices [75]. One of the advantages of *ZnO* based *SAW* devices is that the velocity and mode of acoustic waves can be changed by changing the ratio of substrate thickness and wavelength [36], [75]. Moreover, *ZnO* is believed to be bio-safe and appropriate for biomedical purposes [36]. Since this study is based on low frequency (< 60 MHz) and one of the aims is to find out the comparison of different wave modes on the kinetic and thermal mechanism, that is another reason why *ZnO* is the right choice.

4.1.2 Thin-film deposition for IDT

There are many methods available to prepare *ZnO* [163] such as physical vapour deposition (*PVD*), sputtering [164]–[167], evaporation, pulsed laser deposition (*PLD*) [168]–[170], molecular beam epitaxy (*MBE*) [171], [172], chemical vapour deposition (*CVD*) [173]–[175] and sol-gel processing [176], [177].

The choice of deposition technique depends on the quality of the film, the control of temperature, the cost and availability of the resources [36]. *PLD* requires high-power laser pulses with deposition from room temperature to 600 °C. As compared with other techniques, good crystalline structure and quality are observed with high-quality film growth with *PLD* but this process is expensive and not suitable for industrial applications [170]. *CVD* is good for bulk production, deposition temperature from 300-800 °C, quality of films produced are good, but the deposition rate is less. High temperature is a potential issue to carry out this technique [173]. On the other hand, the sol-gel technique is simple, low cost and can be completed at low temperatures but the quality of the film is poor and fewer applications for acoustic waves based device fabrication [176].

Direct current (*DC*) and *RF* magnetron sputtering are mostly used because of low deposition temperature (*ZnO* film with temperature 300 °C). Moreover, it is compatible with microelectromechanical systems (*MEMS*), high deposition rate and this technique can be used on a large scale [176]. Therefore, in this study, *DC* magnetron sputtering has been used because of its simplicity, low cost, less deposition temperature.

ZnO thin film with a thickness ≈5 µm has been deposited on aluminium (*Al*) plate substrate with thickness 600 µm and 200 µm using a *DC* magnetron sputtering from zinc (*Zn*) target at power of 430 W and Ar/O_2 (10 *SCCM*/15 *SCCM*) mixture gas. Aluminium *IDT* electrodes are fabricated using thermal evaporation and lift-off processes on the top of the *ZnO* film. The devices used in this study consists of 50 finger pairs of electrodes with an aperture of approximately 10 mm.

The schematic diagram of the *SAW IDT* device is shown in Figure 4.1 where *ZnO* thin film of 5 µm, is deposited on an *Al* plate substrate with the *IDT* patterned on the *ZnO* thin film to generate *SAWs*. The substrate with different thicknesses has been used in this study those are discussed in section 4.3.4.

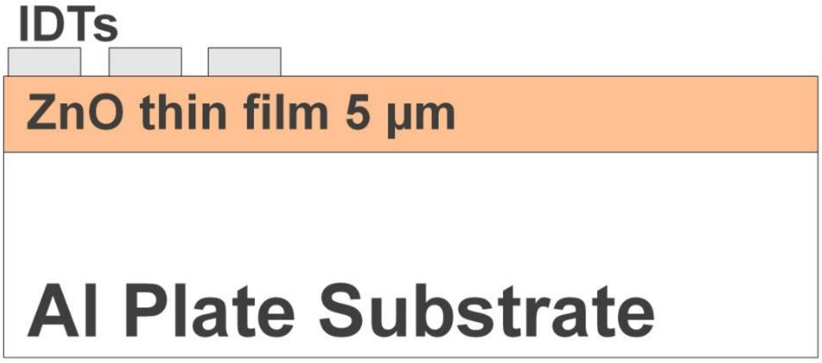

Figure 4.1: Device specifications with *Al* electrodes as *IDT*s, *ZnO* thin film of thickness 5 µm and *Al* plate substrate.

4.2 The design of the system to detecting the data for model analysis

As discussed in the previous chapter, the experimental data is required to implement the mass, momentum and energy conservation models to understand thermal and kinetic coupling impacts of *SAW* on the droplet. Therefore, in this section, the strategy has been discussed to collect the data for these models.

4.2.1 The data for mass and momentum models

From the model equations (3.1 to 3.12), mass and velocity of the droplet can be measured directly or indirectly. In terms of mass, it can be measured by detecting the droplet volume and the density of the fluid which may change with the change in temperature of the droplet. Therefore, the temperature measured for thermal impact can also be helpful to measure the volume. The *CCD* camera with a resolution suitable for the microfluidics is a good option for volume detection. Meanwhile, this camera can also be used to detect the velocity of the droplet [178], [179].

4.2.2 The data for the energy model

The temperature distribution inside the droplet is necessary for the energy model to predict the heat fluxes and kinetic energies. The temperature of the droplet can be measured by both thermal sensors (thermocouples) [180] and infrared (*IR*) cameras [181]–[183]. Thermal data measured by the latter technique is called infrared thermography (*IRT*) [184].

No suitable conventional thermal sensor (thermocouple), so far, can be applied to measure the temperature distribution inside the droplet with a droplet size (diameter) of 5.0 mm. However, *IRT* is a non-contact sensing technique, non-invasive and one can get two-dimensional thermal images with temperature distribution inside the droplet which can not be obtained by thermal sensors. Therefore, in this study, *IR* thermal camera has been used, detail of which is in section 4.5.2. It has been noticed, however, that the temperature measured by the infrared camera is the surface temperature of the droplet. The high-resolution, infrared camera is quite expensive but can provide the temperature distribution on the droplet surface. Therefore, assumptions are made to get precise temperature distribution using the data from the analysis models, the details are available in section 4.4 and Figure 3.3.

For the kinetic energy inside the droplet, particle image velocimetry (*PIV*) is employed, which has been widely used in the studies of microfluidics [185]. The *CCD* camera required for mass and momentum analysis can be used to record the images of particles.

4.3 The experimental setup

The schematic diagram of the complete experimental setup is shown in Figure 4.2 with a *CCD* camera, an IR thermal camera, a light source and a water droplet placed on the *IDT*. Both cameras are used to get the side view of the droplet separately. The light source is used to illuminate the droplet to help in visualisation.

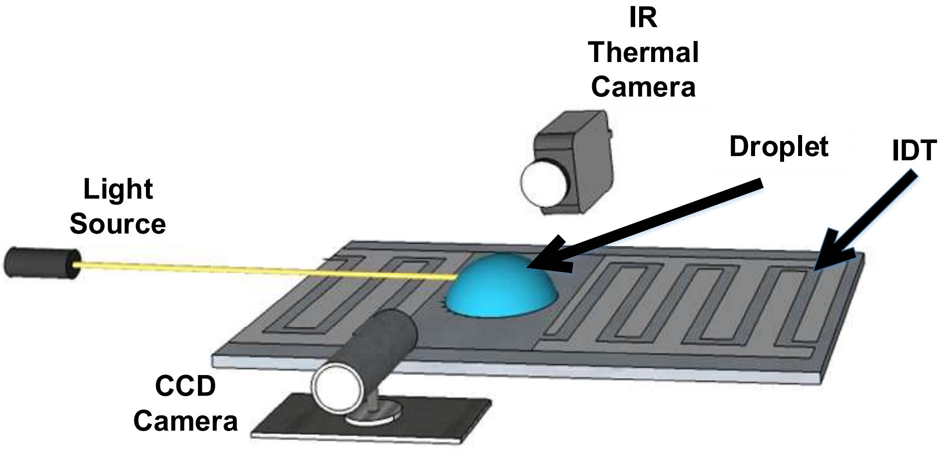

Figure 4.2: Schematic diagram of the experimental setup with the IR thermal camera, *CCD* camera, a lighting source, water droplet placed on the *IDT*.

4.3.1 Equipment required to generate SAW

Basic equipment to generate, and amplify the signal is shown in Figure 4.3 whereas, a block diagram explaining the working of the experimental setup is shown in Figure 4.4. The signal was generated using an *RF* signal generator (Marconi Instruments 2024) which was then amplified using a power amplifier (Amplifier Research 75A250) as shown in Figure 4.3-a and b respectively. Values from the power amplifier (dBm) were calibrated by using an *RF* power meter Racal 9104 (Figure 4.3-c) in Watts. It was used to measure the *RF* power applied to the *IDT*. 25 µl of deionized (*DI*) water droplet was placed with the help of a micropipette on the surface of the substrate at the distance of ≈2.5 mm in front of the *IDT*. *SAW* powers were given to the *IDT* in the range of 0.30 to 4.0 W.

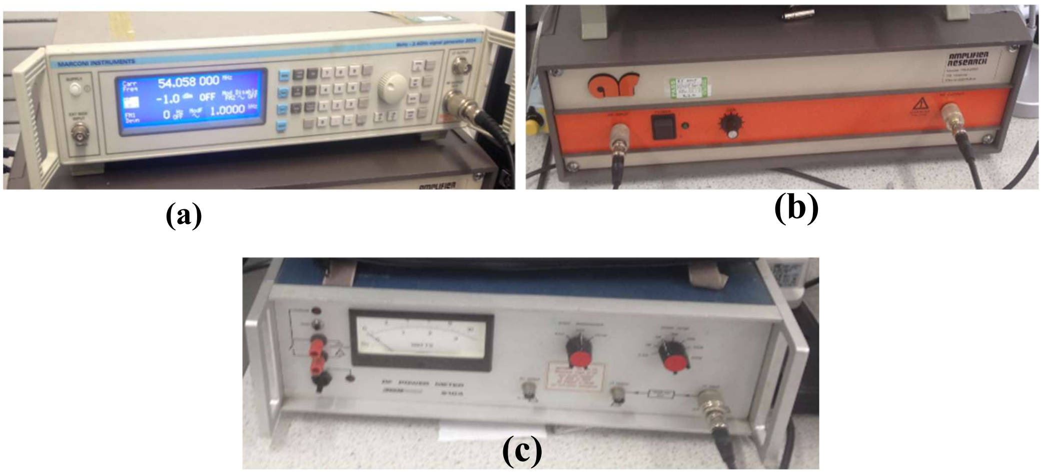
(a) (b) (c)

Figure 4.3: Equipment to generate and amplify signals (a) Signal generator to generate electrical signals (b) Power amplifier to amplify the signals (c) Power meter to measure input in watts.

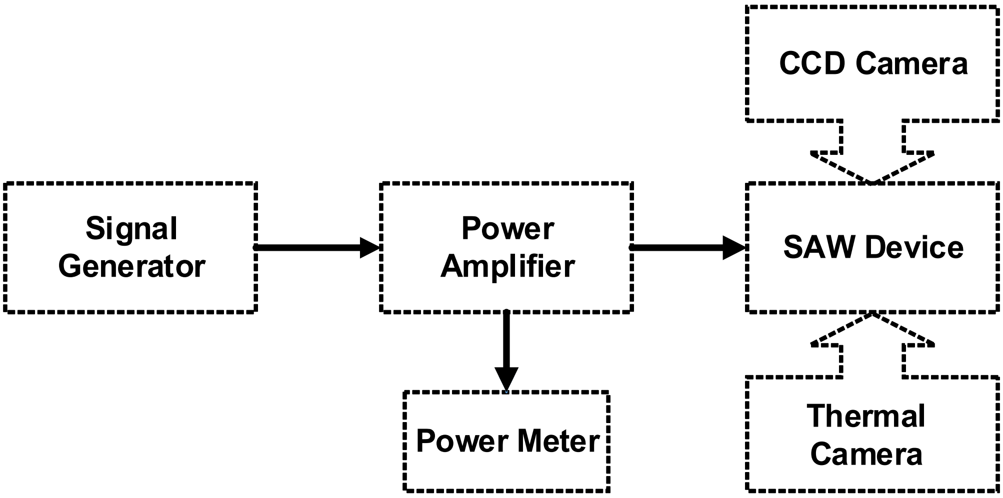

Figure 4.4: Flow chart for working of the experimental setup. Signal generator, power amplifier, power meter, a *SAW* device. A side view image is captured by *CCD* and *IR* thermal camera.

4.3.2 Identification of resonant frequency of the device

The resonant frequency of the *SAW* device was measured by the vector network analyser (Agilent 8712ET). Figure 4.5 shows the network analyser which has a bandwidth from 300 kHz to 1200 MHz. The network analyser can measure both the transmission and reflection coefficient, S_{12}/S_{21} and S_{11}/S_{22}, respectively. Transmission coefficients are measured for a pair of *IDT*s to determine the insertion loss of the component, while reflection coefficients are used for a single *IDT* to determine its resonant frequency and bandwidth. The signal is given to the device then the analyser measures both the signal reflected from the input side and that passed from the output side. It then compares both signals, evaluates the resulting signal and compares it with the injected input signal. Finally, the results are processed by *PC* and the final signal is displayed on the screen. The signal with minimum insertion loss is the desired signal with a maximum amplitude [186]. Since in S_{21}, waves generated and travel to the droplet from both sides, the droplet is pushed up from both sides by the opposing waves, causing the droplet to break up and form smaller droplets called as jetting [38]. Since this work is limited to streaming without aiming jetting/nebulization, therefore, the author used S_{11} to determine the working frequency of the device.

After connecting the device to the network analyser, the sharp peak shows the resonant and harmonic frequencies of the device. At the resonant frequency, signal and insertion loss is minimum with maximum acoustic velocity travelled on the device. The first peak from left on the spectrum indicates the fundamental frequency (f_0) of the device.

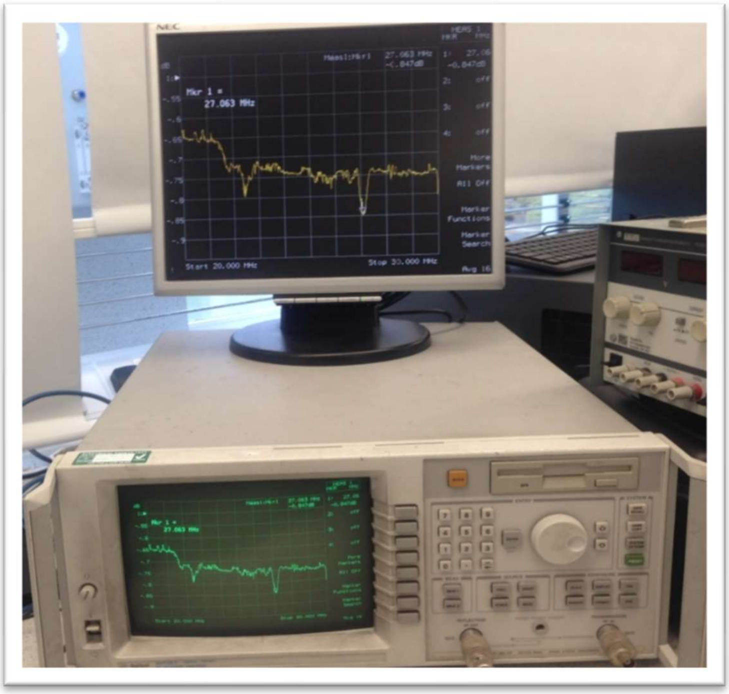

Figure 4.5 The network analyser to identify the resonant frequencies of the device.

4.3.3 *Surface treatment of the device*

The device with *ZnO* normally has a hydrophilic surface with a contact angle of water droplet between 40°-80° [36]. The surface condition of the device decides the contact angle [187]. The contact angle can be increased by increasing the *ZnO* film thickness that increases the surface roughness. With the increase in contact angle, droplet streaming, pumping and deformation can be easily visualised [45]. The difference between hydrophilic and hydrophobic surface is shown in Figure 4.6. It is clear from Figure 4.6-a and b that the contact angle for the hydrophilic surface is less than 70º whereas the contact angle for the hydrophobic surface is more than 90º.

There are different methods to make the surface hydrophobic like *TEFLON* solutions, cyclic transport optical polymer (*CYTOP*) layer, Octadecyltrichlorosilane (*OTS*), a layer of octadecyl thiol (*ODT*) or octadecyl silane (*ODS*), hydrophobic nanostructures or microwave plasma-enhanced chemical vapour deposition (*MPECVD*) [36], [188], [189]. Amongst all these, *CYTOP* is easily available and require less proficiency. Therefore, in this study, the *ZnO* surface is coated with 200 nm *CYTOP* (Asahi Glass Co., Ltd., Tokyo, Japan) to make the surface hydrophobic.

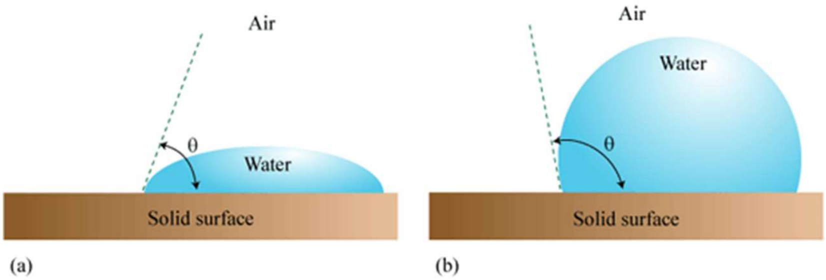

Figure 4.6: Droplet on the solid surface with (a) hydrophilic when the contact angle less than 70° and (b) hydrophobic surface after the treatment when the contact angle more than 90°.

4.3.4 Detail of SAW devices for this study

The description of the devices used in this study is shown in Table 4.2. For the first two devices, it is clear from Table 4.2, with the change in thickness of the device/substrate and by keeping the wavelength the same, resonant, second-order harmonic frequencies and wave mode remain similar. However, resonant frequency changes by changing the wavelength of the waves.

Devices mentioned in Table 4.2 are shown in Figure 4.7. Two and three *IDT* pairs are shown in Figure 4.7-a & b respectively but only one pair of *IDT* has been used. The selection of the pair depends on getting a sharp peak when connected to the network analyser.

Table 4.2: Summaries of devices with the detail of wavelength of the waves, thickness of the substrate, resonant frequencies and wave mode of the waves.

ZnO thickness (μm)	Wavelength λ (μm)	Al plate thickness h (μm)	Resonant frequency f_0 (MHz)	Wave mode	Second harmonic frequency (MHz)	Wave mode
5	100	200	27.063	Rayleigh	54.00	Sezawa
5	100	600	26.305	Rayleigh	52.220	Sezawa
5	200	200	13.500	Hybrid	15.680	No peak

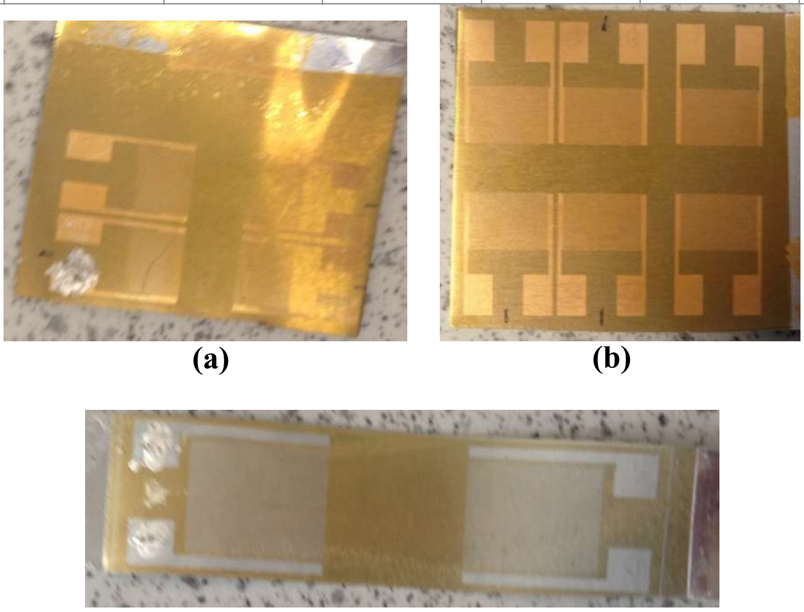
(a) **(b)**

(c)

Figure 4.7: Aluminum plate with different thicknesses (a) h=600 μm, λ= 100 μm, (b) h= 200 μm, λ= 200 μm (c) h= 200 μm, λ= 100 μm.

4.4 Method to measure the mass transfer of the droplet

Experimental equipment and devices used in this study are already discussed in the above sections. However, it is important to discuss a method to measure the mass transfer of the droplet. As discussed in Chapter 3, a mass transfer can take place either by evaporation or with phase change. However, the temperature of the droplet is much lower than the saturation temperature, more detail in section 5.4.1. Therefore, no phase change occurs inside the droplet. However, mass transfer due to evaporation can be detected by a change in the size and the density of the droplet. If there is a significant change in the size of the droplet, then there is a mass transfer [190]. The images shown in Figure 4.8 illustrates how the volume is calculated by two parameters of the length (a) and height (b) detected using both *IR* and *CCD* camera.

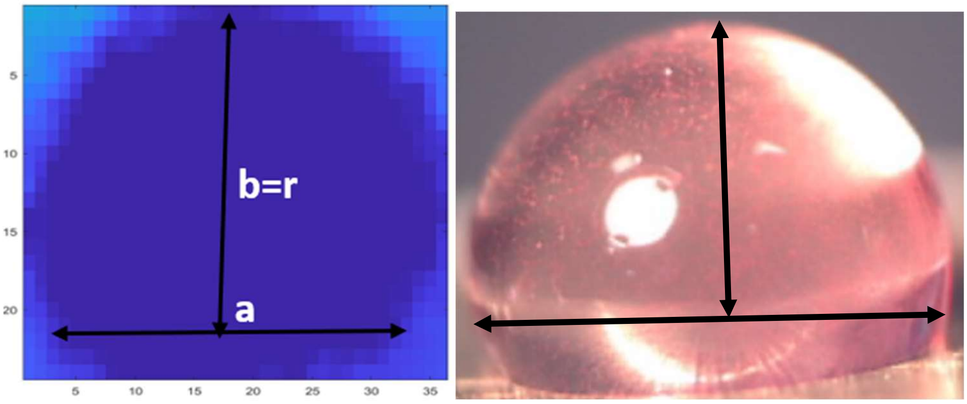

Figure 4.8: Measurement of length and height of the droplet (a) using *IR* camera (b) using the *CCD* camera.

Changes in the mass of the droplet can be calculated using equations (4.1) and (4.2), given below;

$$\frac{dm}{dt} = \frac{d}{dt}(\rho V_d) = \rho \frac{dV_d}{dt} + V_d \frac{d\rho}{dt} \tag{4.1}$$

$$\frac{d\rho}{dt} = \frac{d\rho}{dT}\frac{dT}{dt} \tag{4.2}$$

The volume of the droplet, V_{d}, can be found by considering the droplet as half-spherical whereas length (a) and height (b) of the droplet can be measured using "*imageJ*". ImageJ is a Java-written program, used for many imaging applications, easy to use and has a huge and knowledgeable user community [191]. The detail of mass transfer using Rayleigh and Sezawa waves can be found in Chapter 5 and Chapter 6 respectively.

4.5 Method to measure the velocity and temperature distribution

To implement the energy conservation principle, it is important to get temperature distribution and velocity of the particles. The methods and tools required to find these parameters have been presented here in this section.

4.5.1 Measurement of velocity of particles using PIV

A *CCD* camera (imaging source DFK 22BUC03) with a resolution 720*480 pixels is used to capture the kinetic impacts of the *SAW*. To visualise the streaming, 10 µm red polystyrene particles were added into the water droplet. The camera is shown in Figure 4.9-a and the configuration of the device, droplet and the light source is shown in Figure 4.9-b.

(a)

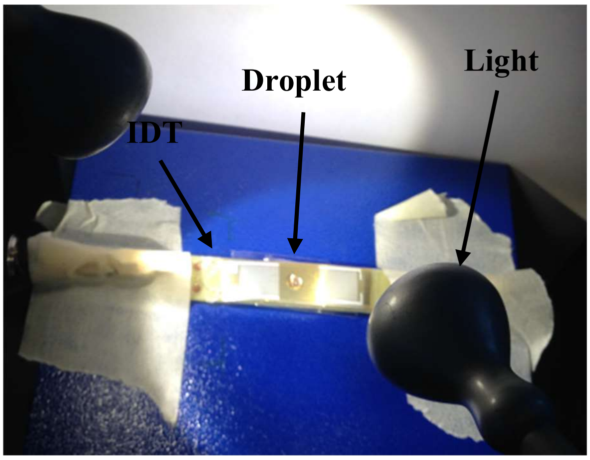

(b)

Figure 4.9 (a) *CCD* video camera (b) Configuration to capture videos with the camera.

A tool called ‘tracker’ has been used to implement *PIV* to measure the velocity of particles inside the droplet. By tracking the movement of the particles from one frame to another, the velocity of particles can be calculated. A frame is a unit of a video camera in which it saves and collects the data. Frame per second (fps) is the speed of the camera in which it collects data (30 fps in this case). The velocity of particles can be different in different locations of the droplet.

To understand the coupling mechanism of kinetic and thermal impact, the velocities of the particles at three positions are considered, as shown in Figure 4.10. The velocity data of those three positions are used for calculations of kinetic energies inside the droplet. Meanwhile, the positions are designed to estimate bottom fraction energy, position 1 (U_1, mm/s), helps to find the heat flux between device/substrate and droplet. However, position 2 (U_2, mm/s) helps to predict the heat flux to the air, and the vortex velocities, position 3 (U_3, mm/s) helps to find overall kinetic energy inside the droplet. All positions are shown in Figure 4.10. Vortex velocity is the velocity where vortices are visible, and it is either in the middle of the droplet or in the right corner. Furthermore, values of streaming velocities used to associate the data with the temperature values to find the heat transfers from the substrate to the droplet, from droplet to the air, and to find kinetic energy inside the droplet. The small numbers shown at three different locations of the droplet in Figure 4.10 represents frame numbers. For instance, position 1 tracks particles from 263 to 265 frames, 276 to 278 for position 2 and 274 to 278 for tracking at position 3. The tool “*tracker*” measures the distance travelled by each particle from one frame to another in both x and y-direction. This data can be used to calculate the velocity of particles by equation (4.3),

$$U = \sqrt{\left(\frac{\Delta x}{\Delta t}\right)^2 + \left(\frac{\Delta y}{\Delta t}\right)^2} \tag{4.3}$$

The results form this equation give the value in pixel/s, that can be converted to millimetre (mm) using “*imageJ*”, where one pixel equals to 0.009264 mm. The velocities of particles can be different at the start of applying input power, in the middle and the end, that is why ten different time frames have been selected from the start of the *SAW* power to the end. The times are (0.65, 2.5, 5.0, 6.84, 9.50, 11.50, 16.84, 19.0, 23.0, 30, 36 and 43) seconds.

The calculations required to find the coupling mechanism between the streaming and thermal part is discussed in the following sections.

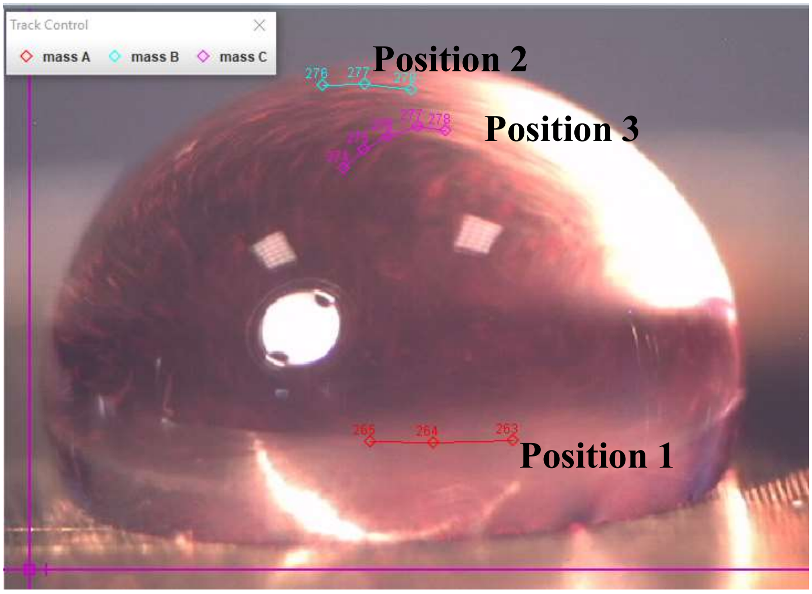

Figure 4.10: Image from the tracker showing three different positions inside the droplet: Position 1 close to the substrate, position 2 on the top of the droplet and position 3 is where vortices generate.

4.5.2 Analysis of the thermal impacts

The surface temperature of the droplet and the device is measured and recorded using an infrared thermal camera (FLIR T-620) with a resolution of 480×640 pixels and speed of 30 fps. The configuration of the thermal camera capturing the side view of the device without droplet is shown in Figure 4.11, where the device is fixed on the printed circuit board (*PCB*) and connected to the signal generator through wires. Figure 4.11 is showing the temperature of the device without applying *SAW* input power.

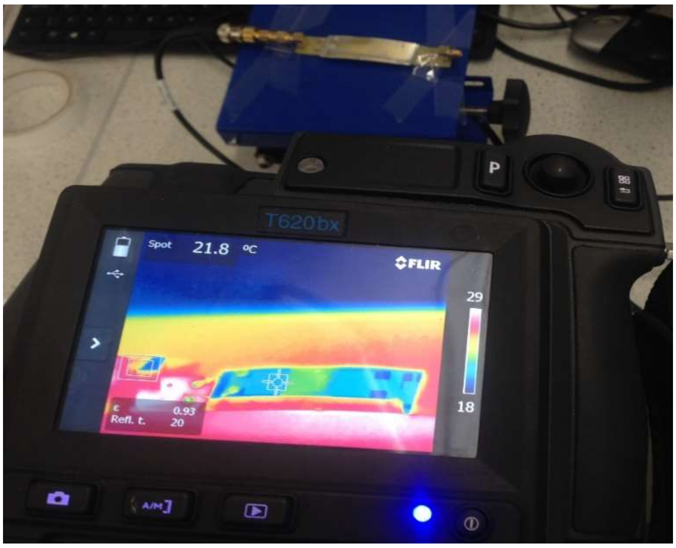

Figure 4.11: FLIR thermal camera (T-620) with a side view of the device fixed on a printed circuit board (*PCB*).

The side-view thermal image of the droplet without applying *SAW* is shown in Figure 4.12. It is clear from Figure 4.12-a that the frame has the dimension of 480*640 that contains a lot of background information other than the droplet. To get only the droplet image, the whole frame needs to cut into the section where the droplet is zoomed and only visible as shown in Figure 4.12-b. The zoomed image of the droplet has a matrix size of 28 rows and 40 columns. Therefore a frame of 480*640 is converted to 28*40 using MATLAB code developed by the author.

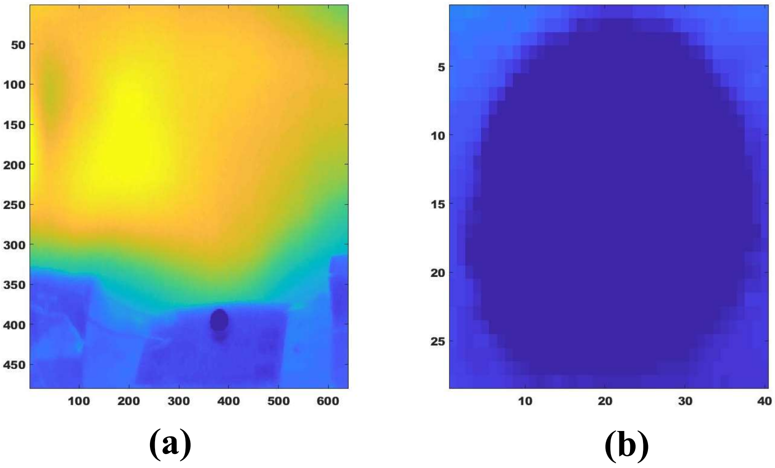

Figure 4.12: Side View image from the thermal camera (a) Whole frame 480*640 matrix (b) Zoomed and cut image of the droplet with dimension 28*40 with the help of MATLAB.

4.5.3 Temperature data treatments

Video images from FLIR T-620 converted to comma-separated values (*CSV*) file using FLIR tools package. This file is readable in Microsoft excel that contains data for each frame in the form of rows and columns. Since already discussed, each frame has 480 rows and 640 columns and the camera capture 30 fps, so, for instance, 30.0 s video contains 432000 rows and 640 columns. The data can be read by MATLAB and the code is made to divide the droplet (28*40 matrix) further into 16 elements and read each element's temperature data frame by frame. The temperature distribution treated by MATLAB code is presented in Figure 4.13 (refer to the appendix A for MATLAB code detail), where the results have been taken from Rayleigh at 26.300 MHz at 2.0 W. Figure 4.13-a presents a spectrum of the whole droplet being divided into four layers with four elements in each row. This treatment is made for the recorded videos to finally obtain the temperature data for each element and the temperature distribution. The data then analysed and demonstrated against time at selected P_{in}.

The assumption that considers the droplet surface temperature as the temperature of the fluid of the segment, is one of the 'big' assumptions that have to be made in this study for analysing the data by the infrared camera.

This means that the temperature is uniform at the direction perpendicular to the *IR* camera's surface and equal to the surface temperature. The row of the elements, as shown in Figure 4.13-a, is called a 'layer', for instance, the bottom layer includes the elements of number 13 to 16, and the top layer includes the elements of number 1 to 4, respectively. Figure 4.13-a represents results before SAW input power whereas Figure 4.13-b, c and d after 5.0, 10.0 and 15.0 s of *SAW* acting time respectively.

The colour in each element shown in Figure 4.13 is associated with the temperature of each element. It is clear from Figure 4.13 that as soon as *SAW* penetrates inside the droplet, it increases the temperature at the corner of the droplet from the left side (Figure 4.13-b), where the *SAW* transfers. Therefore, the first column on the left has a higher temperature as compared to other portions of the droplet. It is evident from Figure 4.13-c that the heating from the bottom to droplet becomes stable after 10.0 s of the input *SAW*. The heating from the bottom and the convection of the heat from the *SAW* radiation source at the left corner make the temperature on the bottom layer higher than those of other layers (Figure 4.13-c). The top right portion of the droplet is still not heated well, as shown in Figure 4.13-c clearly from the colour of the element compared with the temperature bar. However, in Figure 4.13-d all the elements have a certain temperature rise with maximum temperature on the bottom layer and minimum on the top layer after 15.0 s of input *SAW*. The details of heat transportations inside the droplet and further data treatment are discussed in the following results chapters.

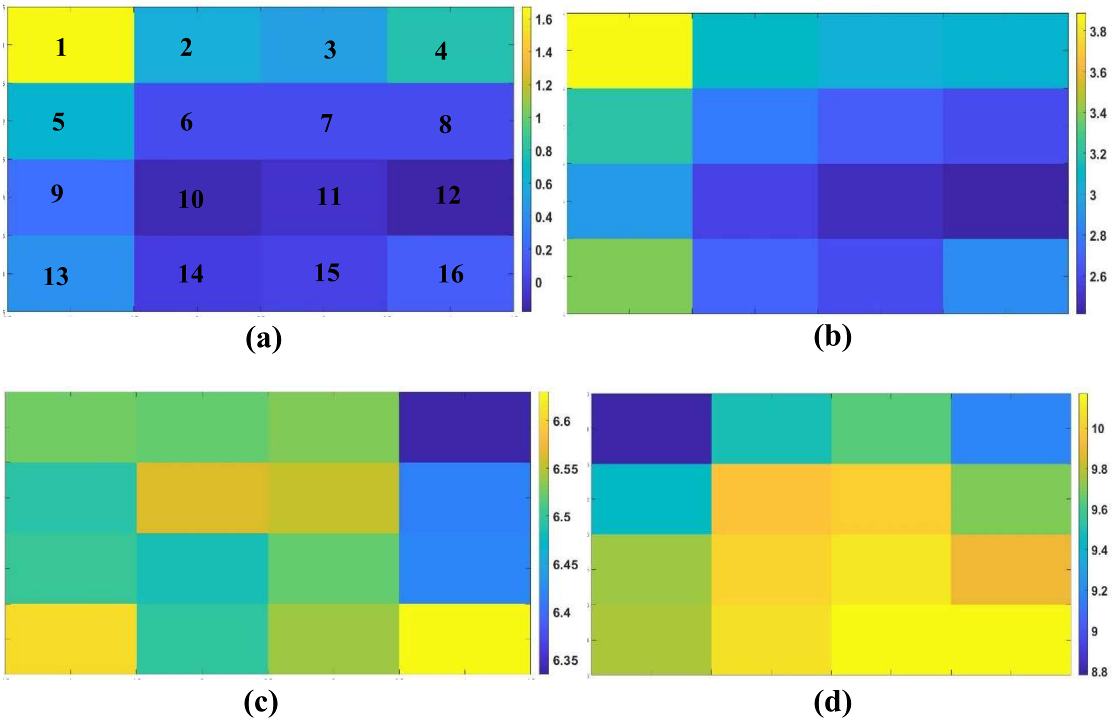

(a) **(b)**

(c) **(d)**

Figure 4.13: Four layers of droplet showing 16 elements, MATLAB treated with temperature distribution at 2.0 W Rayleigh waves (a) 0.0 s (b) 5.0 s (c) 10.0 s (d) 15.0 s. The number of elements is showing in (a) from 1 to 16.

The temperature rise (final minus initial temperature) of each element against time is illustrated in Figure 4.14 where it also demonstrates how the methods of the data treatment work. These results are with *SAW* input power of 2.0 W, Rayleigh waves at the resonant frequency of 26.300 MHz.

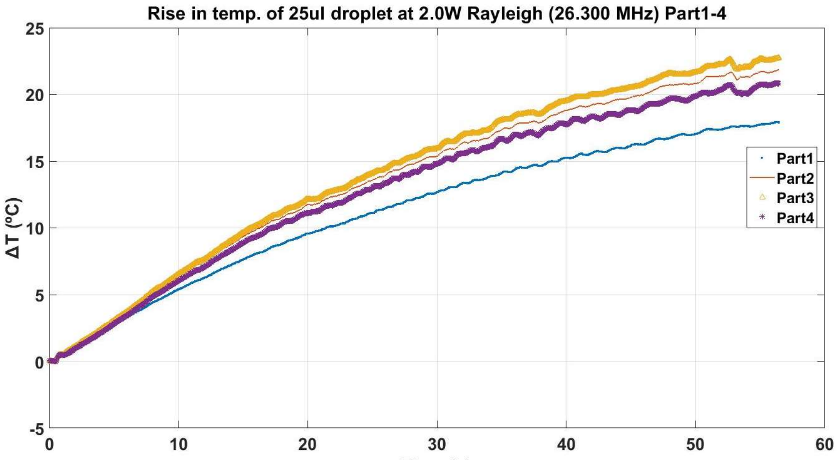
Rise in temp. of 25ul droplet at 2.0W Rayleigh (26.300 MHz) Part1-4
ΔT (ºC)
Time (s)
25
20
15
10
5
0
-5
0
10
20
30
40
50
60
Part1
Part2
Part3
Part4

(a)

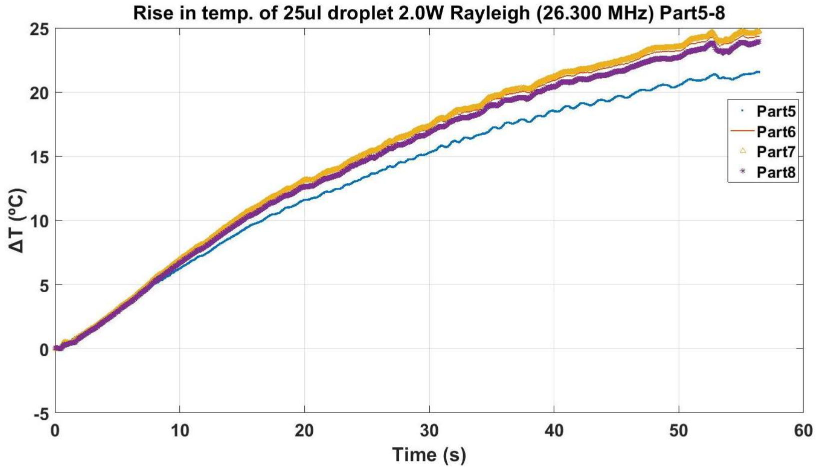
Rise in temp. of 25ul droplet 2.0W Rayleigh (26.300 MHz) Part5-8
ΔT (ºC)
Time (s)
25
20
15
10
5
0
-5
0
10
20
30
40
50
60
Part5
Part6
Part7
Part8

(b)

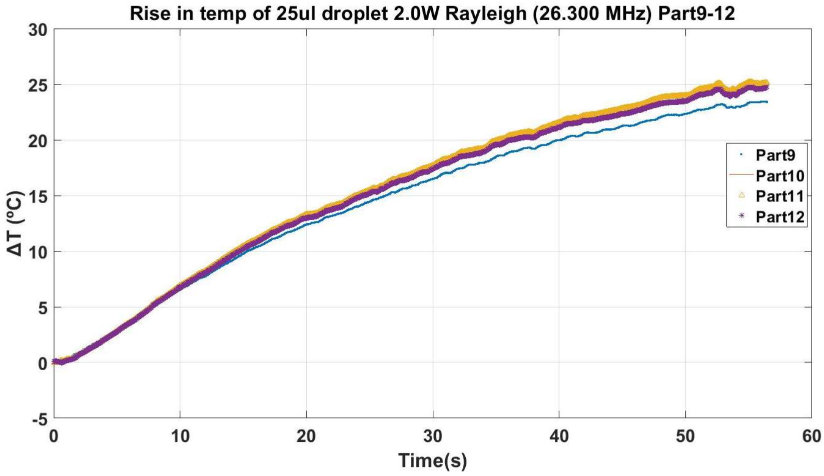
Rise in temp of 25ul droplet 2.0W Rayleigh (26.300 MHz) Part9-12
ΔT (ºC)
Time(s)
30
25
20
15
10
5
0
-5
0
10
20
30
40
50
60
Part9
Part10
Part11
Part12

(c)

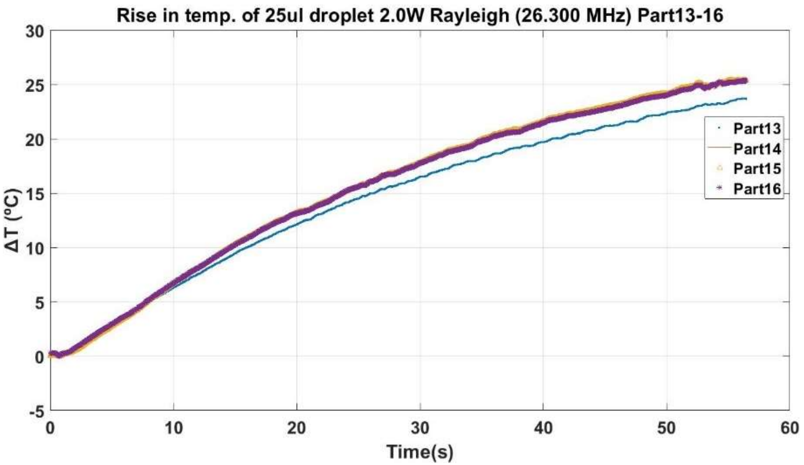

(d)

Figure 4.14: Rise in temperature of each element of the droplet using Rayleigh waves at 26.300 MHz for Rayleigh with power of 2.0 W (a) Elements 1-4 (b) Elements 5-8 (c) Elements 9-12 (d) Elements 13-16.

4.5.4 Coupling of thermal and kinetic impacts

Association of kinetics with the thermal change inside the droplet is made by following the same position for both. For example, U_1, the velocity of particles close to the substrate, is associated with the average temperature of 13-16 elements of the droplet. U_2, velocity on the top of the droplet, is associated with all the elements, that have direct interaction with the air (number 1,2,3,4,5,8,9,12,13 and 16). Figure 4.15 illustrates the coupling of the streaming and thermal part. The red oval shape shows the temperature of these elements, added up to associate with U_2 (see Figure 4.15-a). However, black oval shows the temperature associated with U_1. By using different co-relations discussed in section 4.5.6, different heat transfer mechanisms inside the droplet and kinetics involving friction and momentum are found. Finally, radiation heat transfer ($\dot{Q}_r$), because of *SAW* entering from edge of the droplet is calculated.

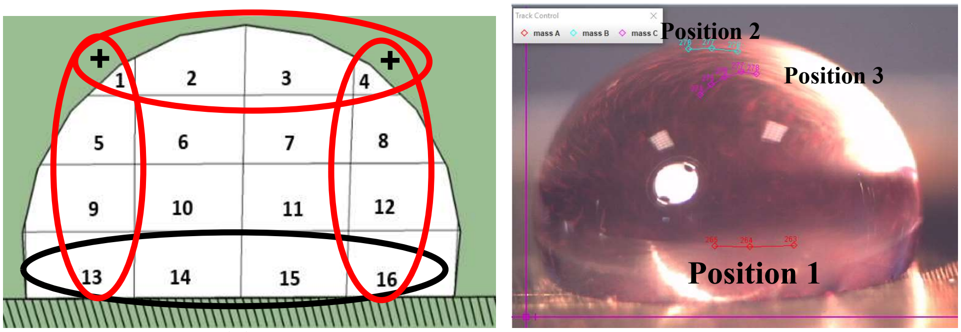

(a) **(b)**

Figure 4.15: Coupling of streaming and thermal part (a) thermal part showing 16 elements with ovals to represent the element's temperature for $\dot{Q}_s$ and $\dot{Q}_a$ (b) streaming image from the tracker, tracking of particles at three different positions.

4.5.5 Calculation of the average temperature of the whole droplet

There are methods to estimate the thermal/internal energy of the droplet using the data taken from the infrared camera. It is unacceptable to calculate average T_d by simply taking the mean average, the sum of the values of temperature divided by the total number of elements. The volume of each layer of the droplet is different. As the droplet is hydrophobic, therefore, the bottom layer is flat having more fluid and the top layer less. Therefore, the volume average is considered for calculating average T_d using equation (4.4) since variation in the density of the fluid is relatively small,

$$\mathrm{T}_d = \sum_{i=1}^{16} \frac{V_i}{V_d} \; T_i \tag{4.4}$$

where the volume ratio of $V_\mathrm{i}/V_\mathrm{d}$ of each element can be calculated by considering the droplet as a half-spherical. Because of the same size of the element on each layer, equation (4.4) becomes,

$$\mathrm{T}_d = \sum_{L=1}^{4} \frac{V_L}{V_d} \; T_L \tag{4.5}$$

where, T_L is a simple mean temperature of the layer, $\mathrm{T}_\mathrm{L} = (\sum_{i=1}^{4} T_{i,L}\ )/4$ and V_L is the volume of the layer 'L' (L=1,2,3,4 from top to bottom) and can be calculated when the droplet is considered as a half-sphere. V_L and the volume ratio of the segment can be calculated by equations (4.6) and (4.7),

$$\mathrm{V_L} = \frac{\pi}{6} h^3 (3 \left(\frac{2r_L}{h_L}\right) - 2) \tag{4.6}$$

$$\frac{V_L}{V_d} = \left(\frac{h_L}{h}\right)^3 \frac{3\left(\frac{r_L}{h_L}\right) - 2}{3\left(\frac{r}{h}\right) - 2} \tag{4.7}$$

Where 'h' is the total height and 'r' is the maximum radius of the droplet, 'h_L' and 'r_L' are the height and the radius of each layer, assuming the top layer of the droplet as segment one and the bottom layer as segment four, where height is maximum. The volume ratio of each of the droplet layer is calculated as;

$$\left(\frac{V_1}{V}\right) = 0.1086905$$

$$\left(\frac{V_2}{V}\right) = 0.2644842$$

$$\left(\frac{V_3}{V}\right) = 0.3278968$$

$$\left(\frac{V_4}{V}\right) = 0.2989284$$

The average temperatures for each layer can be calculated using equations (4.8) to (4.11);

$$T_{L1} = \frac{T_1 + T_2 + T_3 + T_4}{4} \times 0.1086905 \tag{4.8}$$

$$T_{L2} = \frac{T_5 + T_6 + T_7 + T_8}{4} \times 0.2644842 \tag{4.9}$$

$$T_{L3} = \frac{T_9 + T_{10} + T_{11} + T_{12}}{4} \times 0.3278968 \tag{4.10}$$

$$T_{L4} = \frac{T_{13} + T_{14} + T_{15} + T_{16}}{4} * 0.2989284 \tag{4.11}$$

Then the average temperature of the whole droplet calculated using equation (4.12);

$$T_d = T_{L1} + T_{L2} + T_{L3} + T_{L4} \tag{4.12}$$

4.5.6 *Implementing energy conservation to our model*

Based on the model presented in Figure 3.3, implementing the energy (power) conservation principle, thermal interactions to be balanced by the changes in enthalpies and the kinetic energies of the droplet by neglecting the potential energy. This can be expressed as in equation (4.13);

$$\dot{Q}_r + \dot{Q}_s + \dot{Q}_a + \dot{W} = \dot{E}_d + \dot{K}_{st.} + \dot{K}_f \tag{4.13}$$

where, $\dot{Q}$ (W) is the power sources or sinks due to heat interactions, $\dot{W}$ is the mechanical power due to the changes in the droplet volume against the pressure. $\dot{E}_d$ (W) the power to heat the fluid in the increase of enthalpy, and $\dot{K}$ (W) mechanical (kinetic) powers. In equation (4.13), subscripts r, s, a, d, *st.* and *f*, refer to the radiation, substrate, air, droplet, streaming, and friction, respectively. The power heating the droplet can be calculated by the changes in enthalpy as shown in equation (4.14) below;

$$\dot{E}_d = \rho_d V_d C_p \frac{dT_d}{dt} \tag{4.14}$$

where ρ_d, the density (kg/m^3), V_d, the volume (m^3), C_p the heat capacity (J/kg.K) and T_d (K), the temperature of the water droplet. The rate of heat transfer from substrate to the droplet and from droplet to the air can be calculated by equation (4.15);

$$\dot{Q}_\varphi = A_\varphi \, \alpha_\varphi \left(T_\varphi - T_{d,\varphi}\right) \tag{4.15}$$

$T_{d,\varphi}$ is the droplet temperature at the layer close to the substrate, $\varphi = s$, or air, $\varphi = a$, with the interfacial area, A_φ (m^2). Some dimensionless numbers can help to find the coupling between kinetics (streaming) and heat transfer (thermal impacts) inside the droplet [192]. Nusselt number, *Nu,* depicts the heat transfer of a fluid which can be related to Reynold's number (*Re)* for streaming. A general formula to find co-relation between *Nu* and *Re* for the droplet is shown in equation (4.16) below [193];

$$Nu = \frac{\alpha_s * L}{k} = 2 + \beta_c * Re^{\frac{1}{2}} * Pr^{\frac{1}{3}} \tag{4.16}$$

where α is an effective convection heat transfer coefficient, L is the characteristic length, k is the thermal conductivity, β_c is a constant, which from experimental observation is found to be 0.6 [194]. *Pr* is Prandtl number whose value for water at room temperature is 7.56 [195]. α_s can be calculated from equation (4.16) which then plugged in equation (4.15) to find heat transfers ($\dot{Q}_s$).

4.5.6.1 *Convection heat transfer mechanism between droplet and air*

Since the T_d is more than the surrounding air which is stationary, so natural convection will take place near the droplet. Grashof number (Gr_L) is analogous to *Re* which represents flow regime in natural convection and is calculated by using equation (4.17) [195];

$$G_r = \frac{g\beta(T_d - T_\infty)L^3}{\nu^2} \tag{4.17}$$

where g is the acceleration due to gravity, β is the coefficient of thermal expansion which is $1/T_\infty$ for an ideal gas as the air. T_d is the droplet temperature, T_∞ is the air temperature, L is the diameter of the droplet, and ν is the kinematic viscosity of the air. Correlations between G_r and Nu can be found using equation (4.18) given below [196];

$$Nu = \frac{\alpha_a * L}{k} = 2.65 * (G_r * P_r)^{1/8} \tag{4.18}$$

Effective heat transfer coefficient (α_a) can be predicted using equations (4.18) and (4.17) which helps to find ($\dot{Q}_a$) from equation (4.15). The calculated values of α_s and α_a are given in section 5.4.4 and 6.4.4 for both Rayleigh and Sezawa waves respectively.

By plugging in all the values of heat transfer and kinetic powers in equation (4.13), the power radiated to the droplet by *SAW*, $\dot{Q}_r$, can be calculated. Therefore, the coupling mechanisms of thermal and kinetic (fluid streaming) can be identified.

4.5.6.2 *The kinetics inside the droplet*

The kinetic power because of streaming can be predicted using equation (4.20) whereas kinetic power because of friction near the bottom of the droplet can be calculated either using equation (4.21) or (4.19);

$$\dot{K_{st}} = \rho_d V_d u_d \frac{du_d}{dt} \tag{4.20}$$

$$\dot{K_f} = A_s \mu_d \frac{du_f}{dy} u_f \tag{4.21}$$

Or

$$\dot{K_f} = F_f U_x = \left(0.5 C_f A_f \rho_d U_x^2\right) U_x \tag{4.22}$$

$\dot{K_{st}}$ and $\dot{K_f}$ represents the rate of kinetic and frictional energy (W) caused by streaming and frictional shear force respectively as shown in Figure 3.3. The average streaming velocity of droplet fluids u_d (mm/s) is used for the kinetic energy estimations. However, horizontal velocities u_f (mm/s) of the fluid close to the *IDT* surface are taken for calculation of velocity gradients near the substrate. A_s represents the surface area and μ_d dynamic viscosity (N.s/m^2) of the droplet. The effects of temperature on dynamic viscosity are considered, which leads to an increase in dynamic viscosity from 25 °C to 50 °C within the range of this study [195]. C_f is the friction coefficient, A_f is the effective area of the droplet, ρ_d is the density of the droplet and U_x is the streaming velocity near the bottom of the droplet. The detail description of these equations can be found in section 5.3 and 6.3.

The acceleration of the fluid for kinetic power can be calculated by taking the average velocities as shown in equation (4.23);

$$\frac{du_d}{dt} = \frac{1}{3} \sum_{i=1}^{3} \frac{\left(u_i(t_2) - u_i(t_1)\right)}{\Delta t} \tag{4.23}$$

where u_i is the velocity of particles at positions i=1, 2 and 3, are measured from the experimental data. The velocity gradient in equation (4.21), $\frac{du_f}{dy}$, can be calculated by $\left(\frac{u_{x,x=1}-0}{\Delta y}\right)$, where u_x is the velocity component at x-direction close to the bottom, Δy is the thickness of the bottom boundary layer.

4.5.7 Challenges during data treatment

The initial temperature of each element is different which appeared as a result of analysis performed using MATLAB at different power values. For each power level, the droplet is replaced to ensure that there is no heat inside the droplet before the input is provided. However, it is observed that there is residual heat on the substrate that is transferred to the droplet before turning on the *SAW*. Therefore, to obtain accurate results for each power level, the different initial temperature has been used. Since the room temperature has not been measured before data collection, therefore, atmospheric temperature for $\dot{Q}_a$ is used as the initial T_d. The thermal camera used in this study has less resolution with the only zoom of '4x' which hinders to have a precise temperature of the droplet.

4.6 Summary

The details of the experimental setup, devices used in this study, design for the system to detect mass, momentum and energy conservation models with necessary methods and calculations are presented in this chapter. The details of piezoelectric material with fabrication techniques along with the flow chart for the experimental setup has been presented. Moreover, a methodology is introduced for measuring streaming velocities by *PIV* and thermal energy analysed by temperature distribution with the help of MATLAB. This leads to finding the coupling mechanism and way to implement conservation principles. Furthermore, how this methodology can be implemented by Rayleigh and Sezawa waves is a discussion in the following chapters.

Chapter 5: Analysis of The Impact Mechanisms of Rayleigh SAW on Microdroplet

The analysing model proposed in Chapter 3 can be applied to diagnose the impact mechanisms of *SAW* on droplet with the data obtained from the experimental work and the methodology discussed in Chapter 4. In this chapter, the model is applied to the droplet with Rayleigh waves (R-waves). The mass impacts are due to the transfer of mass by phase change and/or evaporation, both associate with the thermal impact. The momentum impact of the *SAW* on the droplet leads to the pumping of the droplet, where pumping is defined as moving or sliding of the droplet in the direction of the waves, opposite to the source *IDT*. Furthermore, the energic (or power) impact of the *SAW* on droplet can be diagnosed by energy conservation including the dynamics of heat transfer of droplet with surroundings and kinetic energy conversions inside the droplet. Heat transfer (HT) comprises of HT from the substrate to the droplet, droplet to the air, and heat radiated by *SAW* into the droplet. The kinetic energy converted from *SAW* to droplet fluid creates the fluid streaming and the friction close to the substrate.

5.1 Introduction

The results discussed in this chapter are based on the device having an *Al* plate substrate with a thickness of 600 μm and *ZnO* with thickness 5 μm. The simulation results of vibration modes for this device with a variable wavelength of the waves are shown in Figure 5.1-a whereas measured results are shown in Figure 5.1-b [197]. The device used in this study has a wavelength (λ) of 100 μm which is shown with a black line in Figure 5.1-b, where the resonant frequency and insertion loss for both R-waves and S-waves are shown. It is understandable from Figure 5.1-b that Sezawa does not have a sharp peak which leads to more insertion loss and less acoustic velocity as compared to the R-waves [197].

Different wave modes can be observed with a change in wavelength (λ) of the waves. The device with λ 100 μm has both Rayleigh at 27.90 MHz and Sezawa wave at 52.530 MHz as shown in the second column of Figure 5.1-a [197]. This chapter only discusses the results using R-waves, whereas results related to the S-waves are part of Chapter 6.

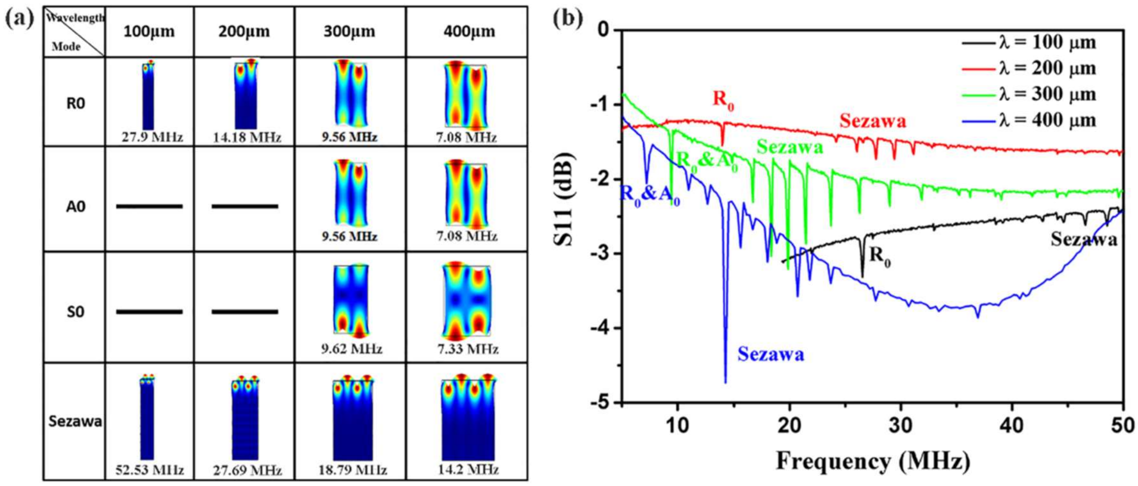

Figure 5.1: (a) Numerical simulation of vibration modes for *ZnO* (5 µm)/Al (600 µm) based *SAW* devices. The wavelength of *SAW* devices is varied from 100 µm to 400 µm. (b) The simulated and measured resonant frequencies of different types of wave modes depend on the wavelength of the *SAW* devices [197].

The empirical value of the resonant frequency may vary from the literature due to several reasons [197]. Therefore, the resonant frequency with a reflection signal measured by the network analyser is 26.300 MHz whereas the literature is showing 27.90 MHz. Since the wavelength of the waves is 100 µm, therefore, the calculated velocity of the wave is 2630 m/s (v = f*λ). The model presented in Figure 3.1, Figure 3.2 and Figure 3.3 are implemented here to validate mass, momentum and energy conservation principles.

5.2 Analysing of the mass impact of SAW on droplet using mass conservation principle.

The method used to measure mass transfer is presented in section 4.4. The volume of the droplet at two different input power values of 2.0 W and 3.2 W using Rayleigh waves is shown in Figure 5.2. It is clearly shown from the data that the change in volume of the droplet with time is not significant if the measurement errors are considered. However, at the higher input power of 3.2 W, the expansion in volume can be identified, which is due to the relative decreases in density because of the increase in temperature.

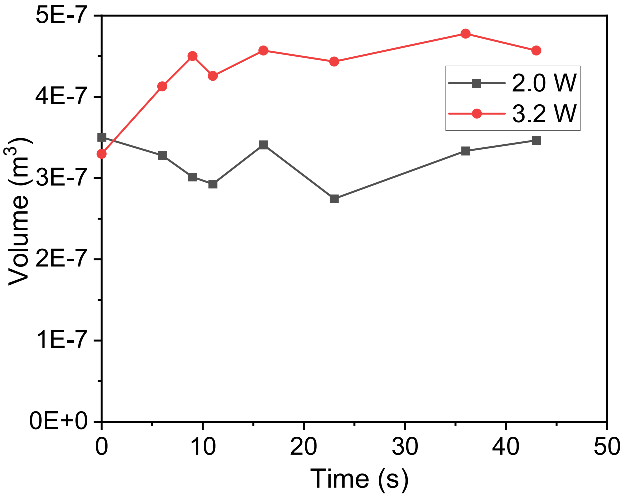

Figure 5.2: Volume of the droplet versus time at an input power of 2.0 W and 3.2 W using Rayleigh waves.

The rate of the change of volume of the droplet, $\frac{dV_d}{dt}$, can be calculated either by curve fitting or simple differentiation. Similarly, temperature gradient, $\frac{dT}{dt}$ and density change with temperature, $\frac{d\rho}{dT}$, can be calculated using data of temperature and density with necessary differentiation. Finally, the mass change can be calculated using equation (4.1) and is presented in Table 5.1 for an input power of 2.0 W. From the results, it can be identified that the changes in volume and mass of the droplet versus time are both within the errors of measurements. For example, if the initial mass is 0.000349 kg, then the maximum relative mass change regarding the initial mass is less than 2%.

Table 5.1: Mass change of droplet versus time at P_{in} 2.0 W using Rayleigh waves.

Time (s)	**The volume of the droplet (m^3)**	**dm/dt (kg/s)**	**Initial Mass (kg)**	**Relative mass change (kg)**
0	3.5E-07	0	0.000349	0
6	3.28E-07	-3.8E-06		-0.0053

9	3.01E-07	-8.9E-06		-0.01248
11	2.93E-07	-4.3E-06		-0.00605
16	3.41E-07	9.51E-06		0.013331
23	2.75E-07	-9.5E-06		-0.01327
36	3.33E-07	4.45E-06		0.00624
43	3.47E-07	1.81E-06		0.00254

Similarly, the mass transfer using R-waves at an input power of 3.2 W is calculated using the same method, found a relative error of less than 5%, as presented in Table 5.2. Therefore, in this study, the mass of the droplet can be considered as a constant. This conclusion will be applied in the following sections and chapters for the analysis of momentum and thermal impacts.

Table 5.2: Mass change of the droplet versus time at P_{in} 3.2 W using Rayleigh waves.

Time (s)	**The volume of the droplet (m^3)**	**dm/dt (kg/s)**	**Initial Mass (kg)**	**Relative mass change (kg)**
0	3.3E-07	0	0.000329	0
6	4.13E-07	1.37E-05		0.041523
9	4.5E-07	1.22E-05		0.037082
11	4.26E-07	-1.2E-05		-0.0372

16	4.57E-07	6.03E-06		0.01834
23	4.43E-07	-2E-06		-0.00618
36	4.78E-07	2.52E-06		0.007653
43	4.57E-07	-3E-06		-0.00913

5.3 Analysis of the mechanical impact mechanism of *SAW* on droplet by momentum conservation.

Applying the momentum conservation principle from section 3.1.2, the entire droplet velocity can be measured using the data recorded from the *CCD* camera. However, the streaming velocity inside the droplet can be measured by the method described in section 4.5.1, the *PIV* method.

It is identified from the experiments that up to the *SAW* power of 3.2 W, the droplet keeps its original position without moving or the significant deformation. This means that the *SAW*-induced force acting on the droplet is balanced by the internal friction force generated by internal streaming, as given in equations (3.4) and (3.8).

At the *SAW* power of 3.2 W, as shown in Figure 5.3, where the purple line on the left of each figure shows the original position of the droplet. The droplet starts to deform somehow and move on the substrate surface, from 1.0 s of *SAW* elapsed time, then it stopped and keeps the same position after 2.0 s of *SAW* acting time. In this case, the *SAW* force is balanced by surface tension and the internal friction force.

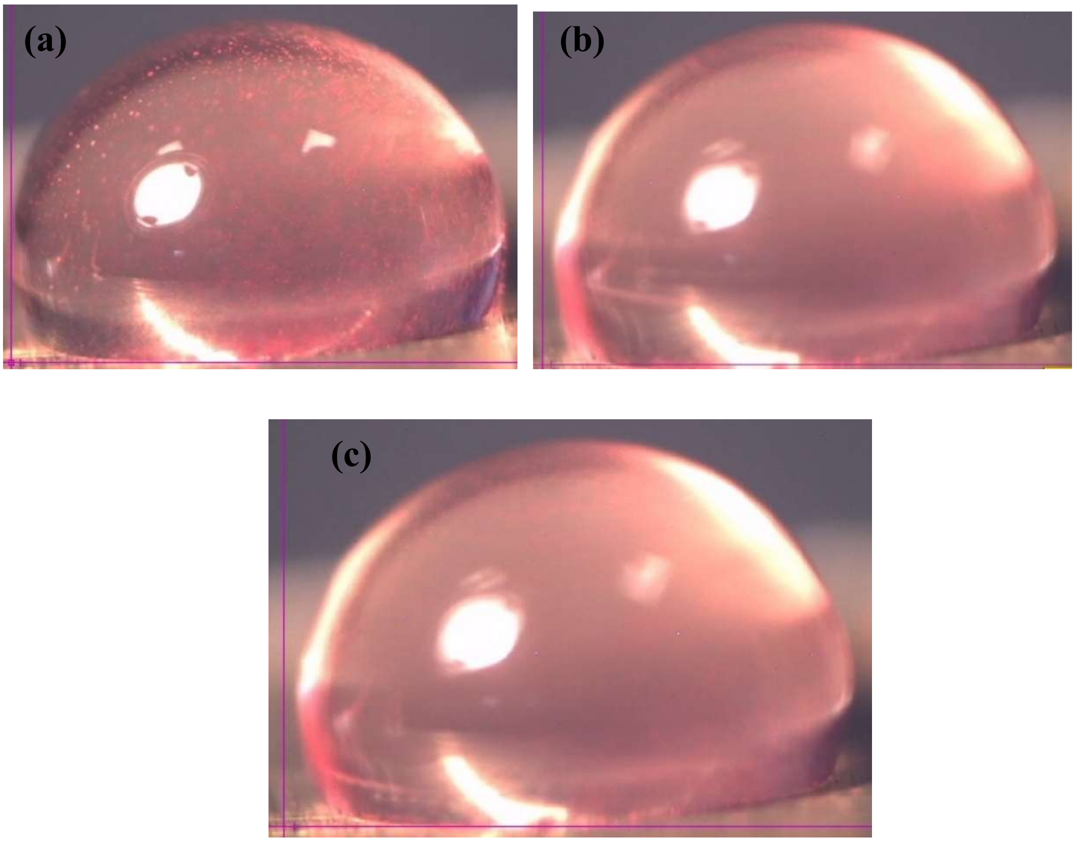

Figure 5.3: Droplet movement/pumping (a) Before providing *SAW* (b) After 1.0 s of input power (c) After 2.0 s of input power at 3.2 W using R-waves.

The droplet movement has been observed when the input power reaches 4.0 W as shown in Figure 5.4. The droplet moves from the original position (the purple line on the left of each figure) with more displacement as compared to the lower power. Figure 5.4-a shows stationary droplet without applying *SAW* power. It starts moving horizontally on the substrate surface immediately after applying input power as shown in Figure 5.4-b, more displacement can be observed after 1.0 s of input *SAW* as shown in Figure 5.4-c. It then keeps the same position with somehow deformation after 3.0 s of an input SAW as shown in Figure 5.4-d. When the surface tension between the droplet and the substrate becomes larger than the *SAW* force, then the droplet sticks to the surface and does not move further. At this time, the input power is only used to generate streaming and heating inside the droplet.

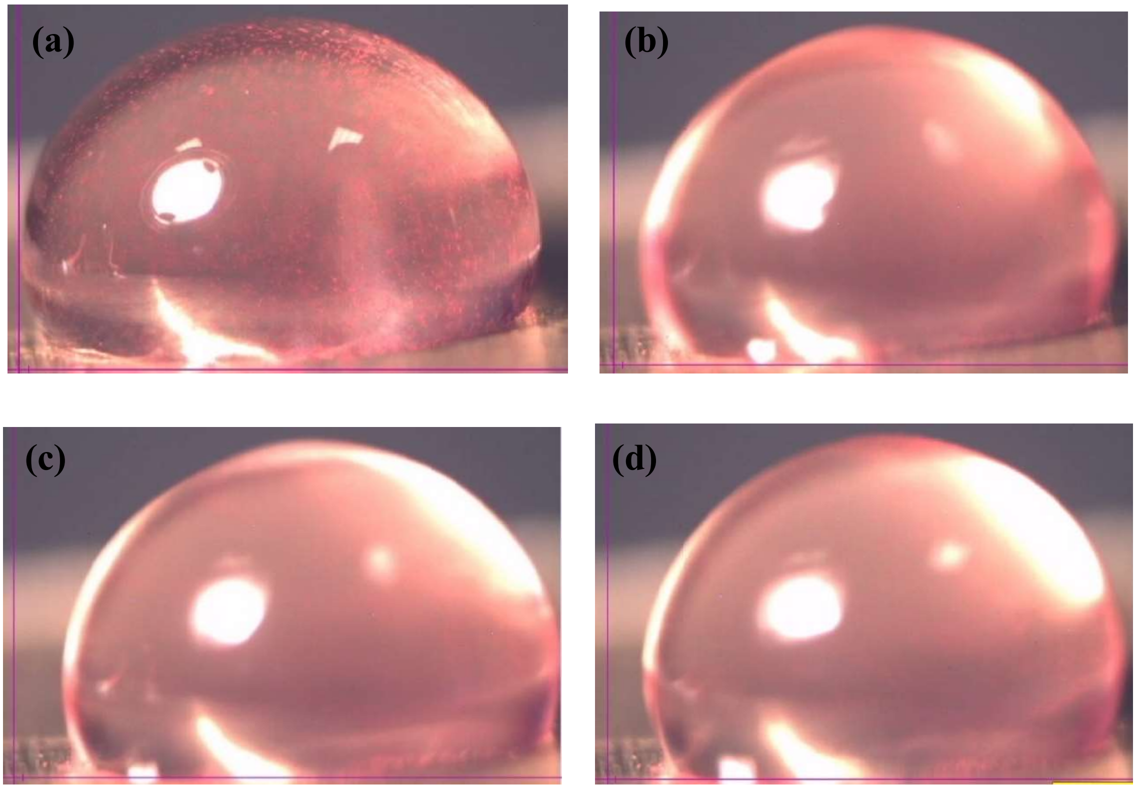

Figure 5.4: Droplet movement/pumping (a) Before providing *SAW* (b) After 0.66 s of input power (c) After 1.0 s of input power (d) After 3.0 s of input power at 4.0 W using R-waves.

The data of the droplet moving velocities and the momentum at two different input power levels are presented in the graphical form in Figure 5.5 and Figure 5.6 respectively. On one hand, it is found from Figure 5.5 that the droplet velocity increases with the increase in input power, while, the droplet stops moving after almost 4.0 s. On the other hand, the acceleration and the inertial force are more significant. The acceleration varies from 0.20 mm/s^2 to 0.55 mm/s^2 and the inertial force varies from 6.58 E-8 (N) to 1.8E-7 (N) at P_{in} 3.2 W to 4.0 W. The drag force of the entire droplet can be calculated using equations (3.6) and (3.7), the friction force and interfacial tension force can be estimated by equations (3.8) and (3.9) by neglecting the static friction force. Then the SAW force driving the droplet can then be predicted by equation (3.4) with no buoyancy force on horizontal.

The bottom streaming (position 1, Figure 4.10) velocities are measured from the *CCD* camera by the method described in section 4.5.1. At P_{in} 3.2 W, the bottom streaming velocities are from 0.0 to 0.033 m/s, Re_x of 166.5 after 1.0 s of input *SAW*, then reach to 0.034 m/s with Re_x of 169.5 after 2.5 s. By this set of data and the data of density of water

(996.6 kg/m^3), the bottom area of 1.64E-5 (m^2), the bottom friction force can be estimated by equations (3.8) and (3.9) as F_f= 8.37E-5 N. By the data of droplet velocity shown in Figure 5.5, using equation (3.7), C_d = 0.3-0.4 [144], where an area of the half-spherical droplet is 3.28E-5 m^2, the drag force can be calculated using equation (3.6) as F_d = 3.06E-11 N.

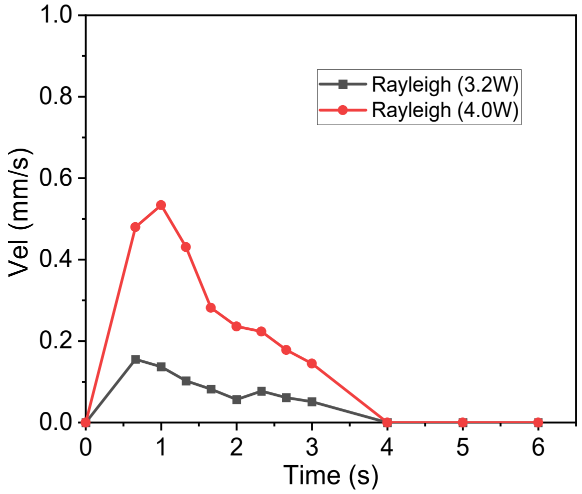

Figure 5.5: Pumping velocity of the droplet versus time at different input power levels 3.2 W and 4.0 W with Rayleigh waves.

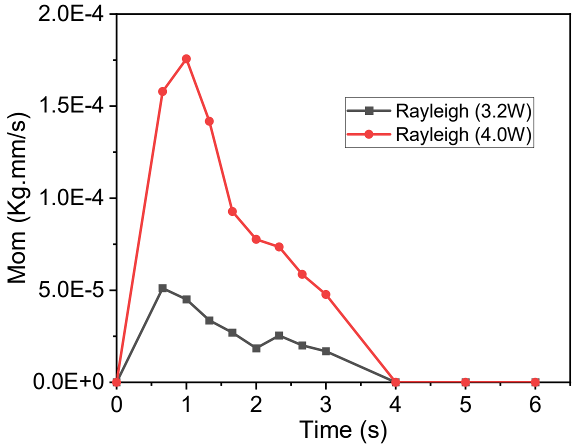

Figure 5.6: Momentum of the droplet versus time at an input power of 3.2 W and 4.0 W with Rayleigh waves.

The force from interfacial tension of the water droplet with *ZnO* surface calculated using equation (3.11) is 4.3E–4 N with the value of 'σ' to be 27.8 (mN/m) [146] and the droplet size of 5.0 mm. As those sets of data, the drag force is 10^{-3} smaller than the inertial force and the inertial force is 10^{-3} smaller than the friction force, F_f. Therefore, the interfacial tension force is one order of magnitude larger than friction force. Furthermore, it can be concluded that the SAW force (the force driving the entire droplet movement) is generally balanced by both the interfacial tension force and the bottom friction force because the drag and inertial forces are much smaller.

The above analysis is also suitable for the deceleration period from 1.0 sec to 4.0 sec of SAW acting, the period of steady-state. The same is for the case of the input power of 4.0 W, where the friction force may make more contribution as the increases in streaming. It can be predicted, although not in the range of this study, increasing the SAW force (input power) further, the droplets may jump from the surface [198].

5.4 The diagnostics of the thermal and kinetic coupling mechanism of *SAW* on droplet using the energy conservation principle.

Energy conservation includes heat transfers and kinetic energies inside the droplet caused by the SAW. For the thermal impacts of SAW on the entire droplet, the discussion begins from the thermal images from *IR* camera that leads to finding the temperature rise of the droplet (T_d). The temperature of the substrate (T_s) can be found directly from the *IR* camera. Once T_d is found, then the temperature difference between droplet and substrate, the temperature of the outer layer of the droplet and heat transfer coefficients can be predicted to calculate heat transfers inside the droplet.

5.4.1 The mechanical power due to the changes in the volume of the droplet

Applying the energy balance to the droplet, equation (3.13), the mechanical work done can be calculated using equation (5.1) as following.

$$\dot{W} = -p_a \frac{dV_d}{dt} \tag{5.1}$$

where p_a is the atmospheric pressure with a value of 101.325 kPa. The rate of volume change of the droplet can be calculated by the data obtained from mass analysis in section 5.2 (Table 5.1and Table 5.2). It is found that the average rate of volume changes with time is -1.25E-9 m^3/s and 2.26E-9 m^3/s at input powers of 2.0 W and 3.2 W, respectively. The work done per unit time for these cases is 1.27E-4 W and -2.29E-4 W, respectively. The positive work means the droplet delivering the energy to the atmosphere (expansion), while, the negative works mean the droplet being compressed by the atmosphere pressure, which is unreasonable. As such, it is suggested that the measured data on the change in volume is within measurement error, therefore, the assumption of a constant volume of the droplet in this study, is acceptable. This leads to the conclusion that the effect of this mechanical power is also negligible. However, the effect of this mechanical power on diagnostics of the *SAW* radiation power will be discussed in section 5.4.6.

5.4.2 The thermal impacts of SAW on the droplet

The side view thermal images of the droplet taken from experiments with input power values of 0.38 W, 0.96 W, 2.0 W, and 3.2 W are presented in Figure 5.7. *SAW* is acting from the left with varied time frames up to 43.0 s. The colour images show not only the temperature increase with time but also the temperature distributions on the droplet surface.

At lower power (0.38 W), there is an impact delay of 5.0 s as there is no significant change in the colour of the image, shown in Figure 5.7-a. The visible change in colour can be identified from Figure 5.7-a at 11.50 s, where the change started from the bottom. The clear colour distribution is identified after 43.0 s of input *SAW*, which means that the droplet does not reach to the thermal steady state for P_{in} 0.38 W.

At 0.96 W, the change in colour (the temperature) appears at 5.0 s but the clear temperature distribution identified at 11.50 s of *SAW* elapsed time and high temperature at the bottom layer of the droplet can be identified at 23.0 s as given in Figure 5.7-b. It is also evident that after 43.0 s of input power, almost uniform temperature distribution achieved.

When the input power increases to 2.0 W, significant colour changes even at 5.0 s of input SAW, however, a clear temperature distribution is identified at 11.50 s with the bottom layer having higher temperature and top having less as shown in Figure 5.7-c. At this input power, the uniform temperature distribution is achieved after 23.0 s, quicker than input power of 0.96 W and it continues even up to 43.0 s as given in Figure 5.7-c.

At the high input power of 3.2 W, a non-uniform temperature distribution starts after 5.0 s, which is quickest as compared to other input power values as shown in Figure 5.7-d. Similarly, almost uniform temperature distribution achieved after 11.50 s which is fastest as compared to lower power levels. After 11.50 s, input power continues to increase the overall temperature of the droplet which causes complex heat transfer mechanisms inside the droplet, that will be discussed in section 5.4.4. The maximum temperature achieved by the input power of 3.2 W is 30.80 °C (55.70-24.90) °C after 43.0 s of an input *SAW* as shown in Figure 5.7-d.

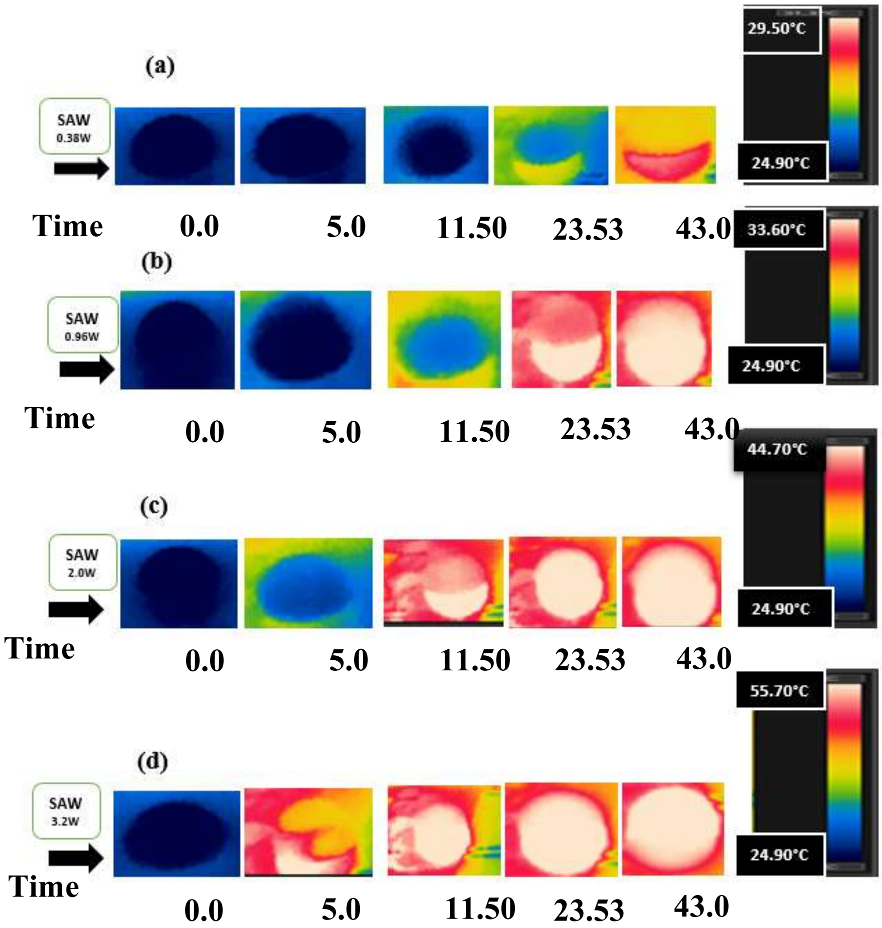

Figure 5.7: Thermal images of droplet by Rayleigh at (a) 0.38 W, (b) 0.96 W, (c) 2.0 W, (d) 3.2 W (Time 0.0, 5.0, 11.50, 23.53 and 43.0 s from left to right) observed by FLIR (T-620).

5.4.2.1 The rise in the average temperature by R-SAW

The average temperature rise (the temperature of droplet related to its initial temperature) of the droplet (T_d) can be calculated using equations (4.4) and (4.12), given in Figure 5.8 at different power levels against time. T_d for $P_{in} \leq 0.96$ W shows no significant increase as identified in Figure 5.7-a and b. The impact delay for these power levels shown in Figure 5.7 has also a reflection in Figure 5.8 as the temperature of the droplet starts increasing after a few seconds of input power. For $P_{in} > 0.96$ W, the temperature of the droplet abruptly increases with time and has more gradient as compared to the lower input power levels. It is found that the maximum average temperature of the droplet increases linearly with the input power with the rate of about 9.92 °C/W as presented in Figure 5.9. The maximum precise T_d at input power levels of 0.38 W, 0.96 W, 2.0 W, and 3.2 W is 4.5 °C, 10.05 °C, 21.92 °C, and 31.33 °C, respectively as given in Figure 5.8.

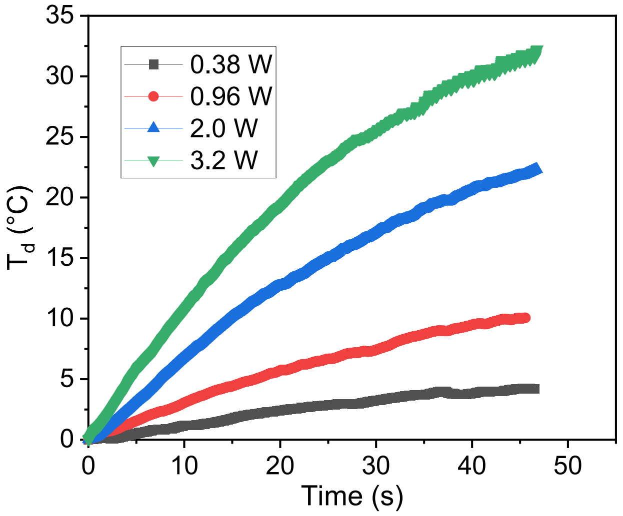

Figure 5.8: T_d using Rayleigh waves from 0.0 to 43.0 s at different power levels (0.38 W, 0.96 W, 2.0 W & 3.2 W). T_d is the rise in temperature of the droplet and time is measured in seconds.

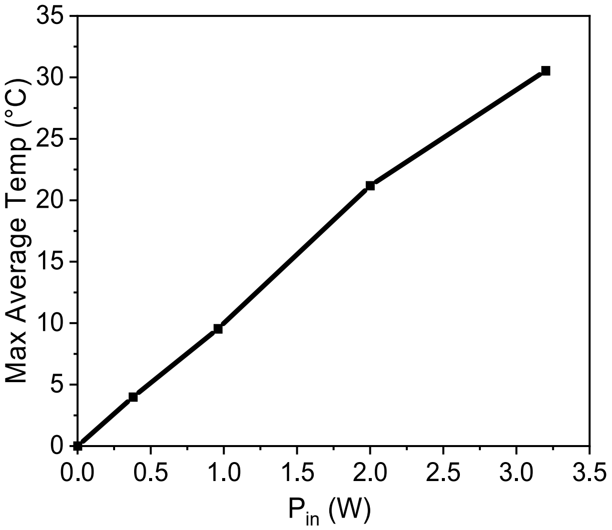

Figure 5.9: Maximum average temperature of the droplet after 43.0 s of *SAW* acting time for input power values from 0.38 W to 3.2 W.

The temperature gradient of the droplet at different P_{in} versus time are calculated using the curve fitting of the temperature data and presented in Figure 5.10. For all input power levels, a 'jump' at the temperature gradient occurs once the *SAW* acts. This 'jump', however, is relatively small at lower input power, say about 0.05 °C/s, which is almost invisible from the images presented in Figure 5.7 and is defined as an 'impact delay'. However, this can be 'seen' from the data treated by the method discussed in Chapter 4. A significant jump can be observed when the input power increases to 0.96 W when the temperature gradient is 0.18 °C/s at the start of SAW elapsed time.

In addition to the initial jump, the temperature gradients make a 'wave' like evolution, especially at an input power of 0.38 W and 0.96 W. This 'wave' is the reflection from the plays between the *SAW* radiation (the thermal source), heat transfers, and the kinetic energy convections. The frequencies of the 'waves' are smaller at lower input power. This frequency can be measured by the time at the first peak of the 'waves' as the half-frequency. At lower input power levels, the half-frequencies are 1/14 (1/s) for P_{in} 0.38 W and about 1/7.5 (1/s) for P_{in} 0.96 W, while at P_{in} 2.0 W, it increases to 1/3 (1/s), then becomes almost infinite at P_{in} 3.2 W. This means that the significant thermal impact occurs immediately due to the SAW radiations at the larger input power. The maximum temperature gradient increases with input power quadratically, as shown in Figure 5.11. The detailed discussion about the thermal impacts of *SAW*, the analysis of energy distributions is in section 5.4.4.

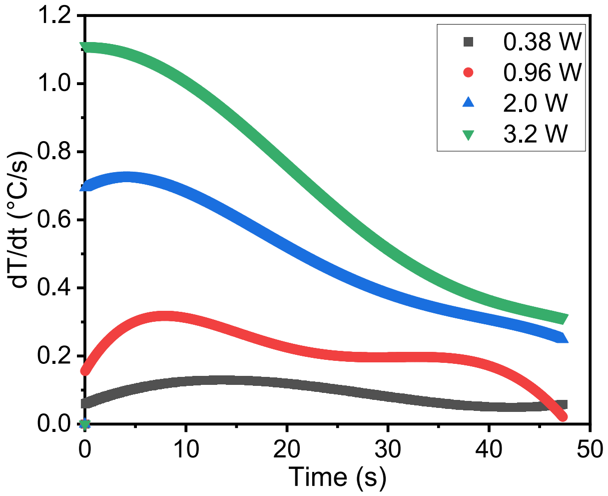

Figure 5.10: Droplet temperature gradient vs time at variable power levels (0.38 W, 0.96 W, 2.0 W and 3.2 W) by Rayleigh *SAW*.

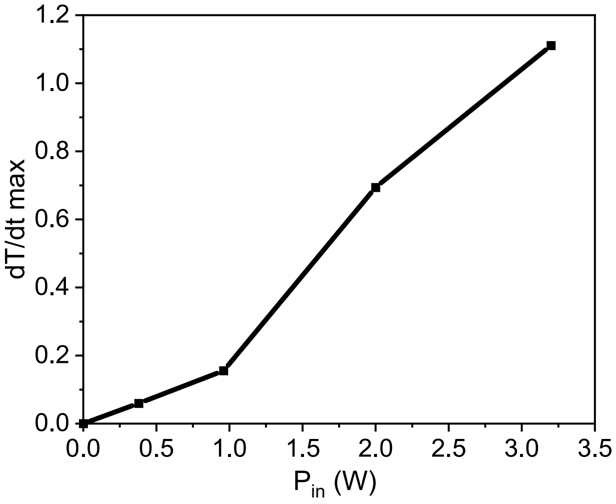

Figure 5.11: Max. *dT/dt* vs input power values of 0.38 W, 0.96 W, 2.0 W and 3.2 W using Rayleigh waves.

5.4.2.2 The temperature difference between substrate and the droplet

The temperature difference, ($T_{s\text{-}d}$), between the substrate surface and the temperature of the droplet at the bottom layer (T_{db}) is used to predict the heat transfer from droplet to the substrate. The temperature of the substrate surface (T_s) is measured by the infrared camera at the position close to the droplet. This difference ($T_{s\text{-}d}=T_s-T_{db}$) versus time at different input power is shown in Figure 5.12. At P_{in} 0.38 W, the temperature of the substrate is higher than the droplet temperature, which leads to a positive temperature difference. At P_{in} of 0.96 W, $T_{(s\text{-}d)}$ becomes negative after 10.0 s of input *SAW*, which means that the droplet temperature becomes higher than the substrate after this time.

At higher input power values, 2.0 W and 3.2 W, the temperature difference is positive for the initial five seconds, then it becomes negative. This means that the droplet is heated from *SAW* radiation quicker than the lower input power, $P_{in} < 1.0$ W as shown in Figure 5.12. This temperature difference remains negative for the rest of the time up to 43.0 s for higher P_{in}. The detailed discussion about heat transfers between the substrate and the droplet is presented in section 5.4.4.

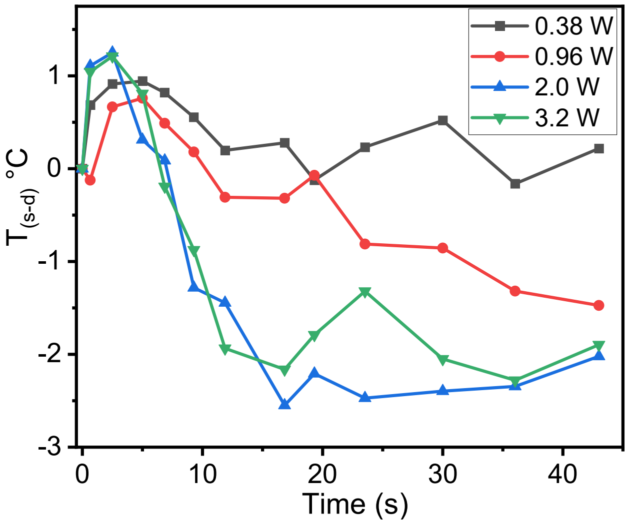

Figure 5.12: Temperature difference of droplet and substrate at different P_{in} values (0.38 W, 0.96 W, 2.0 W and 3.2 W) by Rayleigh. $T_{(s-d)}$ is in °C and time is measured in seconds.

5.4.3 The kinetic impacts of SAW on the droplet: streaming inside the droplet

Velocities of particles at three different positions have been estimated using *PIV*, detail of which has already been discussed in section 4.5.1. The velocities of particles at the input power of 0.38 W to 3.2 W are shown in Figure 5.13. It is found from Figure 5.13 that U_1 is highest as compared to U_2 and U_3 for all input power levels, except the lowest input power of 0.38 W. This indicates that the friction or the friction coefficient of water fluid with the substrate at this lower input power (the lower velocity) is larger than fluid viscosity. At $P_{in} > 0.38$ W, the velocity at the bottom layer increases, as shown in Figure 5.13-b,c and d, driven by more SAW power, which leads to a decrease in the friction coefficient of water fluid with the substrate [144] (refer to equation (3.9)). The streaming velocities are associated with the thermal data as explained in Figure 4.15 and section 4.5.4.

It has been noticed, from Figure 5.7, that the temperature of the droplet layer next to the substrate is higher as compared to other portions of the droplet. For instance, in the case of P_{in} 0.38 W, the bottom heating from the substrate plays the role. However, at the higher input power cases ($P_{in} > 0.90$ W), the streaming of the fluid at the bottom layer increases which causes force convection and enhances the heat transfer. The more heat is transferred from SAW, acting from edge to the entire droplet, including the bottom layer.

This leads to the coupling of the streaming with the thermal impact of *SAW*. The temperature distributions of the droplet can be referred to as section 5.4.1.

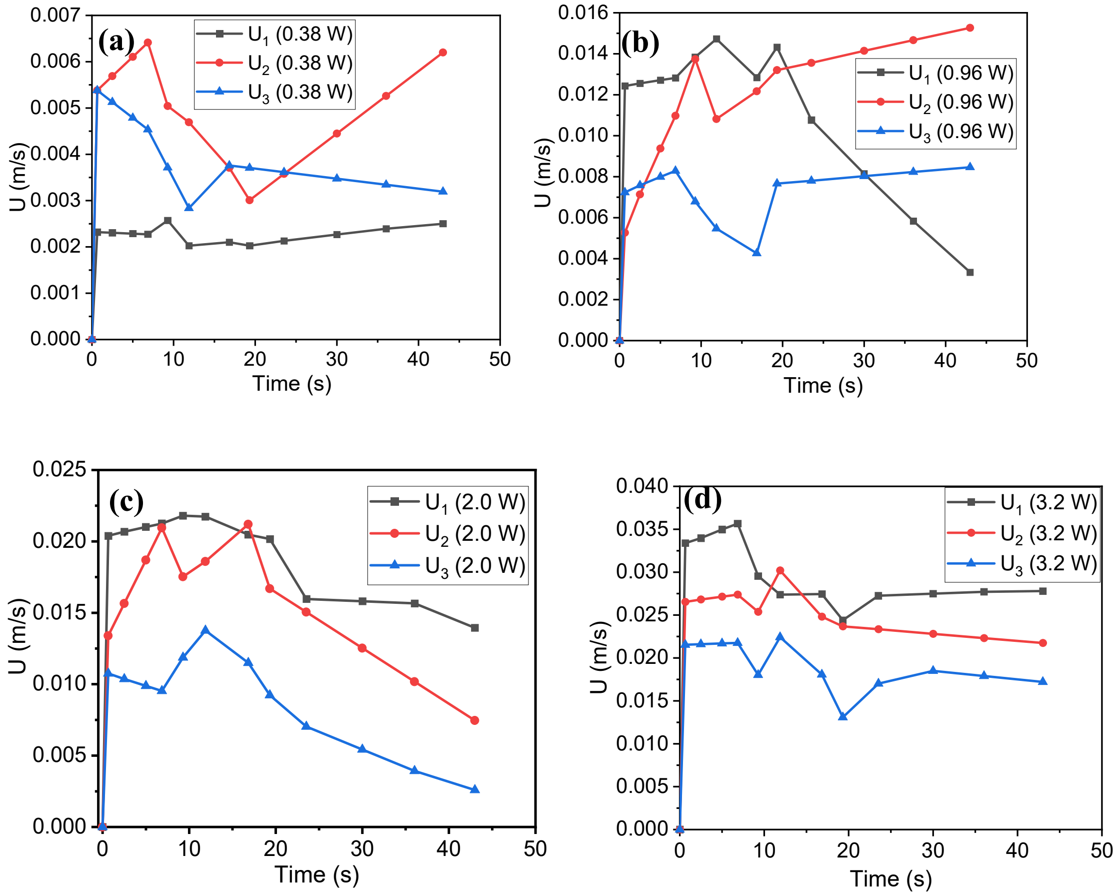

Figure 5.13: Velocity of particles at three different positions with Rayleigh waves for an input power of (a) 0.38 W (b) 0.96 W, (c) 2.0 W and (d) 3.2 W. U_1 is the velocity at a position close to the substrate inside the droplet, U_2 is on the top and U_3 is the vortex velocity.

5.4.4 Diagnosis of heat transfers inside the droplet

As presented in section 3.1.3 and Figure 3.3, input *SAW* contributes to the energy absorbed by droplet ($\dot{E}_d$,W), heat transfers from the substrate to the droplet ($\dot{Q}_s$), from droplet to the air ($\dot{Q}_a$), and heat radiated from *SAW* ($\dot{Q}_r$).

The first kind of the thermal impact of *SAW* on the droplet is the increase in the enthalpy (or internal energy) of the droplet, $\dot{E}_d$, can be calculated using equation (4.14) and presented in Figure 5.14 (a).

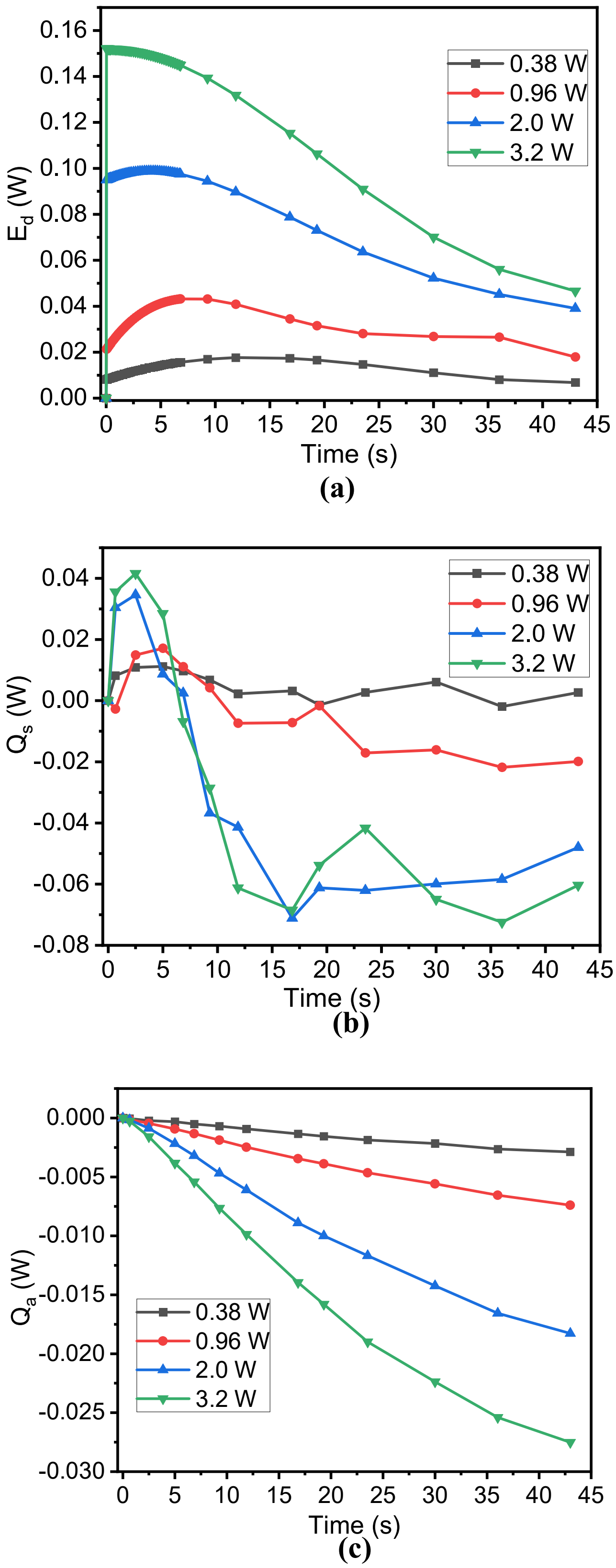

Figure 5.14: Rates of energy absorbed, heat transfers inside and outside of the droplet at power levels of 0.38 W, 0.96 W, 2.0 W and 3.2 W (a) $\dot{E}_d$ (rate of energy absorbed by the droplet), (b)

$\dot{Q}_s$ rate of heat transfer from substrate to the droplet, (c) $\dot{Q}_a$ rate of heat transfer from air to the droplet. Rates of heat transfers are measured in watts and time is measured in seconds.

The data required to calculate the total energy absorbed by the is listed in Table 5.3. From the results, it is found that the total energy change in enthalpy of the droplet is directly proportional to the input power as presented in Figure 5.14-a. At $P_{in} \leq 0.96$ W, $\dot{E}_d$ becomes almost steady after 15.0 s of input power, however, at $P_{in} > 0.96$ W, absorbed energy continuously decreases with time. $\dot{E}_d$, as given in equation (4.14), is proportional to the temperature gradient (dT/dt) since other values do not vary significantly. For instance, the specific heat capacity of water, C_p= 4.184 kJ/kg.K at T_d= 20 °C and 4.181 kJ/kg.K at T_d =50 °C [199] and density of water for this temperature range changes from 998.20 kg/m^3 to 987.83 kg/m^3 [200]. Therefore, $\dot{E}_d$ has similar trend as for the temperature gradient as presented in Figure 5.14-a.

Table 5.3: Specific heat capacity and the density of the water within temperature range 0 to 50.0 °C [199], [200].

Temperature (°C)	Specific heat capacity (KJ/kg.K)	Density (kg/m^3)
0	4.219	999.80
20	4.184	998.20
25	4.181	997.02
30	4.180	995.54
40	4.179	992.10
50	4.181	987.83

The next is the rate of heat transfer from the substrate to the droplet, $\dot{Q}_s$, calculated by equation (4.15). As previously discussed, the heat transfer from the substrate to the droplet is dominated by both the convection of fluid flows, α_s, the effective heat transfer coefficient, and the temperature difference, $T_{(s\text{-}d)}$. The α_s calculated by equation (4.16), and T_{db}, required to find $\dot{Q}_s$ is given in Figure 5.15 and Figure 5.16, respectively.

$\dot{Q}_s$ for different input power levels for R-waves is shown in Figure 5.14-b. For lower input power, 0.38 W, heat is transferred from the substrate to the droplet all over the time from start to the end of *SAW* input. As discussed in section 5.4.2.2, the results from interplays of heating both from *SAW* radiation and the heating from the substrate. When analysing the data of each term, it can be realized that the power of the droplet absorbed and the received from the substrate are all at the same orders of magnitude, say ~ 0.01 W to 0.02 W. However, the power lost by the droplet to the surrounding air is one order of magnitude lower, ~0.002 W. This means, the heating to the droplet is mostly due to the heat transfer from the substrate where the droplet placed on. The smaller losses in heat to air lead to the temperature of droplet increase to 4.6 °C. However, the droplet cannot be heated at a temperature higher than the temperature of the substrate, as indicated by the data of $T_{s\text{-}d}$ in Figure 5.12.

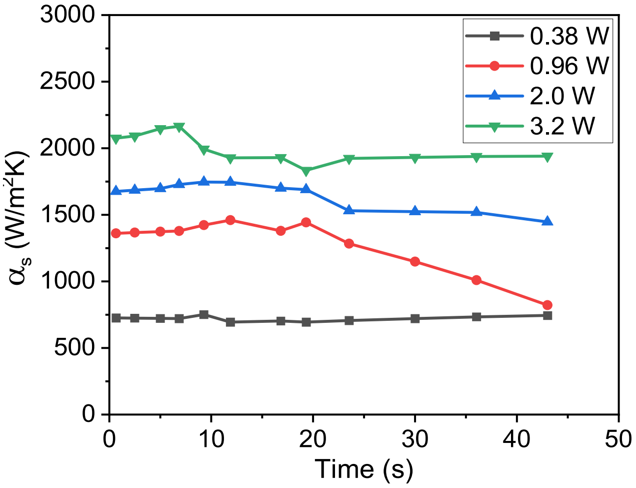

Figure 5.15: Effective heat transfer coefficient (α_s) for power values 0.38 W, 0.96 W, 2.0 W and 3.2 W against time 0.0 to 43.0 for R-waves, where α is in W/m^{2}K and time is in seconds.

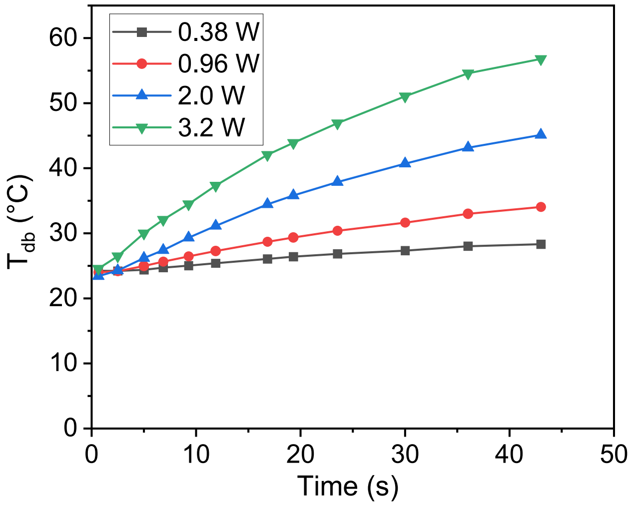

Figure 5.16: Temperature of the bottom layer of the droplet (T_{db}) directly contacts with the substrate at P_{in} values of 0.38 W to 3.2 W using R-waves.

However, it is interesting to find out a so-called 'inverse heat transfer' at an input power of 0.96 W, that causes the heat transfer from droplet to the substrate just after 10.0 s of input power as shown in Figure 5.14-b. The increased *SAW* power transfers much more power to the droplet. The input power is partially absorbed by the fluid, converted to the thermal power to increase the fluid temperature. On the other hand, part of the *SAW* power penetrated inside the droplet is converted to the kinetic energy to enhance fluid streaming. It is this streaming which transfers the thermal power of the fluid at the edge of the droplet, where the *SAW* penetrated to, to rest part of the droplet, including the bottom layer where it is heated by the substrate as well. This dynamic process takes about 10.0 s in this case, then the fluid on the bottom layer is heated up to a temperature higher than the temperature of the substrate. Therefore, the reverse heat transfer takes place to transfer heat from droplet to the substrate. This 'reverse time', the time of the reverse heat transfer occurs, decreases as the input power increases.

For power values 2.0 W and 3.2 W, the droplet is heated more effectively to increase the temperature higher than the substrate temperature just after five seconds of input *SAW*. This means that inverse heat transfer takes place from droplet to the substrate quicker than 0.96 W, say from 10.0 s at an input power of 0.96 W to 5.5 s and 6.0 s at input power values of 2.0 W and 3.2 W, respectively, as shown in Figure 5.14-b. Although the substrate is already heated, however, when the droplet temperature becomes higher than the substrate, according to the general heat transfer rule, heat will flow from higher to the lower temperature. However, such a small ‘reverse’ heat flux makes an insignificant impact on the large volume of the substrate.

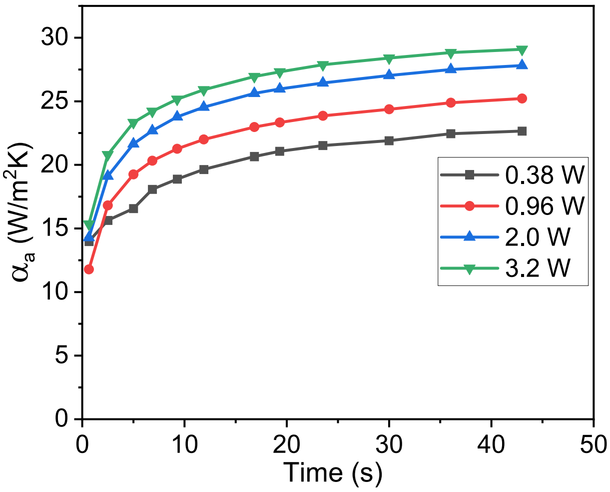

Figure 5.17: Effective heat transfer coefficient (α_a) for power values 0.38 W, 0.96 W, 2.0 W and 3.2 W against time 0.0 to 43.0 for R-waves, where α is in W/m^{2}K and time is in seconds.

The only sink of the heat is the heat transfer from the droplet to the air, $\dot{Q}_a$, that can be diagnosed by equation (4.15), presented in Figure 5.14-c. The heat transfer from the droplet to the air, $\dot{Q}_a$, is dependent on the effective heat transfer coefficient, α_a, and the temperature difference, (T_a-T_{ds}). T_a is the temperature of the surrounding air (room temperature) and T_{ds} is the temperature of the outer layer of the droplet directly in contact with the air as explained in Figure 4.15. Natural convection heat transfer takes place near the droplet which is already discussed in section 4.5.6.1. α_a estimated by equations (4.17) and (4.18), shown in Figure 5.17. It is clear from Figure 5.15 and Figure 5.17 that α_a due to natural convection of air is much smaller than the α_s, which is because of forced convection of streaming at the bottom layer. The temperature of the surrounding air as recorded during experiments is 24.0 $^\circ$C and the temperature of the droplet outer layer, T_{ds}, of each power is presented in Figure 5.18. Note that these values are the actual temperature of the droplet, not the temperature rise.

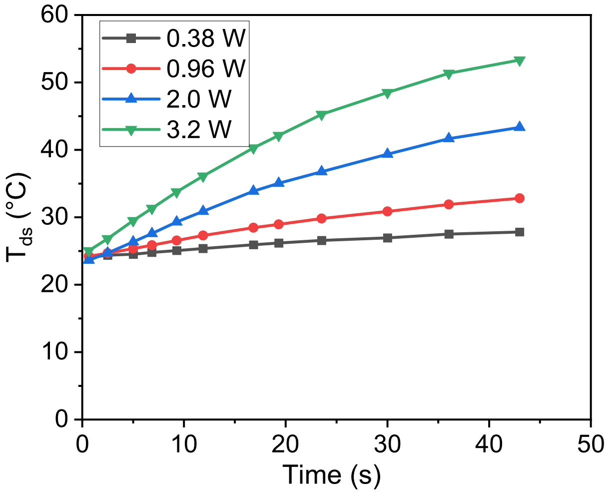

Figure 5.18: Temperature of the outer layer of the droplet (T_{ds}) directly contact with air at P_{in} values of 0.38 W to 3.2 W using R-waves.

The heat lost to the air has a direct relation with the input power; the higher the power input, the more heat transferred to the air. In general, the heat transfer rate to the air is always smaller in comparison with those of heat transfers to the substrate (Figure 5.14-b). In principle, it is the reflection of the heat transfer mechanism of natural convection and forced convection. The forced heat convection due to high streaming velocity at the bottom layer of the droplet causes the heat transfer to increase when the input power is larger than 0.90 W. Therefore, $\dot{Q}_a$ is smaller than $\dot{Q}_s$ since natural convection involves $\dot{Q}_a$ and forced convection causes $\dot{Q}_s$ to be more significant. In comparison to the increase in enthalpy of the droplet, the heat transfer rate to the air is at least one order of magnitude smaller (Figure 5.14-a).

5.4.5 Diagnostics of kinetics inside the droplet

The model presented in Figure 3.3 describes kinetic energy inside the droplet mainly because of viscous streaming and friction near the substrate. How these mechanisms contribute to energy conservation is diagnosed and discussed here.

The rates of kinetic energies of streaming $\dot{K}_{st}$ and friction $\dot{K}_f$ inside the droplet are calculated by equations (4.20) and (4.21) and presented in Figure 5.19 and Figure 5.20, respectively. The dynamic viscosity of the droplet, μ_d, (N.s/m^2), against temperatures from 20 °C to 50 °C is listed in Table 5.4 [195]. It can be seen that both of these two kinetic powers are in the order of 10^{-6} and 10^{-8} W that is not significant as compared to the heat transfers inside the droplet, shown in Figure 5.14. The positive value of these kinetic means the fluid absorbs the power from *SAW* or other thermal sources, while, the negative value means the conversion of kinetic power to thermal energy. The results show that friction powers are much larger than the power of the droplet streaming (rotational acceleration of the fluids) as given in Figure 5.19 and Figure 5.20.

Table 5.4: Dynamics viscosity of the droplet (water) at temperature values 20 °C to 50 °C.

Temperature (°C)	Dynamic Viscosity (N.s/m^2)
20	1.002E-3
30	0.7978E-3
40	0.6531E-3
50	0.5471E-3

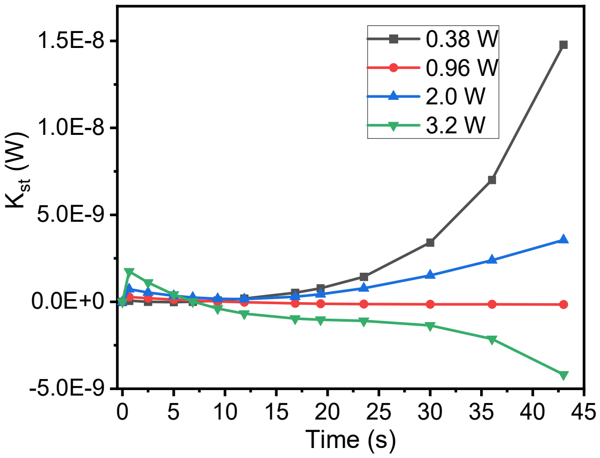

Figure 5.19: Rate of kinetic energy, $\dot{K}_{st}$(W), Kinetic streaming power inside the droplet for P_{in} (0.38 W, 0.96 W, 2.0 W and 3.2 W), kinetic power is measured in watts and time is measured in seconds.

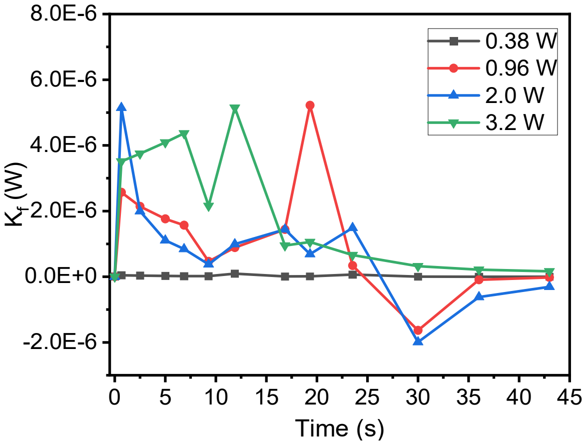

Figure 5.20: Rate of kinetic energy, $\dot{K}_f$(W), Kinetic power due to friction near the bottom of the droplet for P_{in} (0.38 W, 0.96 W, 2.0 W and 3.2 W), kinetic power is measured in watts and time is measured in seconds.

5.4.6 Estimation of heat radiated inside the droplet

It has been noted that it is difficult by both the theories and the direct experimental observations to identify how much the power radiated into the droplet. As proposed in section 3.1.3, the rate of radiated power ($\dot{Q}_r$) can be estimated by the proposed energy model and equation (4.13), whereas all other terms in equation (4.13) are diagnosed and discussed in section 5.4.4. Note, it is the radiated heat as the source to heat the droplet in terms of heat absorption by water and then transfers to the surroundings (air and substrate).

In addition to the general trend, $\dot{Q}_r$, increases with an increase in input power as shown in Figure 5.21. It is identified that the *SAW* power penetrates inside the droplet that varies with time. At the lowest input power of 0.38 W, the *SAW* power is penetrating to the droplet eventually without a notable 'jump'. It reaches a peak at about 19.0 s of the *SAW* elapsed time, then shows some fluctuations, which also shows the development of the droplet absorption power given in Figure 5.14-a. From this result, it seems that at lower input *SAW* power, the droplet is possible to reach to a 'wave-like' steady-state with the interaction balance of all the thermal and mechanical (kinetic powers) impacts.

When the input power increases to 0.96 W, a 'jump' occurs as soon as the R-waves penetrates inside the droplet, then it shows the trend as is for 0.38 W, a steady-state approaching with the interaction balance of all the impacts.

However, in addition to a big jump start, when the input power increases to 2.0 W and 3.2 W, more power is transferred to the droplet which causes to achieve the peak quicker than the lower input power. It can be confirmed for these larger input power cases, that the droplet does not reach a steady-state also evident in Figure 5.8. The summary of all heat transfers and kinetic energies inside the droplet using Rayleigh waves is shown in Figure 5.22.

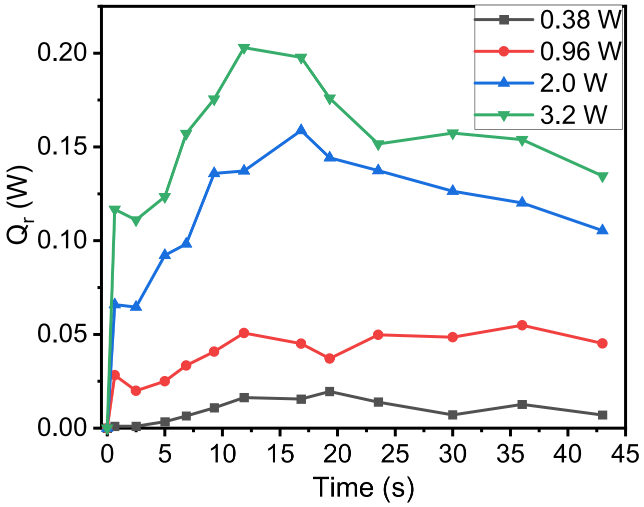

Figure 5.21: $\dot{Q}_r$ rate of heat radiated from left edge of the droplet. $\dot{Q}_r$ is measured in watts whereas *SAW* is applied for 43.0 seconds.

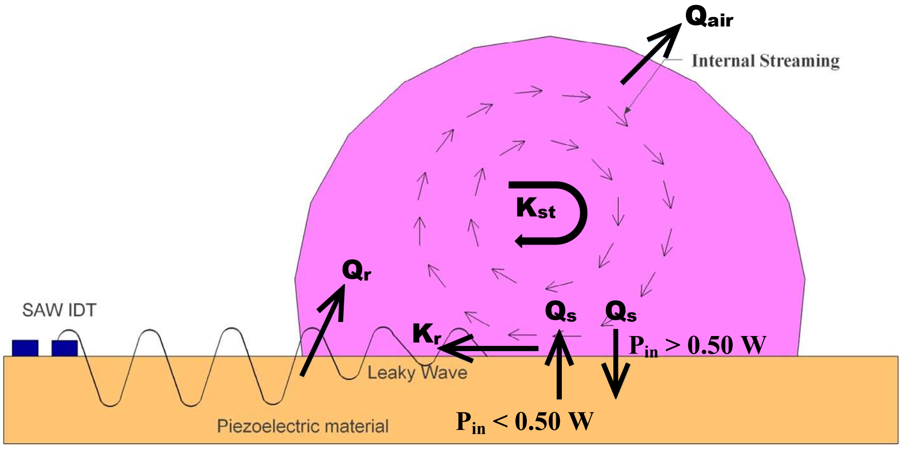

Figure 5.22: Summary of kinetic energies (K_{st} & K_f) and heat transfers (Q_r, Q_s & Q_a) inside the droplet using Rayleigh waves. Heat transfer from substrate to the droplet (Q_s) takes place when $P_{in} < 0.50$ W and inverse will be the case when $P_{in} > 0.50$ W.

5.4.6.1 The effect of mechanical work on the $\dot{Q}_r$

It is important to discuss the impact of work done, $\dot{W}$, as estimated in section 5.4.1, on the diagnostics of $\dot{Q}_r$. Since this work is based on the data of the volume of the droplet. Therefore, how much accuracy of predicted $\dot{W}$ depends on the accuracy of the measurements of the volume of droplet. It has been discussed in section 5.2 that the changes in volume (mass) of the droplet is in the range of measurement errors, say less than 5%. Therefore, it is reasonable to keep the assumption of the constant mass of the droplet, meanwhile, the constant volume of the droplet as well. The errors lead by this assumption on diagnostics is checked and the results are shown in Figure 5.2, from where it can be identified that the volume effect is negligible.

5.5 Repeatability of experiments

Experiments showed good repeatability when repeated with the same device, same parameters, same wave mode, frequency and with the same input power values. Some of the important results are presented in Figure 5.23 where the rate of energy absorbed, heat transfer from substrate to the droplet and heat radiated inside the droplet are shown. It is understandable that when experiments are repeated, even by keeping all the parameters similar, results may differ. In this study, when results were repeated, get a similar trend but values are slightly different.

When compare energy absorbed by the droplet, Figure 5.23-a, the overall trend is similar but results do not show a wave-like structure as in Figure 5.14-a. Similarly, when comparing heat transfer from the substrate to the droplet and heat radiated inside the droplet, Figure 5.23-b and c, a similar trend has been observed with some different values.

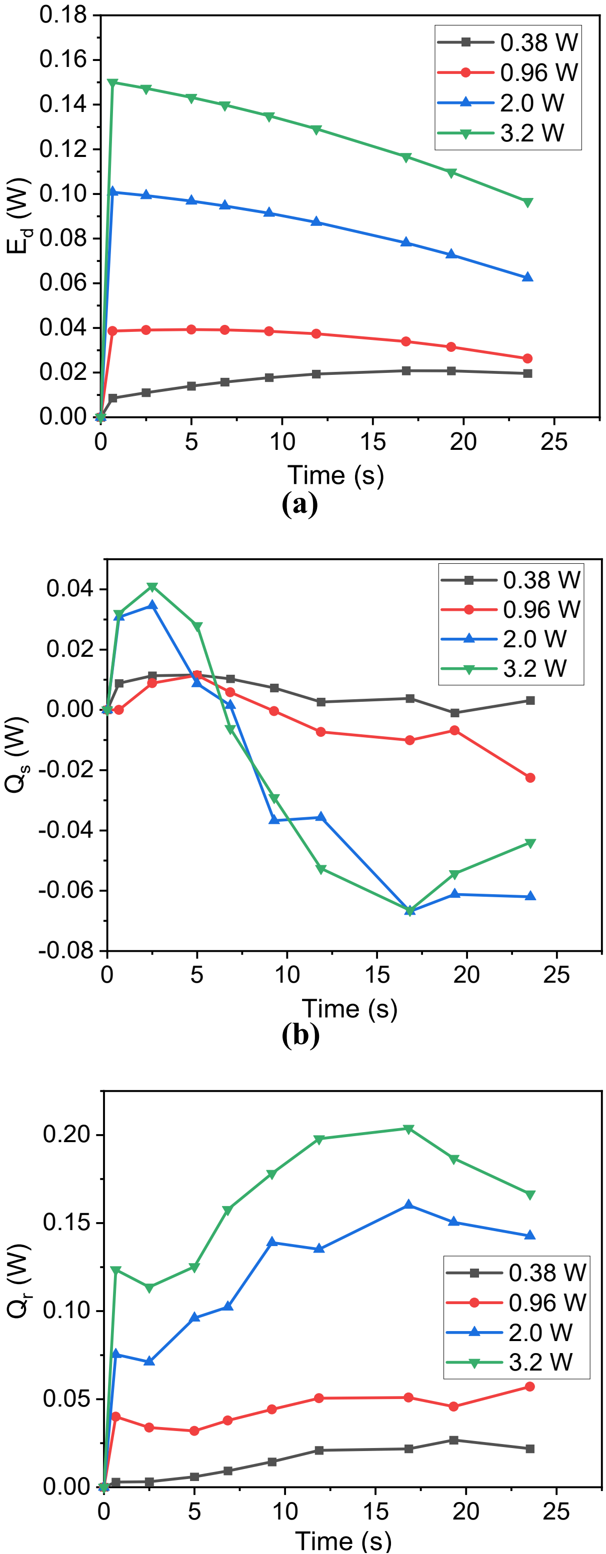

Figure 5.23: (a) Rate of energy absorbed ($\dot{E}_d$), (b) Heat transfer from substrate to the droplet ($\dot{Q}_s$) (c) Heat radiated from the edge of the droplet ($\dot{Q}_r$) at input power of 0.38 W, 0.96 W, 2.0 W, 3.2 W using Rayleigh waves.

5.6 Summary

In this chapter, mass, momentum, and energy conservation principles have been implemented using R-waves. It is concluded from the above discussion that no significant mass transfer takes place in the power range 0.38 W to 3.2 W. Results from higher power levels, 2.0 W and 3.2 W, are presented here for illustration which shows that the relative mass change regarding original mass is less than 5% for both cases.

From 0.38 W to 2.0 W, there is no significant deformation or movement of the droplet, only the streaming inside the droplet has been observed. However, at the input power of 3.2 W, the droplet moves with a velocity of 0.15 mm/s within 1.0 s of SAW elapsed time which stops after 4.0 s of input power. Since inertial and drag forces are much smaller, therefore, the SAW force is balanced by the friction force and interfacial tension force at an input power of 3.2 W. However, at the input power of 4.0 W, SAW force is much larger than friction and drag force which pushes the droplet to move with a velocity of 0.6 mm/s. Then deceleration occurs from 1.0 s to 4.0 s and droplet stops when the surface tension and the drag force overcomes the SAW force.

For the energy conservation principle, thermal and kinetic impacts of the SAW have been identified. Energy absorbed by the droplet is mainly dependent on the temperature gradient which decreases with time as the temperature approaches to steady-state. Impact delay has been observed for an input power of 0.38 W where the droplet temperature starts increasing after a few seconds of input SAW. However, a clear temperature distribution is observed for power values greater than 0.38 W.

The reverse time is defined as the time it takes for the droplet to get heat more than the substrate which leads to reverse heat transfer from substrate to the droplet. Heat transfer from the substrate to the droplet takes place when $P_{in} < 0.50$ W. However, inverse heat transfer takes place from the droplet back to the substrate after a few seconds of SAW when $P_{in} > 0.50$ W.

Heat transfer always takes place from droplet to the air since this is heat leaving the system and the droplet temperature is always higher than the surrounding temperature. Heat transfer from the edge of the droplet, rate of radiated heat transfer, $(\dot{Q}_r)$ has an important role in the heating of the droplet. At lower power, $\dot{Q}_r$ is not playing a vital role, however, most of the energy being transferred to the droplet is from the substrate at this power. But, at higher P_{in}, the value of $\dot{Q}_r$ is highest amongst all other heat transfer mechanisms inside the droplet. Besides, kinetic powers (streaming and friction) are not as significant as compared to heat transfers.

The results obtained from the Rayleigh waves are satisfactory. Considering the need to compare and validate these results, it is necessary to apply another wave mode for empirical comparison. Therefore, the next chapter discusses the implementation of the proposed model to find the coupling mechanism using Sezawa waves.

Chapter 6: Analysis of The Impact Mechanisms of Sezawa SAW on Microdroplet

This chapter is focussed on thermal and kinetic impacts of Sezawa waves (S-waves) on the water droplet. The mechanism of S-waves has been discussed in section 2.3.2 and 2.4.2. The resonant frequency of Sezawa mode is normally double of R-waves [201]. The phase velocity and amplitude of Sezawa are higher than Rayleigh. However, R-waves travel on the top surface whereas Sezawa waves travel in interlayers between the substrate and piezoelectric material [74], [108]. Therefore, it is important to investigate the impact mechanisms of S-waves on microdroplet and apply conservation principles.

6.1 Introduction

Sezawa waves are the second-order harmonic wave obtained using the same device (*Al* plate with thickness 600 μm and λ 100 μm) as presented in Figure 5.1-a. Through a network analyser, the resonant frequency for this wave is found to be 52.220 MHz that is almost double than Rayleigh (26.300 MHz). The same experimental setup and the methodology has been used for these waves to find the mass, momentum and energy transfers as presented in Chapter 3 and Chapter 4.

The model presented in Chapter 3 is applied here to investigate the transfer mechanisms of mass, momentum and energy of the droplet acted by Sezawa SAW. The input power values range from 0.30 W to 3.34 W, trying to match those with the Rayleigh for comparison.

6.2 Analysing of the mass impact of SAW on droplet by mass conservation principle

To calculate the volume and mass change of the droplet, the same method and calculations have been used as discussed in section 4.4. The volume of the droplet at input power values of 2.07 W and 3.34 W are presented in Figure 6.1. The results showed that there are no significant changes in the volume of the droplet.

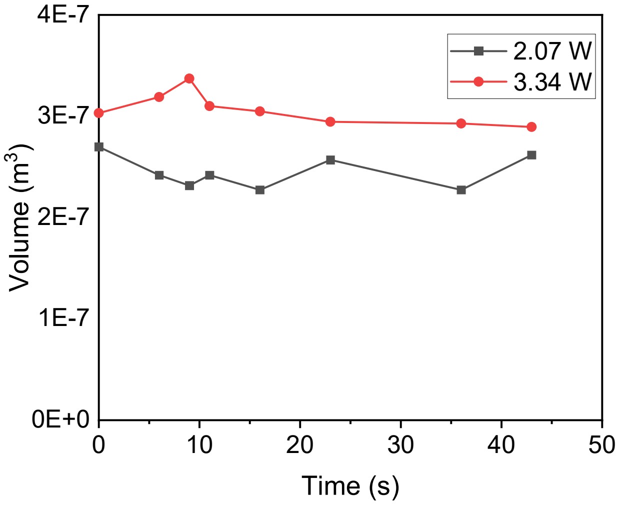

Figure 6.1: Volume of the droplet versus time at an input power of 2.07 W and 3.34 W using Sezawa waves.

The mass change of the droplet at an input power of 2.07 W is listed in Table 6.1. It is evident that if the original mass of the droplet is 0.000269 kg, then mass change with regards to the original mass is 3.5% which is less than 5% thus within the error range.

Table 6.1: Mass change of the droplet versus time at P_{in} 2.07 W using Sezawa waves.

Time (s)	**The volume of the droplet (m^3)**	**dm/dt (kg/s)**	**Initial Mass (kg)**	**Relative mass change (kg)**
0	2.6973E-07	0	0.000269	0
6	2.4191E-07	-4.66E-06		-0.01734
9	2.3162E-07	-3.46E-06		-0.01284
11	2.5096E-07	9.57E-06		0.035563
16	2.2731E-07	-4.74E-06		-0.01761

23	2.5696E-07	4.17E-06		0.015502
36	2.2731E-07	-2.28E-06		-0.00847
43	2.618E-07	4.86E-06		0.01808

Mass transfer using Sezawa waves at an input power of 3.34 W is listed in Table 6.2. The volume of the droplet and ultimately mass versus time does not change significantly. If the initial mass is 0.0003021 kg, then relative mass change versus the initial mass is 4.4% which is again less than 5% means and hence within the error range.

Table 6.2: Mass change of the droplet versus time at P_{in} 3.34 W using Sezawa waves.

Time (s)	**The volume of the droplet (m^3)**	**dm/dt (kg/s)**	**Initial Mass (kg)**	**Relative mass change (kg)**
0	3.0307E-07		0.000302139	0
6	3.1892E-07	2.535E-06		0.008395
9	3.3718E-07	5.943E-06		0.019677
11	3.1005E-07	-1.36E-05		-0.04494
16	3.048E-07	-1.13E-06		-0.00373
23	2.9449E-07	-1.53E-06		-0.00506
36	2.9279E-07	-1.69E-07		-0.00056

43	2.8942E-07	-5.09E-07		-0.00169

6.3 Analysis of the mechanical impact mechanism of SAW on droplet using momentum conservation

Principally, when the *SAW* force overcomes the drag force then the droplet moves in the direction of the waves opposite to the *IDT*. Equation (3.4) and Figure 3.2 shows several forces acting on the droplet. According to the conservation principle, all forces should balance each other. Figure 6.2 and Figure 6.3 show a possible movement of the droplet at a different time frame with an input power of 3.34 W and 4.18 W, respectively. The purple line on the left of the droplet shows the original position of the droplet before applying *SAW*. It is evident from Figure 6.2 and Figure 6.3 that the droplet remains stationary and does not move or slide away. Since Sezawa travels in the interlayers, that is why they have less SAW force which does not overcome other forces to move the droplet.

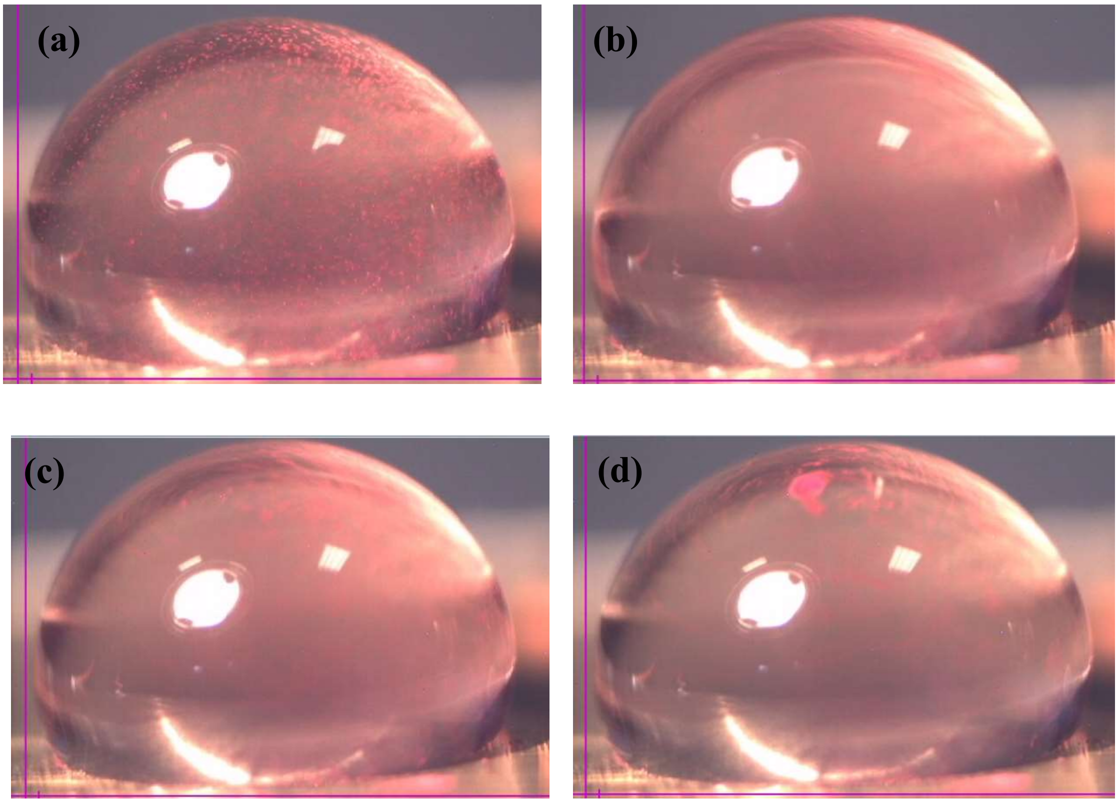

Figure 6.2: Droplet movement/pumping (a) Before providing *SAW* (b) After 1.0 s (c) After 2.50 s (d) After 9.0 s of the *SAW* acting time at 3.34 W with Sezawa waves.

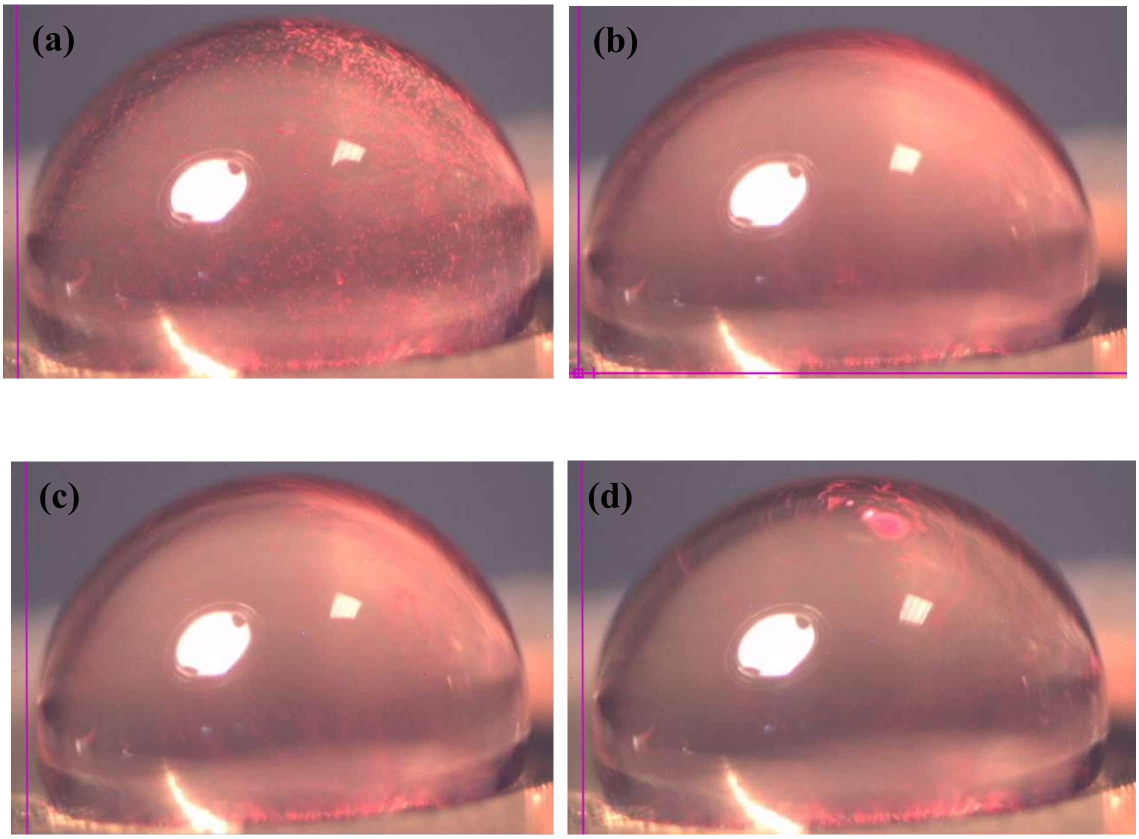

Figure 6.3: Droplet movement/pumping (a) Before providing *SAW* (b) After 1.0 s (c) After 2.50 s (d) After 9.0 s of the *SAW* acting time at 4.18 W with Sezawa waves.

The velocities of the particles at the bottom of the droplet are calculated as described in section 4.5.1. At an input power of 3.34 W, the bottom streaming velocities are from 0.0 to 0.014 m/s and Re_x of 70.99 at SAW acting time to 1.0 sec and then reach to 0.019 m/s with Re_x of 95.87 at 2.50 sec. From this set of data and the data of density of water (996.6 kg/m^3), the bottom area of the droplet is 1.64E-5 (m^2), the bottom friction force calculated by equations (3.8) and (3.9) is F_f= 9.85E-6 N. Buoyancy force can be neglected, the drag and inertial force are dependent on the droplet acceleration moving along the substrate surface. Since the droplet velocity is zero, no momentum has been observed, therefore, there will be no drag and inertial forces. Hence, the SAW force will be equal to the friction force in the opposite direction. The same is the case for an input power of 4.18 W.

6.4 The diagnostics of the thermal and kinetic coupling mechanism of SAW on the droplet using the energy conservation principle.

Energy conservation includes heat transfers and kinetic energies inside the droplet caused by the waves as discussed in section 3.1.3. Firstly, it is important to diagnose the thermal impact (internal energy) of the droplet caused by these waves. The internal energy can be estimated from the thermal images which lead to finding the temperature rise of the droplet (T_d). The thermal images obtained using the same method as for the R-waves discussed in section 4.4. Once T_d is known, then the temperature of the bottom layer, the outer layer of the droplet can be predicted. However, the data from streaming and friction can be associated with the thermal energy to find the coupling mechanism and finally to find the heat transfers inside the droplet.

6.4.1 The mechanical power due to the changes in the volume of the droplet

Applying the first law of thermodynamics, equation (3.13) to our analysing model, work done can be calculated using equation (5.1). The volume change of the droplet with time, $\frac{dV_d}{dt}$ can be calculated using the data listed in Table 6.1 and Table 6.2. The average rate of change of volume for input power values of 2.07 W and 3.34 W is -2.16E-09 m^3/s and 8.85E-10 m^3/s, respectively. Therefore, the work done is found to be -2.19E-04 W and 8.97E-05 W for input power values of 2.07 W and 3.34 W, respectively. This reveals that changes in the volume of the droplet are not significant, hence, our assumption the volume of the droplet remains constant in this study is reasonable. Furthermore, the work done using Sezawa waves is not significant, therefore, mechanical power is very small and can be neglected in further discussion.

6.4.2 The thermal impacts of SAW on the droplet

The thermal images for the droplet using Sezawa waves with input power values of 0.30 W, 0.99 W, 2.07 W, and 3.34 W are presented in Figure 6.4. Times are shown at the bottom of each droplet and the colours shown in each droplet represents temperature distribution inside the droplet with temperature bar on the right side for each case.

Impact delay has been observed for the first 11.50 s for an input power of 0.30 W, as presented in Figure 6.4-a. Since, at low power, most of the energy dissipates inside the substrate and does not add to increase the temperature of the droplet. However, the colour starts to change after 23.53 s and more heat is observed at the bottom layer of the droplet after 43.0 s of input *SAW* as shown in Figure 6.4-a. At this low power, a non-uniform temperature distribution is observed even after 43.0 s of SAW elapsed time.

The impact delay time reduced when input power given to the droplet increased from 0.30 W to 0.99 W as shown in Figure 6.4-b. Therefore, the colour of the droplet starts changing after 5.0 s of *SAW* acting time but there is no clear temperature distribution. However, the temperature distribution starts after 11.50 s with more temperature at the bottom side of the droplet. A clear temperature distribution observed after 23.53 s of the *SAW* elapsed time and temperature becomes almost uniform after 43.0 s of input power as presented in Figure 6.4-b.

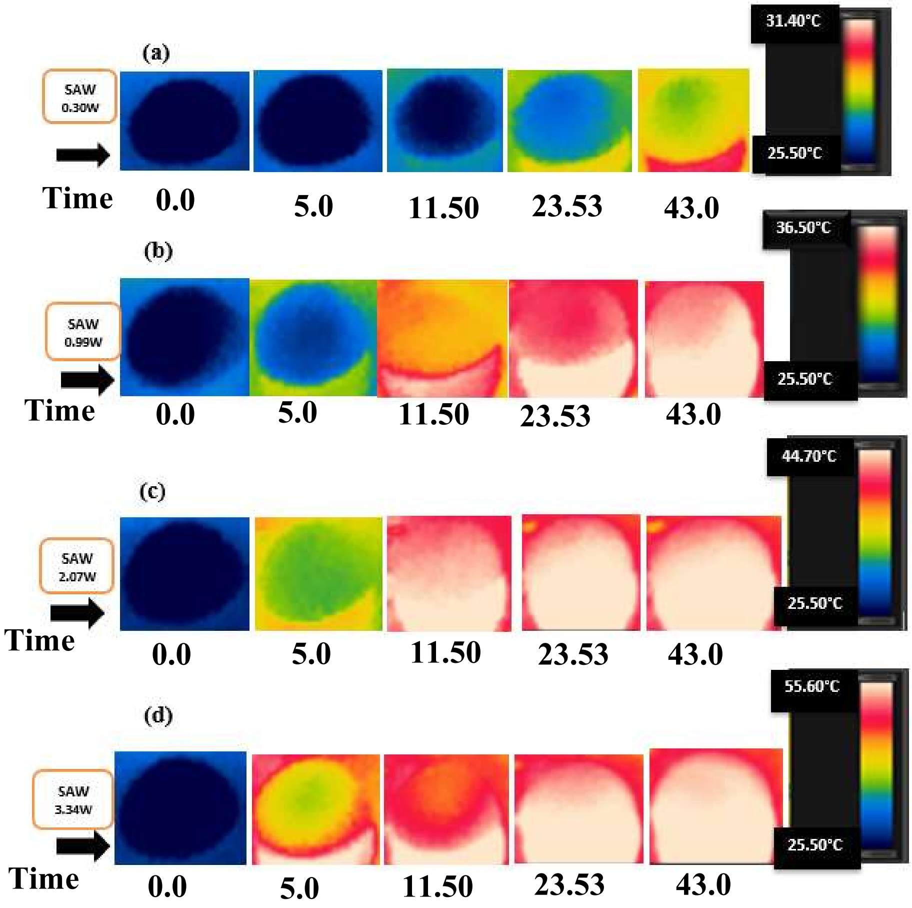

Figure 6.4: Thermal images of droplet by Sezawa waves at (a) 0.30 W, (b) 0.99 W, (c) 2.07 W, (d) 3.34 W (Time 0.0, 5.0, 11.50, 23.53 and 43.0 s from left to right) observed by FLIR (T-620). Temperature is measured in °C and time in seconds.

By increasing the input power, the temperature uniformity is achieved quicker than the lower input power. For P_{in} 2.07 W, a very clear temperature distribution has been observed after 11.50 s of *SAW* acting time and the temperature of the droplet becomes uniform after 23.53 s as identified in Figure 6.4-c.

Similar behaviour is observed for an input power of 3.34 W with temperature distribution to start after 5.0 s of *SAW* acting time and uniformity of the droplet achieved after 23.53 s of input power as shown in Figure 6.4-d. It is evident from all these cases that the T_d increases linearly with the increase in input power and T_d becomes uniform quicker with the higher P_{in} as compared to the lower. At higher input power, once T_d becomes uniform, then input power continues to increase the average temperature of the droplet which causes heat transfer mechanisms to increase both inside and outside of the droplet. Therefore, the maximum temperature achieved by Sezawa waves is 30.10 °C (55.60-25.50) °C at an input power of 3.34 W after 43.0 s of input *SAW* as predicted from Figure 6.4-d.

6.4.2.1 The rise in the average temperature of the droplet using Sezawa waves

The graphical form of average temperature increase inside the droplet at four different input power levels is presented in Figure 6.5. The average temperature of the droplet is not significant for low input power values as it is also depicted in Figure 6.4. For a low input power of 0.30 W, between time 2.0 to 3.0 s, the temperature gradient is 0.121 °C/s and for an input power of 3.34 W, it is 1.19 °C/s. Therefore, the gradient increases with the increase in input power, as shown in Figure 6.5.

Since high power has high streaming and vibration inside the droplet, that is why there are some fluctuations in the average T_d at an input power of 3.34 W, as presented in Figure 6.5. Moreover, it has been found that the temperature of the droplet increases linearly with the input power. For instance, the maximum rise in temperature at the input power of 0.30 W, 0.99 W, 2.07 W and 3.34 W is 3.82 °C, 9.91 °C, 18.61 °C and 29.65 °C respectively after 43.0 s of *SAW* elapsed time as shown in Figure 6.5. This means that the droplet temperature increases approximately by the rate of 9.91 °C/W. The relation between input power and the average temperature of the droplet has been presented graphically in Figure 6.6.

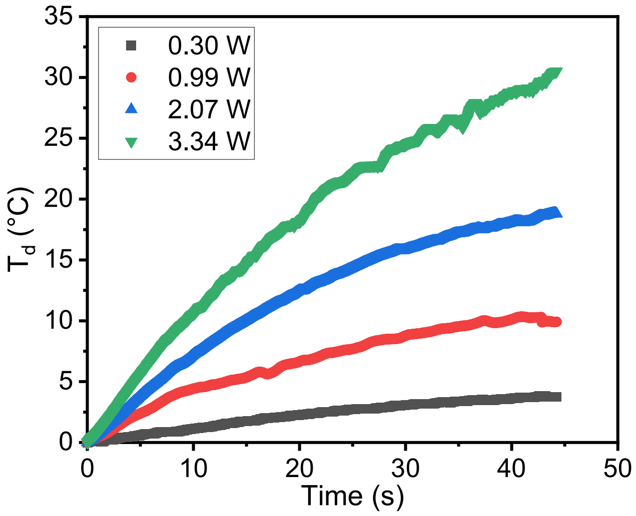

Figure 6.5: Average temperature increase inside the droplet using Sezawa waves at a power input of 0.30 W, 0.99 W, 2.07 W and 3.34 W. Temperature is measured in °C and time in seconds.

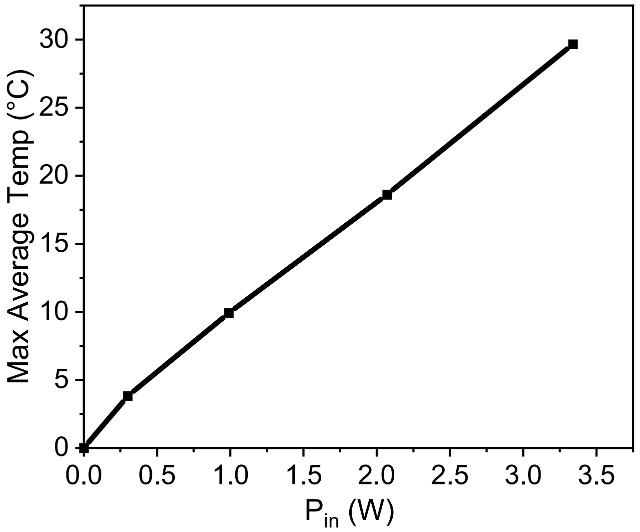

Figure 6.6: Maximum average temperature of the droplet after 43.0 s of *SAW* acting time for the input power values from 0.30 W to 3.34 W using Sezawa waves.

Temperature increase inside the droplet can be well explained from the gradient curves (*dT/dt*) against input power, as presented in Figure 6.7. The gradient can be obtained using curve fitting method or simple differentiation of average temperature values against time. An initial 'jump' has been observed for all power values at the start of input power. This 'jump' is not significant for an input power of 0.30 W. The impact delay identified in Figure 6.4-a has the reflection in Figure 6.7 for lower power value (0.30 W). However, a big jump has been observed for 0.99 W which is also clear from Figure 6.4-b. It is important to note that all the gradient lines make a 'wave' like visualization with frequencies vary from lower to higher power. This frequency can be measured by measuring the peak value which will be half of the frequency. For example, 0.30 W has 1/10 (1/s), for 0.99 W it increases to 1/14 (1/s) and infinity for higher power values of 2.07 W and 3.34 W.

The gradient for P_{in}, 0.30 W and 0.99 W, approaches to zero after 43.0 s of *SAW* elapsed time that means the droplet temperature reaches to the steady-state after 43.0 s of input *SAW* as shown in Figure 6.7. The highest gradient is accomplished with an input power of 3.34 W at the start of applying *SAW*. The maximum gradient attained by each input power value is presented in Figure 6.8. The abrupt increase in the temperature gradient of the droplet at the start of the input power of 0.99 W, as shown in Figure 6.8 is also clear from Figure 6.4.

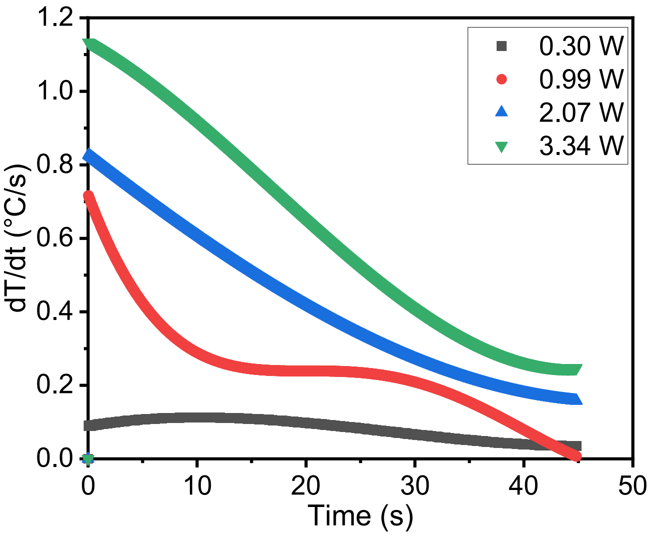

Figure 6.7: Temperature gradient *dT/dt* using Sezawa waves at 52.220 MHz with a power input values of 0.30 W, 0.99 W, 2.07 W and 3.34 W using S-waves.

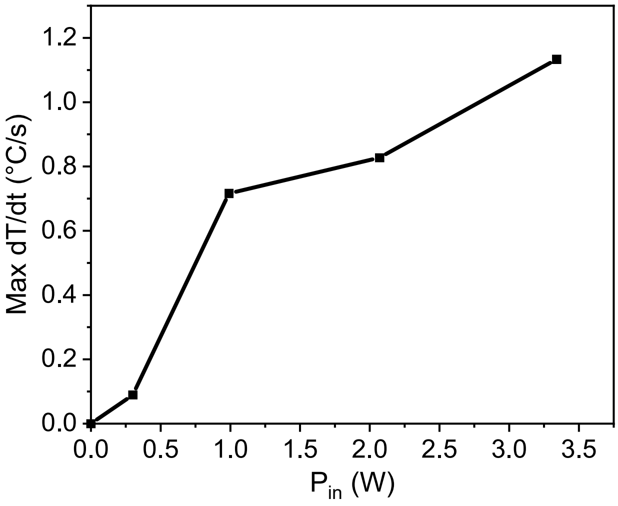

Figure 6.8: Max *dT/dt* at input power values of 0.30 W, 0.99 W, 2.07 W and 3.34 W using S-waves.

6.4.2.2 The temperature difference of substrate and the droplet

It has been observed that other than the *SAW* heating the droplet, the temperature of the substrate also changes which has an impact on the T_d. The temperature of the substrate is measured directly from the FLIR camera videos. The temperature of the bottom layer of the droplet, T_{db}, elements (13-16) close to the substrate, as shown in Figure 4.13, help to find $T_{(s\text{-}d)}$. The difference ($T_{(s\text{-}d)} = T_s - T_{db}$) versus time at four input power values is shown in Figure 6.9. It is evident from Figure 6.9 that $T_{(s\text{-}d)}$ is positive for power values < 1.0 W even after 43.0 s of *SAW* elapsed time which means that the substrate temperature remains higher than the droplet temperature in this power range. However, in the case of power values > 1.0 W, the difference $T_{(s\text{-}d)}$ remains positive for an initial 10.0 s, then it becomes negative, which means droplet temperature becomes higher than substrate temperature at 2.07 W and 3.34 W as shown in Figure 6.9. The detailed discussion about the heat transfer from the substrate to the droplet is presented in section 6.4.4.

T_{db} for different input power values is presented in Figure 6.10. The trend is almost similar as for the average temperature of the whole droplet but it is clear that T_{db} is higher than T_d as shown in Figure 6.10 and Figure 6.5. This is also evident from the thermal images of the droplet shown in Figure 6.4.

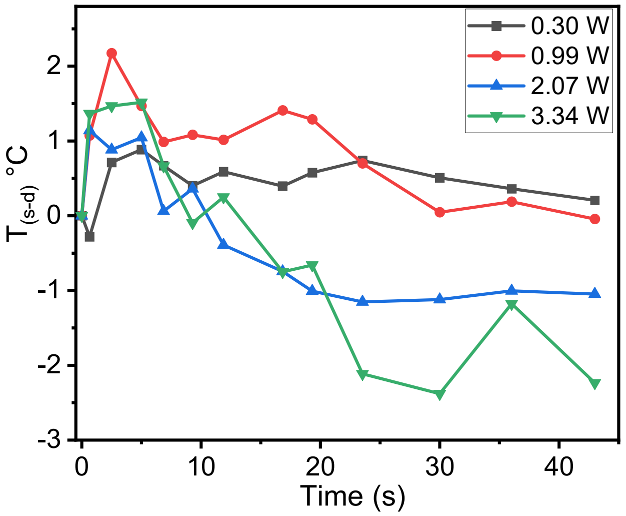

Figure 6.9: Temperature difference $T_{(s-d)}$ at different power levels using Sezawa waves at 0.30 W, 0.99 W, 2.07 W and 3.34 W from zero to 43.0 s. The negative difference means the temperature of the droplet is more as compared to the substrate.

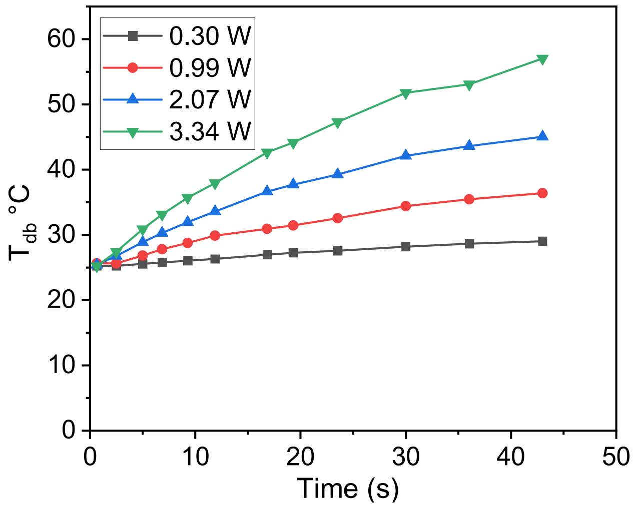

Figure 6.10: Temperature of the bottom boundary layer of the droplet T_{db} at power input values of 0.30 W, 0.99 W, 2.07 W and 3.34 W required to calculate $\dot{Q}_S$. T_{db} is measured in °C and time is measured in seconds.

6.4.3 The kinetic impacts of SAW on the droplet

The velocity of the particles estimated using the *PIV* method, detail of which is available in section 4.5.1. Average velocities of particles at three different positions inside the droplet at input power values of 0.30 W, 0.99 W, 2.07 W and 3.34 W are shown in Figure 6.11. It is evident from Figure 6.11 that similar to the T_d, average velocities of the droplet also increases with the time and with input power.

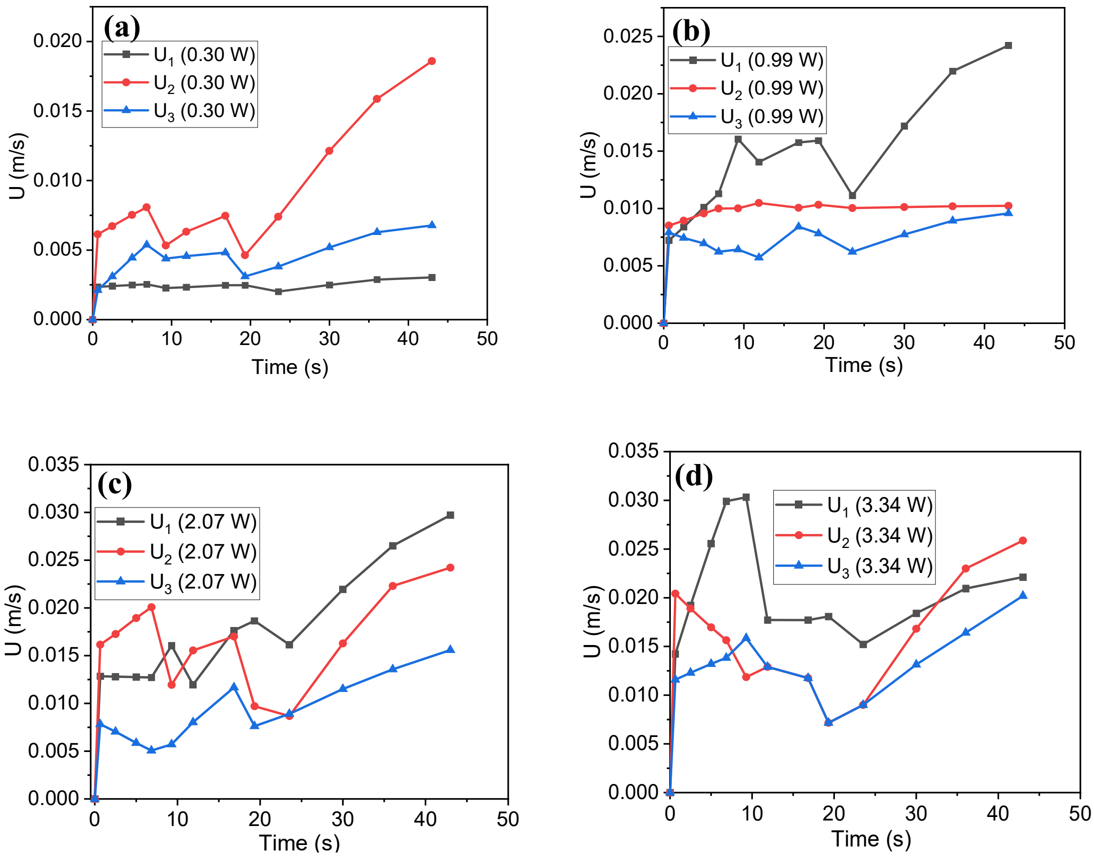

Figure 6.11: Average velocities of particles at three different positions inside the droplet at an input power of (a) 0.30 W (b) 0.99 W (c) 2.07 W (d) 3.34 W from zero to 43.0 s. U_1 belongs to the velocity close to the substrate, U_2 on the top of the droplet and U_3 is the vortex velocity.

Like R-waves, the average velocity of the particles for S-waves, near to the substrate (U_1) is the highest for all the cases except for the input power of 0.30 W. This means that, at lower power, near the substrate, friction is high enough which hinders the particles to move and increase their velocities, the inverse is the case for a higher power. Equations (3.8) and (3.9) show the relation for friction or friction coefficient. Velocity can be associated with the temperature of the droplet since where the velocity is higher, the temperature is also higher as compared to other portions inside the droplet. The detail for the influence of these streaming velocities on the kinetic energies has been presented in section 6.4.5.

6.4.4 *Diagnostics of heat transfers inside the droplet*

The proposed model shown in Figure 3.3 depicts that input power given to the droplet is utilized to absorb the energy by the droplet ($\dot{E}_d$), transfer heat from the edge of the droplet ($\dot{Q}_r$), from the substrate to the droplet ($\dot{Q}_s$), and from droplet to the surroundings ($\dot{Q}_a$).

The energy absorbed by the droplet ($\dot{E}_d$) is the rate of change in enthalpy which can be calculated using equation (4.14) as shown in Figure 6.12-a. It is clear from equation (4.14) that $\dot{E}_d$ is dependent on the temperature gradient of the droplet since other values do not change significantly. However, the change in heat capacity and density of the water within the temperature range of this study has been considered in the calculation and values listed in Table 5.3. Since other values in calculating $\dot{E}_d$ do not influence too much, that is why the trend of $\dot{E}_d$ is almost similar as for the temperature gradient of the droplet (Figure 6.7 for *dT/dt*).

More data points showing in the start of input *SAW* power in Figure 6.12-a is to focus on how energy entering inside the droplet changes the enthalpy of the droplet. The gradient decreases with time since T_d approaches the steady state. Moreover, $\dot{E}_d$ at 3.34 W is 1.5 times more as compared to $\dot{E}_d$ at 0.99 W. This means by increasing the input power three times increases the energy absorbed half of it.

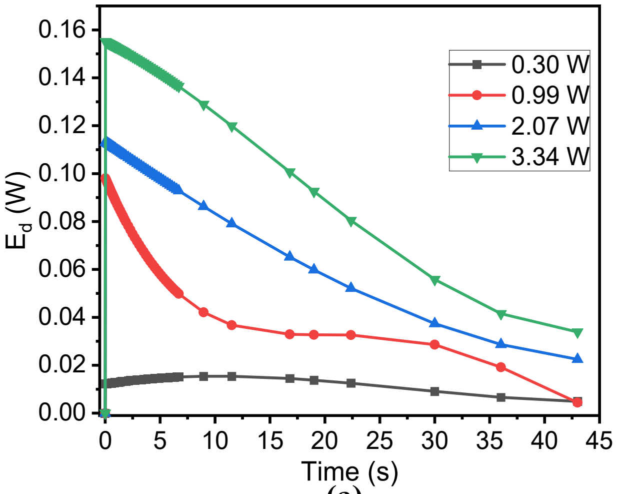

(a)

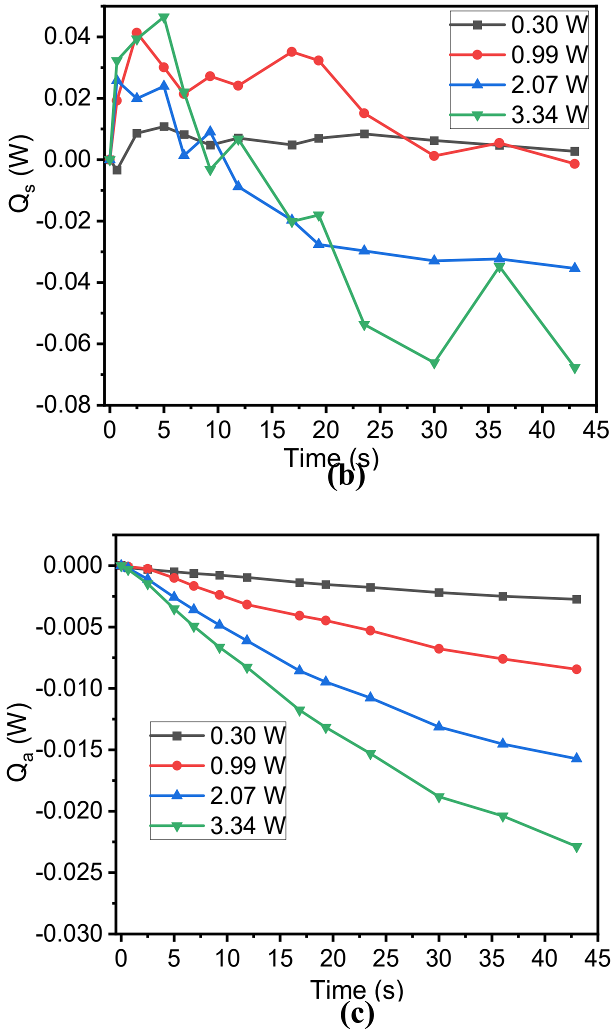

(b)

(c)

Figure 6.12: Rates of energy absorbed, heat transfers inside and outside of the droplet (a) $\dot{E}_d$ (rate of energy absorbed by the droplet), (b) $\dot{Q}_s$ rate of heat transfer from substrate to the droplet, (c) $\dot{Q}_a$ rate of heat transfer from air to the droplet using Sezawa waves at power input values of 0.30 W, 0.99 W, 2.07 W and 3.34 W.

The rate of heat transfer from the substrate to the droplet ($\dot{Q}_s$) is calculated by equation (4.15) and presented in Figure 6.12-b. $\dot{Q}_s$ is dependent on the effective heat transfer coefficient (α_s), the temperature difference between substrate and the droplet, $T_{(s\text{-}d)}$. The value of α_s has been calculated using co-relations mentioned in equation (4.16) and presented in Figure 6.13. The effective heat transfer coefficient does not influence too much since the droplet area is in the order of 10^{-5}, therefore, the trend for $\dot{Q}_s$ is quite similar to Figure 6.9 where the temperature difference, $T_{(s\text{-}d)}$, is presented against input power values.

Heat transfer takes place from substrate to the droplet when $P_{in} < 1.0$ W, however, the inverse is the case when $P_{in} > 1.0$ W after a few seconds of the input power as presented in Figure 6.12-b. The 'reverse time' has been introduced which means the time it takes for the heat transfer to go in the opposite direction, for instance, from droplet back to the substrate. For the case of power values, 2.07 W and 3.34 W, reverse time is 10.0 s after that heat starts flowing from droplet to the substrate as clearly shown in Figure 6.12-b.

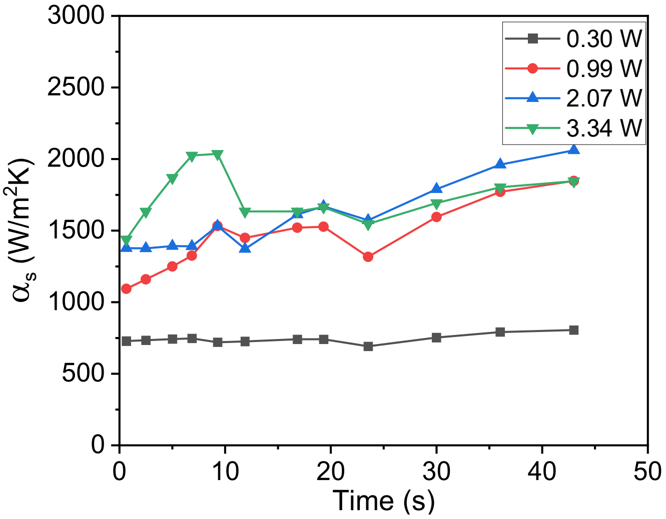

Figure 6.13: Effective heat transfer coefficient (α_s) for power values 0.30 W, 0.99 W, 20.7 W and 3.34 W against time 0.0 to 43.0 s for Sezawa. α_s is in W/m^{2}K and time is in seconds.

Rate of heat transfer from droplet to the air ($\dot{Q}_a$) is shown in Figure 6.12-c, calculated by equation (4.15). Effective heat transfer coefficient (α_a) has been used to find $\dot{Q}_a$ since natural convection heat transfer occurs in the surrounding near the droplet surface, calculated by equations (4.17) and (4.18) and presented in Figure 6.14 for illustration. Note that because of streaming inside the droplet, forced convection heat transfer takes place when considering $\dot{Q}_s$ which causes α_s to increase. The temperature difference between the air and the droplet outer layer is estimated by T_a-T_{ds}, where T_{ds} is calculated using the temperature of the elements of the outer layer and plotted in Figure 6.15. Note that these are the actual temperature values, not temperature rise.

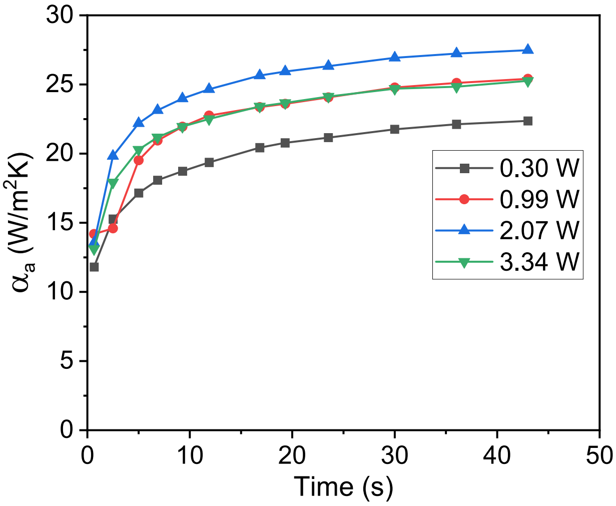

Figure 6.14: Effective heat transfer coefficient (α_a) for power values 0.30 W, 0.99 W, 20.7 W and 3.34 W against time 0.0 to 43.0 s for Sezawa. α_a is in W/m^{2}K and time is in seconds.

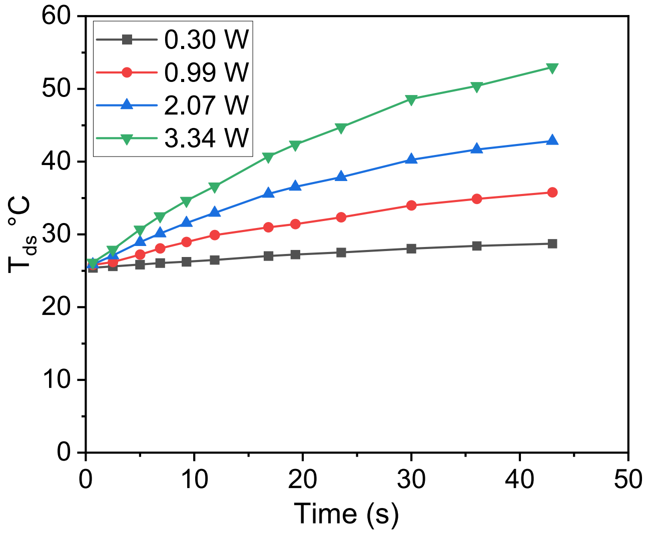

Figure 6.15: Temperature of the outer layer of the droplet (T_{ds}) directly in contact with air at power input values of 0.30 W, 0.99 W, 2.07 W and 3.34 W using Sezawa waves.

6.4.5 Diagnostics of kinetics inside the droplet using Sezawa

The model presented in Figure 3.3 also describes kinetic energies inside the droplet mainly because of streaming and friction near the substrate. How these mechanisms contribute to energy conservation is discussed in the following section.

The rates of kinetic energies of streaming $\dot{K}_{st}$ and friction $\dot{K}_f$ inside the droplet are calculated by equations (4.20) and (4.21) and presented in Figure 6.16 and Figure 6.17, respectively. The change in dynamic viscosity of the droplet, μ_d, (N.s/m^2), against temperatures from 20 °C to 50 °C is considered and listed in Table 5.4 [195]. Both kinetic energies are in the range of 10^{-7} to 10^{-9} (W) which are insignificant as compared to other heat transfers discussed in the above section. The positive value of kinetic energies means fluid absorbs power from the SAW, however, the negative value means the power being utilized in the increase in thermal energy of the droplet.

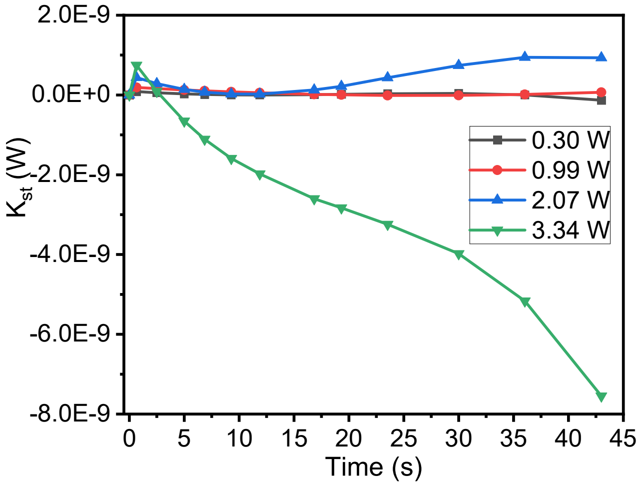

Figure 6.16: Rate of kinetic energies $\dot{K}_{st}$ (W), frictional power near the at power input values of 0.30 W, 0.99 W, 2.07 W and 3.34 W using S-waves. The rate of kinetic energies is measured in watts and time is measured in seconds.

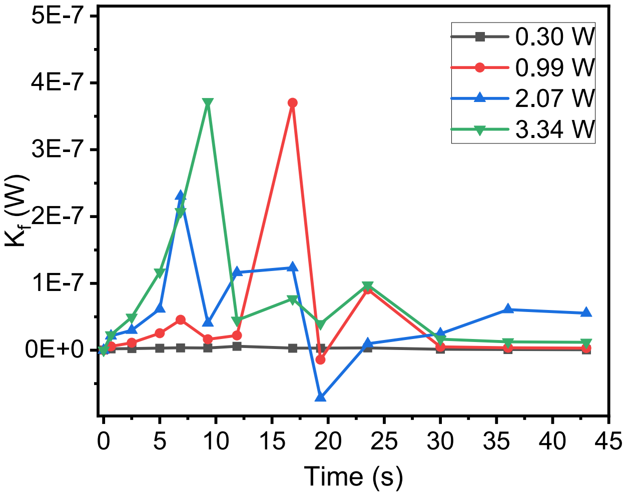

Figure 6.17: Rate of kinetic energies, $\dot{K}_f$ (W), Kinetic streaming power inside the droplet at power input values of 0.30 W, 0.99 W, 2.07 W and 3.34 W using S-waves. The rate of kinetic energies is measured in watts and time is measured in seconds.

6.4.6 Estimation of heat radiated inside the droplet

Radiated heat transfer ($\dot{Q}_r$) for four input power levels is calculated by equation (4.13) and are presented in Figure 6.18. $\dot{Q}_r$ is the heat transfer caused by *SAW* which enters from the edge of the droplet.

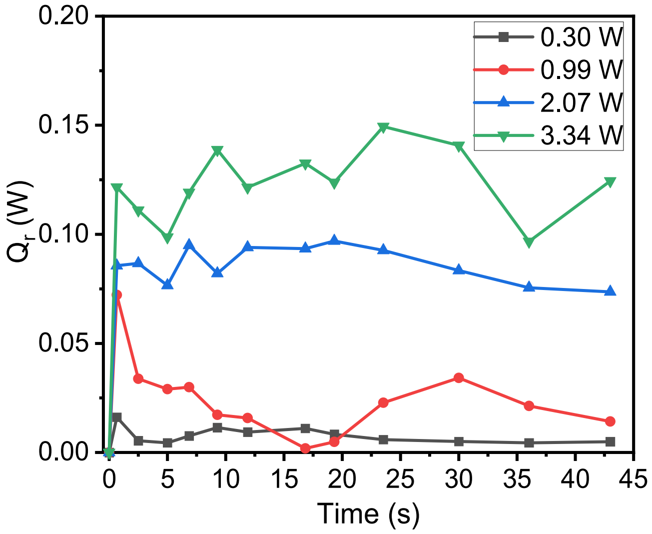

Figure 6.18: $\dot{Q}_r$ rate of heat radiated using Sezawa waves at power input values of 0.30 W, 0.99 W, 2.07 W, 3.34 W.

It is clear from Figure 6.18 that $\dot{Q}_r$ increases with the increase in input power and it varies with time. It has almost the same trend as depicted in Figure 5.21 for the Rayleigh waves. $\dot{Q}_r$ plays a significant role in the start of input power as an abrupt increase is shown just after the SAW penetrates inside the droplet. At a lower input power of 0.30 W, $\dot{Q}_r$ is not significant throughout the SAW acting time.

At 0.99 W, it shows an abrupt increase in the start with 0.07 W, then it shows some fluctuations and approaches to zero after 43.0 of *SAW* acting time as shown in Figure 6.18.

However, other than the abrupt increase in the start for the input power values of 2.07 W and 3.34 W, more power transferred into droplet and $\dot{Q}_r$ reaches to the peak quicker than the lower input power. It can be confirmed for these larger input power cases, that the droplet does not reach a steady-state as shown in Figure 6.18. Therefore, $\dot{Q}_r$ plays an important role in the increase in the thermal impact of the SAW especially in the start of input power. The maximum value of 0.15 W is obtained when P_{in} is 3.34 W. The summary of all the heat transfers and kinetic energies inside the droplet using Sezawa waves is presented in the form of droplet model in Figure 6.19.

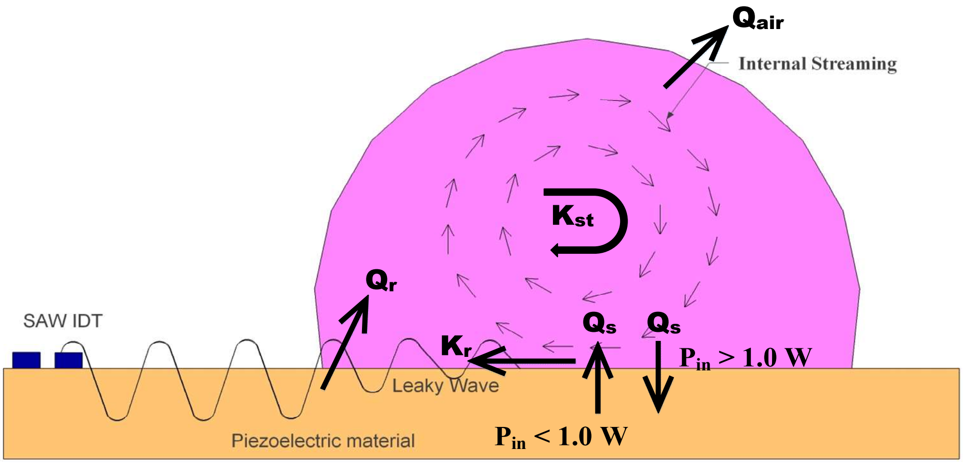

Figure 6.19: Summary of kinetic energies (K_{st} & K_f) and heat transfers (Q_r, Q_s & Q_a) inside the droplet using Sezawa waves.

6.5 Repeatability of experiments

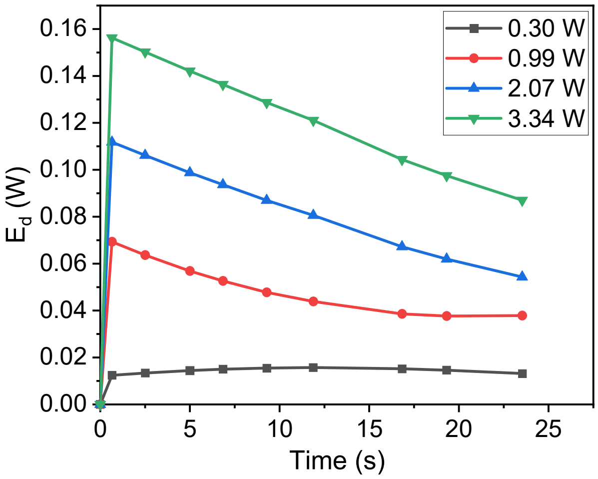

(a)

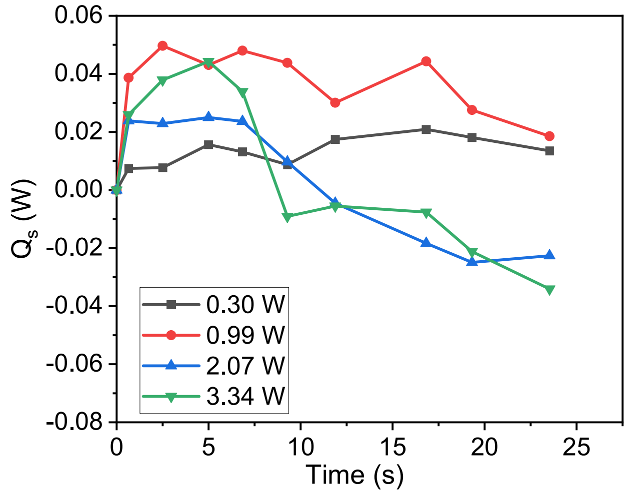

(b)

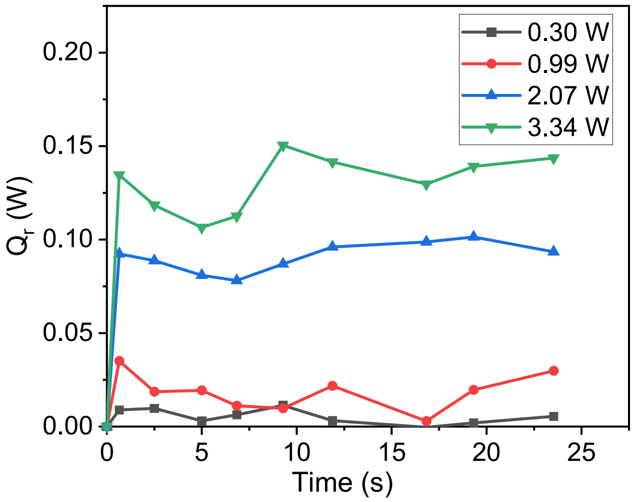

(c)

Figure 6.20: Rate of energy absorbed ($\dot{E}_d$), heat transfer from substrate to the droplet ($\dot{Q}_s$), heat radiated inside the droplet ($\dot{Q}_r$) at input power values of 0.30 W, 0.99 W, 2.07 W and 3.34 W using Sezawa waves.

It was observed during the lab experiment that device showed excellent repeatability when the experiments were repeated keeping the same parameters. Since kinetic energies are not significant, therefore, only terminologies related to the heat transfer are presented in Figure 6.20.

Figure 6.20-a, b can be compared with Figure 6.12-a and b where energy absorbed and heat transfer from the substrate to the droplet can be compared. Similarly, Figure 6.20-c can be compared with Figure 6.18. It is important to note from these figures that a similar trend has been observed when the tests were repeated, only there is a small difference in their values.

6.6 Summary

Mass, momentum, and energy conservation principles have been implemented using Sezawa waves in this chapter. Above discussion concludes that there is no significant mass transfer in the power range 0.30 W to 3.34 W. Relative mass change regarding original mass is less than 5%, within the error range. Results from only higher power levels i.e. 2.07 W and 3.34 W are presented here for illustration.

Momentum conservation has been analysed using the same model with input power levels of 3.34 W and 4.18 W. Since Sezawa waves travel inside the layers, that is why these waves have less acoustic velocity due to which droplet remains stationary and no significant deformation observed in these cases. Since inertial and the drag force become zero with no buoyancy force, then *SAW* force become equal to the friction force (9.85E-6 N for P_{in} 3.34 W)**.**

The thermal impacts dominate when the energy conservation principle has been implemented. The mechanical power is not significant as the volume change inside the droplet with time is in the order of (10^{-9} to 10^{-10}) m^3/s.

The impact delay is significant at lower input power, however, there is no impact delay at the higher input power. Clear and quicker temperature distribution is achieved at higher input power values which leads to faster uniformity of the droplet within *SAW* elapsed time. The reflection of this is also identified in the average temperature of the droplet. Moreover, the temperature of the droplet increases linearly with the input power. The temperature gradient of the droplet is significant in the start of input power which then reduces with time as T_d approaches to the steady state, especially at the lower input power.

Energy absorbed by the droplet ($\dot{E_d}$) is maximum as compared to all other heat transfers and kinetic energies inside the droplet. The impact of the change of heat capacity of the water and the density with the temperature has been considered which is not significant within the temperature range of this study. $\dot{E_d}$ showed a similar trend as for the temperature gradient as other values remain almost constant.

Heat transfer from substrate to the droplet for ($\dot{Q_s}$) takes place when $P_{in} < 1.0$ W, however, inverse heat flux will take place from the droplet to the substrate after the 'reverse time' when $P_{in} > 1.0$ W. The 'reverse time' has been introduced as the time when the droplet temperature becomes higher than the substrate. Since other values in calculating $\dot{Q}_s$ do not change significantly, that is why, $\dot{Q}_s$ showed a similar trend as the temperature difference between substrate and the droplet $T_{(s\text{-}d)}$.

The natural convection heat transfer takes place between the droplet and the surroundings which causes the heat to flow from droplet to the air ($\dot{Q}_a$). Due to natural convection heat transfer, effective heat transfer coefficient, α_a, is much smaller than α_s, where forced convection has been observed because of streaming inside the droplet.

Kinetic energies due to friction and streaming inside the droplet are in the order of 10^{-7} and 10^{-9} W which is not significant as compared to other heat transfers inside the droplet. $\dot{Q}_r$ does not play a vital role for the lower power but the higher power, it has a significant part in the start of input power which means that more power penetrates inside the droplet at the higher power.

A similar trend has been observed for the mass and energy conservation principles using Sezawa waves. However, no momentum has been observed in the case of Sezawa because of the difference in wave transportation. This proves our assumptions and model works for other wave modes as well. It will be quite interesting to know how these waves behave differently in terms of energy and kinetic inside the droplet which is part of the next chapter.

Chapter 7: Comparison of The Impacts of SAW Modes and Other Parameters on The Droplet

The mass, momentum and energy impacts of SAW with Rayleigh and Sezawa mode are analyzed or diagnosed in Chapter 5 and Chapter 6, respectively. In this chapter, the discussions are made to the specifics of the impacts of those two SAW modes in terms of comparison of the results obtained from the last two chapters, a summarization. The second section of this chapter is for the comparisons of the impacts of Rayleigh and Lamb hybridized wave with those from the pure Rayleigh, followed with investigations of the impacts of SAW with different frequencies on the droplet.

7.1 The comparison of impacts of Rayleigh and Sezawa waves on droplet

The difference between the transportation mechanisms of Rayleigh and Sezawa on the SAW devices has already been discussed in section 2.3.1 and 2.3.2 of Chapter 2. The comparisons are made to examine the impacts on droplet mass, momentum and energy using the data diagnosed in Chapter 5 and Chapter 6. The comparisons are made for two wave modes at the powers most closely with each other.

7.1.1 The mass impacts of R-wave Vs S-wave

The conclusions from both the SAW mode in the droplet mass impacts are that the impacts on droplet mass and even the volume are the neglectable small. The measurement errors on droplet volume from two SAW modes are within the same order of the magnitude, which leads to a maximum change in mass smaller than 5%. However, it is found that changes in mass from measurements of Rayleigh mode are relatively smaller than those from Sezawa mode, as shown in Figure 7.1 and Figure 7.2**.** At input power values of 2.0 W and 3.2 W of Rayleigh mode with droplet initial mass of 3.49E-4 kg and 3.29E-4 kg, the maximum relative mass changes are 1.3% and 4.2% respectively. While, for Sezawa mode, the maximum relative mass changes are 3.5% and 4.4% from the initial mass of the droplet of 2.69E-4 kg and 3.02E-4 kg at 2.07 W and 3.34 W, respectively. This is also clear from in Figure 7.1 and Figure 7.2. As the changes in mass discussed here actually are the errors from measurements which may be from the camera resolution, the smaller size of the droplet or the surrounding light and temperature.

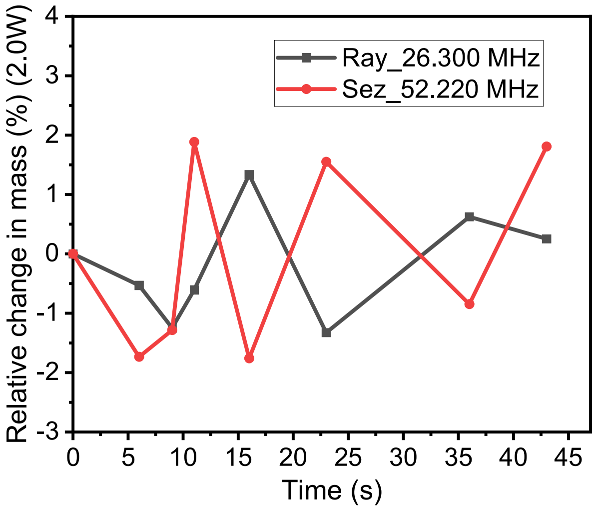

Figure 7.1: Comparison of relative change in mass of the droplet versus time for Rayleigh and Sezawa at 2.0 W.

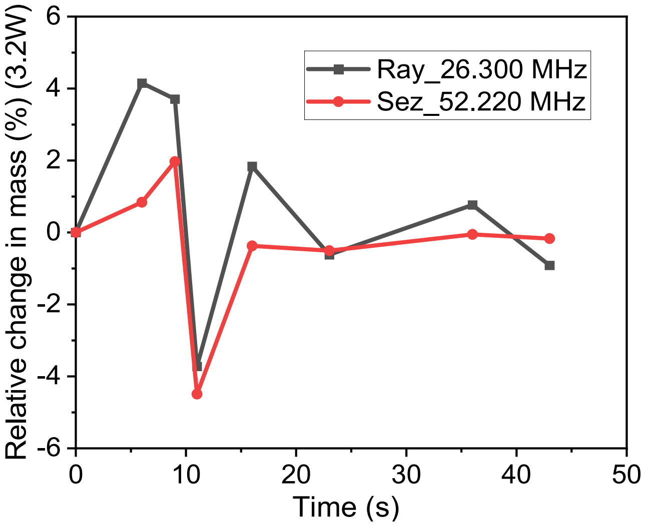

Figure 7.2: Comparison of relative change in mass of the droplet versus time for Rayleigh and Sezawa at 3.2 W.

7.1.2 The momentum impacts of R-wave Vs S-wave

The *SAW* forces acting to the droplet by Rayleigh mode drives the droplet to a certain distance from the original position. In the Sezawa mode, no droplet movement is observed from experimental data, due to the relatively smaller *SAW* force. As the interfacial tension force is the force governed by the physical property of interfacial tension, which is same for both modes. This can be identified by the difference between the friction forces of two modes. The friction force using Rayleigh is 8.37E-5 N at an input power of 3.2 W whereas

9.85E-6 N using Sezawa mode at input power of 3.34 W which is about 10 times smaller. This means that Sezawa waves result in weaker streaming inside the droplet.

7.1.3 The thermal impacts of R-wave Vs S-wave on droplet

From the diagnosed results, it can be concluded that both modes show the same trend for heat transfers and the kinetic energies inside the droplet. The significant difference is in the radiation power penetrated inside the droplet. Therefore, only this source term is discussed for the thermal impacts of these two modes.

The first difference is that the radiation powers from Sezawa mode (Figure 6.18) are all smaller than those of the Rayleigh mode (Figure 5.21), which associates with the difference in the leakage power from those two modes. More power can be leaked into droplet by Rayleigh mode *SAW*.

Another significant difference is the evaluations of the radiation power with time. From the results presented in Figure 5.21 of the Rayleigh waves, a significant change has been observed when the *SAW* input power becomes greater than 0.90 W. This phenomenon or dynamic mechanism may be understood by the theory of the *SAW* transportation from the films to the water droplet, the mechanism of *SAW* power leakage into the droplet.

However, the results from Sezawa mode plotted in Figure 6.18, especially the high input powers (2.07 W and 3.34 W), are kept approximately stable with some fluctuations.

The difference between these two modes lies in the transportation of the waves on the *SAW* device. The Sezawa *SAW* transfers through the interface between the substrate and the *ZnO* film, which makes a relative lower leaked power to the droplet. However, the Rayleigh waves transfer on the thin *ZnO* film and leak more power into the droplet, causing more energy and more thermal impact inside the droplet.

7.2 The thermal impacts of hybridized waves on the droplet

The coupling impacts mechanisms discussed in previous chapters are from the *SAW* device with a fixed thickness of the substrate and film, which generates Rayleigh and Sezawa. In this section, the thermal impacts of a hybrid mode SAW on droplet are investigated. The hybridized (hybrid) wave is defined as a mixture of pure Lamb and the Rayleigh at one fixed frequency.

For the hybrid *SAW*, a device with a thickness of 200 µm and a *ZnO* thin film of thickness 5 µm has been used. The structure of the device, fabrication of *IDT* and the sputtering process is similar as shown in Figure 4.1 and section 4.1.2, respectively. However, the specific characteristics and the vibration modes of the SAW with variable wavelengths (λ) can be found from Figure 7.3 [197]. On the middle column in Figure 7.3, the first resonant frequency can be obtained by this device at 13.80 MHz with Rayleigh, but at the same frequency, there is a zero-order anti-symmetric mode of Lamb wave (A_0). This means at 13.80 MHz, the wave is not purely Rayleigh but a mixture of two waves of Lamb and Rayleigh. This *SAW* wave mode is called as a hybrid mode. The devices with λ 300 µm and 400 µm have not been used in this study.

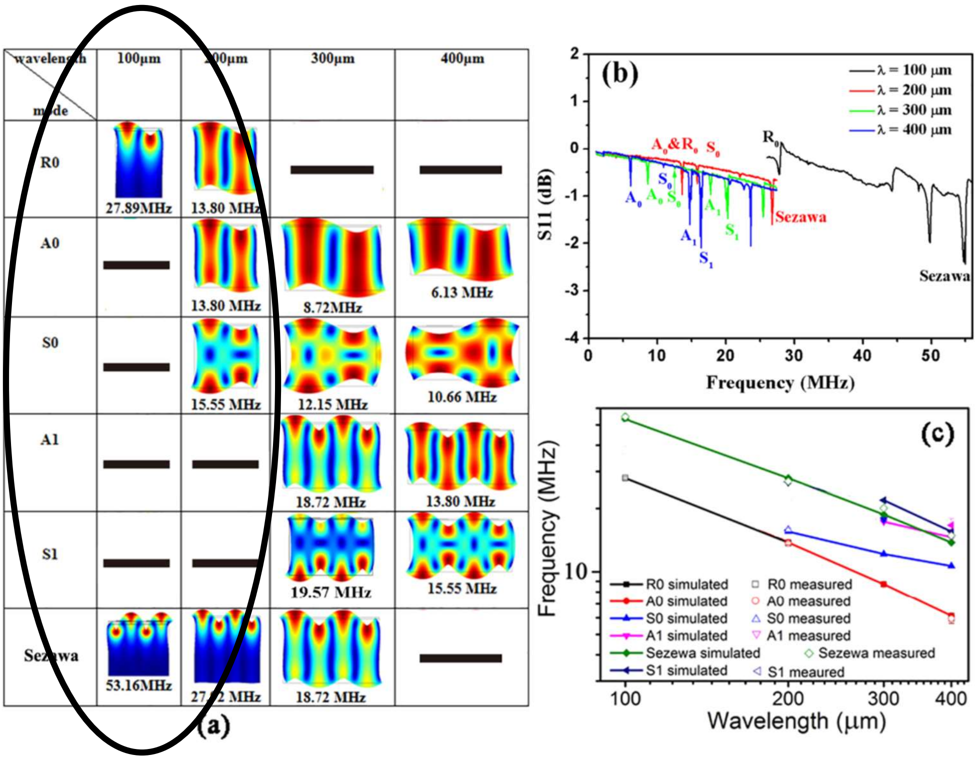

Figure 7.3: Numerical simulation of vibration modes for *ZnO* (5 µm)/Al(200 µm) based *SAW* devices. The wavelength of the *SAW* device varies from 100 µm to 400 µm. (b) The measured S_{11} of the devices with different wavelengths (c) the simulated and measured resonant frequencies of different types of wave modes depend on the wavelength of the *SAW* devices fabricated on *Al* plates with thickness of 200 µm [197].

The thermal impacts of such a hybrid mode *SAW* on the droplet is investigated and the results are discussed in terms of the rise in droplet temperatures as compared to those from pure Rayleigh or Sezawa modes to see how this hybrid *SAW* works.

7.2.1 Comparison of thermal impact of hybridized wave versus pure Rayleigh

The vibrational velocity for hybrid waves is higher than pure Rayleigh waves which means these waves have more acoustic efficiency than Rayleigh waves [111]. Hybrid waves generated from the device having a thickness, 200 µm, and wavelength, 200 µm, whereas Rayleigh waves generated from the device with thickness, 200 µm, and wavelength, 100 µm. Both Rayleigh and hybrid waves are observed at their fundamental resonant frequencies of 27.063 MHz and 13.500 MHz, respectively. Hybrid waves produce a strong thermal impact as compared to those from purely Rayleigh waves for both power inputs as shown in Figure 7.4 and Figure 7.5**.** For a low input power of 2.2 W, the temperature T_d from hybrid wave mode is 3.5 times higher than the T_d from Rayleigh mode at a time after 32.0 s of an input *SAW*. However, this drop to 2.5 times at higher input of 3.2 W.

It is also clear from Figure 7.4 and Figure 7.5 that with the hybrid waves, the gradient of the T_d becomes zero (steady-state) after 25.0 s of input *SAW* for both input power values, whereas there is still some gradient shown by Rayleigh waves. This is very useful for processes where quicker thermal steady-state required.

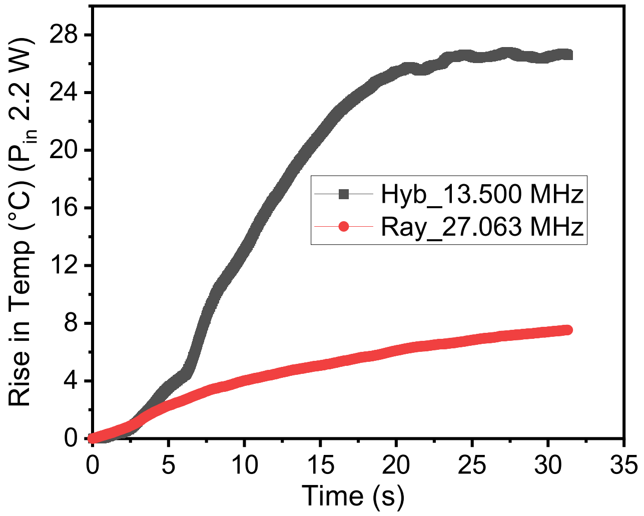

Figure 7.4: Comparison of temperature rise of the droplet by Rayleigh and hybridized mode using the same thickness of the substrate at the power input of 2.2 W. The average temperature is measured in °C whereas time is measured in seconds.

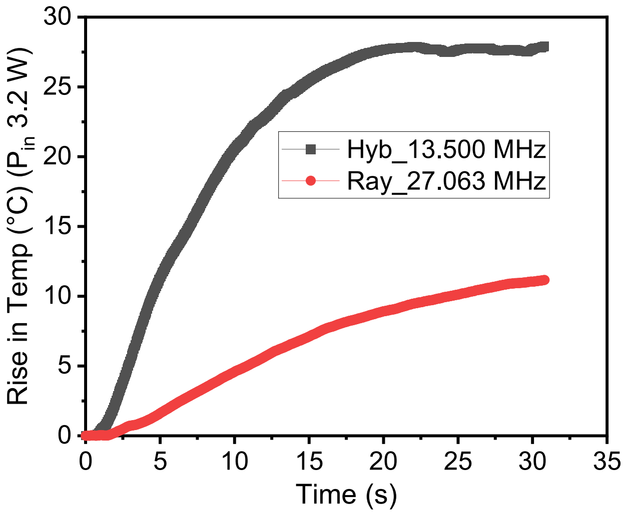

Figure 7.5: Comparison of Rayleigh and hybridized mode using the same thickness of the substrate at P_{in} of 3.2 W. The average temperature is measured in °C whereas time is measured in seconds.

7.2.2 Comparison of thermal impact of hybridized wave versus pure Sezawa

The same device having hybrid wave mode at the first resonant peak shows pure Sezawa with higher-order harmonics at 27.92 MHz as presented in Figure 7.3-a

It is identified from Figure 7.6 and Figure 7.7 that the same trend has been observed with pure Sezawa as it was for pure Rayleigh. For Sezawa wave, the gradient is still increasing with the time but with the hybrid wave mode, it gets stable after 20.0 s of the input *SAW*, quicker than Rayleigh. It is identified in Chapter 5 and Chapter 6 that the difference in temperature rise from Rayleigh and Sezawa modes are not significant. However, it is significant between those of the hybrid wave and those from both the Rayleigh and Sezawa as shown in Figure 7.6 and Figure 7.7.

At lower input power, T_d is 2.5 times more as compared to the Sezawa after just 5.0 s of input *SAW* because of a hybridized wave. However, it increases to 4.0 times after 10.0 s and the same trend is observed after 30.0 s of an input *SAW* as shown in Figure 7.6.

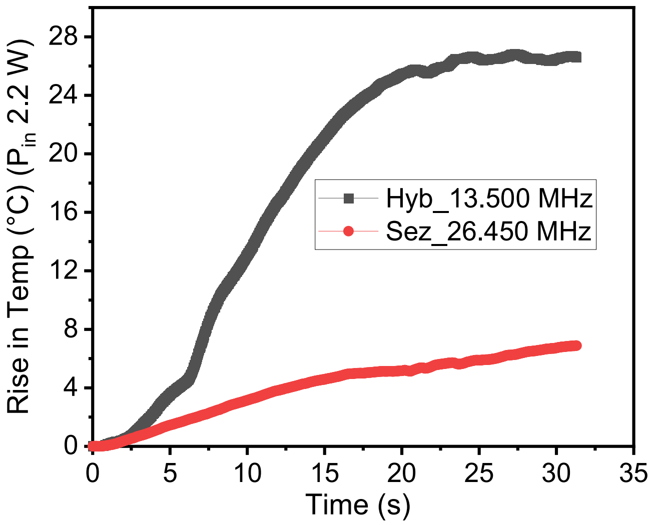

Figure 7.6: Comparison of temperature rise of the droplet by hybridized mode and Sezawa using the same device at the input power of 2.2 W. The average temperature is measured in °C whereas time is measured in seconds.

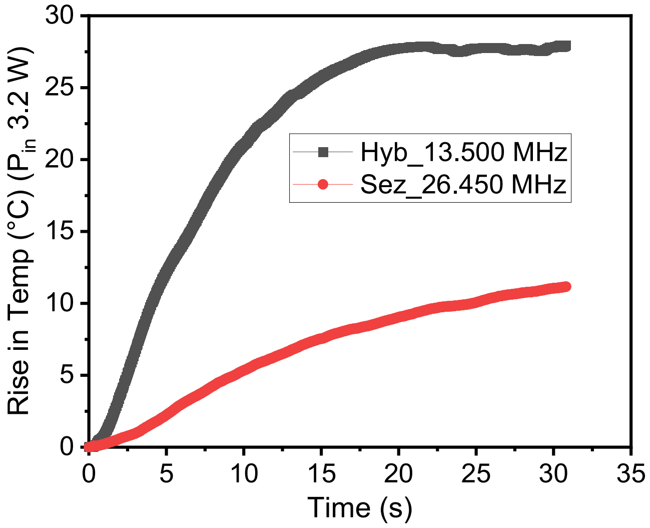

Figure 7.7: Comparison of temperature rise of the droplet by hybridized mode and Sezawa using the same device at the input power of 3.2 W. The average temperature is measured in °C whereas time is measured in seconds.

At power input of 3.2 W, just after 5.0 s of *SAW* input, hybridized wave showed almost 5.5 times more T_d as compared to pure Sezawa. However, the difference decreases with time as the gradient for both cases increases from 5.0 to 15.0 seconds. Sezawa showed 3.5 times less temperature as compared to the hybridized wave after 15.0 s of input power as shown in Figure 7.7. This difference further decreases to 2.5 times after 30.0 s of the input power.

7.3 Thermal impacts of Sezawa at two different frequencies

The temperature increases inside the droplet, is dependent on the frequency of the wave and wave mode. The devices in this study have at least two wave modes, one is the Rayleigh at the fundamental resonant frequency (f_0) and the other is Sezawa. By changing the wavelength of the waves with different devices, resonant frequencies and the wave mode changes [197]. In this way, one can use the same wave (either Rayleigh or Sezawa) at a different resonant frequency to check how much a frequency of the waves influence the thermal impacts by T_d.

The resonant frequency for Sezawa wave for the device h=200 μm, λ=200 μm is 27.92 MHz shown in Figure 7.3-a whereas for the device h=600 μm, λ =100 μm is 52.53 MHz as shown in Figure 5.1-a. Therefore, a good comparison can be made using these two different devices generating Sezawa mode at different resonant frequencies to discuss the thermal impact of frequency on droplet by T_d. The resonant frequency showing in the literature [197] may differ from the real-time values when checked from the network analyser due to the number of reasons. Therefore, for the first device, a frequency of 26.450 MHz was obtained whereas, for the second one, a frequency of 52.220 MHz was measured. A comparison of the temperature rise of the droplet at these two different frequencies using the Sezawa wave is shown in Figure 7.8 and Figure 7.9 at different power levels.

It is evident from Figure 7.8 and Figure 7.9 that device with higher frequency has higher thermal impact using Sezawa waves for both input power of 2.0 W and 3.20 W. It is also clearly shown from Figure 7.8, an input power of 2.0 W, with lower frequency, that temperature rises at a larger gradient until to 15.0 s and then at a relative lower gradient till to 32.0 s of input *SAW*. The largest temperature rise is 6.73 $^{\circ}$C. However, with higher frequency, the temperature increases at a larger gradient and it increases with time until the end with a temperature rise of 15.5 $^{\circ}$C. This is because, at low frequency, waves are damped more quickly as compared to the high frequency that results in less thermal impacts.

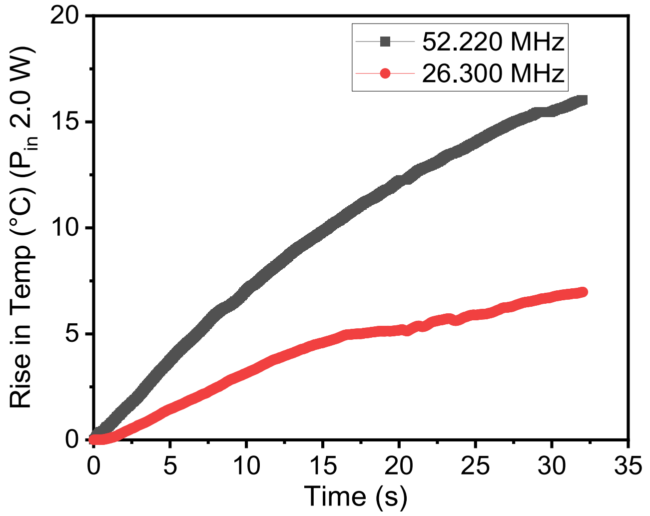

Figure 7.8: Temperature rise of the droplet using Sezawa waves at two different frequencies (26.450 MHz and 52.220 MHz) at an input power of 2.0 W. The average temperature is measured in °C whereas time is measured in seconds.

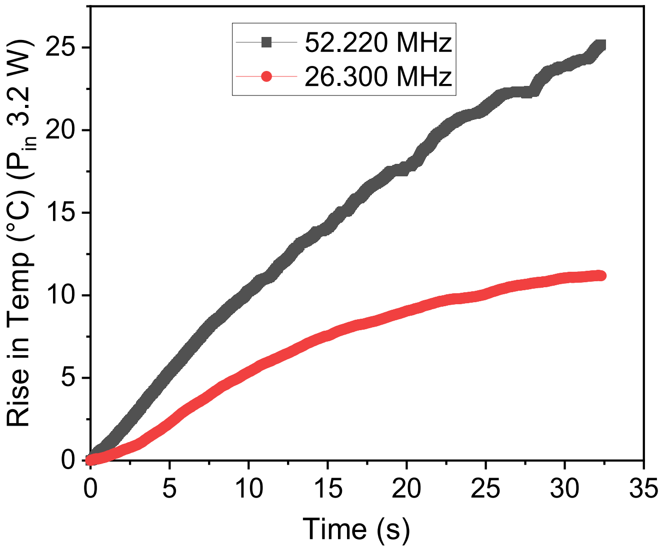

Figure 7.9: Temperature rise of the droplet using Sezawa waves at two different frequencies at P_{in} 3.20 W. The average temperature is measured in °C whereas time is measured in seconds.

The similar behaviour is observed with a high input power of 3.20 W, as given in Figure 7.9. Increasing the input power increases the temperature rise linearly. For instance, temperature rise after 30.0 s of an input *SAW* by the higher frequency at 3.2 W is 1.5 times more than at 2.0 W. Therefore, with the power increase of 1.6 times, the temperature increases with the almost similar factor. The temperature difference between lower and higher frequency is almost similar as was at 2.0 W as shown in Figure 7.9.

It can be concluded that with the same wave mode, the waves at higher frequency has more mechanical vibration and stress inside the substrate, which leads to more power leakage into the droplet, the stronger thermal impact [36], [202].

7.4 Summary

Comparison of Rayleigh and Sezawa in terms of mass, momentum and energy conservation has been presented in this chapter. There is no mass transfer from both waves as the size of the droplet remains unchanged and the droplet temperature is much lower than the saturation temperature.

Since Sezawa travels in the interlayers, therefore, less *SAW* force and less temperature have been observed using Sezawa as compared to the Rayleigh. Rayleigh showed momentum at input power of 3.2 W and 4.0 W, however, no momentum has been observed using Sezawa.

In terms of thermal impact, Sezawa showed less temperature rise, therefore, energy absorbed, and heat radiated with Sezawa wave is less than the Rayleigh waves. The mixture of Rayleigh and Lamb hybridized wave has more acoustic energy consequently having higher temperatures as compared to the pure Rayleigh and Sezawa waves. Moreover, temperature increase inside the droplet increases linearly with the increase in input power. Furthermore, because of more attenuation, higher frequency causes higher temperature as compared to the lower frequency at the same power level with the same wave mode.

Chapter 8: Conclusions and Future Recommendations

In this study, a model has been proposed based on mass, momentum, and energy conservation principles to investigate thermal and kinetic impacts of *SAW* on the droplet. Since this study is focussed on less input power (0.30 W to 4.0 W) and less temperature rise (5 to 30 °C), therefore, mass and momentum of the droplet are not significant. However, a significant change in the thermal impact has been observed. Energy transfer leads to finding the coupling mechanism between streaming and thermal impact using Rayleigh and Sezawa waves. Furthermore, the impact of change in wave mode and frequency by changing the device on T_d has also been explored. Derived key conclusions along with the limitations of this research and future suggestions are outlined in the following sections.

8.1 Conclusions

Since this study is based on temperature much lower than the saturation temperature, therefore, no phase change has been observed. However, evaporation has been detected by detecting the change in the mass of the droplet. For R-waves, it has been observed that the mass change to the initial mass is less than 5%, 1.3% and 4.2% for the input power of 2.0 W and 3.2 W, respectively.

At the input power of 3.2 W, just after applying the input power, the *SAW* force dominates other forces which push the droplet to move in the direction of the waves at the velocity of 0.1 mm/s within 1.0 s of *SAW* elapsed time. Then interfacial tension force becomes dominant, so deceleration starts from 1.0 s to 4.0 s and the droplet completely stops after 4.0 s of the *SAW* elapsed time.

At the input power of 4.0 W, just after applying the input power, the same mechanism occurs but the *SAW* force is higher as compared to lower input power. Therefore, the droplet moves with a higher velocity of 0.60 mm/s after 1.0 s of *SAW* elapsed time. However, as time passes, deceleration occurs, surface tension forces become dominant which stops the droplet after 4.0 s of *SAW* elapsed time.

The mass transfer for the S-waves has been calculated using the same method which showed an exactly similar trend as shown by R-waves. The mass change to the original mass is also less than 5%, which is within the range of measurement error. For the input power of 2.07 W and 3.34 W, the change is 3.5% and 4.4%, respectively. Since S-waves travel between layers, that is why no momentum has been observed within the power range of this study. Therefore, the drag force and the inertial force is zero which means the *SAW* force is balanced by the friction force.

The temperature of the droplet has a linear relation with the input power as illustrated in for both Rayleigh and Sezawa waves. There are two main reasons to increase T_d. Firstly, because of waves penetrating inside the droplet, secondly, heat transfer from the substrate to the droplet. Maximum temperature rise by the R-waves at the P_{in} 3.2 W is 30.86 °C, however, the temperature of 29.76 °C has been observed using Sezawa waves at 3.34 W. Therefore, Sezawa has 3.7% lesser temperature rise as compared to the Rayleigh.

It has been observed that the input energy (power) given to the droplet is converted majorly into two portions: kinetic and thermal energy. It can be concluded that the thermal energy dominates than kinetic energies inside the droplet. To find the heat transfer from the substrate to the droplet $\dot{Q}_s$ and from droplet to the air $\dot{Q}_a$, streaming (kinetic, '*Re*') has been associated with the temperature values. Dimensionless numbers, '*Nu*' and '*Gr*' helped to find co-relations to find the coupling mechanism. Forced convection takes place when heat transfers from the substrate to the droplet takes place. This can be identified by calculating an effective heat transfer coefficient (α_s) between the substrate and the droplet.

The heat transfer from the substrate to the droplet ($\dot{Q}_s$) changes its direction when moving from lower input power to the higher input power. In the case of Rayleigh waves, it has been observed that the temperature of the bottom layer of the droplet (T_{db}) is lower than that of the substrate at $P_{in} < 0.50$ W. The data showed that the substrate (solid) has 1.9% more temperature as compared to the T_{db} after 30.0 s of the *SAW* acting time at P_{in} of 0.38 W. However, at $P_{in} > 0.50$ W, T_{db} has 2.7% more temperature as compared to the substrate after the same time of input *SAW*. Therefore, heat transfer takes place from the substrate to the droplet ($\dot{Q}_s$ is positive) when $P_{in} < 0.50$ W and the inverse is the case when $P_{in} >$ 0.50 W after 'reverse time'.

In the case of Sezawa, the same trend has been observed as with the Rayleigh. The substrate has 2.2% more temperature as compared to T_{db} after 23.0 s of input *SAW* at P_{in}

< 1.0 W. However, at P_{in} > 1.0 W, T_{db} has 3.01% more temperature as compared to the substrate after the same time of input *SAW*. Therefore, heat transfer takes place from substrate to the droplet when P_{in} < 1.0 W and the inverse is the case when P_{in} > 1.0 W after 'reverse time'.

The heat transfer from the droplet to the air ($\dot{Q}_a$) is negative for both Rayleigh and Sezawa since heat is always leaving the system. The temperature of the droplet is higher than the surrounding temperature which causes the natural convection heat transfer. This phenomenon can be identified by calculating effective heat transfer coefficient (α_a) between the droplet and the air. Due to forced convection inside the droplet, α_s is much larger than α_a where natural convection takes place.

$\dot{E}_d$ increases linearly with the input power for both Rayleigh and Sezawa waves. $\dot{E}_d$ is mainly dependent on the temperature gradient. Since T_d approaches the steady-state, that is why the gradient decreases over time and approaches zero for lower input power values.

The heat penetrated from the edge of the droplet ($\dot{Q}_r$) has an important role. In the case of Rayleigh waves, it increases with the increase in input power. For lower input power, it reaches to the steady state after 25.0 s of the *SAW* elapsed time. However, for higher input power, it reaches to the peak quicker than lower input power but it does not reach the steady-state.

Almost the same trend has been observed with Sezawa waves. Since Sezawa has less temperature gradient than Rayleigh, that is why the value of $\dot{Q}_r$ is also less as compared to the Rayleigh. At lower input power value of 0.99 W, $\dot{Q}_r$ shows a big jump in the start of input power but it approaches zero after 43.0 s of *SAW* acting time. However, for larger input power values, it touches the peak quicker but does not reach the steady state.

It has been found that the frequency of *SAW* is directly proportional to the temperature rise of the droplet. For example, when considering the Sezawa mode with resonant frequencies of 26.450 MHz and 52.220 MHz. The droplet on a device with higher frequency showed a double temperature as compared to the device with lower frequency observed at P_{in} of 2.0 W and 4.70 W. This is because high frequency has more attenuation and dissipation of the waves which causes more power radiated into the droplet as compared to the lower one using the same wave.

Since Lamb and Rayleigh hybridized waves have more vibrational velocity and acoustic energy that gives higher temperature gradient than pure Rayleigh and Sezawa. Therefore, hybridized waves give 3.5 times and 2.5 times more T_d as compared to pure R-waves and S-waves with the input power levels of 2.0 W and 3.2 W, respectively. Moreover, droplet reaches to steady state quicker (~ 20.0 s of an input *SAW*) with hybridized mode as compared to pure Rayleigh mode.

8.2 Answer to the questions from literature

The literature only gives information about the temperature rise of the droplet. However, this study demonstrates different heat transfer mechanisms inside the droplet with the help of coupling kinetic and thermal data. The results have been validated with both Rayleigh and Sezawa waves.

The information that the substrate and the droplet have a different temperature but how long does it take place is not clear. However, in this study, this has been extensively investigated and discussed with the calculation of heat transfer. Moreover, a 'reverse time' has been introduced which gives the information of when the droplet temperature becomes higher than the substrate.

The portion of the droplet near the *SAW* has more temperature as compared to the other portion of the droplet but there is no evidence of temperature in other portions of the droplet. However, in this study, with the help of FLIR camera and MATLAB image processing technique, very precise temperature distribution has been observed which gives clear information about temperature in different portions of the droplet.

Bulk piezoelectric material ($LiNbO_3$) has been used before this study for both thermal and kinetic impacts. However, in this study, thin-film piezoelectric material has been used to find out both thermal and kinetic impacts.

Till now, hybridized waves only used for the nebulization of the droplet but in this study, the thermal impact of these waves have also been investigated and results compared with pure Rayleigh waves.

8.3 Limitations of this work

Both *CCD* and FLIR thermal cameras can capture 2D images only which results in kinetic and thermal impacts only from two dimensions and do not give any information for the third dimension. Moreover, the thermal camera has only a zoom of 4x which hinders to get a high-quality picture. Furthermore, the study has been conducted with only one size of the droplet (25 µl) which do not give an idea of how the coupling mechanism will change by changing the droplet size. Therefore, how this study can be the basis of further research work has been discussed in the following section.

8.4 Future work

Although mass, momentum and energy conservations have been implemented using Rayleigh and Sezawa waves and results have been completely presented and discussed. However, this is limited to low power values before significant deformation or pumping. At higher power, the droplet may breakup to have atomization or jetting phenomenon. It can also evaporate or phase change due to the rise in temperature. Therefore, to investigate further, future work should be aimed at the following points.

Conservation principles have been implemented using *ZnO* as thin-film material and *Al* plate as a substrate. In future, these models can be applied to other thin-film materials such as *AlN*, *PZT* and other substrates to explain the mechanism further.

This study has been performed using 25 µl water droplet. It will be interesting to implement these models for different sizes of water droplets and perform the comparison.

This research is limited to low power and less temperature; however, future work can aim at a higher temperature range and high-power values to investigate and implement all conservation principles.

Future study is suggested with the high-quality cameras with more resolution, with more frames per second values and those which can capture the data in three dimensions.

Finally, this study has been conducted using Rayleigh, Sezawa and hybridized waves. This provided the foundation to apply other wave modes such as pure Lamb wave, Shear horizontal waves, transverse waves and *SSAW*.

References

[1] Lord Rayleigh, "On waves propagated along the plane surface of an elastic solid," *Proc. London Math. Soc.*, vol. 1, no. 1, pp. 4–11, 1885.

[2] R. M. White and F. W. Voltmer, "Direct piezoelectric coupling to surface elastic waves," *Appl. Phys. Lett.*, vol. 7, no. 12, pp. 314–316, 1965.

[3] Y. Q. Fu *et al.*, "Recent developments on ZnO films for acoustic wave based bio-sensing and microfluidic applications: a review," *Sensors Actuators B Chem.*, vol. 143, no. 2, pp. 606–619, 2010.

[4] N.-T. Nguyen, S. T. Wereley, and S. A. M. Shaegh, *Fundamentals and applications of microfluidics*. Artech house, 2019.

[5] G. Destgeer and H. J. Sung, "Recent advances in microfluidic actuation and micro-object manipulation via surface acoustic waves," *Lab Chip*, vol. 15, no. 13, pp. 2722–2738, 2015.

[6] D. W. Galipeau, P. R. Story, K. A. Vetelino, and R. D. Mileham, "Surface acoustic wave microsensors and applications," *Smart Mater. Struct.*, vol. 6, no. 6, p. 658, 1997.

[7] K. Sritharan, C. J. Strobl, M. F. Schneider, A. Wixforth, and Z. von Guttenberg, "Acoustic mixing at low Reynold's numbers," *Appl. Phys. Lett.*, vol. 88, no. 5, p. 54102, 2006.

[8] Z. Wang and J. Zhe, "Recent advances in particle and droplet manipulation for lab-on-a-chip devices based on surface acoustic waves," *Lab Chip*, vol. 11, no. 7, pp. 1280–1285, 2011.

[9] C. Chen *et al.*, "Three-dimensional numerical simulation and experimental

investigation of boundary-driven streaming in surface acoustic wave microfluidics," *Lab Chip*, vol. 18, no. 23, pp. 3645–3654, 2018.

[10] H. Zec, D. J. Shin, and T.-H. Wang, "Novel droplet platforms for the detection of disease biomarkers," *Expert Rev. Mol. Diagn.*, vol. 14, no. 7, pp. 787–801, 2014.

[11] A. Wixforth, C. Strobl, C. Gauer, A. Toegl, J. Scriba, and Z. v Guttenberg, "Acoustic manipulation of small droplets," *Anal. Bioanal. Chem.*, vol. 379, no. 7–8, pp. 982–991, 2004.

[12] W. Connacher *et al.*, "Micro/nano acoustofluidics: materials, phenomena, design, devices, and applications," *Lab Chip*, vol. 18, no. 14, pp. 1952–1996, 2018.

[13] J. Kondoh, N. Shimizu, Y. Matsui, M. Sugimoto, and S. Shiokawa, "Development of temperature-control system for liquid droplet using surface Acoustic wave devices," *Sensors Actuators A Phys.*, vol. 149, no. 2, pp. 292–297, 2009.

[14] S. Ito, M. Sugimoto, Y. Matsui, and J. Kondoh, "Study of surface acoustic wave streaming phenomenon based on temperature measurement and observation of streaming in liquids," *Jpn. J. Appl. Phys.*, vol. 46, no. 7S, p. 4718, 2007.

[15] A. Renaudin, V. Chabot, E. Grondin, V. Aimez, and P. G. Charette, "Integrated active mixing and biosensing using surface acoustic waves (SAW) and surface plasmon resonance (SPR) on a common substrate," *Lab Chip*, vol. 10, no. 1, pp. 111–115, 2010.

[16] G. Greco, M. Agostini, R. Shilton, M. Travagliati, G. Signore, and M. Cecchini, "Surface Acoustic Wave (SAW)-Enhanced Chemical Functionalization of Gold Films," *Sensors*, vol. 17, no. 11, p. 2452, 2017.

[17] S. Li, J. Desrosiers, and V. R. Bhethanabotla, “Heating of Rayleigh surface acoustic wave devices in 128° YX LiNbO 3 and ST X quartz substrates,” in *2017 IEEE SENSORS*, 2017, pp. 1–3.

[18] T. Roux-Marchand, D. Beyssen, F. Sarry, S. Grandemange, and O. Elmazria, “Rayleigh surface acoustic wave compatibility with microdroplet polymerase chain reaction,” *Int. J. Microscale Nanoscale Therm. Fluid Transp. Phenom.*, vol. 4, no. 3/4, p. 231, 2013.

[19] E. Fradet, C. McDougall, P. Abbyad, R. Dangla, D. Mcgloin, and C. N. Baroud, “Combining rails and anchors with laser forcing for selective manipulation within 2D droplet arrays,” *Lab Chip*, vol. 11, no. 24, pp. 4228–4234, 2011.

[20] C. Cortez-Jugo, A. Qi, A. Rajapaksa, J. R. Friend, and L. Y. Yeo, “Pulmonary monoclonal antibody delivery via a portable microfluidic nebulization platform,” *Biomicrofluidics*, vol. 9, no. 5, p. 52603, 2015.

[21] J. Kondoh, N. Shimizu, Y. Matsui, and S. Shiokawa, “Liquid heating effects by SAW streaming on the piezoelectric substrate,” *IEEE Trans. Ultrason. Ferroelectr. Freq. Control*, vol. 52, no. 10, pp. 1881–1883, 2005.

[22] R. G. Kryshtal, A. P. Kundin, A. V Medved, and V. V Shemet, “Surface acoustic wave gas sensor of the sorption type sensitive to the thermal properties of gases,” *Tech. Phys. Lett.*, vol. 28, no. 1, pp. 50–51, 2002.

[23] A. E. Rajapaksa *et al.*, “Effective pulmonary delivery of an aerosolized plasmid DNA vaccine via surface acoustic wave nebulization,” *Respir. Res.*, vol. 15, no. 1, pp. 1–12, 2014.

[24] M. Alvarez, L. Y. Yeo, J. R. Friend, and M. Jamriska, “Rapid production of

protein-loaded biodegradable microparticles using surface acoustic waves," *Biomicrofluidics*, vol. 3, no. 1, p. 14102, 2009.

[25] A. Qi, L. Yeo, J. Friend, and J. Ho, "The extraction of liquid, protein molecules and yeast cells from paper through surface acoustic wave atomization," *Lab Chip*, vol. 10, no. 4, pp. 470–476, 2010.

[26] Y. K. Lentz, T. J. Anchordoquy, and C. S. Lengsfeld, "DNA acts as a nucleation site for transient cavitation in the ultrasonic nebulizer," *J. Pharm. Sci.*, vol. 95, no. 3, pp. 607–619, 2006.

[27] A. Manz, N. Graber, and H. áM Widmer, "Miniaturized total chemical analysis systems: a novel concept for chemical sensing," *Sensors actuators B Chem.*, vol. 1, no. 1–6, pp. 244–248, 1990.

[28] C. Zhang, D. Xing, and Y. Li, "Micropumps, microvalves, and micromixers within PCR microfluidic chips: Advances and trends," *Biotechnol. Adv.*, vol. 25, no. 5, pp. 483–514, 2007.

[29] F. Zhang, B. Liu, W. Liu, and Q. Zhang, "DNA computing model based on lab-on-a-chip and its application on solving the timetabling problem," *Prog. Nat. Sci.*, vol. 18, no. 5, pp. 633–637, 2008.

[30] A. Qi, J. R. Friend, L. Y. Yeo, D. A. V Morton, M. P. McIntosh, and L. Spiccia, "Miniature inhalation therapy platform using surface acoustic wave microfluidic atomization," *Lab Chip*, vol. 9, no. 15, pp. 2184–2193, 2009.

[31] Z. J. Jiao, X. Y. Huang, and N.-T. Nguyen, "Scattering and attenuation of surface acoustic waves in droplet actuation," *J. Phys. A Math. Theor.*, vol. 41, no. 35, p. 355502, 2008.

[32] H. Nakahata *et al.*, “Diamond-based surface acoustic wave devices,” *Semicond. Sci. Technol.*, vol. 18, no. 3, p. S96, 2003.

[33] D. Morgan, *Surface acoustic wave filters: With applications to electronic communications and signal processing*. Academic Press, 2010.

[34] M. Darmawan and D. Byun, “Focused surface acoustic wave induced jet formation on superhydrophobic surfaces,” *Microfluid. Nanofluidics*, vol. 18, no. 5–6, pp. 1107–1114, 2015.

[35] T.-T. Wu and I.-H. Chang, “Actuating and detecting of microdroplet using slanted finger interdigital transducers,” *J. Appl. Phys.*, vol. 98, no. 2, p. 24903, 2005.

[36] Y. Q. Fu *et al.*, “Advances in piezoelectric thin films for acoustic biosensors, acoustofluidics and lab-on-chip applications,” *Prog. Mater. Sci.*, 2017.

[37] M. M. de Lima Jr, F. Alsina, W. Seidel, and P. V Santos, “Focusing of surface-acoustic-wave fields on (100) GaAs surfaces,” *J. Appl. Phys.*, vol. 94, no. 12, pp. 7848–7855, 2003.

[38] M. Jangi *et al.*, “Concentrated vertical jetting mechanism for isotropically focused Zno/Si surface acoustic waves,” *Int. J. Multiph. Flow*, vol. 114, pp. 1–8, 2019.

[39] X. He *et al.*, “Bendable ZnO thin film surface acoustic wave devices on polyethylene terephthalate substrate,” *Appl. Phys. Lett.*, vol. 104, no. 21, p. 213504, 2014.

[40] D. L. Kim, W. H. Jeong, G. H. Kim, and H. J. Kim, “Solution-processed indium–zinc oxide with carrier-suppressing additives,” *J. Inf. Disp.*, vol. 13, no. 3, pp.

113–118, 2012.

[41] Y. Sun and J. A. Rogers, “Inorganic semiconductors for flexible electronics,” *Adv. Mater.*, vol. 19, no. 15, pp. 1897–1916, 2007.

[42] L. Zhou, A. Wanga, S.-C. Wu, J. Sun, S. Park, and T. N. Jackson, “All-organic active matrix flexible display,” *Appl. Phys. Lett.*, vol. 88, no. 8, p. 83502, 2006.

[43] M. Focke, D. Kosse, C. Müller, H. Reinecke, R. Zengerle, and F. von Stetten, “Lab-on-a-Foil: microfluidics on thin and flexible films,” *Lab Chip*, vol. 10, no. 11, pp. 1365–1386, 2010.

[44] D. Son *et al.*, “Multifunctional wearable devices for diagnosis and therapy of movement disorders,” *Nat. Nanotechnol.*, vol. 9, no. 5, p. 397, 2014.

[45] Y. Liu *et al.*, “Flexible and bendable acoustofluidics based on ZnO film coated aluminium foil,” *Sensors Actuators B Chem.*, vol. 221, pp. 230–235, 2015.

[46] A. V Mamishev, K. Sundara-Rajan, F. Yang, Y. Du, and M. Zahn, “Interdigital sensors and transducers,” *Proc. IEEE*, vol. 92, no. 5, pp. 808–845, 2004.

[47] V. P. Plessky and L. M. Reindl, “Review on SAW RFID tags,” *IEEE Trans. Ultrason. Ferroelectr. Freq. Control*, vol. 57, no. 3, pp. 654–668, 2010.

[48] P. Delsing *et al.*, “The 2019 surface acoustic waves roadmap,” *J. Phys. D. Appl. Phys.*, vol. 52, no. 35, p. 353001, 2019.

[49] M. J. Vellekoop, “Acoustic wave sensors and their technology,” *Ultrasonics*, vol. 36, no. 1–5, pp. 7–14, 1998.

[50] T. Franke, S. Braunmüller, L. Schmid, A. Wixforth, and D. A. Weitz, “Surface acoustic wave actuated cell sorting (SAWACS),” *Lab Chip*, vol. 10, no. 6, pp. 789–794, 2010.

[51] A. Wixforth, “Acoustically driven planar microfluidics,” *Superlattices Microstruct.*, vol. 33, no. 5–6, pp. 389–396, 2003.

[52] S. P. Zhang *et al.*, “Digital acoustofluidics enables contactless and programmable liquid handling,” *Nat. Commun.*, vol. 9, no. 1, pp. 1–11, 2018.

[53] R. N. Thurston, A. D. Pierce, and E. P. Papadakis, *Reference for Modern Instrumentation, Techniques, and Technology: Ultrasonic Instruments and Devices I: Ultrasonic Instruments and Devices I.* Academic Press, 1998.

[54] C. S. Hartmann, “Systems impact of modern Rayleigh wave technology,” in *Rayleigh-Wave Theory and Application*, Springer, 1985, pp. 238–253.

[55] I. M. Mason and E. A. Ash, “Acoustic Surface-Wave Beam Diffraction on Anisotropic Substrates,” *J. Appl. Phys.*, vol. 42, no. 13, pp. 5343–5351, 1971.

[56] A. J. Slobodnik and E. D. Conway, “New high-frequency high-coupling low-beam-steering cut for acoustic surface waves on LiNbO3,” *Electron. Lett.*, vol. 6, no. 6, pp. 171–173, 1970.

[57] A. Takayanagi, K. Yamanouchi, and K. Shibayama, “Piezoelectric leaky surface wave in LiNbO3,” *Appl. Phys. Lett.*, vol. 17, no. 5, pp. 225–227, 1970.

[58] K. Shibayama, K. Yamanouchi, H. Sato, and T. Meguro, “Optimum cut for rotated Y-cut LiNbO 3 crystal used as the substrate of acoustic-surface-wave filters,” *Proc. IEEE*, vol. 64, no. 5, pp. 595–597, 1976.

[59] H. Campanella *et al.*, “Localized and distributed mass detectors with high sensitivity based on thin-film bulk acoustic resonators,” *Appl. Phys. Lett.*, vol. 89, no. 3, p. 33507, 2006.

[60] K. M. Lakin, “Thin film resonator technology,” in *IEEE International Frequency*

Control Symposium and PDA Exhibition Jointly with the 17th European Frequency and Time Forum, 2003. Proceedings of the 2003, 2003, pp. 765–778.

[61] J. Du, G. L. Harding, A. F. Collings, and P. R. Dencher, "An experimental study of Love-wave acoustic sensors operating in liquids," *Sensors Actuators A Phys.*, vol. 60, no. 1–3, pp. 54–61, 1997.

[62] M.-I. Rocha-Gaso, C. March-Iborra, Á. Montoya-Baides, and A. Arnau-Vives, "Surface generated acoustic wave biosensors for the detection of pathogens: A review," *Sensors*, vol. 9, no. 7, pp. 5740–5769, 2009.

[63] N. Barie and M. Rapp, "Covalent bound sensing layers on surface acoustic wave (SAW) biosensors," *Biosens. Bioelectron.*, vol. 16, no. 9–12, pp. 979–987, 2001.

[64] G. Kovacs and A. Venema, "Theoretical comparison of sensitivities of acoustic shear wave modes for (bio) chemical sensing in liquids," *Appl. Phys. Lett.*, vol. 61, no. 6, pp. 639–641, 1992.

[65] F. Josse, F. Bender, and R. W. Cernosek, "Guided shear horizontal surface acoustic wave sensors for chemical and biochemical detection in liquids," *Anal. Chem.*, vol. 73, no. 24, pp. 5937–5944, 2001.

[66] G. McHale, M. I. Newton, and F. Martin, "Theoretical mass, liquid, and polymer sensitivity of acoustic wave sensors with viscoelastic guiding layers," *J. Appl. Phys.*, vol. 93, no. 1, pp. 675–690, 2003.

[67] G. Lindner, "Sensors and actuators based on surface acoustic waves propagating along solid–liquid interfaces," *J. Phys. D. Appl. Phys.*, vol. 41, no. 12, p. 123002, 2008.

[68] E. Gizeli, F. Bender, A. Rasmusson, K. Saha, F. Josse, and R. Cernosek,

"Sensitivity of the acoustic waveguide biosensor to protein binding as a function of the waveguide properties," *Biosens. Bioelectron.*, vol. 18, no. 11, pp. 1399–1406, 2003.

[69] D. S. Brodie, Y. Q. Fu, Y. Li, M. Alghane, R. L. Reuben, and A. J. Walton, "Shear horizontal surface acoustic wave induced microfluidic flow," *Appl. Phys. Lett.*, vol. 99, no. 15, p. 153704, 2011.

[70] G. McHale, "Generalized concept of shear horizontal acoustic plate mode and Love wave sensors," *Meas. Sci. Technol.*, vol. 14, no. 11, p. 1847, 2003.

[71] A. J. Flewitt *et al.*, "ZnO based SAW and FBAR devices for bio-sensing applications," *J. Nonnewton. Fluid Mech.*, vol. 222, pp. 209–216, 2015.

[72] P. Hess, "Surface acoustic waves in materials science," *Phys. Today*, vol. 55, no. 3, pp. 42–47, 2002.

[73] J. D. N. Cheeke, *Fundamentals and applications of ultrasonic waves*. CRC press, 2016.

[74] K. Sezawa and K. Kanai, "Discontinuity in dispersion curves of Rayleigh-waves," *Proc. Imp. Acad.*, vol. 11, no. 1, pp. 13–14, 1935.

[75] X. Y. Du *et al.*, "ZnO film thickness effect on surface acoustic wave modes and acoustic streaming," *Appl. Phys. Lett.*, vol. 93, no. 9, p. 94105, 2008.

[76] W. Macke, "MR Redwood,(Lecturer in Electrical Engineering. Queen Mary college, Univ. of London), Mechanica-Waveguides. The propagation of acoustic and ultra 1 sonic waves in fluids and solids with boundaries. VIII+ 300 S. Oxford/London/New York/Paris 1960, Pergamon ," *ZAMM-Journal Appl. Math. Mech. für Angew. Math. und Mech.*, vol. 41, no. 7-8, p. 336, 1961.

[77] J. W. Grate, S. W. Wenzel, and R. M. White, “Frequency-independent and frequency-dependent polymer transitions observed on flexural plate wave ultrasonic sensors,” *Anal. Chem.*, vol. 64, no. 4, pp. 413–423, 1992.

[78] H. Lamb, “On waves in an elastic plate,” *Proc. R. Soc. London. Ser. A, Contain. Pap. a Math. Phys. character*, vol. 93, no. 648, pp. 114–128, 1917.

[79] P. Muralt *et al.*, “Piezoelectric micromachined ultrasonic transducers based on PZT thin films,” *IEEE Trans. Ultrason. Ferroelectr. Freq. Control*, vol. 52, no. 12, pp. 2276–2288, 2005.

[80] R. M. Moroney, R. M. White, and R. T. Howe, “Microtransport induced by ultrasonic Lamb waves,” *Appl. Phys. Lett.*, vol. 59, no. 7, pp. 774–776, 1991.

[81] J. C. Pyun, H. Beutel, J.-U. Meyer, and H. H. Ruf, “Development of a biosensor for E. coli based on a flexural plate wave (FPW) transducer,” *Biosens. Bioelectron.*, vol. 13, no. 7–8, pp. 839–845, 1998.

[82] J. Pepper *et al.*, “Detection of proteins and intact microorganisms using microfabricated flexural plate silicon resonator arrays,” *Sensors Actuators B Chem.*, vol. 96, no. 3, pp. 565–575, 2003.

[83] I.-Y. Huang and M.-C. Lee, “Development of a FPW allergy biosensor for human IgE detection by MEMS and cystamine-based SAM technologies,” *Sensors Actuators B Chem.*, vol. 132, no. 1, pp. 340–348, 2008.

[84] C.-M. Lin *et al.*, “Temperature-compensated aluminum nitride Lamb wave resonators,” *IEEE Trans. Ultrason. Ferroelectr. Freq. Control*, vol. 57, no. 3, pp. 524–532, 2010.

[85] J. Shi, X. Mao, D. Ahmed, A. Colletti, and T. J. Huang, “Focusing microparticles

in a microfluidic channel with standing surface acoustic waves (SSAW)," *Lab Chip*, vol. 8, no. 2, pp. 221–223, 2008.

[86] L. Y. Yeo and J. R. Friend, "Surface acoustic wave microfluidics," *Annu. Rev. Fluid Mech.*, vol. 46, pp. 379–406, 2014.

[87] J. Shi, H. Huang, Z. Stratton, Y. Huang, and T. J. Huang, "Continuous particle separation in a microfluidic channel via standing surface acoustic waves (SSAW)," *Lab Chip*, vol. 9, no. 23, pp. 3354–3359, 2009.

[88] F. Petersson, A. Nilsson, H. Jönsson, and T. Laurell, "Carrier medium exchange through ultrasonic particle switching in microfluidic channels," *Anal. Chem.*, vol. 77, no. 5, pp. 1216–1221, 2005.

[89] T. Uchida, T. Suzuki, and S. Shiokawa, "Investigation of acoustic streaming excited by surface acoustic waves," in *1995 IEEE Ultrasonics Symposium. Proceedings. An International Symposium*, 1995, vol. 2, pp. 1081–1084.

[90] L. A. Kuznetsova and W. T. Coakley, "Applications of ultrasound streaming and radiation force in biosensors," *Biosens. Bioelectron.*, vol. 22, no. 8, pp. 1567–1577, 2007.

[91] A. A. Doinikov, "Acoustic radiation interparticle forces in a compressible fluid," *J. Fluid Mech.*, vol. 444, p. 1, 2001.

[92] J. Nam, H. Lim, D. Kim, and S. Shin, "Separation of platelets from whole blood using standing surface acoustic waves in a microchannel," *Lab Chip*, vol. 11, no. 19, pp. 3361–3364, 2011.

[93] Y. Q. Fu *et al.*, "Microfluidics based on ZnO/nanocrystalline diamond surface acoustic wave devices," *Biomicrofluidics*, vol. 6, no. 2, p. 24105, 2012.

[94] T. Dung Luong and N. Trung Nguyen, “Surface acoustic wave driven microfluidics-a review,” *Micro Nanosyst.*, vol. 2, no. 3, pp. 217–225, 2010.

[95] W.-L. Su *et al.*, “Acoustic and ultrasonic monitoring of inkjet droplets.” Google Patents, 27-Jul-1999.

[96] K. Chono, N. Shimizu, Y. Matsui, J. Kondoh, and S. Shiokawa, “Development of Novel Atomization System Based on SAW Streaming,” *Jpn. J. Appl. Phys.*, vol. 43, no. 5B, pp. 2987–2991, 2004.

[97] A. Qi, J. R. Friend, L. Y. Yeo, D. A. V Morton, M. P. McIntosh, and L. Spiccia, “Miniature inhalation therapy platform using surface acoustic wave microfluidic atomization,” *Lab Chip*, vol. 9, no. 15, pp. 2184–2193, 2009.

[98] Y. Q. Fu, Y. Li, C. Zhao, F. Placido, and A. J. Walton, “Surface acoustic wave nebulization on nanocrystalline ZnO film,” *Appl. Phys. Lett.*, vol. 101, no. 19, p. 194101, 2012.

[99] S. K. R. S. Sankaranarayanan, S. Cular, V. R. Bhethanabotla, and B. Joseph, “Flow induced by acoustic streaming on surface-acoustic-wave devices and its application in biofouling removal: A computational study and comparisons to experiment,” *Phys. Rev. E*, vol. 77, no. 6, p. 66308, 2008.

[100] J. Zhou *et al.*, “Nebulization using ZnO/Si surface acoustic wave devices with focused interdigitated transducers,” *Surf. Coatings Technol.*, vol. 367, pp. 127–134, 2019.

[101] M. Alvarez, J. Friend, and L. Y. Yeo, “Rapid generation of protein aerosols and nanoparticles via surface acoustic wave atomization,” *Nanotechnology*, vol. 19, no. 45, p. 455103, 2008.

[102] J. R. Friend, L. Y. Yeo, D. R. Arifin, and A. Mechler, “Evaporative self-assembly assisted synthesis of polymeric nanoparticles by surface acoustic wave atomization,” *Nanotechnology*, vol. 19, no. 14, p. 145301, 2008.

[103] L. Y. Yeo, J. R. Friend, M. P. McIntosh, E. N. T. Meeusen, and D. A. V Morton, “Ultrasonic nebulization platforms for pulmonary drug delivery,” *Expert Opin. Drug Deliv.*, vol. 7, no. 6, pp. 663–679, 2010.

[104] M. K. Tan, J. R. Friend, and L. Y. Yeo, “Interfacial jetting phenomena induced by focused surface vibrations,” *Phys. Rev. Lett.*, vol. 103, no. 2, p. 24501, 2009.

[105] D. Lee, N. Lee, G. Choi, and H. Cho, “Heat Transfer Characteristics of a Focused Surface Acoustic Wave (F-SAW) Device for Interfacial Droplet Jetting,” *Inventions*, vol. 3, no. 2, p. 38, 2018.

[106] M. Aslam, V. Jeoti, S. Karuppanan, A. Malik, and A. Iqbal, “FEM analysis of sezawa mode SAW sensor for VOC based on CMOS compatible AlN/SiO2/Si multilayer structure,” *Sensors*, vol. 18, no. 6, p. 1687, 2018.

[107] Y.-C. Chen, W.-T. Chang, C.-C. Cheng, J.-Y. Shen, and K.-S. Kao, “Development of human IgE biosensor using Sezawa-mode SAW devices,” *Curr. Appl. Phys.*, vol. 14, no. 4, pp. 608–613, 2014.

[108] F. Hadj-Larbi and R. Serhane, “Sezawa SAW devices: Review of numerical-experimental studies and recent applications,” *Sensors Actuators A Phys.*, 2019.

[109] A. Müller *et al.*, “Sezawa propagation mode in GaN on Si surface acoustic wave type temperature sensor structures operating at GHz frequencies,” *IEEE Electron Device Lett.*, vol. 36, no. 12, pp. 1299–1302, 2015.

[110] X. Y. Du, Y. Q. Fu, J. K. Luo, A. J. Flewitt, and W. I. Milne, “Microfluidic

pumps employing surface acoustic waves generated in ZnO thin films," *J. Appl. Phys.*, vol. 105, no. 2, p. 24508, 2009.

[111] A. R. Rezk, J. K. Tan, and L. Y. Yeo, "HYbriD resonant acoustics (HYDRA)," *Adv. Mater.*, vol. 28, no. 10, pp. 1970–1975, 2016.

[112] E. P. Nguyen, L. Lee, A. R. Rezk, Y. M. Sabri, S. K. Bhargava, and L. Y. Yeo, "Hybrid Surface and Bulk Resonant Acoustics for Concurrent Actuation and Sensing on a Single Microfluidic Device," *Anal. Chem.*, vol. 90, no. 8, pp. 5335–5342, 2018.

[113] M. Alghane, Y. Q. Fu, B. X. Chen, Y. Li, M. P. Y. Desmulliez, and A. J. Walton, "Streaming phenomenon in microdroplets induced by Rayleigh surface acoustic wave," *Microfluid. Nanofluidics*, vol. 13, no. 6, pp. 919–927, 2012.

[114] X. Y. Du *et al.*, "Surface acoustic wave induced streaming and pumping in 128 Y-cut LiNbO3 for microfluidic applications," *J. Micromechanics Microengineering*, vol. 19, no. 3, p. 35016, 2009.

[115] A. Renaudin, P. Tabourier, J.-C. Camart, and C. Druon, "Surface acoustic wave two-dimensional transport and location of microdroplets using echo signal." AIP, 2006.

[116] L. Masini, M. Cecchini, S. Girardo, R. Cingolani, D. Pisignano, and F. Beltram, "Surface-acoustic-wave counterflow micropumps for on-chip liquid motion control in two-dimensional microchannel arrays," *Lab Chip*, vol. 10, no. 15, pp. 1997–2000, 2010.

[117] T. Zheng, C. Wang, Q. Hu, and S. Wei, "The role of electric field in microfluidic heating induced by standing surface acoustic waves," *Appl. Phys. Lett.*, vol. 112,

no. 23, p. 233702, 2018.

[118] D. Beyssen, F. Sarry, and T. Roux-Marchand, “Correlation of heat transfers mechanism (s) and time constant equilibrium on digital Rayleigh-SAW microfluidic system,” *Procedia Eng.*, vol. 120, pp. 1067–1070, 2015.

[119] T. Roux-Marchand, D. Beyssen, F. Sarry, and O. Elmazria, “Rayleigh surface acoustic wave as an efficient heating system for biological reactions: investigation of microdroplet temperature uniformity,” *IEEE Trans. Ultrason. Ferroelectr. Freq. Control*, vol. 62, no. 4, pp. 729–735, 2015.

[120] D. Lee, N. Lee, G. Choi, and H. H. Cho, “Heat transfer characteristics of a focused surface acoustic wave (F-SAW) device for interfacial droplet jetting,” *Inventions*, vol. 3, no. 2, 2018.

[121] B. H. Ha *et al.*, “Acoustothermal heating of polydimethylsiloxane microfluidic system,” *Sci. Rep.*, vol. 5, p. 11851, 2015.

[122] D. Beyssen, L. Le Brizoual, O. Elmazria, P. Alnot, I. Perry, and D. Maillet, “6I-2 Droplet Heating System Based on SAW/Liquid Interaction,” in *2006 IEEE Ultrasonics Symposium*, 2006, pp. 949–952.

[123] M. U. Kopp, A. J. De Mello, and A. Manz, “Chemical amplification: continuous-flow PCR on a chip,” *Science (80-.).*, vol. 280, no. 5366, pp. 1046–1048, 1998.

[124] K. B. Mullis, F. Ferré, and R. A. Gibbs, “The polymerase chain reaction. 1994,” *Binkhauser, Bost.*, 1994.

[125] M. J. Adler, C. Coronel, E. Shelton, J. E. Seegmiller, and N. N. Dewji, “Increased gene expression of Alzheimer disease beta-amyloid precursor protein in senescent cultured fibroblasts,” *Proc. Natl. Acad. Sci.*, vol. 88, no. 1, pp. 16–

20, 1991.

[126] G. Maltezos *et al.*, “Exploring the limits of ultrafast polymerase chain reaction using liquid for thermal heat exchange: A proof of principle,” *Appl. Phys. Lett.*, vol. 97, no. 26, p. 264101, 2010.

[127] G. Maltezos, A. Gomez, J. Zhong, F. A. Gomez, and A. Scherer, “Microfluidic polymerase chain reaction,” *Appl. Phys. Lett.*, vol. 93, no. 24, p. 243901, 2008.

[128] W. J. Benett, J. B. Richards, and F. P. Milanovich, “Convectively driven PCR thermal-cycling.” Google Patents, 01-Jul-2003.

[129] A. Sano, Y. Matsui, and S. Shiokawa, “New manipulator based on surface acoustic wave streaming,” *Jpn. J. Appl. Phys.*, vol. 37, no. 5S, p. 2979, 1998.

[130] K. Chono, N. Shimizu, Y. Matsui, J. Kondoh, and S. Shiokawa, “Development of novel atomization system based on SAW streaming,” *Jpn. J. Appl. Phys.*, vol. 43, no. 5S, p. 2987, 2004.

[131] S. Shiokawa and Y. Matsui, “The dynamics of SAW streaming and its application to fluid devices,” *MRS Online Proc. Libr. Arch.*, vol. 360, 1994.

[132] R. J. Shilton *et al.*, “Rapid and controllable digital microfluidic heating by surface acoustic waves,” *Adv. Funct. Mater.*, vol. 25, no. 37, pp. 5895–5901, 2015.

[133] A. S. Bell and L. C. Ranford-Cartwright, “Real-time quantitative PCR in parasitology,” *TRENDS Parasitol.*, vol. 18, no. 8, pp. 338–342, 2002.

[134] J. Kondoh, N. Shimizu, Y. Matsui, M. Sugimoto, and S. Shiokawa, “Development of SAW thermocycler for small liquid droplets,” in *IEEE Ultrasonics Symposium, 2005.*, 2005, vol. 2, pp. 1023–1027.

[135] N. Ohashin and J. Kondoh, “Temperature control of a droplet on disposable type microfluidic system based on a surface acoustic wave device for blood coagulation monitoring,” in *Ultrasonics Symposium (IUS), 2015 IEEE International*, 2015, pp. 1–4.

[136] H. Berney and J. J. O’riordan, “Impedance measurement monitors blood coagulation,” *Analog Dialogue*, vol. 42, no. 3, pp. 8–42, 2008.

[137] A. Ur, “Changes in the electrical impedance of blood during coagulation,” *Nature*, vol. 226, no. 5242, pp. 269–270, 1970.

[138] J. Park, J. H. Jung, G. Destgeer, H. Ahmed, K. Park, and H. J. Sung, “Acoustothermal tweezer for droplet sorting in a disposable microfluidic chip,” *Lab Chip*, vol. 17, no. 6, pp. 1031–1040, 2017.

[139] M. Alghane, B. X. Chen, Y. Q. Fu, Y. Li, J. K. Luo, and A. J. Walton, “Experimental and numerical investigation of acoustic streaming excited by using a surface acoustic wave device on a 128° YX-LiNbO3 substrate,” *J. Micromechanics Microengineering*, vol. 21, no. 1, p. 15005, 2010.

[140] P. K. Das, A. D. Snider, and V. R. Bhethanabotla, “Acoustothermal heating in surface acoustic wave driven microchannel flow,” *Phys. Fluids*, vol. 31, no. 10, p. 106106, 2019.

[141] A. Wixforth, C. Strobl, C. Gauer, A. Toegl, J. Scriba, and Z. v Guttenberg, “Acoustic manipulation of small droplets,” *Anal. Bioanal. Chem.*, vol. 379, no. 7–8, pp. 982–991, 2004.

[142] V. K. Dhir, “Boiling heat transfer,” *Annu. Rev. Fluid Mech.*, vol. 30, no. 1, pp. 365–401, 1998.

[143] W. A. Sirignano, *Fluid dynamics and transport of droplets and sprays*. Cambridge university press, 2010.

[144] F. M. White, *Fluid mechanics*. McGraw-hill, 1999.

[145] M. M. Alghane, “Surface acoustic wave streaming in a microfluidic system.” Heriot-Watt University, 2013.

[146] B. Sun and H. Sirringhaus, “Surface tension and fluid flow driven self-assembly of ordered ZnO nanorod films for high-performance field effect transistors,” *J. Am. Chem. Soc.*, vol. 128, no. 50, pp. 16231–16237, 2006.

[147] R. M. Arzt, E. Salzmann, and K. Dransfeld, “Elastic surface waves in quartz at 316 MHz,” *Appl. Phys. Lett.*, vol. 10, no. 5, pp. 165–167, 1967.

[148] K. Dransfeld and E. Salzmann, “Excitation, detection, and attenuation of high-frequency elastic surface waves,” *Phys. Acoust.*, vol. 7, pp. 219–272, 2012.

[149] M. J. Fernández *et al.*, “Discrimination of volatile compounds through an electronic nose based on ZnO SAW sensors,” *Sensors Actuators B Chem.*, vol. 127, no. 1, pp. 277–283, 2007.

[150] L. Bo *et al.*, “Surface acoustic wave devices for sensor applications,” *J. Semicond.*, vol. 37, no. 2, p. 21001, 2016.

[151] I. Bretos, R. Jiménez, J. Garcïa-López, L. Pardo, and M. L. Calzada, “Photochemical solution deposition of lead-based ferroelectric films: avoiding the PbO-excess addition at last,” *Chem. Mater.*, vol. 20, no. 18, pp. 5731–5733, 2008.

[152] E. U. Directive, “95/EC of the European Parliament and of the Council of 27 January 2003 on the restriction of the use of certain hazardous substances in

electrical and electronic equipment," *Off. J. L*, vol. 37, p. 13, 2002.

[153] J. Olivares, E. Iborra, M. Clement, L. Vergara, J. Sangrador, and A. Sanz-Hervás, "Piezoelectric actuation of microbridges using AlN," *Sensors Actuators A Phys.*, vol. 123, pp. 590–595, 2005.

[154] T. Aubert *et al.*, "In situ high-temperature characterization of AlN-based surface acoustic wave devices," *J. Appl. Phys.*, vol. 114, no. 1, p. 14505, 2013.

[155] J. Hernando, J. L. Sánchez-Rojas, S. González-Castilla, E. Iborra, A. Ababneh, and U. Schmid, "Simulation and laser vibrometry characterization of piezoelectric AlN thin films," *J. Appl. Phys.*, vol. 104, no. 5, p. 53502, 2008.

[156] G. Piazza, V. Felmetsger, P. Muralt, R. H. Olsson III, and R. Ruby, "Piezoelectric aluminum nitride thin films for microelectromechanical systems," *MRS Bull.*, vol. 37, no. 11, pp. 1051–1061, 2012.

[157] J.-B. Lee, D.-H. Cho, D.-Y. Kim, C.-K. Park, and J.-S. Park, "Relationships between material properties of piezo-electric thin films and device characteristics of film bulk acoustic resonators," *Thin Solid Films*, vol. 516, no. 2–4, pp. 475–480, 2007.

[158] H. P. Loebl, M. Klee, C. Metzmacher, W. Brand, R. Milsom, and P. Lok, "Piezoelectric thin AlN films for bulk acoustic wave (BAW) resonators," *Mater. Chem. Phys.*, vol. 79, no. 2–3, pp. 143–146, 2003.

[159] M. Clement, L. Vergara, J. Sangrador, E. Iborra, and A. Sanz-Hervás, "SAW characteristics of AlN films sputtered on silicon substrates," *Ultrasonics*, vol. 42, no. 1–9, pp. 403–407, 2004.

[160] L. Fan, S. Zhang, H. Ge, and H. Zhang, "Theoretical investigation of acoustic

wave devices based on different piezoelectric films deposited on silicon carbide," *J. Appl. Phys.*, vol. 114, no. 2, p. 24504, 2013.

[161] S. R. Heron, R. Wilson, S. A. Shaffer, D. R. Goodlett, and J. M. Cooper, "Surface acoustic wave nebulization of peptides as a microfluidic interface for mass spectrometry," *Anal. Chem.*, vol. 82, no. 10, pp. 3985–3989, 2010.

[162] G. Wingqvist, "AlN-based sputter-deposited shear mode thin film bulk acoustic resonator (FBAR) for biosensor applications—A review," *Surf. Coatings Technol.*, vol. 205, no. 5, pp. 1279–1286, 2010.

[163] F. Claeyssens, C. L. Freeman, N. L. Allan, Y. Sun, M. N. R. Ashfold, and J. H. Harding, "Growth of ZnO thin films—experiment and theory," *J. Mater. Chem.*, vol. 15, no. 1, pp. 139–148, 2005.

[164] H.-E. Cheng, T.-C. Lin, and W.-C. Chen, "Preparation of [0 0 2] oriented AlN thin films by mid frequency reactive sputtering technique," *Thin Solid Films*, vol. 425, no. 1–2, pp. 85–89, 2003.

[165] M.-S. Wu, W.-C. Shih, and W.-H. Tsai, "Growth of ZnO thin films on interdigital transducer/Corning 7059 glass substrates by two-step fabrication methods for surface acoustic wave applications," *J. Phys. D. Appl. Phys.*, vol. 31, no. 8, p. 943, 1998.

[166] S. Shikata *et al.*, "High frequency SAW devices using SiO2/ZnO/diamond," in *Proc. Int. Symp. Acoust. Wave Devices for Future Mobile Comm. Syst.*, 2001, pp. 227–231.

[167] K. B. Sundaram and A. Khan, "Characterization and optimization of zinc oxide films by rf magnetron sputtering," *Thin Solid Films*, vol. 295, no. 1–2, pp. 87–91,

1997.

[168] W. Wang, W. Yang, H. Wang, and G. Li, “Epitaxial growth of GaN films on unconventional oxide substrates,” *J. Mater. Chem. C*, vol. 2, no. 44, pp. 9342–9358, 2014.

[169] J. Narayan and K. Dovidenko, “Sharma AK and Oktyabrsky S,” *J. Appl. Phys.*, vol. 1998, p. 84, 1998.

[170] A. Szekeres *et al.*, “Structural characterization of AlN films synthesized by pulsed laser deposition,” *Appl. Surf. Sci.*, vol. 257, no. 12, pp. 5370–5374, 2011.

[171] D. C. Look, D. C. Reynolds, and C. W. Litton, “RL: Jones, DB Eason and G Cantwell,” *Appl. Phys. Lett*, vol. 81, p. 1830, 2002.

[172] Y. Chen *et al.*, “Plasma assisted molecular beam epitaxy of ZnO on c-plane sapphire: Growth and characterization,” *J. Appl. Phys.*, vol. 84, no. 7, pp. 3912–3918, 1998.

[173] F. Huber, M. Madel, A. Reiser, S. Bauer, and K. Thonke, “New CVD-based method for the growth of high-quality crystalline zinc oxide layers,” *J. Cryst. Growth*, vol. 445, pp. 58–62, 2016.

[174] T. P. Smith, W. J. Mecouch, P. Q. Miraglia, A. M. Roskowski, P. J. Hartlieb, and R. F. Davis, “Evolution and growth of ZnO thin films on GaN (0 0 0 1) epilayers via metalorganic vapor phase epitaxy,” *J. Cryst. Growth*, vol. 257, no. 3–4, pp. 255–262, 2003.

[175] Y. A. Xi *et al.*, “Very high quality AlN grown on (0001) sapphire by metal-organic vapor phase epitaxy,” *Appl. Phys. Lett.*, vol. 89, no. 10, p. 103106, 2006.

[176] T. Shinagawa, S. Otomo, J. Katayama, and M. Izaki, “Electroless deposition of

transparent conducting and< 0 0 0 1>-oriented ZnO films from aqueous solutions,” *Electrochim. Acta*, vol. 53, no. 3, pp. 1170–1174, 2007.

[177] L. Znaidi, “doi: 10.1016/j. mseb. 2010.07. 001,” *Mater. Sci. Eng. B*, vol. 174, p. 18, 2010.

[178] S. Krüger and G. Grünefeld, “Droplet velocity and acceleration measurements in dense sprays by laser flow tagging,” *Appl. Phys. B*, vol. 71, no. 4, pp. 611–615, 2000.

[179] Z. Guttenberg *et al.*, “Planar chip device for PCR and hybridization with surface acoustic wave pump,” *Lab Chip*, vol. 5, no. 3, pp. 308–317, 2005.

[180] S. D. Aziz and S. Chandra, “Impact, recoil and splashing of molten metal droplets,” *Int. J. Heat Mass Transf.*, vol. 43, no. 16, pp. 2841–2857, 2000.

[181] J. Jung, S. Jeong, and H. Kim, “Investigation of single-droplet/wall collision heat transfer characteristics using infrared thermometry,” *Int. J. Heat Mass Transf.*, vol. 92, pp. 774–783, 2016.

[182] F. Girard, M. Antoni, and K. Sefiane, “Infrared thermography investigation of an evaporating sessile water droplet on heated substrates,” *Langmuir*, vol. 26, no. 7, pp. 4576–4580, 2010.

[183] R. Tuckermann, S. Bauerecker, and H. K. Cammenga, “IR-thermography of evaporating acoustically levitated drops,” *Int. J. Thermophys.*, vol. 26, no. 5, pp. 1583–1594, 2005.

[184] X. Maldague, “Theory and practice of infrared technology for nondestructive testing,” 2001.

[185] A. Saha, S. Basu, and R. Kumar, “Particle image velocimetry and infrared

thermography in a levitated droplet with nanosilica suspensions," *Exp. Fluids*, vol. 52, no. 3, pp. 795–807, 2012.

[186] H. Heuermann, "GSOLT: The calibration procedure for all multi-port vector network analyzers," in *IEEE MTT-S International Microwave Symposium Digest, 2003*, 2003, vol. 3, pp. 1815–1818.

[187] G. Kenanakis, E. Stratakis, K. Vlachou, D. Vernardou, E. Koudoumas, and N. Katsarakis, "Light-induced reversible hydrophilicity of ZnO structures grown by aqueous chemical growth," *Appl. Surf. Sci.*, vol. 254, no. 18, pp. 5695–5699, 2008.

[188] N. Andreeva, T. Ishizaki, P. Baroch, and N. Saito, "High sensitive detection of volatile organic compounds using superhydrophobic quartz crystal microbalance," *Sensors Actuators B Chem.*, vol. 164, no. 1, pp. 15–21, 2012.

[189] K. D. Esmeryan, G. McHale, C. L. Trabi, N. R. Geraldi, and M. I. Newton, "Manipulated wettability of a superhydrophobic quartz crystal microbalance through electrowetting," *J. Phys. D. Appl. Phys.*, vol. 46, no. 34, p. 345307, 2013.

[190] M. Rayner, G. Trägårdh, and C. Trägårdh, "The impact of mass transfer and interfacial expansion rate on droplet size in membrane emulsification processes," *Colloids Surfaces A Physicochem. Eng. Asp.*, vol. 266, no. 1–3, pp. 1–17, 2005.

[191] M. D. Abràmoff, P. J. Magalhães, and S. J. Ram, "Image processing with ImageJ," *Biophotonics Int.*, vol. 11, no. 7, pp. 36–42, 2004.

[192] A. Cavallini and R. Zecchin, "A dimensionless correlation for heat transfer in forced convection condensation," in *International Heat Transfer Conference Digital Library*, 1974.

[193] S. S. Sazhin, “Advanced models of fuel droplet heating and evaporation,” *Prog. Energy Combust. Sci.*, vol. 32, no. 2, pp. 162–214, 2006.

[194] R. B. Bird, W. E. Stewart, and E. N. Lightfoot, *Transport phenomena*. John Wiley & Sons, 2007.

[195] Y. Cengel, *Heat and mass transfer: fundamentals and applications*. McGraw-Hill Higher Education, 2014.

[196] D. Gosselin, D. Chaussy, N. Belgacem, F. Navarro, and J. Berthier, “Heat Transfer Correlations for Free Convection from Suspended Microheaters,” *Sensors & Transducers*, vol. 203, no. 8, p. 16, 2016.

[197] R. Tao *et al.*, “Thin film flexible/bendable acoustic wave devices: Evolution, hybridization and decoupling of multiple acoustic wave modes,” *Surf. Coatings Technol.*, vol. 357, pp. 587–594, 2019.

[198] M. H. Biroun, M. T. Rahmati, M. Jangi, R. Tao, B. X. Chen, and Y. Q. Fu, “Computational and experimental analysis of droplet transportation/jetting behaviours driven by thin film surface acoustic waves,” *Sensors Actuators A Phys.*, vol. 299, p. 111624, 2019.

[199] M. J. Moran, H. N. Shapiro, B. R. Munson, D. P. DeWitt, and F. M. Thermodynamics, “Introduction to thermal systems engineering,” *Thermodyn. Fluid Mech. Heat Transf.*, 2003.

[200] J. H. Lienhard, *A heat transfer textbook*. Courier Dover Publications, 2019.

[201] W. Wang *et al.*, “Comparative study on microfluidic performance of ZnO surface acoustic wave devices on various substrates,” *J. Electrochem. Soc.*, vol. 161, no. 10, pp. B230–B236, 2014.

[202] T. Roux-Marchand, F. Sarry, D. Beyssen, and O. Elmazria, “Temperature uniformity of microdroplet heated by buried surface acoustic wave device,” in *Ultrasonics Symposium (IUS), 2014 IEEE International*, 2014, pp. 1956–1959.

Appendices

Appendix A: MATLAB code to get temperature distribution inside the droplet

Following is the example code to get temperature distribution inside the droplet for Al plate substrate with thickness h= 200 μm and wavelength λ=200 μm with 25 μl droplet at power level +3.0 dBm (5.60W). **The text after the % sign is the comments for MATLAB.**

```
%Al plate with wavelength 200 μm and thickness 200 μm
%First peak 26.450 MHz (25 μl) droplet SIDE VIEW
%This code reads a matrix for 1853 frames of 5.60 W (+3.0 dBm).
```

First of all, I find out the exact location of the droplet from the whole frame, getting its dimensions. Then dividing the whole droplet into 16 elements of equal matrix size. After this, using for loop, it will continue for all of the frames available in the original file to get temperature rise of each droplet elements. Then we are taking the mean of all the pixels for each frame.

```
%Each frame has 480 rows and 640 columns (this is a resolution of a camera)
%This code only displays temperature graph data against frames, not difference or rise in temperature

clear all;
close all;
clear TotalIm;
clear TotalIm1;
clear I
%clear I1
clc

TotalIm =csvread('+3.0dbm.csv',10,1);

%Reading and saving original data file CSV format. 10,1 means it will start reading from 11th row and 2nd column since the first 10 rows have raw data for MATLAB which it can’t read.
```

```
TotalIm1 =csvread('+3.0dbm.csv',10,1,[10,1,490,640]);

%This will read the first frame only, this will start reading from under 11th row and second column and it will read the next 480 rows and 640 columns since one frame equals 480*640.
%Clearing data from previously saved data if any

clear I_area;
clear I_area2;
clear I_area3;
clear I_area4;
clear I_area5;
clear I_area6;
clear I_area7;
clear I_area8;
clear I_area9;
clear I_area10;
clear I_area11;
clear I_area12;
clear I_area13;
clear I_area14;
clear I_area15;
clear I_area16;
%main program here
 num_frames = 1853;
 for i=1:num_frames
   I    = TotalIm((i-1)*480+1:480*i ,:);  %it will increase number of frames from 1 to 2,3,4,5, . . . .(when i=1, 1:480, when i=2,481:960
```

%Following section is to find out the exact location of the droplet in picture

This limits colour bar from 20 to 30 rather any other value, c-axis [20 30], 20 is min value of bar and 30 is the maximum value

```
% subplot(1,2,1);imagesc(TotalIm1)  %this is to know which matrix size is the best area of our interest.
%     caxis([22 30])
%     subplot(1,2,2),imagesc(TotalIm1(359:402,339:398)) %this makes 60*60 matrix
%     caxis([22 30])

%Following code will divide the whole droplet into 16 portions to get
  %for 1st element of the droplet
  x = 359:369;
  y = 339:353;
  I_area(:,i)  = reshape(I(x,y),[length(x)*length(y), 1]); %it will reshape 16*16 matrix to 256*1, there was problem in saved value of I_area that is why number of elements were not matching.

  %for 2nd element of the droplet
  x = 359:369;
  y = 354:368;
  I_area2(:,i)  = reshape(I(x,y),[length(x)*length(y), 1]);

  %for 3rd element of the droplet
  x = 359:369;
  y = 369:383;
  I_area3(:,i)  = reshape(I(x,y),[length(x)*length(y), 1]);

  %for 4th element of the droplet
  x = 359:369;
  y = 384:398;
  I_area4(:,i)  = reshape(I(x,y),[length(x)*length(y), 1]);

  %for 5th element of the droplet
  x = 370:380;
  y = 339:353;
  I_area5(:,i)  = reshape(I(x,y),[length(x)*length(y), 1]);
```

```
%for 6th element of the droplet
x = 370:380;
y = 354:368;
I_area6(:,i)  = reshape(I(x,y),[length(x)*length(y), 1]);

%for 7th element of the droplet
x = 370:380;
y = 369:383;
I_area7(:,i)  = reshape(I(x,y),[length(x)*length(y), 1]);

%for 8th element of the droplet
x = 370:380;
y = 384:398;
I_area8(:,i)  = reshape(I(x,y),[length(x)*length(y), 1]);

%for 9th element of the droplet
x = 381:391;
y = 339:353;
I_area9(:,i)  = reshape(I(x,y),[length(x)*length(y), 1]);

%for 10th element of the droplet
x = 381:391;
y = 354:368;
I_area10(:,i)  = reshape(I(x,y),[length(x)*length(y), 1]);

%for 11th element of the droplet
x = 381:391;
y = 369:383;
I_area11(:,i)  = reshape(I(x,y),[length(x)*length(y), 1]);

%for 12th element of the droplet
x = 381:391;
```

```
  y = 384:398;
  I_area12(:,i)  = reshape(I(x,y),[length(x)*length(y), 1]);

  %for 13th element of the droplet
  x = 392:402;
  y = 339:353;
  I_area13(:,i)  = reshape(I(x,y),[length(x)*length(y), 1]);

  %for 14th element of the droplet
  x = 392:402;
  y = 354:368;
  I_area14(:,i)  = reshape(I(x,y),[length(x)*length(y), 1]);

  %for 15th element of the droplet
  x = 392:402;
  y = 369:383;
  I_area15(:,i)  = reshape(I(x,y),[length(x)*length(y), 1]);

  %for 16th element of the droplet
  x = 392:402;
  y = 384:398;
  I_area16(:,i)  = reshape(I(x,y),[length(x)*length(y), 1]);
end

%Following code will take a mean of 256 pixels for each frame because our matrix is
256*159 that is why we used the command 'mean' (I_area,1). If we want to take the mean
of 159 frames

% mean of all pixels in the first element of the droplet
I_final = mean(I_area,1);    %1 means all columns in that matrix

% mean of all pixels in the second element of the droplet
```

```
I_final2 = mean(I_area2,1);

% mean of all pixels in the third element of the droplet

I_final3 = mean(I_area3,1);

% mean of all pixels in the fourth element of the droplet

I_final4 = mean(I_area4,1);

% mean of all pixels in the fifth element of the droplet

I_final5 = mean(I_area5,1);

% mean of all pixels in the sixth element of the droplet

I_final6 = mean(I_area6,1);

% mean of all pixels in the seventh element of the droplet

I_final7 = mean(I_area7,1);

% mean of all pixels in the eighth element of the droplet

I_final8 = mean(I_area8,1);

% mean of all pixels in the ninth element of the droplet
I_final9 = mean(I_area9,1);

% mean of all pixels in the tenth element of the droplet
I_final10 = mean(I_area10,1);

% mean of all pixels in the eleventh element of the droplet
```

```
I_final11 = mean(I_area11,1);

% mean of all pixels in the twelfth element of the droplet
I_final12 = mean(I_area12,1);

% mean of all pixels in the thirteenth element of the droplet
I_final13 = mean(I_area13,1);

% mean of all pixels in the fourteenth element of the droplet
I_final14 = mean(I_area14,1);

% mean of all pixels in the fifteenth element of the droplet
I_final15 = mean(I_area15,1);

% mean of all pixels in the sixteenth element of the droplet
I_final16 = mean(I_area16,1);
```

%Now plotting a graph for each element against the number of frames

```
figure;plot(I_final,'.')        %plot first element, ‘.’ Is specifying graph line with dots
xlabel('Time(sec)')
ylabel('Rise in temp (C)')
title('Temp of 25 ul droplet Part1 Al Pl3 (26.450 MHz) 5.60W')

%plot 2nd element
figure;plot(I_final2,'.')
xlabel('Time(sec)')
ylabel('Rise in temp (C)')
title('Temp of 25 ul droplet Part2')

%plot 3rd element
figure;plot(I_final3,'.')
xlabel('Time(sec)')
```

```
ylabel('Rise in temp (C)')
title('Temp of 25 ul droplet Part3')

%plot 4th element
figure;plot(I_final4,'.')
xlabel('Time(sec)')
ylabel('Rise in temp (C)')
title('Temp of 25 ul droplet Part4')

%plot 5th element
figure;plot(I_final5,'.')
xlabel('Time(sec)')
ylabel('Rise in temp (C)')
title('Temp of 25 ul droplet Part5')

%plot 6th element
figure;plot(I_final6,'.')
xlabel('Time(sec)')
ylabel('Rise in temp (C)')
title('Temp of 25 ul droplet Part6')

%plot 7th element
figure;plot(I_final7,'.')
xlabel('Time(sec)')
ylabel('Rise in temp (C)')
title('Temp of 25 ul droplet Part7')

%plot 8th element
figure;plot(I_final8,'.')
xlabel('Time(sec)')
ylabel('Rise in temp (C)')
title('Temp of 25 ul droplet Part8')
```

```
%plot 9th element
figure;plot(I_final9,'.')
xlabel('Time(sec)')
ylabel('Rise in temp (C)')
title('Temp of 25 ul droplet Part9')

%plot 10th element
figure;plot(I_final10,'.')
xlabel('Time(sec)')
ylabel('Rise in temp (C)')
title('Temp of 25 ul droplet Part10')

%plot 11th element
figure;plot(I_final11,'.')
xlabel('Time(sec)')
ylabel('Rise in temp (C)')
title('Temp of 25 ul droplet Part11')

%plot 12th element
figure;plot(I_final12,'.')
xlabel('Time(sec)')
ylabel('Rise in temp (C)')
title('Temp of 25 ul droplet Part12')

%plot 13th element
figure;plot(I_final13,'.')
xlabel('Time(sec)')
ylabel('Rise in temp (C)')
title('Temp of 25 ul droplet Part13')

%plot 14th element
figure;plot(I_final14,'.')
xlabel('Time(sec)')
```

```
ylabel('Rise in temp (C)')
title('Temp of 25 ul droplet Part14')

%plot 15th element
figure;plot(I_final15,'.')
xlabel('Time(sec)')
ylabel('Rise in temp (C)')
title('Temp of 25 ul droplet Part15')

%plot 16th element
figure;plot(I_final16,'.')
xlabel('Time(sec)')
ylabel('Rise in temp (C)')
title('Temp of 25 ul droplet Part16 Al Pl3 (26.450 MHz) 5.60W')
```

Appendix B: Code for the rise in T_d and generating multiple lines on graphs

```
%This code will take diff. and then plotting multiple lines (4 elements) on one graph for whole data
%Using one initial temp (21.90 C) which is the temperature before giving SAW power to the droplet)
%for +3.0 dBm_5.60 W (26.450 MHz) Top Side_Side View_25 ul
%Taking rise in temp by substrating initial temp.

close all;
%Code for diff. and plotting 1-4 elements
I_diff1=minus(I_final,21.90); %digit values are initial values of each part/element which will be subtracted.
b = 0:1/30:70;                    %for converting frames into seconds, since 1 second has 30 frames, so 1/30, 70 is presenting a maximum number of seconds
I_diff2=minus(I_final2,21.90);

I_diff3=minus(I_final3,21.90);

I_diff4=minus(I_final4,21.90);

%For multiple lines on the same graph
%1853 is the number of frames

figure;
p1=plot(b(1:1853),(I_diff1),'.');grid on; hold on;             %plot first portion
p2=plot(b(1:1853),(I_diff2),'-');grid on; hold on;             %plot second portion
p3=plot(b(1:1853),(I_diff3),'^');grid on; hold on;             %plot third portion
p4=plot(b(1:1853),(I_diff4),'*');grid on; hold on;             %plot fourth portion

h_legend = legend ([p1 p2 p3 p4],{'Part1','Part2', 'Part3', 'Part4'});  %change names as relevant
%set(h_legend,'FontSize',14);  %change size of legend as relevant
xlabel('Time (s)')
```

```
ylabel('Temp Diff (C)')
title('Temp diff. of 25 ul 5.60W Al Pl3 (26.450 MHz) Part1-4')

%Code for diff. and plotting  5-8 portions

I_diff5=minus(I_final5,21.90);
b = 0:1/30:70;                    %for converting frames into seconds, since 1 second have 30 frames, so 1/30, 50 is presenting maximum number of seconds

I_diff6=minus(I_final6,21.90);

I_diff7=minus(I_final7,21.90);

I_diff8=minus(I_final8,21.90);

%plotting multiple lines on same figure 5-8
figure;
p5=plot(b(1:1853),(I_diff5),'.');grid on; hold on;              %plot fifth portion
p6=plot(b(1:1853),(I_diff6),'-');grid on; hold on;              %plot sixth portion
p7=plot(b(1:1853),(I_diff7),'^');grid on; hold on;               %plot seventh portion
p8=plot(b(1:1853),(I_diff8),'*');grid on; hold on;               %plot eighth portion

h_legend = legend ([p5 p6 p7 p8],{'Part5','Part6', 'Part7', 'Part8'});  %change names as relevant
%set(h_legend,'FontSize',14);  %change size of legend as relevant
xlabel('Time (s)')
ylabel('Temp Diff (C)')
title('Temp diff. of 25 ul 5.60W Al Pl3 (26.450 MHz) Part5-8')

%Code for diff. and plotting  9-12 elements
I_diff9=minus(I_final9,21.90);

I_diff10=minus(I_final10,21.90);
```

```
I_diff11=minus(I_final11,21.90);

I_diff12=minus(I_final12,21.90);

%plotting multiple lines on same figure 9-12

figure;
p9=plot(b(1:1853),(I_diff9),'.');grid on; hold on;          %plot ninth element and hold
p10=plot(b(1:1853),(I_diff10),'-');grid on; hold on;         %plot tenth element and hold
p11=plot(b(1:1853),(I_diff11),'^');grid on; hold on;         %plot eleventh element and hold
p12=plot(b(1:1853),(I_diff12),'*');grid on; hold on;         %plot twelvth element and display

h_legend = legend ([p9 p10 p11 p12],{'Part9','Part10', 'Part11', 'Part12'});   %change names as relevant
%set(h_legend,'FontSize',14);  %change size of legend as relevant
xlabel('Time(s)')
ylabel('Temp Diff (C)')
title('Temp diff. of 25 ul 5.60W Al Pl3 (26.450 MHz) Part9-12')

%Code for diff. and plotting  13-16 elements
I_diff13=minus(I_final13,21.90);

I_diff14=minus(I_final14,21.90);

I_diff15=minus(I_final15,21.90);

I_diff16=minus(I_final16,21.90);

%now plotting 13-16 portions of droplet
figure;
```

```
p13=plot(b(1:1853),(I_diff13),'.');grid on; hold on;               %plot thirteenth element and hold
p14=plot(b(1:1853),(I_diff14),'-');grid on; hold on;               %plot fourteenth element and hold
p15=plot(b(1:1853),(I_diff15),'^');grid on; hold on;               %plot fifteenth element and hold
p16=plot(b(1:1853),(I_diff16),'*');grid on; hold on;               %plot sixteenth element and hold

h_legend = legend ([p13 p14 p15 p16],{'Part13','Part14', 'Part15', 'Part16'});  %change names as relevant
%set(h_legend,'FontSize',14);  %change size of legend as relevant
xlabel('Time(s)')
ylabel('Temp Diff (C)')
title('Temp diff. of 25 ul 5.60W Al Pl3 (26.450 MHz) Part13-16')
%end

%code for writing all this data in excel file

filename='data1.xlsx';

data1 = [b(1:1853)' I_diff1' I_diff2' I_diff3' I_diff4' I_diff5' I_diff6' I_diff7' I_diff8' I_diff9' I_diff10' I_diff11' I_diff12' I_diff13' I_diff14' I_diff15' I_diff16'];
xlswrite(filename,data1)
```